Turbulent Partially Premixed Combustion: DNS Analysis and RANS Simulation

Shaohong Ruan

Wolfson College

Department of Engineering

University of Cambridge

A dissertation submitted to the
University of Cambridge

for the degree of
Doctor of Philosophy

September 2012

Turbulent Partially Premixed Combustion: DNS Analysis and RANS Simulation

Shaohong Ruan

Increasingly stringent regulation of pollutant emission has motivated the search for cleaner and more efficient combustion devices, which remain the primary means of power generation and propulsion for all kinds of transport. Fuel-lean premixed combustion technology has been identified to be a promising approach, despite many difficulties involve, notably issues concerning flame stability and ignitability. A partially premixed system has been introduced to remedy these problems, however, our understanding on this combustion mode needs to be greatly improved to realise its full potential.

This thesis aims to further the understanding of various fundamental physical processes in turbulent partially premixed flames. DNS data of a laboratory-scale hydrogen turbulent jet lifted flame is analysed in this study. The partially premixed nature of this flame is established by examining the instantaneous and averaged reaction rates and the "Flame Index", which indicate premixed and diffusion burning modes coexisting.

The behaviour of turbulent flame stretch and its relation to other physical processes, in particular the scalar-turbulence interaction, the effects of partial premixing on the displacement speed of iso-scalar surface and its correlation with the surface curvature are explored using DNS data. The scalar gradient alignment characteristics change from aligning with the most compressive strain to aligning with the most extensive one in regions of intensive heat release. This alignment change creates negative normal strain rate which can result in negative surface averaged tangential strain rate. The partial premixing affects the flame surface displacement speed through the mixture fraction dissipation rate and a second derivative in the mixture fraction space. The correlation of curvature and displacement speed is found to be negative in general and the effects of partial premixing act to reduce this negative correlation. The combined effects of the normal strain rate and the displacement speed/curvature correlation contribute to the negative mean flame stretch observed in the flame brush.

Scalar dissipation rates (SDR) of the mixture fraction $\widetilde{\epsilon}_{ZZ}$, progress variable $\widetilde{\epsilon}_{cc}$ and their cross dissipation rates (CDR) $\widetilde{\epsilon}_{cZ}$ are identified as important quantities

in the modelling of partially premixed flames. Their behaviours in the lifted flame stabilisation region are examined in a unified framework. It is found that SDR of mixture fraction is well below the quenching value in this region while SDR of progress variable is smaller than that in laminar flames. The CDR changes from weakly positive to negative at the flame leading edge due to the change in scalar gradient alignment characteristics. Axial and radial variation of these quantities are analysed and it is found that $\widetilde{\epsilon}_{cc}$ is an order of magnitude bigger than $\widetilde{\epsilon}_{ZZ}$. $\widetilde{\epsilon}_{cZ}$ is two orders of magnitude smaller than $\widetilde{\epsilon}_{cc}$ and it can be either positive or negative depending on local flow and flame conditions. Simple algebraic models show reasonable agreement compared to DNS when a suitable definition of c is used. Further statistics of the scalar gradients are presented and a presumed lognormal distribution is found to give reasonable results for their marginal PDFs and a bivariate lognormal distribution is a good approximation for their joint PDF.

Four mean reaction rate closures based on presumed PDF and flamelets are assessed *a priori* using DNS data. The turbulent flame front structure is first compared with unstrained and strained laminar premixed and diffusion flamelets. It is found that unstrained premixed flamelets give overall reasonable approximation in most parts of this flame. A joint PDF model which includes the correlation between mixture fraction and progress variable using a "copula" method shows excellent agreement with DNS results while their statistical independence does not hold in the burning regions of this partially premixed flame. The unstrained premixed flamelet with the correlated joint PDF method is identified to be the most appropriate model for the lifted jet flame calculation.

This model is then used in the RANS simulation of turbulent jet lifted flames. A new model to include the contribution from diffusion burning and the effects of partial premixing due to SDR of mixture fraction is also identified and included in the calculation. These models are implemented in a commercial CFD code "Fluent" with user defined scalars and functions. It is found that both the correlated joint PDF model and the model accounting for the diffusive burning in partial premixing are important in order to accurately predict flame lift-off height compared to the experiments.

Declaration

This dissertation is the result of my own work and includes nothing which is the outcome of work done in collaboration except where specifically indicated in the text. It has not been submitted for another qualification to this or any other university.

The full length of this thesis is approximately 40,000 words and includes 70 figures.

Shaohong Ruan

28th September 2012

Acknowledgements

I would like to express my sincere gratitude to Dr. N. Swaminathan for his advice, guidance, patience, support and encouragement. It is my privilege to work under his supervision. There is never a time when he is too busy to answer any of my questions, for which I am forever in his debt. It also my honor to have the opportunities to discuss with Professor K. N. C. Bray occasionally during my PhD. I have benefited immensely from his insightful advices and suggestions. I would also like to thank Professor Epaminondas Mastorakos for providing helpful advice and encouragement and Dr. Yasuhiro Mizobuchi of JAXA for his invaluable help with the interpretation of DNS data base. The DNS data was transferred to Cambridge from JAXA, Japan through a research collaboration. The financial supports of Mitsubishi Heavy Industries (MHI) and travel grant from the Engineering Department are gratefully acknowledged. I would also like to thank Mr. Peter Benie for his amazing IT support. I would like to express my sincere gratitude to Dr. Jim Rogerson who kindly helped me to proofread this thesis.

I am grateful to the members of the former Heat Gallery, for their friendship and enjoyable discussions: Drs. Hemanth Kolla, Oliver Darbyshire, Shokri Amzin and Tom Dunstan, Yuki Mimamoto, Irufan Ahmed and Zacharias Nicolaou. In particular, I would like to especially thank Ruigang Zhou and Huangwei Zhang for general discussions, Oliver Darbyshire for allowing me to use his PDF codes and Vijay Veera for invaluable help with Fluent and UDFs. The discussions with visiting Professor Gang Xu from Chinese Academy of Science provided great advise and encouragement.

Finally, none of this would have been possible without the full support of my loving grandparents, parents, my brother and my small family. Thanks for being with me.

To my loving grandparents, parents, brother and my family

Contents

List of Figures

List of Tables

Nomenclature

Roman Symbols

c	Reaction progress variable
D	Diameter of fuel jet nozzle, $D = 2$ mm
dh	Uniform grid spacing in the DNS
dr	Ring width in the ring averaging procedure
Ka	Karlovitz number
N_{cc}	Instantaneous scalar dissipation rate of progress variable, $N_{cc} = \mathcal{D}_c(\nabla c \cdot \nabla c)$
N_{cZ}	Instantaneous cross scalar dissipation rate, $N_{cZ} = \mathcal{D}_Z(\nabla c \cdot \nabla Z)$
N_{ZZ}	Instantaneous scalar dissipation rate for mixture fraction, $N_{ZZ} = \mathcal{D}_Z(\nabla Z \cdot \nabla Z)$
p	The correlation coefficient of a joint lognormal PDF
R	Radial distance to jet centre, $R = (x^2 + z^2)^{1/2}$
S_L^0	unstrained laminar premixed flame speed
Sc_m	Turbulent Schmidt number
x	Cross stream direction of the jet
y	Streamwise direction of the jet
Y_i	Mass fraction of species i

Z Mixture fraction

z Cross stream direction of the jet

Z_i Mass fraction of element i

$\mathcal{D}_c$ Diffusivity of the progress variable

$\mathcal{D}_Z$ Diffusivity of the mixture fraction

F complex function

$\tilde{k}$ Turbulent kinetic energy

Greek Symbols

δ Zeldovich thickness

δ_L^0 unstrained laminar premixed flame thermal thickness

$\dot{\omega}_c^*$ Apparent Reaction rate of c, defined in Eq.(2.70)

$\dot{\omega}_i$ Reaction rate of scalar i

ϕ Mixture equivalence ratio

ρ Mixture density

τ Normalised temperature rise

$\tilde{\epsilon}$ Turbulent dissipation

$\tilde{\epsilon}_{ZZ}$ Favre averaged scalar dissipation rate of mixture fraction, $\tilde{\epsilon}_{ZZ} = \overline{\rho\mathcal{D}_Z(\nabla Z'' \cdot \nabla Z'')}/\bar{\rho}$

$\widetilde{\epsilon}_{cc}$ Favre averaged scalar dissipation rate of progress variable, $\widetilde{\epsilon}_{cc} = \overline{\rho\mathcal{D}_c(\nabla c'' \cdot \nabla c'')}/\bar{\rho}$

$\widetilde{\epsilon}_{cZ}$ Favre averaged cross scalar dissipation rate, $\widetilde{\epsilon}_{cZ} = \overline{\rho\mathcal{D}_Z(\nabla c'' \cdot \nabla Z'')}/\bar{\rho}$

η_k Kolmogorov length scale

γ a simply closed curve on a complex plane

ι unit imaginary number $\sqrt{-1}$

Λ Turbulent integral length scale

π $\simeq 3.14\ldots$

μ Dynamic visocity $\mu = \rho\nu$

ν Kinematic visocity

$\bar{Q}$ Ensemble averaged of quantity Q

$\tilde{Q}$ Favre averaged of quantity Q, $\tilde{Q} \equiv \overline{\rho Q}/\bar{\rho}$

Q'' Favre fluctuation of quantity Q, $Q'' \equiv Q - \tilde{Q}$

Superscripts

j superscript index

Subscripts

0 subscript index

Other Symbols

$\oint_\gamma$ integration around a curve γ

Acronyms

BML Bray-Moss-Libby

CDR Cross Dissipation Rate

CFD Computational Fluid Dynamics

CMC Conditional Moment Closure

DNS Direct Numerical Simulation

EBU Eddy Break Up

EDC Eddy Dissipation Concept

FGM Flamelet Generated Manifold

FPI Flamelet Prolongation ILDM

GHG Green House Gas

ILDM Intrinsic Low Dimensional Manifold

JAXA Japan Aerospace Exploration Agency

LES Large Eddy Simulation

PDF Probability Density Function

PM Particulate Matter

RANS Reynolds Averaged Navier-Stokes

SDR Scalar Dissipation Rate

SGS Sub-Grid Scaled

UHC Unburnt Hydrocanbons

Chapter 1

Introduction

The energy provided by combustion of various fuels has enabled human beings to cook and stay warm in winter for thousands of years. Since the industrial revolution, the capability of further utilising combustion technology has turned over a new page in human history. The development of reciprocating internal combustion engines for land, sea and air transport has made long distance travelling easier and the world smaller. Large scale land-based coal-fired and gas turbines generate a significant amount of energy for our daily use, which is considered to be a very basic need in modern society.

All these advancements in the quality of life are not without consequence, notably at the expense of environment. The major drawback for combustion technology is the emission of pollutants. They include sulphur oxides (SOx) and particulate matter (PM) which caused the notorious smog in London UK in the 1950s; sulphur and nitric oxides (NOx) which can lead to formation of acid rain; un-burnt hydrocarbons (UHC), soots and carbon monoxide (CO) are other examples. In recent years, it has been widely recognised that greenhouse gases (GHG), mainly consisting of carbon dioxide (CO2), are having detrimental effects on the environment with dire consequences such as global warming. All of these lead to the development of alternative energy technologies and increasingly stringent regulation on the emission from modern combustion devices. Despite recent progress in alternative energy technologies, such as solar cell, wind power, fuel cell and nuclear energy, significant limitation remains, such as high capital costs, low energy conversion efficiency, and low public acceptance level due to

safety and security concerns (US Energy Information Administration, 2010). It is likely that combustion technology will remain as the primary means of energy production in the foreseeable future. This is particularly the case in high power density applications such as transport. It is thus compelling to improve the efficiency and environmental friendliness of combustion devices.

Practical combustion devices are traditionally considered to operate in two different combustion modes. In the non-premixed mode, the fuel and air are separated and only meet in the reacting region through molecular diffusion. The compression-ignition diesel engine is one example. In the premixed mode, fuel and oxidizer (air) are fully mixed at molecular level before they are consumed in the flames. The standard spark-ignited gasoline engine is one example. In practice, most combustion systems operate in a combination of these two modes, known as partially premixed burning mode, either due to practical limitations or intentional design for improved performance.

Fuel-lean premixed combustion is known [80] to have the potential to simultaneously reduce emissions and to increase cycle efficiency. The resulting low temperature leads to low NOx production, and the lean-premixing helps to reduce CO, UHC and PM. Significant advances are yet to be made for lean premixed systems operating over a wide range of conditions with desirable characteristics, mainly due to issues such as flame stability, extinction, and mixture ignitability. Lean premixed combustion is highly susceptible to flame instability issues, due to relatively low flame speed and strong variation with mixture compositions. While small fluctuations of mixture composition at the combustor inlet may be inevitable, this can cause large changes in the local heat release rate. This unsteady heat release coupled with pressure fluctuations can result in combustion instability that can damage the combustion system.

A new generation of combustion systems tries to overcome the above mentioned problems by intentionally introducing partially premixed burning mode. For example, the direct-injection spark-ignited and multiple-injection diesel [124] and lean, fast mixing gas turbine combustors [127], involve uneven mixing of fuel and air. This uneven premixing creates zones with slightly rich mixture that can enhance flame stability or ignitability, but is overall lean enough to reduce NOx, PM and UHC. Unfortunately, research on turbulent combustion has primarily

focused on either premixed or non-premixed combustion and our understanding on partially premixed combustion physics needs to be greatly improved to realise its full potential.

Computational Fluid Dynamics (CFD) has become a widely used tool in the design cycle, research and development in industry as it can provide quicker and more economical solutions while experimental approaches can be extremely expensive and difficult for the harsh environment inside the combustor. However, accurate prediction and design hinges on validation of the models for the physics of partially premixed combustion. The current work aims to improve our understanding of various physical processes involved in partially premixed combustion and thereby to further our modelling capabilities. To this end, data from high fidelity numerical simulation of a lifted turbulent jet diffusion flame, conducted at Japan Aerospace Exploration Agency (JAXA) in Tokyo, are analysed. The broad objectives of this thesis are:

1. to analyse the burning modes in the jet flame and explore if this is indeed a non-premixed flame or a good example of partially premixed combustion.

2. to study many fundamental quantities that are crucial for the modelling of turbulent combustion;

3. to appraise and assess the validity of some common turbulent combustion models based on flamelet approaches for partially premixed combustion;

4. to apply the new insights gained in 2 and 3 and develop models if required.

5. to implement the validated models in a commercial CFD code and demonstrate their benefits.

1.1 Thesis Outline

The outline of this thesis is as follows. Chapter 2 starts with the background information on turbulent combustion by firstly discussing the canonical premixed, diffusion and partially premixed flames. The governing equations for turbulent

combustion are then presented and the multiscale nature of turbulent combustion is discussed to elucidate the challenges. The numerical simulation framework is then outlined along with a brief review of various modelling approaches for turbulent non-premixed, premixed and partially premixed combustion. This chapter concludes with the specific issues that would be addressed in later chapters of this thesis.

Chapter 3 introduces the Direct Numerical Simulation (DNS) of a hydrogen turbulent jet lifted flame performed in JAXA. The data processing techniques are presented, followed by a discussion of the general feature of this flame. The partially premixed nature of this lifted flame is then highlighted and discussed.

Chapter 4 investigates flame stretch in partially premixed flames using the JAXA DNS data. The effects of partial premixing on various important quantities, notably the turbulent-scalar interaction, the displacement speed and flame curvature, are analysed and discussed.

Chapter 5 presents detailed results and discussion on the scalars and their dissipation rates extracted from the DNS data. The dissipation rates in the flame stabilisation region are analysed and discussed to elucidate their important roles in the stabilisation mechanism. Algebraic models for the dissipation rates of both reacting and nonreacting scalars are tested. Statistics of scalars and their gradients are presented and discussed.

A priori assessment of various models for the mean reaction rate is conducted in Chapter 6 . The flame front structure in the DNS data is compared with laminar flame calculations. Various presumed PDF models for scalars are tested against DNS results. The best possible modelling approach is then identified.

Chapter 7 describes RANS simulations for turbulent jet lifted flames using the models identified in the previous chapters. Model implementation and the effects of various modelling assumptions are discussed. The variation of flame lift-off heights with the jet velocity is shown to be captured well by the modelling approach followed in this work. Comparisons are also made with experimental measurements .

The conclusions are summarised in chapter 8 along with suggestions for future work.

Chapter 2

Background

2.1 Flames Classification

2.1.1 Non-premixed and Premixed Flames

As noted in Chapter 1, combustion systems can be divided into two categories. In a non-premixed system, the fuel and oxidizer enter the reaction zone separately by molecular diffusion. To describe the mixing state between the fuel and oxidizer, an inert scalar known as the mixture fraction Z, can be constructed. It has a value of zero in the unmixed oxidant and unity in the unmixed fuel. The archetypical 1D laminar non-premixed flame is the counter flow diffusion flame where the fuel and air are injected from nozzles opposing each other as shown in Fig.2.1(a). Diffusion flame normally occurs at the stoichiometric mixture, where fuel and air are mixed to the right composition for complete combustion. Peak value of temperature and reaction rate also occur close to stoichiometric region.

In a premixed system, reactants are fully mixed at the molecular level before they encounter the flame. Typically, the thermo-chemical state of the flame can be described by a carefully constructed reactive scalar, known as progress variable c, such that it is zero in the unburnt reactants and unity in the fully burnt products. In stagnant mixture, a premixed flame can propagate into the unburnt mixture at a speed known as the laminar flame speed. Fig.2.1(b) shows a 1D archetypical freely propagating laminar flame. We will see later that these 1D laminar flames, known as flamelets, are the fundamental building blocks for

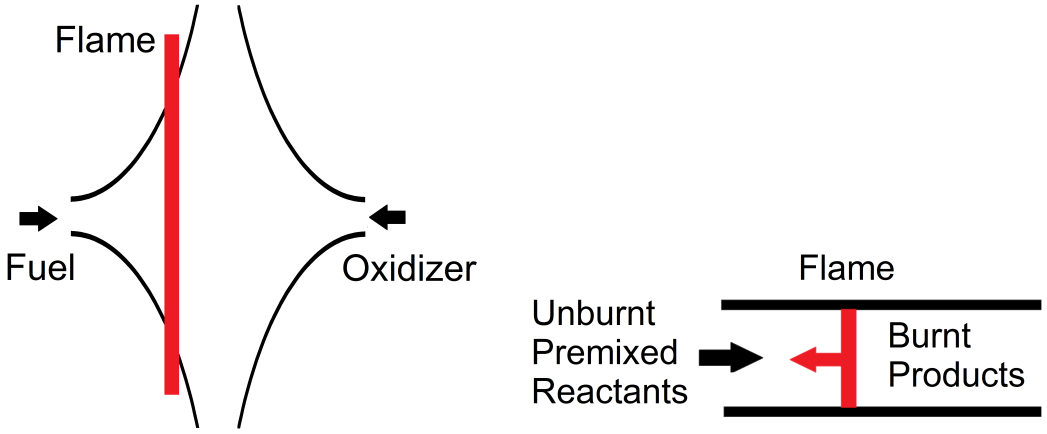

Figure 2.1: One Dimensional Laminar canonical flame. (a) Counterflow laminar diffusion flame. (b) Freely propagating laminar premixed flame.

turbulent combustion modelling [142, 148].

2.1.2 Partially Premixed Flames

In practical devices, fully premixed flames may not always burn in the manner as intended, mostly due to insufficient mixing between fuel and oxidizer as a result of the constraints on the space and time available for mixing. This type of system departs from the theoretical fully premixed system with varying degrees of "non-premixedness". From another perspective, a fuel jet issuing into open air, entrains air leading to a certain level of mixing before establishing a flame away from the nozzle exit - this example departs from the theoretical non-premixed system with varying degree of "premixedness". In between the theoretical definition of fully premixed and fully non-premixed systems, is what we refer to here as a "partially premixed" system. Partially premixed combustion is not yet well understood and has been the subject of active research recently.

Figure 2.2 presents typical illustrations of the different type of combustion in the mixture fraction space. In a premixed flame, combustion occurs at one pre-determined mixture fraction value, as denoted by arrow 1 in Fig.2.2. The arrow indicates a delta function for the PDF of the mixture fraction ξ. In a diffusion flame, flame 2 in the figure, the fuel and oxidizer enter the combustion

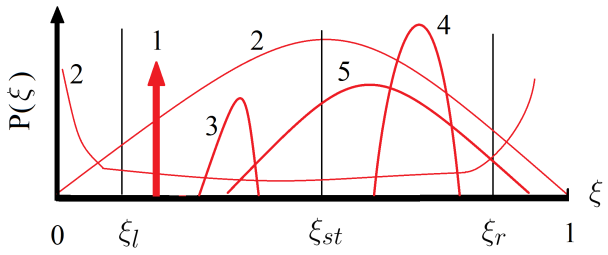

Figure 2.2: Illustration of different types of combustion in the mixture fraction space ξ. (1) premixed; (2) diffusion; (3) lean stratified; (4) rich stratified; (5) partially premixed flames.

zone separately by molecular diffusion and thus there is a possibility to have the full range of mixture fraction from 0 to 1. Thus, the PDF of ξ can be either broad and monomodal or bimodal, marked as 2 in the figure. However, the most intensive reaction is limited in region close to stoichiometric mixture. The situations denoted by 3, 4 and 5 can all be considered as partially premixed combustion. One important feature is the spatial and temporal fluctuation of the mixture fraction or equivalence ratios and there are different types of partially premixed flames depending on its distribution [22, 161].

In the first scenario, the equivalence ratio distribution covers only entirely lean, marked as 3 in Fig. 2.2, or entirely rich mixture, marked as 4, so that no diffusion flame can exist. The variation of ξ is usually within the lean and rich flammability limits. One example is the slotted burner [5] which issues two or more streams of reactants with different equivalence ratios that are within the flammability limits and also close to one another. Mixture stratification occurs in a direction transverse to the flow and flame propagation, resulting in flame propagating through mixtures of variable stoichiometry. The bulk of fuel is often consumed in the premixed mode, and the mixing behind is relevant only to slow reactions such as NOx formation and CO oxidation [72]. Another example is the so called "stratified combustion" in reciprocating engines. For easy startup, the flames are ignited in a very rich mixture and allowed to propagate towards lean mixture to reduce CO and NOx formation [124]. A clear equivalence ratio gradient is intentionally introduced in this case in a direction normal to the flame propagation. Other examples can be found in [1, 82, 161]. As these types of

combustion are closer to the purely premixed mode, this is commonly referred as "stratified combustion" or "premixed combustion with variable stoichiometry".

A second scenario is more general where both the lean and rich mixtures coexist leading to a combination of premixed and diffusion combustion denoted by curve 5 in Fig. 2.2. The variation of equivalence ratio can go beyond the flammability limits. This is closer to the non-premixed extrema as the bulk of heat release and fuel consumption can be in either the diffusion mode or the stratified mode. This general case is usually referred to "partially premixed combustion". Examples include lifted jet flame, direct fuel injection IC engines [76] and combustion with local extinction and reignition [101].

The variation of equivalence ratio from lean to rich can give rise to the development of the so called "triple flame" structure. The tri-branchial feature was first experimentally observed by Phillips [144] in the mixing layers of methane and air. It consists of a lean premixed, a rich premixed and a trailing diffusion flame in between the two. The diffusion flame is formed by excessive oxidizer from the lean branch and excessive fuel from the rich branch. The three branches join at the "triple point". The triple flame is the canonical representation of partially premixed combustion and has been the subject of many studies [81, 90, 91, 147, 156, 164].

2.2 Governing Equations

Within the continuum limit, turbulent reacting flows are governed by the conservation equations for the mass, momentum, the chemical species and energy. The instantaneous equations are written as follows: [142, 148, 189]

Mass Conservation:

$$\frac{\partial \rho}{\partial t} + \frac{\partial \rho u_i}{\partial x_i} = 0 \tag{2.1}$$

Momentum Conservation:

$$\frac{\partial \rho u_j}{\partial t} + \frac{\partial \rho u_i u_j}{\partial x_i} = -\frac{\partial p}{\partial x_j} + \frac{\partial \tau_{ij}}{\partial x_i} + \rho \sum_{k=1}^{N} Y_a f_{a,j}, \tag{2.2}$$

where $\tau_{ij} = \mu \left(\partial u_i / \partial x_j + \partial u_j / \partial x_i - 2(\delta_{ij} \partial u_k / \partial x_k)/3 \right)$ is the viscous tensor and

δ_{ij} is Kronecker delta, p is pressure, Y_a is the mass fraction for species a, and $f_{a,j}$ is the body force acting on the species a in the j direction.

Species conservation:

$$\frac{\partial \rho Y_a}{\partial t} + \frac{\partial \rho u_i Y_a}{\partial x_i} = \frac{\partial}{\partial x_i}\left(-\rho V_{a,i} Y_a\right) + \dot{\omega}_a, \tag{2.3}$$

where $V_{a,i}$ is the diffusion velocity of species a in direction i, and $\dot{\omega}_a$ is the reaction rate of the species a. For simplicity, if one considers a one step irreversible reaction, $\mathrm{F} + s\mathrm{O} \rightarrow (1+s)\mathrm{P}$, the reaction rate for the product is

$$\dot{\omega}_P = k_r \rho^2 Y_F Y_O, \tag{2.4}$$

where the k_r is the reaction rate coefficient given by the Arrhenius expression

$$k_r = A T^B \exp\left(-\frac{T_a}{T}\right), \tag{2.5}$$

where A is the pre-exponential factor, B is the temperature exponent and T_a the activation temperature and T is the mixture absolute temperature. It is clear that the reaction rate is highly non-linear and this poses great challenges for turbulent combustion modelling. We shall revisit this issue in Section 2.4.1.

The energy equation can take multiple forms [148]. One may consider the enthalpy per unit mass h, which includes the chemical and sensible part h_s as

$$h = h_s + \sum_{a=1}^{N} \Delta h^0_{f,a} Y_a = \int_{T^0}^{T} C_p dT + \sum_{a=1}^{N} \Delta h^0_{f,a} Y_a, \tag{2.6}$$

where C_p is the specific heat capacity at constant pressure for the mixture, $\Delta h^0_{f,a}$ is the enthalpy of formation of the species a. Sometimes the internal energy $e = h - p/\rho$, or the total energy $E = e + u_i u_i/2$ which includes the kinetic energy contribution may be considered. The choice depends on the physics of the problem: E is usually preferred for compressible flow and for the combustion problems of engineering interest h is usually preferred. The balance equation for

enthalpy is [148]

$$\frac{\partial \rho h}{\partial t} + \frac{\partial \rho u_i h}{\partial x_i} = \frac{\partial p}{\partial t} + u_i \frac{\partial p}{\partial x_i} - \frac{\partial q_i}{\partial x_i} + \tau_{ij} \frac{\partial u_i}{\partial x_j} + \dot{\mathcal{Q}} + \rho \sum_{a=1}^{N} Y_a f_{a,i} V_{a,i}, \tag{2.7}$$

where q_i is the heat flux given by $q_i = -\lambda \partial T / \partial x_i + \rho \sum_{a=1}^{N} h_a Y_a V_{a,i}$ with λ as the thermal conductivity of the mixture and $\dot{\mathcal{Q}}$ is a heat source term (due to laser or radiative flux for example).

2.3 Numerical Simulation for Turbulent Combustion

The challenge of numerical simulation for turbulent combustion lies in its multi-scale nature. Turbulence itself has a wide range of physical length and time scales. Turbulence kinetic energy is transferred from the energy containing large scales which are of the order of integral length scale Λ, to small scales until it is dissipated as heat due to viscous effects [155, 180]. The scales at which the viscous effects are important are known as Kolmogorov scales, given by $\eta_k = (\nu^3/\epsilon)^{1/4}$, where ν is the kinematic viscosity, and ϵ is the dissipation of the turbulent kinetic energy. An estimate for ϵ can be written as $\epsilon \sim u'^3/\Lambda$ [180], where u' is the RMS (root mean square) of the turbulent fluctuations. The ratio between the length scales can be shown as [155, 180] $\eta_k/\Lambda \sim Re^{-3/4}$, where $Re = u'\Lambda/\nu$ is the turbulent Reynolds number. Similarly the ratio for the corresponding time scales is $Re^{1/2}$. These scaling clearly indicate that for non-reacting turbulent flows at large Re, the range of scales increases with Re, which makes the numerical simulation using the above instantaneous equations very expensive.

Chemical reactions introduce additional length and time scales, ranging from as large as the integral scales to substantially smaller than the Kolmogorov scales. This further compounds the multiscale problem and also increases the stiffness of the system of equations. These additional factors pose significant challenges for numerical simulation of turbulent combustion.

Computational Fluid Dynamics (CFD) of turbulent reacting flow can be divided into three categories, namely Direct Numerical Simulation (DNS), Large

Eddy Simulation (LES) and Reynolds Averaged Navier-Stokes Simulation (RANS), in the order of decreasing resolution and computational cost and increasing modelling assumptions involved.

2.3.1 Direct Numerical Simulation

Direct Numerical Simulation resolves all the scales in turbulence, including the Kolmogorov scale η_k, while solving Eqs.(2.1)-(2.3) and Eq.(2.7) and thus no turbulence model is used. Various complexities of chemical kinetics, from simple one step irreversible reaction to multistep chemistry with detailed transport, can be incorporated. Therefore DNS is the most accurate and contains a wealth of information useful to improve our understanding and to build and verify simple models. It requires high-order accurate, non-dissipative numerical schemes for spatial and temporal discretisation [87, 106]. DNS also requires sufficiently fine grids to adequately resolve the smallest scale involved. Since few integral scales are required for statistical accuracy, the DNS computational domain size, L, must be larger than Λ. These requirements and the relation between Λ and η_k noted earlier leads to $\mathcal{N} > Re_t^{3/4}$, where $\mathcal{N}$ is the number of grid points in one direction required for the DNS of non-reacting turbulence. For reacting flows, this requirement is further constrained by the numerical resolution required for the smallest scale of the chemical reaction [38, 149]. DNS is therefore extremely expensive. The computational cost for 3D high Reynolds number reacting flows quickly becomes prohibitive. As a result DNS of realistic flow in industrial devices with complex geometry and detailed chemistry is still beyond the reach of even today's Petaflop supercomputer. However, DNS has emerged as a useful research tool to further our understanding, appraise and validate turbulent combustion models and develop new ones [38]. It has been used to study non-premixed [125, 186, 195], premixed [30, 149, 165], triple [53, 81, 164] and stratified [76, 78, 82, 117] flames.

2.3.2 Large Eddy Simulation

In Large Eddy Simulation (LES), Eq.(2.1)-(2.3) and Eq.(2.7) are filtered. The filtered quantity Q is defined as [148]

$$\overline{Q}(x;\Delta) = \int Q(x')F[(x-x');\Delta]dx', \tag{2.8}$$

where F is the filter function chosen so that it is zero when $x - x'$ exceeds the filter size Δ. Thus the scales larger than Δ are resolved while the smaller scales, known as the sub-grid scale (SGS), are modelled. The computational cost for LES is lower compared to DNS. It is also capable of capturing the dynamics of large scaled structure in complex flow. The SGS models are usually built by extending and modifying the models constructed for the RANS approach. These SGS models have been reviewed in [148, 189] and numerous studies using LES for turbulent non-premixed and premixed flames are reviewed by Pitsch [145] and Swaminathan and Bray [177].

2.3.3 Reynolds Averaged Navier Stokes Simulation

In this approach, an instantaneous quantity Q is written as $Q = \overline{Q} + Q'$, where $\overline{Q}$ is the mean and Q' the fluctuation over the mean. The averaging can be done over either space or time or ensemble depending on the problem. Substituting this decomposition into the transport equation for Q, one obtains a transport equation for $\overline{Q}$. It is easy to verify that it involves correlations of appropriate fluctuations, which need to be modelled. These correlations are usually known as Reynolds stress, $\overline{\rho u_i' u_j'}$, and Reynolds flux, $\overline{\rho u_i' Y_a'}$, respectively for the momentum and scalar transport. For reacting flows, because of density fluctuation, a density weighted, or Favre averaging is introduced as $\widetilde{Q} = \overline{\rho Q}/\bar{\rho}$. The Favre fluctuation is $Q'' = Q - \widetilde{Q}$. For the RANS approach, the conservation equations for mass, momentum, chemical species and energy can be written [108, 148, 189] as

$$\frac{\partial \bar{\rho}}{\partial t} + \frac{\partial \bar{\rho}\widetilde{u_i}}{\partial x_i} = 0, \tag{2.9}$$

$$\frac{\partial \bar{\rho}\widetilde{u_i}}{\partial t} + \frac{\partial \bar{\rho}\widetilde{u_i u_k}}{\partial x_k} = -\frac{\partial \bar{p}}{\partial x_i} + \frac{\partial}{\partial x_k}\left(\overline{\tau_{ik}} - \widetilde{\bar{\rho} u_i'' u_k''}\right), \tag{2.10}$$

$$\frac{\partial \bar{\rho}\widetilde{Y_a}}{\partial t} + \frac{\partial \bar{\rho}\widetilde{u_i}\widetilde{Y_a}}{\partial x_i} = \frac{\partial}{\partial x_i}\left(\overline{\rho D \frac{\partial Y_a}{\partial x_i}} - \overline{\rho u_i'' Y_a''}\right) + \overline{\dot{\omega}_a}, \tag{2.11}$$

where the species molecular diffusion flux $\mathcal{J}_i$ is written using the Fick's law $\mathcal{J}_i = -D\partial Y_a/\partial x_i$. The energy equation can be written as [142, 148]

$$\frac{\partial \bar{\rho}\tilde{h}}{\partial t} + \frac{\partial \bar{\rho}\widetilde{u_k}\tilde{h}}{\partial x_k} = \frac{\partial}{\partial x_k}\left[\overline{\frac{\mu}{\sigma}\frac{\partial h}{\partial x_k}} - \overline{\rho u_k'' h''}\right], \tag{2.12}$$

with the assumption of low Mach number flow and unity Lewis number. σ is the mixture Prandtl number and $\mu = \rho\nu$ is the dynamic viscosity. The equation of state for an ideal gas is

$$\bar{p} = \bar{\rho} R \tilde{T}, \tag{2.13}$$

where $R = \mathcal{R}/\overline{W}$, the mixture averaged molecular weight is given by $\overline{W} = (\sum Y_k/W_k)^{-1}$, the universal gas constant is $\mathcal{R} = 8.314$ J/mole/K. In Eq.(2.10), $\overline{\tau_{ij}} = \mu\left(\partial\widetilde{u_j}/\partial x_i + \partial\widetilde{u_i}/\partial x_j\right) - 2(\delta_{ij}\mu\partial\tilde{u_k}/\partial x_k)/3$ and δ_{ij} is the Kronecker delta. The Boussinesq approximation [148, 180] relates the Reynolds stress to the mean strain rate using an eddy viscosity μ_t in a manner similar to the molecular viscous stress tensor

$$\widetilde{\bar{\rho} u_i'' u_j''} = -\mu_t\left(\frac{\partial \tilde{u}_i}{\partial x_j} + \frac{\partial \tilde{u}_j}{\partial x_i} - \frac{2}{3}\delta_{ij}\frac{\partial \tilde{u}_k}{\partial x_k}\right) - \frac{2}{3}\bar{\rho}\delta_{ij}\tilde{k}, \tag{2.14}$$

where $\widetilde{k}$ is the turbulent kinetic energy.

A more advanced approach [73, 103] involves solving the modelled transport equation for individual components of the Reynolds stress and avoids the Boussinesq approximation in Eq.(2.14). However, this approach involves further modelling to close the Reynolds stress transport equations and is more complex and computationally expensive. Care must also be taken in its numerical implementation.

The turbulent scalar flux term $\widetilde{\bar{\rho} u_i'' Y_a''}$ is unclosed and requires modelling.

Typically a gradient transport assumption can be used

$$\overline{\rho u_i'' Y_a''} = -\frac{\mu_t}{\sigma_t}\frac{\partial \widetilde{Y}_a}{\partial x_i}, \tag{2.15}$$

where μ_t is turbulent eddy viscosity to be calculated using turbulence modelling and $\sigma_t \approx 0.7$ is the turbulent Schmidt number.

The two equation k-ϵ modelling approach of Jones and Launder [84] is widely used due to its simplicity, low computational cost and surprisingly reasonable accuracy in a wide range of flow configurations. $\tilde{k}$ is the turbulent kinetic energy and $\tilde{\epsilon}$ is its dissipation rate. The model equations are written as [83]

$$\frac{\partial \overline{\rho}\tilde{k}}{\partial t} + \frac{\partial \overline{\rho}\widetilde{u}_i\tilde{k}}{\partial x_i} = \frac{\partial}{\partial x_j}\left[\left(\mu + \frac{\mu_t}{Sc_k}\right)\frac{\partial \widetilde{k}}{\partial x_j}\right] + P_k - \bar{\rho}\tilde{\epsilon}, \tag{2.16}$$

$$\frac{\partial \overline{\rho}\tilde{\epsilon}}{\partial t} + \frac{\partial \overline{\rho}\widetilde{u}_i\tilde{\epsilon}}{\partial x_i} = \frac{\partial}{\partial x_j}\left[\left(\mu + \frac{\mu_t}{Sc_\epsilon}\right)\frac{\partial \tilde{\epsilon}}{\partial x_j}\right] - C_{\epsilon 1}\frac{\tilde{\epsilon}}{\tilde{k}}P_k - C_{\epsilon 2}\bar{\rho}\frac{\tilde{\epsilon}^2}{\tilde{k}}, \tag{2.17}$$

$$P_k = -\bar{\rho}\widetilde{u_i'' u_j''}\frac{\partial \tilde{u}_i}{\partial x_j} - \overline{u_i''}\frac{\partial \overline{p}}{\partial x_i} + \overline{p'\frac{\partial u_i''}{\partial x_i}}. \tag{2.18}$$

The turbulent eddy viscosity is calculated by $\mu_t = \bar{\rho}C_\mu\tilde{k}^2/\tilde{\epsilon}$ with C_μ=0.09, $C_{\epsilon 1}$=1.44 and $C_{\epsilon 2}$=1.92 are standard model constants. These constants may have to be tuned appropriately to obtain good agreement with experimental measurements in a variety of flow configurations.

2.4 Turbulent Combustion Modelling

2.4.1 Challenges and Strategies

In Eq.(2.11), the closure of the mean reaction rate $\overline{\dot{\omega}_i}$ poses a great challenge due to its highly non-linear dependence on temperature and species concentration. To expose this clearly, let us consider a simple reaction $R_1 + R_2 \rightarrow P$. The

instantaneous reaction rate can be written as

$$\dot{\omega}_f = \overline{\dot{\omega}_f} + \dot{\omega}'_f = A\bar{\rho}^2(\widetilde{Y}_o + y''_o)(\widetilde{Y}_f + y''_f)(\widetilde{T} + T'')^b \exp\left(-\frac{T_a}{\widetilde{T} + T''}\right). \tag{2.19}$$

A Taylor expansion of the mean reaction rate can be shown to give [189]

$$\overline{\dot{\omega}_f} = -A\bar{\rho}^2\widetilde{T}^b\widetilde{Y}_f\widetilde{Y}_o \exp\left(-\frac{T_a}{\widetilde{T}}\right) \times \left[1 + \frac{\widetilde{Y''_f Y''_o}}{\widetilde{Y}_f\widetilde{Y}_o} + (P_1 + Q_1)\left(\frac{\widetilde{Y''_f T''}}{\widetilde{Y}_f\widetilde{T}} + \frac{\widetilde{Y''_o T''}}{\widetilde{Y}_o\widetilde{T}}\right) + ...\right], \tag{2.20}$$

where

$$P_n = \sum_{k=1}^{n}(-1)^{n-k}\frac{(n-1)!}{(n-k)![(k-1)!]^2 k}\left(\frac{T_a}{\widetilde{T}}\right)^k,$$

$$Q_n = \frac{b(b+1)...(b+n-1)}{n!}. \tag{2.21}$$

The higher order terms contain $(T_a/\widetilde{T})^k$ and the activation temperature is typically an order of magnitude greater than the Favre mean temperature. The temperature and species fluctuations can be the same order with respect to their Favre means. Therefore, this series can not be approximated even with many terms which makes it extremely difficult to model. Even if the higher order moments of the fluctuation correlation can be modelled, this is notably only for a simple one step irreversible reaction. Realistic fuel involves hundreds of elementary reactions and tens of species, which makes direct evaluation of the mean reaction rate intractable and thus the above method is seldom used.

Various different strategies have been developed. There are two main categories of strategies [11] for turbulent combustion modelling, namely the separation of scales and/or separation of model elements that address the modelled moment description of the scalars in state space on one hand and the model for its distribution function on the other.

The first approach involves an important assumption that chemistry is fast compared with other physical processes so that the reaction rate of species is limited by the rate of turbulent mixing of either the fuel and oxidizer in the case of non-premixed flames; or the cold reactants and hot products in the case of premixed flames. The Eddy Break Up model [168], the Eddy Dissipation

Concept model [115] and the laminar flamelet concept [20, 140] where the flame thickness is smaller than the smallest turbulence scale are some examples of this approach.

In the RANS context, the Eddy Break Up (EBU) [168] model gives a mean reaction rate of a reaction progress variable c as

$$\bar{\dot{\omega}}_c = C_{EBU} \frac{\tilde{\epsilon}}{\tilde{k}} \overline{\rho c''^2}, \tag{2.22}$$

where the rate of mixing is given by the inverse of the turbulence time scale $\tilde{k}/\tilde{\epsilon}$. The advantage of this model is its simplicity and low computational cost. This model does not depend on chemistry, which apparently has its limitations. The model constant C_{EBU} also needs to be adjusted appropriately case-by-case to produce reasonable results.

This concept has also been applied to non-premixed flames - known as the Eddy Dissipation Concept (EDC) [115], where a certain level of dependence on mixture composition is also included. For a simple non-premixed system, F + sO $\rightarrow$ $(1+s)$P, the mean reaction rate is given by

$$\bar{\dot{\omega}}_F = \alpha \bar{\rho} \frac{\tilde{\epsilon}}{\tilde{k}} \min\left(\tilde{Y}_F, \frac{\tilde{Y}_O}{s}, \frac{\beta \tilde{Y}_P}{1+s} \right), \tag{2.23}$$

where α and β are model parameters here. The reaction rate is limited by the deficient species.

The second approach can be illustrated by writing the mean reaction rate in its statistical representation as

$$\overline{\dot{\omega}_i} = \int_{\mathbf{\Psi}} \dot{\omega}_i(\Psi) f(\Psi)\, d\Psi \tag{2.24}$$

where $\dot{\omega}_i$ is an instantaneous reaction rate and $f(\Psi)$ is the joint probability density function (PDF) of the state space vector ψ which typically includes pressure, temperature and species concentrations. This joint PDF contains complete statistical information for all scalars and thus all statistical moments and related

functions can be evaluated using, for example

$$\overline{Q} = \int_{\mathbf{\Psi}} Q(\Psi) f(\Psi)\, d\Psi. \tag{2.25}$$

It is clear from Eq.(2.24) that the mean reaction rate requires a model for $\dot{\omega}_i$. The laminar flamelet model [20, 140] and Conditional Moment Closure [92] are two examples.

Different strategies exist for the modelling of the distribution function depending on whether a reduced number, usually one or two, of controlling parameters for accurate description of the state is available. In non-premixed flames, a conserved scalar, known as mixture fraction Z, can be constructed so that it uniquely determines the thermo-chemical state of the mixture. Similarly in premixed flames, a reactive scalar, known as reaction progress variable c, can be constructed by careful combination of different species and/or temperature. In these cases, reasonable presumed forms of the PDF are available, for example beta and delta functions are commonly used. The validity of the presumed PDF shape is not always guaranteed, a more general approach is to solve a modelled transport equation for the PDF [152].

In the following sections, modelling strategies for turbulent non-premixed and premixed flames are briefly reviewed, and their implications are discussed for turbulent partially premixed and stratified flames.

2.4.2 Turbulent Non-Premixed Flames

2.4.2.1 Flamelet Model

Peters [140, 142] developed the diffusion flamelet model for turbulent non-premixed flames, which considered the turbulent combustion as an ensemble of laminar flamelets embedded in turbulence, each experiencing a range of strain rates. The fundamental building block for these flamelets is the 1D laminar counter flow diffusion flame presented in Fig.2.1. It can be shown [7, 140, 142] that the mean quantities (e.g. temperature, species) can be obtained using

$$\tilde{\varphi}_i = \int\int \varphi_i(\xi, \chi_{st}) \tilde{P}(\xi, \chi_{st}) d\xi d\chi_{st}, \tag{2.26}$$

where ξ and χ_{st} are the sample space variable for the mixture fraction Z and the scalar dissipation rate of mixture fraction N_{zz} at the stoichiometry $Z = Z_{st}$. $\varphi_i(\xi, \chi_{st})$ denotes the relevant quantity in the 1D counter flow diffusion flame with different strain rate, which can be characterised by the scalar dissipation rate. In a presumed PDF approach, the mixture fraction is assumed to follow a beta distribution while a log-normal distribution is found [59, 60] to be a good approximation for the scalar dissipation rate. Practically, the joint PDF is calculated as $P(\xi, \chi) = P(\xi)P(\chi)$, since the statistical independence of mixture fraction and its dissipation has been proven mathematically in isotropic turbulence [68]. The beta PDF is given by [140]

$$\tilde{P}(\xi) = \frac{\xi^{\alpha-1}(1-\xi)^{\beta-1}}{\Gamma(\alpha)\Gamma(\beta)}\Gamma(\alpha+\beta) \tag{2.27}$$

where Γ is the Gamma function $\Gamma(\alpha) = \int_0^\infty t^{\alpha-1}e^{-t}dt$ and α and β are the coefficients related to the first two moments of mixture fraction Z:

$$\alpha = \frac{\widetilde{Z}^2(1-\widetilde{Z})}{\widetilde{Z''^2}} - \widetilde{Z} \quad \text{and} \quad \beta = \frac{\alpha(1-\widetilde{Z})}{\widetilde{Z}} \tag{2.28}$$

In the RANS context, the transport equation for the Favre mean mixture fraction $\widetilde{Z}$ and its variance $\widetilde{Z''^2}$ are usually solved. These equations are written as

$$\frac{\partial \bar{\rho}\widetilde{Z}}{\partial t} + \frac{\partial}{\partial x_k}(\bar{\rho}\tilde{u}_k\tilde{Z}) = \frac{\partial}{\partial x_k}\left(\overline{\rho D\frac{\partial Z}{\partial x_k}} - \overline{\rho u_k'' Z''}\right), \tag{2.29}$$

$$\frac{\partial \bar{\rho}\widetilde{Z''^2}}{\partial t} + \frac{\partial}{\partial x_k}(\bar{\rho}\tilde{u}_k\widetilde{Z''^2}) = \frac{\partial}{\partial x_k}\left(\overline{\rho D\frac{\partial Z''^2}{\partial x_k}} - \overline{\rho u_k'' Z''^2}\right) - 2\bar{\rho}\tilde{\epsilon}_{ZZ} - 2\overline{\rho u_k'' Z''}\frac{\partial \tilde{Z}}{\partial x_k}. \tag{2.30}$$

The turbulent scalar flux terms require modelling and a gradient transport assumption is commonly used, i.e. $\widetilde{u_k'' Z''} = -D_t \partial\widetilde{Z}/\partial x_k$ and $\widetilde{u_k'' Z''^2} = -D_t \partial\widetilde{Z''^2}/\partial x_k$, with a turbulent diffusivity D_t. The Favre averaged scalar dissipation rate

$$\tilde{\epsilon}_{ZZ} = \frac{1}{\bar{\rho}}\left(\overline{\rho D_Z \frac{\partial Z''}{\partial x_k}\frac{\partial Z''}{\partial x_k}}\right), \tag{2.31}$$

is one of the key quantities in turbulent combustion. The instantaneous dissipation rate is defined for the mixture fraction Z as

$$N_{ZZ} = D_Z \frac{\partial Z}{\partial x_i} \frac{\partial Z}{\partial x_i}, \tag{2.32}$$

where D_Z is the diffusivity of the mixture. Physically, the averaged scalar dissipation rate (SDR) describes the rate at which the scalar variance decreases and is thus the rate of turbulent mixing at small scales relevant to combustion [7, 10]. Bilger [7] showed that N_{ZZ} is related to the instantaneous reaction rate by

$$\dot{\omega}_i = -\rho N_{ZZ} \frac{\partial^2 Y_i}{\partial Z^2}. \tag{2.33}$$

with the assumption of fast chemistry, unity Lewis number and that the flame is quasi-steady. In the RANS context, the contribution of the gradient of the mean is typically smaller than the contribution from the gradients of fluctuation [163], i.e. $\widetilde{N}_{ZZ} \approx \tilde{\epsilon}_{ZZ}$. Simple algebraic model exists for $\tilde{\epsilon}_{ZZ}$, assuming a proportionality between the scalar and turbulence time scales. This model is written as [168]:

$$\bar{\rho}\,\tilde{\epsilon}_{ZZ} = \overline{\rho D_Z (\nabla Z'' \cdot \nabla Z'')} \simeq C_d\,\bar{\rho} \left(\frac{\tilde{\epsilon}}{\tilde{k}}\right) \widetilde{Z''^2}, \tag{2.34}$$

where C_d denotes the ratio of scalar to turbulence time scales which is typically between 1 and 2. This effectively gives rise to a constant turbulent Schmidt number for turbulent scalar mixing. Although many studies [6, 60, 166] have shown that this may be inaccurate under certain conditions, this model generally gives reasonable results for passive scalar mixing. More complex models can be derived using the scalar transport equation as has been done in many earlier studies [85].

2.4.2.2 Conditional Moment Closure

The Conditional Moment Closure (CMC) method was developed independently by Klimenko [93] and Bilger [9]. In this method, transport equations for the conditional averages are derived and solved with appropriate submodels [92]. The conditional averaging for species a is defined as $Q_a = \langle Y_a | Z = \eta \rangle$, where the

angled brackets denote ensemble averaging, subject to the condition of $Z = \eta$. To account for strong density fluctuations, density weighted conditional averaging is commonly used in combustion problems, $\widetilde{Q_a} = \langle \rho Y_a | Z = \eta \rangle \,/\, \langle \rho | Z = \eta \rangle$. The transport equation of Q is written as [92]

$$\rho_\eta \frac{\partial Q_a}{\partial t} + \langle \rho u_i | \eta \rangle \frac{\partial Q_a}{\partial x_i} = \rho_\eta \langle N_{ZZ} | \eta \rangle \frac{\partial^2 Q_a}{\partial \eta^2} + \langle \dot{\omega}_a | \eta \rangle + e_Q + e_y \tag{2.35}$$

where $\rho_\eta = \langle \rho | Z = \eta \rangle$ here.

$$e_Q = \left\langle \frac{\partial}{\partial x_i} \left(\rho D \frac{\partial Q_a}{\partial x_i} \right) + \rho D \frac{\partial Z}{\partial x_i} \frac{\partial}{\partial x_i} \left(\frac{\partial Q_a}{\partial \eta} \right) | \eta \right\rangle \tag{2.36}$$

$$e_y = - \left\langle \rho \frac{\partial y_a''}{\partial t} + \rho u_i \frac{\partial y_a''}{\partial x_i} - \frac{\partial}{\partial x_i} \left(\rho D \frac{\partial y_a''}{\partial x_i} \right) | \eta \right\rangle \tag{2.37}$$

where $y_a'' = Y_a - Q_a$. The term e_Q represents the molecular diffusion and can be neglected in high Reynolds number flows. The term e_y includes the effects of fluctuations around the conditional mean and the predominant contribution comes from the convective term. This can be written as [92]

$$e_y P(\eta) = - \frac{\partial}{\partial x} \left[\rho_\eta \langle u_i'' y_a'' | \eta \rangle \, P(\eta) \right], \tag{2.38}$$

where $P(\eta)$ is the PDF of Z. The conditional mean velocity $\langle u_i | \eta \rangle$, scalar dissipation rate $\langle N | \eta \rangle$ and reaction rate $\langle \dot{\omega}_a | \eta \rangle$ require modelling. A linear approximation of the unconditional flux can be used to model the conditional velocity [92]. The amplitude mapping closure [137] can be used to model the conditional dissipation rate. Comparisons of various models for these two terms can be found in [170]. The conditional reaction rate can be modelled with a first order closure, written as

$$\langle \dot{\omega}_a | \eta \rangle = \dot{\omega}_a(\mathbf{Q}). \tag{2.39}$$

This simply means that the conditional reaction rate has the same functional dependence on $\mathbf{Q}$ as the instantaneous rates on $\mathbf{Y}$. The unconditionally averaged quantities can be obtained using $\widetilde{Y}_a = \int Q_a(\eta) \widetilde{P}(\eta) d\eta$.

When the conditional fluctuations are large, second order closure or condi-

tioning on more than one variable may become necessary [102]. CMC has been applied extensively to model non-premixed flames, with good results for finite-rate chemistry effects, ignition and flame extinction, and soot prediction (See recent review in [102]).

2.4.2.3 Transported PDF method

The key idea of the transported PDF method is to solve a transport equation for the joint PDF of velocity, temperature and species composition, in order to obtain a statistical description of the thermo-chemical state at any one time and location. At the simplest level, the transport equation for the joint PDF P_φ of the species composition vector φ can be written as [56, 77, 152]

$$\begin{aligned} \frac{\partial}{\partial t}(\bar{\rho}\tilde{P}_\varphi) + \frac{\partial}{\partial x_i}(\bar{\rho}\tilde{u}_i\tilde{P}_\varphi) \quad &+ \quad \frac{\partial}{\partial \psi_\alpha}(\bar{\rho}S_\alpha\tilde{P}_\varphi) \\ &= \quad -\frac{\partial}{\partial x_i}[\bar{\rho}\left\langle u_i'' | \varphi = \psi \right\rangle \tilde{P}_\varphi] + \frac{\partial}{\partial \psi_\alpha}\left[\bar{\rho}\left\langle \frac{1}{\rho}\frac{\partial J_{i,\alpha}}{\partial x_i} | \varphi = \psi \right\rangle \tilde{P}_\varphi\right] \end{aligned} \tag{2.40}$$

where S is the source term, $J_{i,k}$ is the molecular diffusion flux. The terms on the left are closed. The first two are the rate of change of the PDF following a particle moving with mean flow velocity in the physical space. The third term is the PDF flux in composition space due to chemical reactions. It is a known function in terms of the composition vector φ and the joint PDF $P(\varphi)$. Therefore, the chemical source term appears in exact form and is closed which is the principal advantage of the transport PDF method. The terms on the right are unclosed and require modelling, they are turbulent transport in physical space and micro-mixing in the composition space.

In this method, the information on turbulence time scale needs to be provided externally, for example by using the $k-\epsilon$ turbulence model. Further complexity can be incorporated into the PDF, for example the joint PDF of the composition and velocity $P_{V,\varphi}$, in which case although turbulence time scale information is still required externally, the turbulent kinetic energy can be determined from $P_{V,Y}$. Finally, a turbulence frequency can be included in the joint PDF so that the complete information at one point, one time for the velocity, composition and the inverse of local turbulent time scale can be calculated from the joint PDF. The

key challenge lies in the accurate modelling of the scalar mixing process.

In realistic combustion problems, high dimensionality of the joint pdf is inevitable and the computational cost using traditional finite difference method increases exponentially with the number of scalars [151]. Thus the stochastic particle (Monte Carlo) method pioneered by Pope [151, 152] is commonly used, in which the computational requirement increases only linearly with the number of variables in the joint pdf. In this method, notional particles are used to represent velocities and compositions and they are allowed to evolve according to conservation principles. This method can be formulated in either an Eulerian [151] or Lagrangian framework [152]. The transported PDF method is computationally expensive compared to presumed PDF/Flamelet and CMC methods. However, its mathematical robustness and principal advantage that the mean reaction rate is closed make it a very useful tool. It is especially suitable for problem with finite rate reactions and the simulation of pollutants formation where the premises for presumed PDF method may not be valid [56, 67, 77, 152].

2.4.3 Turbulent Premixed Flames

Depending on the ratio of turbulence to the chemical scales involved, turbulent premixed combustion is categorised into various combustion regimes [142, 148]. Figure 2.3 provides an illustration of the premixed combustion regimes using a velocity ratio of turbulent fluctuation to laminar flame speed, u_{RMS}/S_L^0, and the length scale ratio of the turbulence integral length scale to the laminar flame thickness, Λ/δ, where $\delta = D/S_L^0$ and D is the molecular diffusion coefficient for the deficient species in the reactants. Other parameters appearing in this figure are the Damköhler number Da, the Karlovitz number Ka, and the turbulence Reynolds number Re. The Damköhler number is defined as the ratio of the flow time scale to the chemical time scale, i.e. $\mathrm{Da} \equiv \tau_f/\tau_c = S_L^0\Lambda/(\delta u_{RMS})$. The Karlovitz number is defined as the ratio of chemical to Kolmogorov time scales, $\mathrm{Ka} \equiv \tau_c/\tau_k = \delta^2/\eta_k^2$. If the Schmidt number is unity, the turbulence Reynolds number is $\mathrm{Re} = u_{RMS}\Lambda/(S_L^0\delta)$. The various combustion regimes are also marked in Fig. 2.3. Those of practical interest are the corrugated flamelet regime and the thin reaction zone regime [142]. When $\mathrm{Ka} < 1$, the smallest turbulence scale,

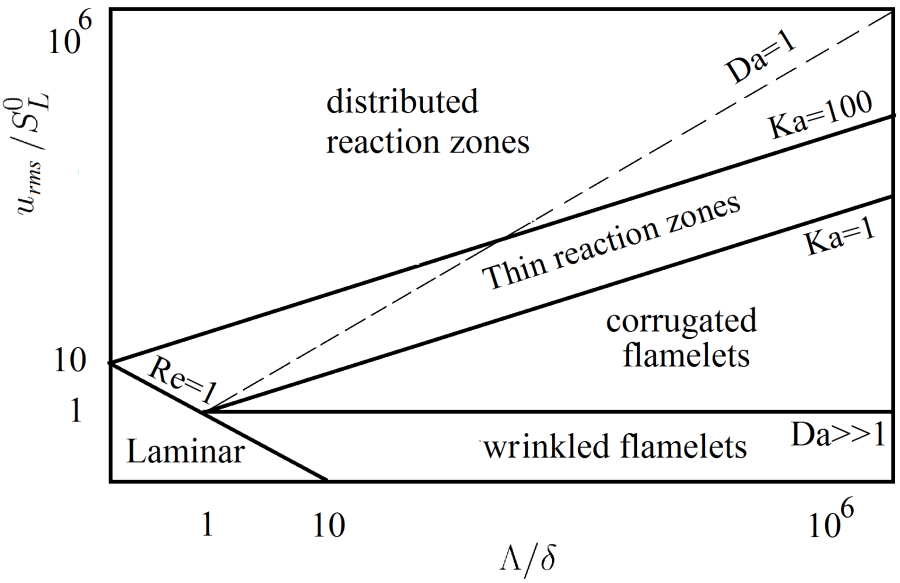

Figure 2.3: Regime diagram for turbulent premixed combustion [142].

the Kolmogorov scale, is larger than the flame thickness and thus the laminar flame structure is not perturbed by turbulence. Turbulence can only wrinkle the flame front and the flame remains quasi-steady. Bounded by the limits of $\mathrm{Ka} < 1$ and $\mathrm{Da} \gg 1$, the regime is known as the corrugated flamelet regime [142]. When $1 < \mathrm{Ka} < 100$, the turbulence eddies are small and can penetrate into the reactive-diffusive flame structure, but they are not small enough to enter the inner reaction zone, which is typically of the size 0.1δ. This combustion regime is known as the thin reaction zone regime [142]. If the turbulence eddies are small enough to enter the inner reaction zone, it is known as the distributed or broken reaction zone regime where local extinction of the flame can be anticipated. The most appropriate modelling strategy for turbulent premixed combustion depends on the different combustion regimes as discussed in the following sections.

Before going into details of the different modelling approaches, it will be beneficial to introduce the progress variable c, which is commonly used to describe the local thermo-chemical state of the mixture in premixed combustion. The statistical distribution of the progress variable can either be assumed to follow a particular distribution or it can be solved by a transport equation. In the

presumed PDF approach, both delta and beta PDF are widely used for the c distribution. In the case of beta function, the first two moments are required and relate to the beta PDF as in Eq.(2.27). In the RANS context, the transport equation for $\widetilde{c}$ and its variance $\widetilde{c''^2}$ can be written as [18, 177]

$$\frac{\partial \bar{\rho}\tilde{c}}{\partial t} + \frac{\partial}{\partial x_k}(\bar{\rho}\tilde{u}_k\tilde{c}) = \frac{\partial}{\partial x_k}\left(\overline{\rho D\frac{\partial c}{\partial x_k}} - \overline{\rho u_k'' c''}\right) + \bar{\dot{\omega}}_c, \tag{2.41}$$

$$\frac{\partial \bar{\rho}\widetilde{c''^2}}{\partial t} + \frac{\partial}{\partial x_k}(\bar{\rho}\tilde{u}_k\widetilde{c''^2}) = \frac{\partial}{\partial x_k}\left(\overline{\rho D\frac{\partial c''^2}{\partial x_k}} - \overline{\rho u_k'' c''^2}\right) - 2\bar{\rho}\widetilde{\epsilon}_{cc} - 2\overline{\rho u_k'' c''}\frac{\partial \tilde{c}}{\partial x_k} + 2\overline{c''\dot{\omega}_c''}, \tag{2.42}$$

where $\widetilde{\epsilon}_{cc}$ is the scalar dissipation rate of c

$$\widetilde{\epsilon}_{cc} = \overline{\rho D\frac{\partial c''}{\partial x_k}\frac{\partial c''}{\partial x_k}}/\bar{\rho}. \tag{2.43}$$

2.4.3.1 BML Model

The Bray-Moss-Libby (BML) model, proposed by Bray and Moss [19] accounting for the thermo-chemical state of premixed flames, and Libby and Bray [107] later extended it to include aerodynamic effects. The chemistry is again assumed to be fast compared to turbulent mixing processes and the flame is considered as a thin surface separating unburnt reactants $0 < c < c^*$ and burnt products $(1 - c^*) < c < 1$. The PDF of the progress variable is written as [18]

$$\tilde{P}(c) = \tilde{\alpha}\delta(c) + \tilde{\beta}\delta(1-c) + \tilde{\gamma}[H(0) - H(1)]f(c). \tag{2.44}$$

where δ is the Dirac delta function and H is the Heaviside function, $f(c)$ is the internal part of the PDF and represents the distribution of c in the reaction zone. In the limit of $Da >> 1$ and $\gamma << 1$,

$$\bar{\rho} = \frac{\rho_u}{1+\tau\tilde{c}}; \quad \alpha = \frac{1-\tilde{c}}{1+\tau\tilde{c}}; \text{ and } \beta = \frac{(1+\tau)\tilde{c}}{1+\tau\tilde{c}}. \tag{2.45}$$

One key success of the BML model is that it provides a theoretical basis for the experimental observation of counter gradient transport in turbulent premixed

flame [107]. The turbulent scalar flux can be expressed as

$$\widetilde{u''c''} = (\widetilde{uc} - \tilde{u}\tilde{c}) = \tilde{c}(1-\tilde{c})(\bar{u}^b - \bar{u}^u), \tag{2.46}$$

where $\bar{u}^b$ and $\bar{u}^u$ are the mean velocities conditioned in burnt and unburnt mixtures. Since burnt gas has higher temperature and lower density, and thus higher velocity, i.e. $\bar{u}^b > \bar{u}^u$, and thus $\widetilde{u''c''} > 0$ in the direction of positive $\tilde{c}$ gradient. This is due to the fact that the lighter burnt products with a higher c value are preferentially accelerated by the pressure gradient as flow field near the flame is dominated by thermal dilatation due to chemical reaction. This is different from the conventional gradient diffusion giving $\widetilde{u''c''} < 0$ along positive $\tilde{c}$ gradient.

The source term $\bar{\dot{\omega}}_c$ requires modelling and is the main challenge. Since the reaction rate is zero everywhere outside the reaction zone, the mean reaction rate is directly related to γ and $\overline{\dot{\omega}_c} = \gamma \int_{c^*}^{1-c^*} \dot{\omega}_c f(c) dc$. However, γ has been neglected in the classic BML approach (there is recent attempt to model γ by Bray et al. [177]) and an alternative method is required to calculate $\bar{\dot{\omega}}_c$.

One approach is to use the flamelet crossing frequency method [21] where the progress variable signal is considered to be a telegraph signal and $\overline{\dot{\omega}_c}$ is directly related to the frequency ν_f, at which an undisturbed laminar flame front crosses a given location in the flow. The mean reaction rate can be modelled as [18]

$$\overline{\dot{\omega}_c} = \nu_f \dot{\omega}_f = \left(\frac{2\bar{c}(1-\bar{c})}{\hat{\mathcal{L}}}\right)\left(\frac{\rho_u S_L^0 I_0}{|\sigma_f|}\right) \tag{2.47}$$

where $\hat{\mathcal{L}}$ is the flame wrinkling length scale, typically set to the integral scale of turbulence; $\dot{\omega}_f$ is the reaction rate in the laminar flame front, given by $\rho_u S_L^0$. I_o is the stretch factor, typically with a value close to unity, to account for stretch effects induced by turbulence eddies and $|\sigma_f|$ is the flame orientation factor.

This equation can be closed based on the concept of Flame Surface Density (FSD) [122] and the scalar dissipation rate (SDR) [15], which will be discussed in the following sections.

2.4.3.2 Flame Surface Density Model

The flame surface density concept was first developed by Marble and Broadwell [122] for non-premixed flames. This concept was applied to premixed flames in later studies [26, 153, 182, 187]. The mean reaction rate is written as

$$\overline{\dot{\omega}_c} = \bar{\rho}_u \left\langle S_c \right\rangle_s \widetilde{\Sigma}. \tag{2.48}$$

where $\langle\rangle_s$ denotes surface averaged value and S_c is the consumption speed of reactants, defined as the integral of the burning rate across a unstretched laminar flame. Σ is the flame surface density (FSD), defined as the flame surface area per unit volume. Algebraic expressions for FSD have been derived based on the flamelet crossing frequency [21] and fractal theories [70]. A balance equation for the flame surface density Σ has also been derived and modelled in past studies [26, 153, 182, 187]. This equation is written as [189]

$$\frac{\partial \Sigma}{\partial t} + \frac{\partial \left\langle u_j + S_d n_j \right\rangle_s \Sigma}{\partial x_j} = \left\langle \Phi \right\rangle_s \Sigma. \tag{2.49}$$

In this equation the surface average or gradient weighted average of a quantity Q is given by $\langle Q \rangle_s = \left(\overline{(Q|\nabla c|)|c=c^*} \right) / \left(\overline{|\nabla c||c=c^*} \right)$, where $c = c^*$ is a given iso-surface. The flame surface density per unit volume can be calculated as [153, 154, 187]

$$\Sigma\left(c^*\right) = \left\langle |\nabla c||c=c^* \right\rangle \overline{P}\left(c^*\right), \tag{2.50}$$

where $\overline{P}$ is the marginal pdf of c. The instantaneous flame stretch rate, Φ, is defined as [26, 104, 153]

$$\begin{aligned} \Phi &= \frac{1}{\delta A}\frac{\mathrm{d}(\delta A)}{\mathrm{d}t} = a_T + 2S_d k_m, \\ &= (\delta_{ij} - n_i n_j)\frac{\partial u_i}{\partial x_j} + S_d \frac{\partial n_i}{\partial x_i}, \end{aligned} \tag{2.51}$$

where n_i is the i-component of the flame normal unit vector, $\mathbf{n} \equiv -\nabla c/|\nabla c|$. The flame normal unit vector points towards the reactant side. The flame stretch consists of two components: the tangential strain rate, a_T, and a contribution from the joint behaviour of the flame surface displacement speed, S_d, and its

mean curvature, k_m. These surface averaged quantities need to be modelled. This has been attempted in many past studies, notably one of the first being by Cant et al. [29] where a model was proposed that is valid in the laminar flamelet regime. These models have been reviewed by Veynante and Vervisch [189] and Cant [27].

2.4.3.3 G Equation / Level set approach

This approach considers the kinematics of the flame front propagation and describes the flame as an interface between fresh reactants and burnt gases. Peters [141, 142] has developed this method for the corrugated flamelets and thin reaction zones regimes. In this geometrical description, the flame surface is defined to be at $G = G_0$. The transport equation for mean G can be written as [142]

$$\bar{\rho}\frac{\partial \widetilde{G}}{\partial t} + \bar{\rho}\tilde{u}_i\frac{\partial \widetilde{G}}{\partial x_i} = \bar{\rho}S_T\left|\frac{\partial \widetilde{G}}{\partial x_i}\right| - \bar{\rho}D_t\tilde{\kappa}\left|\frac{\partial \widetilde{G}}{\partial x_i}\right| \tag{2.52}$$

where S_T is the turbulent flame speed and $\tilde{\kappa}$ is the mean curvature of the surface, both require modelling. Turbulent flame speed can be related to the laminar flame speed and the increase in flame surface area due to turbulence. The thermo-chemical state of the mixture can be parameterised by a distance $x_n = (G - G_0)/|\nabla G|$ to the G_0 surface. Together with a presumed PDF for G, the mean quantities can be obtained. The G equation/level set approach is relatively expensive and complex in the sense that a reinitialisation procedure is needed after each iteration to keep $\left|\nabla \widetilde{G}\right| = 1$ during the calculation. This approach has been widely used to model various turbulent premixed flames with good results [79], see the book by Peters [142] for a review.

2.4.3.4 Scalar Dissipation Rate Modelling approach

In RANS calculation of premixed flame, the SDR for the progress variable is given by [176]

$$\widetilde{\epsilon}_{cc} = \overline{\rho D_c \frac{\partial c''}{\partial x_i}\frac{\partial c''}{\partial x_i}}/\bar{\rho}. \tag{2.53}$$

DNS studies [163] have shown that the contribution from the mean gradients are small, so that $\widetilde{\epsilon}_{cc} \approx \widetilde{N_{cc}}$. Bray [15] analysed the variance transport equation Eq.(2.42) within the BML framework and showed that it reduces to a second equation for $\tilde{c}$ when γ is neglected. This led to the conclusion that the mean reaction rate is directly proportional to SDR through

$$\bar{\dot{\omega}}_c = \frac{2}{2c_m - 1}\rho\tilde{\epsilon}_{cc} \quad \text{with} \quad c_m = \frac{\int c\dot{\omega}_c^0 f(c)dc}{\int \dot{\omega}_c^0 f(c)dc}, \tag{2.54}$$

where c_m can be calculated from 1D laminar premixed flame, and is typically between 0.69 and 0.75 [16] for hydrocarbon flames. A simple model for $\widetilde{\epsilon}_{cc}$ in the form of Eq.(2.34) with $\widetilde{Z''^2}$ replaced by $\widetilde{c''^2}$ can be written as

$$\bar{\rho}\,\widetilde{\epsilon}_{cc} \simeq C_c\,\bar{\rho}\left(\frac{\tilde{\epsilon}}{\tilde{k}}\right)\widetilde{c''^2}. \tag{2.55}$$

However, in the case of reactive scalar, the fluctuations are not only determined by turbulence, but also by chemical reactions and their interaction with turbulence. As a result, this model has been shown to be inadequate to describe reactive SDR behaviour [120, 176].

Borghi and co-workers [12, 121, 130] derived a transport equation for $\widetilde{\epsilon}_{cc}$ by taking the fluid density to be constant. This equation was originally derived for scalar mixing in buoyancy driven turbulence by Lumley and co-workers (see recent review in [37]). Mantel and Borghi [121] proposed models for the unclosed term in $\widetilde{\epsilon}_{cc}$ transport equation. Mura and Borghi [130] extended those ideas to variable density flows, however, the thermal expansion across the flame front was not included.

Swaminathan and Bray [176] included the thermal expansion effects and presented a scaling analysis of various terms in the transport equation. Subsequent studies [31, 32, 34, 97] then used DNS data of premixed flames to develop a new model for $\widetilde{\epsilon}_{cc}$, aimed to capture the correct physics. This model is given as [97]

$$\overline{\rho}\,\widetilde{\epsilon}_{cc} = \overline{\rho\mathcal{D}_c(\nabla c'' \cdot \nabla c'')} \simeq \frac{\bar{\rho}}{\beta'}\left([2K_c^* - \tau C_4]\,\frac{S_L^0}{\delta_L^0} + C_3\frac{\tilde{\epsilon}}{\tilde{k}}\right)\widetilde{c''^2}. \tag{2.56}$$

where K_c^*,β', C_3 and C_4 are model parameters and will be detailed in Chapter 5.

Other propositions to model $\widetilde{\epsilon}_{cc}$ have been made recently and they are reviewed in [37].

With an appropriate SDR submodel, a flamelet model for turbulent premixed flame similar to the one for non-premixed flame can be envisaged. Recently, Kolla and Swaminathan [95, 96] developed a strained flamelet formulation for turbulent premixed flame with the SDR as a parameter to characterise the effects of flame stretching. The mean reaction rate here is given as

$$\overline{\dot{\omega}_c} = \int_0^1 \int_{N_1}^{N_2} \dot{\omega}_c(\zeta, \psi) P(\zeta, \psi) d\psi d\zeta = \int_0^1 \langle \dot{\omega}_c | \zeta \rangle \, P(\zeta) d\zeta, \tag{2.57}$$

where ψ is the sample space variable for the instantaneous SDR N_{cc}. A presumed beta shape can be used as noted earlier. $\dot{\omega}_c(\zeta, \psi)$ can be obtained using strained laminar flames established in opposed flows of cold reactants and hot products. The joint PDF is calculated using Bayes theorem $P(\zeta, \psi) = P(\psi|\zeta)P(\zeta)$ where the conditional PDF $P(\chi|\zeta)$ is assumed to be a lognormal distribution. The lognormal distribution is given by

$$P(\psi|\zeta) = \frac{1}{(\psi|\zeta)\sigma\sqrt{2\pi}} \exp\left(\frac{-[\ln(\psi|\zeta) - \mu]^2}{2\sigma^2}\right), \tag{2.58}$$

where the mean and variance of the natural logarithm $\ln(\psi|\zeta)$ are respectively denoted as μ and σ^2. These two quantities are related to the conditional mean $\langle N_{cc}|\zeta\rangle$ and variance g^2 through

$$\langle N_{cc}|\zeta\rangle = \exp\left(\mu + 0.5\sigma^2\right) \quad \text{and} \quad g^2 = \langle N_{cc}|\zeta\rangle^2[\exp(\sigma^2) - 1]. \tag{2.59}$$

The conditional mean $\langle N_{cc}|\zeta\rangle$ is related to the unconditional mean $\widetilde{\epsilon}_{cc}$ through

$$\langle N_{cc}|\zeta\rangle \approx \frac{\widetilde{\epsilon}_{cc} f(\zeta)}{\int_0^1 f(\zeta) P(\zeta) d\zeta}, \tag{2.60}$$

where $f(\zeta)$ is the the variation of N_{cc} normalised by its value at the location of peak heat release rate in an unstrained planar laminar flame and $\widetilde{\epsilon}_{cc}$ is modelled with Eq.(2.56). The strained flamelet formulation has been validated in the corrugated flamelets and thin reaction zones regimes of turbulent premixed

combustion [95, 96].

2.4.3.5 Conditional Moment Closure

As noted earlier, CMC has been used extensively for non-premixed combustion, but its application to premixed combustion is very limited [3, 123] and still under development [2, 175]. One difficulty seems to be a suitable choice of progress variable [92]. Another major difficulty is in the modelling of the conditional scalar dissipation rate of the reactive scalar and the conditional turbulent scalar flux [174, 175, 179]. One can see from the CMC equation for turbulent premixed flame [92]

$$\rho_\zeta \frac{\partial Q_a}{\partial t} + \langle \rho u_i | \zeta \rangle \frac{\partial Q_a}{\partial x_i} = \frac{Le_\zeta}{Le_a} \langle \rho N_{cc} | \zeta \rangle \frac{\partial^2 Q_a}{\partial \zeta^2} + \langle \dot{\omega}_a | \zeta \rangle - \langle \dot{\omega}_c | \zeta \rangle \frac{\partial Q_a}{\partial \zeta} + e_Q + e_y, \quad (2.61)$$

compared to Eq(2.35), an extra term $-\langle \dot{\omega}_c | \zeta \rangle \, \partial Q_a / \partial \zeta$ appears since the conditioning variable is a reactive scalar. The conditional dissipation rate is linked to the unconditional one by Eq.(2.60). Only recently the above model was implemented in the CMC context by Amzin et al. [2, 3] showing reasonably good agreement with experimental measurements in turbulent premixed flames.

2.4.3.6 Transported PDF method

Relatively few studies have been performed using the transported PDF method to model turbulent premixed flames compared to non-premixed flames. This is due to the strong coupling between molecular diffusion and reaction posing challenges for the modelling of the micro-mixing term [4]. Nevertheless, many past studies have applied standard modelling approaches and achieved reasonable comparison with experimental results. These studies have been reviewed recently by Lindstedt [110].

2.4.4 Turbulent Partially Premixed/Stratified Flames

2.4.4.1 Differentiating Combustion Mode

As partially premixed combustion consists of both premixed and diffusion modes, it is beneficial to identify the local mode of burning. Takeno and co-workers [193] first proposed a flame index to differentiate the local burning mode, which is defined as the scalar product of the fuel mass fraction gradient and oxidizer mass fraction gradient. It is easily seen that in a 1D laminar flame when the gradients are in the same direction, it is a premixed flame; and when gradients are opposite, it is a diffusion flame. Extending this to turbulent flames gives

$$F.I. = \nabla Y_o \cdot \nabla Y_f \begin{cases} > 0 & \text{premixed} \\ < 0 & \text{non-premixed} \end{cases} \tag{2.62}$$

The magnitude of the flame index increases as the " supplying rate of fuel and oxidizer by molecular diffusion increases". Modification and extension of this concept have also been proposed [62, 65, 111]. There is a more complex approach which involves flamelet transformation , however, LES of simple flow geometry, for example lifted jet flames, shows no difference between these indicators [94].

2.4.4.2 Modelling of Partially Premixed/Stratified Flames

Although models specifically for partially premixed combustion have been receiving increasing attention in recent years, only a few are available. The main challenge is to achieve accurate description of both premixed flame fronts, which propagate in mixture of spatially and temporally varying equivalence ratio, and diffusion flames [54] as they are fundamentally different in the sense that premixed flame is propagating while diffusion flame is not. Furthermore, as burning can occur locally in mixture close to the flammability limits, and the Damköhler number can not be considered as infinitely large, finite rate kinetics effects need to be included. Several common strategies exist. The first approach is to use a flame index type of indicator which locally distinguishes premixed and non-premixed burning modes. Models for premixed and non-premixed flames are then either selected exclusively or combined in some form using the flame index to calculate

the mean reaction rate. An extra transport equation is usually required to compute the flame index where further modelling of terms in the equation may be necessary. This approach has been tested against DNS results [55] and used to model turbulent lifted partially premixed flames by Domingo et al.[54], Ferraris and Wen [63], Knudsen and Pitsch [94].

Another common method is to extend pure premixed flame models by including a dependence on mixture fraction for important model parameters such as the turbulent and laminar flame speed. An extra transport equation for mixture fraction is normally included. Müller et al. [128] suggested a formulation to combine the mixture fraction equation for the non-premixed part and the G equation for the propagating flame surface. In the G equation where the turbulent flame speed is present, it is related to the laminar flame speed as a function of local mixture fraction and its dissipation rate as [128]

$$S_T \approx \underbrace{\left[S_L(Z_{st}) + b_2[S_L(Z_{st})u']^{1/2} + b_1 u'\right]}_{\text{premixed}} \underbrace{[P(Z_{st})(\Delta Z)_{S_L}]}_{\text{partially premixed}} \underbrace{\left[1 - a\frac{\bar{N_{ZZ}}}{N^q_{ZZ}}\right]}_{\text{quenching}}, \quad (2.63)$$

where a, b_1, b_2 are model parameters, u' is the turbulent fluctuation and N^q_{ZZ} is the quenching value of SDR. Although the joint PDF of the three variables, mixture fraction, its dissipation and the gradient of G field are assumed to be statistically independent *a priori*, the steady lift-off height agrees well with experiments. Following similar approach, Ovink and Lamers [138] used a presumed double delta function for the progress variable and a single delta for the mixture fraction dissipation at stoichiometry $N_{Z_{st}}$, and the mean scalar quantity is obtained using

$$\begin{aligned} \tilde{\theta} &\approx \int\int\int \theta(\xi, N_{Z_{st}}, \zeta)\tilde{P}(\xi, N_{Z_{st}}, \zeta)d\xi d\zeta dN_{Z_{st}} \\ &= (1-\tilde{c})\int_0^1 \theta_u(\xi)\tilde{P}(\xi)d\xi + \tilde{c}\int_0^1 \theta_b(\xi|N_{Z_{st}})\tilde{P}(\xi)d\xi \end{aligned} \quad (2.64)$$

where $\theta_u(\xi)$ is a mixing solution and $\theta_b(\xi|N_{Z_{st}})$ denotes the burnt side values obtained from a lookup table of laminar flamelet solutions. Further extending the work in [128], Chen et al.[41] introduced a mean turbulent burning velocity

model for partially premixed flame that not only depends on local mixture fraction and local Damköhler number following Peters [141], but also includes an integral across the partially premixed flame brush with presumed PDF for the mixture fraction, i.e. $S_{T,P} = \int_0^1 S_T(\xi)P(\xi)d\xi$.

Following the flamelet concept, another common approach for partially premixed combustion is to consider it as an ensemble of laminar premixed flames with a range of mixture fraction, together with the presumed PDF. The mean reaction rate is then

$$\overline{\dot{\omega}} = \int_0^1 \int_0^1 \dot{\omega}(\zeta,\xi)P(\zeta,\xi)\, d\zeta\, d\xi. \tag{2.65}$$

This is the starting point for various modelling efforts, with different choices of the flamelet models for $\dot{\omega}(\zeta,\xi)$ and different presumed shapes and assumptions in the modelling of the joint PDF $P(\zeta,\xi)$. This concept was originally proposed by Bradley et al. [14] who considered a "mixedness-reactedness flamelet model" for diffusion flames. Vervisch et al. [188] later developed the "Presumed Conditional Moment and FPI (PCM-FPI)" model and essentially used unstrained laminar flamelets and two presumed beta PDFs by assuming ζ and ξ to be statistically independent. Libby and Williams [109] used a presumed joint PDF of two delta functions for the two statistically independent variables, the mixture fraction Z and the fuel mass fraction Y_F, to describe the thermo-chemical and finite rate kinetic effects of stratified lean premixed combustion. This method offers the advantage of simplicity, reasonable computational cost and accuracy, but has the drawback of using simple one-step chemistry and ignoring the correlation between Z and Y_F. Detailed chemistry in the form of lookup tables and more realistic shapes of the presumed PDF have been attempted to improve this method. Ribert et al. [158] constructed the PDF by solving the transport equations for $\widetilde{Z}$, $\widetilde{Y_F}$, $\widetilde{Z''^2}$ and $\widetilde{Y_F''^2}$. However, Robin et al. [160] noted that the method of Ribert et al. [158] implicitly assumed the cross correlation $\widetilde{Y_F''Z''}$ is given by $\sqrt{\widetilde{Z''^2}}\sqrt{\widetilde{Y_F''^2}}$ and this yields the same sign for $\widetilde{Y_F''Z''}$ throughout the flame brush. This may not be so in partially premixed flames as one shall see in Chapter 5. Robin et al. [160] remedied this by generalising the joint PDF with four delta functions. An extra transport equation for the covariance $\widetilde{c''Z''}$ may need to be solved and it is given

as [48, 49, 161]

$$\frac{\partial \bar{\rho}\widetilde{c''Z''}}{\partial t} + \frac{\partial}{\partial x_k}(\bar{\rho}\widetilde{u}_k\widetilde{c''Z''}) = \frac{\partial}{\partial x_k}\left(\overline{\rho D\frac{\partial c''Z''}{\partial x_k}} - \overline{\rho u_k'' c''Z''}\right) - 2\bar{\rho}\widetilde{\epsilon}_{cZ} - \overline{\rho u_k'' c''}\frac{\partial \widetilde{Z}}{\partial x_k} - \overline{\rho u_k'' Z''}\frac{\partial \widetilde{c}}{\partial x_k} + \overline{Z''\dot{\omega}_c''}, \tag{2.66}$$

where $\widetilde{\epsilon}_{cZ} = \overline{\rho\mathcal{D}\nabla Z''\cdot\nabla c''}/\bar{\rho}$ is the cross dissipation rate. One of the issue in the presumed PDF approach is the closure of scalar dissipation rates appearing in the transport equations for the second moment quantities. These dissipation rates require modelling which is not always straight forward.

This was also noted by Domingo et al. [54], who derived a transport equation for progress variable c, defined as

$$c(Z) = \frac{Y^{\mathrm{u}}_{\mathrm{H_2}}(Z) - Y_{\mathrm{H_2}}(Z)}{Y^{\mathrm{u}}_{\mathrm{H_2}}(Z) - Y^{\mathrm{b}}_{\mathrm{H_2}}(Z)}. \tag{2.67}$$

The instantaneous transport equation is

$$\frac{\partial \rho c}{\partial t} + \frac{\partial \rho u_j c}{\partial x_j} = \frac{\partial}{\partial x_j}\left(\rho D\frac{\partial c}{\partial x_j}\right) + \dot{\omega}_c + \underbrace{\left(\frac{2}{Y_F^u Z - Y_F^b(Z)}\right)\left(Y_F^u - \frac{\mathrm{d}Y_F^b(Z)}{\mathrm{d}Z}\right)\rho N_{cZ}}_{(5)} - \underbrace{\left(\frac{c}{Y_F^u Z - Y_F^b(Z)}\right)\frac{\mathrm{d}^2 Y_F^b(Z)}{\mathrm{d}Z^2}\rho N_{ZZ}}_{(6)}. \tag{2.68}$$

The extra terms (5) and (6) involving N_{Zc} and N_{zz} in Eq.(2.68) arise due to the dependence of unburnt and burnt species mass fraction Y_i on c and Z. N_{Zc} is the instantaneous cross dissipation rate and will be defined later. For simplicity, these terms were neglected in their modelling [54].

There have been attempts [64, 66] to avoid modelling the extra term directly by solving the transport equation for a species and later recast it to a normalised progress variable later. A careful choice of the progress variable and mixture fraction definition can result in two statistically independent variables and thus avoid

the closure difficulties for the extra terms, as in Libby and Williams' presumed PDF approach discussed earlier [109]. For example, Fiorina et al. [64, 66] defined the progress variable c using the combined mass fraction of CO and CO_2, and the mixture fraction with the mass fraction of N_2. The transport equations for $\widetilde{Y_c}$ and $\widetilde{Y_c''^2}$ were solved instead of normalised c and then $\overline{c}$ and $\overline{c''^2}$ were constructed using the solutions. Detailed chemistry was included by using a lookup table with entries $\overline{c}$, $\overline{c''^2}$, $\tilde{Z}$ and $\widetilde{Z''^2}$ as the independent variables.

Knudsen and Pitsch [94] discussed the statistical dependence of c and Z and noted the normalisation of c by its chemical equilibrium value can separate c and Z in weakly strained flamelets but is not general. They argued that when flame is highly strained with high scalar dissipation rate, diffusion in mixture fraction space can prevent c from reaching its chemical equilibrium. Statistical independence is not guaranteed for flame close to stoichiometry where the second derivative of species with respect to Z tend to be highest.

Bray et al. [22] rewrote Eq.(2.68) in a general form as

$$\frac{\partial \rho c}{\partial t} + \frac{\partial \rho u_j c}{\partial x_j} = \frac{\partial}{\partial x_j}\left(\rho D \frac{\partial c}{\partial x_j}\right) + \dot{\omega}_c^*, \tag{2.69}$$

and highlighted the contribution from the chemical source term of the species and the three dissipation rates. The source term $\dot{\omega}_c^*$ is given by

$$\dot{\omega}_c^* = \frac{1}{\partial Y_i/\partial c}\left(\dot{\omega}_i + 2\rho N_{cZ}\frac{\partial^2 Y_i}{\partial c \partial Z} + \rho N_{zz}\frac{\partial^2 Y_i}{\partial Z^2} + \rho N_{cc}\frac{\partial^2 Y_i}{\partial c^2}\right). \tag{2.70}$$

The three scalar dissipation rates are defined as

$$N_{zz} = \rho D(\nabla Z \cdot \nabla Z), \quad N_{cz} = \rho D(\nabla c \cdot \nabla Z) \text{ and } N_{cc} = \rho D(\nabla c \cdot \nabla c), \tag{2.71}$$

where D is the molecular diffusivity which is taken to be equal for the progress variable and mixture fraction in this study for the sake of simplicity. Bray et al.[22] argued that whether the model is expressed in terms of c or Y_F, the predictions are sensitive to the mean SDR $\langle N_{cc} \rangle$ or $\langle N_{YY} \rangle$. The following points are worthy of noting

- While $\langle N_{YY} \rangle$ is more difficult to model as it can contain contribution both

from non-reactive turbulent mixing and steep gradients inside flamelet, $\langle N_{cc} \rangle$ only contains gradients in the reaction zone and may be easier to model.

- The dissipation terms are "difficult to avoid in a complete description of the flow" [22].
- These SDRs also influence displacement speed, required in the FSD approach, see Eq.(2.49)-(2.51), through

$$S_d^* = S_d^0 + \frac{1}{\rho|\nabla c|}\frac{1}{\partial Y_i/\partial c}\left[2\rho N_{cz}\frac{\partial^2 Y_i}{\partial Z \partial c} + \rho N_{ZZ}\frac{\partial^2 Y_i}{\partial Z^2} + \rho N_{cc}\frac{\partial^2 Y_i}{\partial c^2}\right], \quad (2.72)$$

where Y_i is the mass fraction of species i and

$$S_d^0 = \frac{1}{\rho|\nabla c|}\left[\dot{\omega}_c + \frac{\partial}{\partial x_i}\left(\rho D \frac{\partial c}{\partial x_i}\right)\right]. \quad (2.73)$$

The last point is also consistent with Müller et al.[128], where the turbulent flame speed is assumed to depend on SDR of the mixture fraction. Malkeson and Chakraborty [117] observed that these additional contributions were small while analysing their DNS data of turbulent planar stratified flames with initial mixture inhomogenity introduced in a direction normal to the mean flame propagation direction. The combustion kinetics of hydrocarbon flames were simulated using a single step reaction with activation energy and heat release depending on local equivalence ratio. The effect of mixture stratification in transverse direction has also been studied in turbulent [5] and laminar [52] flames, but its influence on the additional contributions in Eq. (2.72) has not been addressed yet.

The classical approach to model $\widetilde{\epsilon}_{ZZ}$ uses the inverse turbulent time scale as in Eq.(2.34) and yields reasonable results in general. The model for reactive SDR, $\widetilde{\epsilon}_{cc}$, appeared only recently [97, 132], and little is known about the modelling of the cross dissipation term [119, 163]. Whether a model is required for is still an open question [22, 55]. Mura et al. [132] have attempted to develop models for the three SDRs in partially premixed flames using thin and thickened flamelet limits with constant density approximation. They tested the models for a stratified "V" flame [161] and showed good agreement with experimental data.

Equation (2.56) has also been extended to include a mixture fraction dependence by Darbyshire et al [50]. Substantial differences in scalar mixing rate, variances and turbulence kinetic energy were reported by comparing the results obtained using various models available for SDR. Ruan et al. [163] analysed DNS data of a lifted jet flame to study the three dissipation rates. They found the cross dissipation rate is an order of magnitude smaller than the other two, consistent with previous studies by Domingo et al. [55]. Malkeson and Chakraborty [119] derived a transport equation for the cross dissipation rate and used DNS data of statistically planar stratified flames with simple chemistry to develop algebraic models.

2.5 Summary

In this chapter, premixed, non-premixed and partially premixed flames have been introduced and discussed briefly. The governing equations for turbulent reacting flows have been presented and followed by a discussion on the three numerical simulation frameworks for turbulent combustion. A brief review of various combustion modelling methodologies, both for premixed and non-premixed combustion, and the recent development for partially premixed/stratified combustion were presented. Several issues crucial to the modelling of partially premixed combustion are summarised as follows

1. The behaviour of turbulent flame stretch, including the tangential strain rate, curvature and displacement speed, which has been extensively studied for premixed flames, is less well understood for partially premixed flames. Chapter 4 attempts to shed some light on these topics.

2. The behaviour of scalar dissipation rates in partially premixed flames requires further examination. Statistics of scalars and their gradients need further examination and existing models need to be tested in partialy premixed flames. This is investigated in Chapter 5.

3. The accuracy of various models for the mean reaction rate remains unclear and their underlying assumptions need to be examined. Chapter 6 addresses these issues.

These issues are investigated by analysing DNS data of a laboratory scale lifted jet flame, which is an example of a partially premixed flame. This DNS data and its processing techniques are described in Chapter 3. As noted in Section 1.1, *a posteriori* validation of the findings from the DNS analysis is conducted in Chapter 7 by performing RANS simulations of the lifted jet flame using the model developed in this work.

Chapter 3

DNS Dataset

As noted in Chapter 2, DNS dataset contains a wealth of information to develop fundamental understanding and to test and validate modelling hypotheses. DNS of a turbulent lifted jet flame is explored to further the understanding of partially premixed combustion. The detail of this DNS data and its processing are discussed in this chapter. The partially premixed nature of this flame, not only near the flame stabilisation location, but also at downstream positions is demonstrated and is shown for both an instantaneous and an average sense.

3.1 DNS Data

Details of the DNS data used in this study can be found in Mizobuchi *et al.* [125, 126] and references therein and thus only a brief discussion on attributes relevant to this study is given here. A lifted turbulent hydrogen flame established above a fuel jet issuing from a round nozzle into quiescent air was simulated. This flame was studied experimentally by Cheng *et al.* [46, 47] The jet Mach number is 0.54 based on nozzle exit velocity of 680 m/s and its Reynolds number based on the nozzle diameter, $D = 2$ mm, is 13,600. In this DNS, the three dimensional fully compressible Navier-Stokes equations, together with the conservation equations for mass, total energy and chemical species are solved. The governing equations are discretised using a finite volume formulation. The convective terms are calculated with an upwind total variation diminishing (TVD) numerical

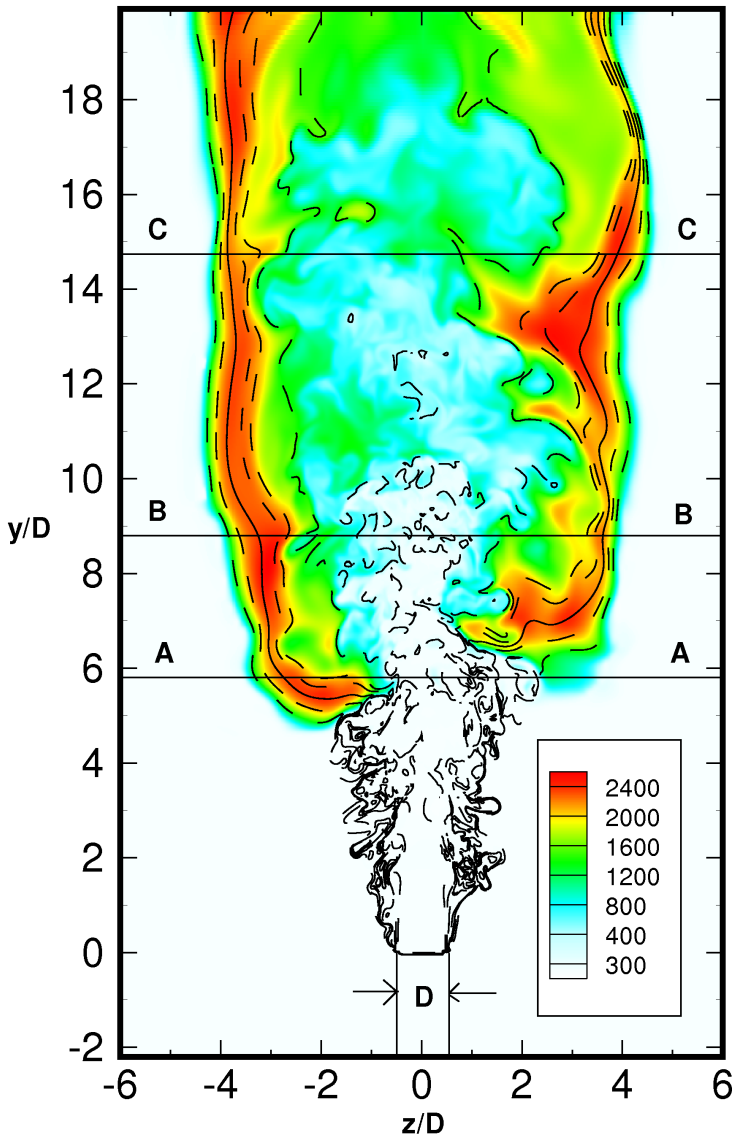

Figure 3.1: Schematic of DNS configuration. Instantaneous temperature (K) field in mid z-y plane. Stoichiometric mixture fraction contour $Z_{st} = 0.03$ (Black solid).

scheme based on Roe's approximate Riemann solver. The viscous terms are calculated using a standard second order difference scheme. A second order explicit Runge-Kutta multistage method is used for time integration.

This DNS employs a chemical kinetics mechanism involving 9 species (including nitrogen as an inert species) and 17 reactions [192]. Detailed transport properties which depend on the temperature and local species concentration are used.

The size of the computational domain is $\pm 12.5D$ in the cross-stream directions and $-2D$ to $20D$ in the streamwise direction. The domain is discretised using a non-uniform grid with a total of 200 million grid points, with a uniform grid spacing of 0.05 mm within $\pm 5D \times 14.75D \times \pm 5D$. This grid spacing is about 2.5 times the Kolmogorov length scale close to the ignition point in the experiment [46, 47]. The ratio between the stoichiometric laminar premixed flame thermal thickness and the mesh resolution is about 10. This numerical resolution was verified to be adequate to study the statistics of scalar and velocity gradients [163].

A schematic diagram of this flow configuration is shown in Fig. 3.1a along with a typical instantaneous temperature field and the stoichiometric mixture fraction contour. The streamwise, y, and cross-stream distances are normalised by the nozzle diameter. The flame lift-off height is about $5.7D$ from the nozzle exit in the DNS while it was $7D$ in the experiments of Cheng *et al.* [46, 47]. The comparison of flame brush structure, in terms of mean species mass fractions and temperature, obtained from the DNS is a close match to the experiment [163].

3.2 Data Processing Methodology

Two data processing methods are used in this study. The first one is similar to a RANS-type averaging [163] in order to investigate the mean flow and flame quantities. The scalar gradients are calculated by a central difference scheme. The statistics in a cross section at a given streamwise location are generated by splitting the cross section into a number of concentric rings as shown in Fig. 3.2 and the symbols Δ, **B1** and **C1** will be explained later. The radial distance $R = \sqrt{x^2 + z^2}$ is measured from the jet centre-line ($R = 0$). All the points in a

particular ring of width dr are averaged to obtain a mean value as

$$\overline{Q}(R,y) \;=\; \frac{1}{N_t\,N}\sum_{t_i=1}^{N_t}\sum^{N} Q(x,z,t_i;\;y), \tag{3.1}$$

where Q is the quantity of interest, N_t (=146) is the number of sampling time steps over a period of 0.09 ms and N is the total number of data points in a particular ring of width dr for one time instant. In this study the temporal and spatial, in the homogeneous direction, averaging is combined to increase the sample size for statistical accuracy since the flow and flame have reached a statistically stationary state. This has been verified by Ruan *et al.* [163] by increasing the sampling period by nearly 3 times and reconstructing appropriate statistics. Sensitivity of these statistics to the ring width dr has also been tested and it was observed to be minor [163]. Thus the results reported in this study are for $dr = 2dx$. Statistical convergence of the results presented in this study has also been verified by increasing the sample size and sampling duration [163]. Although the sample size obtained in this ring averaging method varies with radius, it is generally very large; there are more than 14,000 data points at $R/D = 0.2$. The region of interest where significant reactions occur are located mostly at $R/D > 1.0$ and thus the sample size is sufficiently large to give meaningful statistics. For the centreline values, 969 DNS data samples over 0.5 ms are ensemble averaged to obtain the required statistics. The above method is also used appropriately to obtain Favre averaged quantities.

The second method used is similar to LES-type filtering using a box filter in physical space. In this method, one single ring is split into 72 evenly distributed arc sections and this will reduce the sample size. Thus to maintain the statistical accuracy and convergence the ring width is increased to $6dx$ and the samples in 5 consecutive time steps are combined to get the required statistics such as flame surface density and surface averaged quantities required to obtain the flame stretch. The typical arc width, Δ, is marked in Fig. 3.2 for two arbitrary locations, **B1** and **C1**, chosen for the analysis presented in Chapter 4.

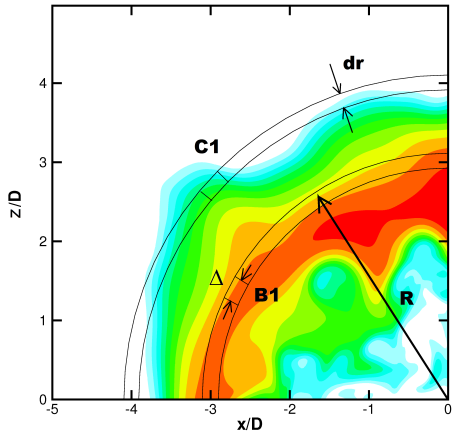

Figure 3.2: Illustration of data processing method, instantaneous temperature field in an arbitrary z-x plane is shown with positions **B1** and **C1** highlighted.

In this study the mixture fraction is calculated using [8]

$$Z = \frac{Z_{\mathrm{H}}/W_{\mathrm{H_2}} + 2(Y_{\mathrm{O_2,air}} - Z_{\mathrm{O}})/W_{\mathrm{O_2}}}{1/W_{\mathrm{H_2}} + 2Y_{\mathrm{O_2,air}}/W_{\mathrm{O_2}}}, \tag{3.2}$$

where the molecular weights are $W_{\mathrm{O_2}} = 32$ and $W_{\mathrm{H_2}} = 2$, Z_i is the mass fraction of element i and $Y_{\mathrm{O_2,air}} = 0.244$ is the mass fraction of O_2 in air with 22% O_2 and 78% N_2 by volume. This definitions gives $Z_{st} \approx 0.03$ for the stoichiometric mixture fraction. The mass diffusivity, D, of Z is calculated with a mass weighted individual species diffusivity D_i as $D = \sum Y_i D_i$.

The progress variable c depends on Z in partially premixed combustion as noted in chapter 2 and is defined in this paper using the product mass fraction Y_{H_2O} as

$$c(Z) \;=\; \frac{Y_{\mathrm{H_2O}}}{Y^{Eq}_{\mathrm{H_2O}}(Z)}, \tag{3.3}$$

where $Y^{Eq}_{\mathrm{H_2O}}(Z)$ is the equilibrium value corresponding to the local mixture fraction Z. The mass diffusivity of c is equal to $D_{\mathrm{H_2O}}$. Another progress variable can be defined using hydrogen mass fraction,

$$c_1(Z) = \frac{Y^{\mathrm{u}}_{\mathrm{H_2}}(Z) - Y_{\mathrm{H_2}}(Z)}{Y^{\mathrm{u}}_{\mathrm{H_2}}(Z) - Y^{\mathrm{b}}_{\mathrm{H_2}}(Z)}, \tag{3.4}$$

where $Y^{u}_{H_2}(Z) = Z$ for an inert mixing situation, and $Y^{b}_{H_2}(Z)$ is the equilibrium value $Y^{Eq}_{H_2}(Z)$ corresponding to the local mixture fraction Z. This c_1 has a diffusivity equal to that of H_2.

Figure 3.3 shows a scatter plot for both definitions for a range of time steps at an arbitrary axial location. Scatter plots for other axial locations show similar behaviour and are not shown here. This result shows that these two progress variables are very similar, except in the regions that are close to the burnt side. Thus, Eq. (3.3) is used for further analysis unless otherwise stated.

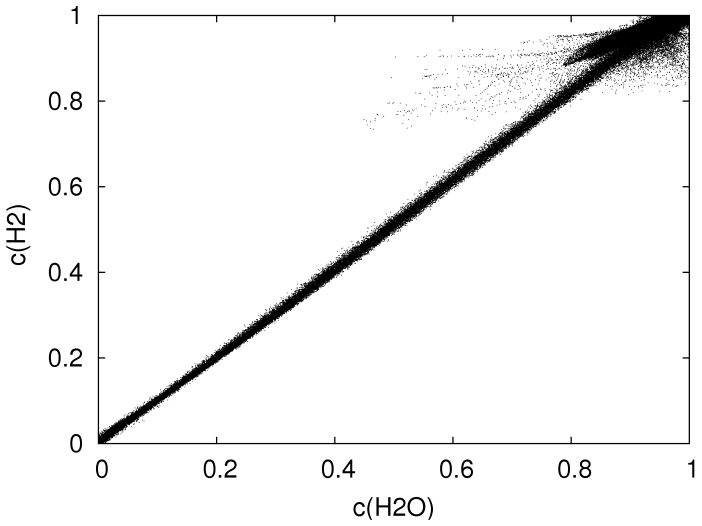

Figure 3.3: Comparison of two progress variable definitions in Eq.(3.3) and Eq.(3.4).

3.3 General Flame Features

Figure 3.1 shows the instantaneous temperature field (as a colour map) and the mixture fraction contours in the mid y-z plane from an arbitrarily selected time snapshot. The general behaviour of the mixing layer is as expected. The temperature map clearly shows a lifted flame and the peak instantaneous temperature is found to be about 2500 K close to stoichiometry.

Figure 3.4 shows the mean temperature and OH mass fraction. The mean stoichiometric mixture fraction is shown by the solid line. The mean values are

obtained using Eq. (3.1). The peak mean OH concentration corresponds to the peak mean temperature as one would expect and these peak locations are in the neighbourhood of the stoichiometric mixture fraction. Also, the averaged fields show that the flame lift-off height is about $5.7D$. Although these averaged temperature, OH and mixture fraction fields suggest a diffusion flame type structure (high $\overline{T}$, $\overline{Y}_{\mathrm{OH}}$ near $\overline{Z}_{st}$) in a mean sense, it will be shown in the next section that it is a predominantly premixed type of combustion with varying equivalence ratio and occasional diffusion flame islands occurring at downstream locations.

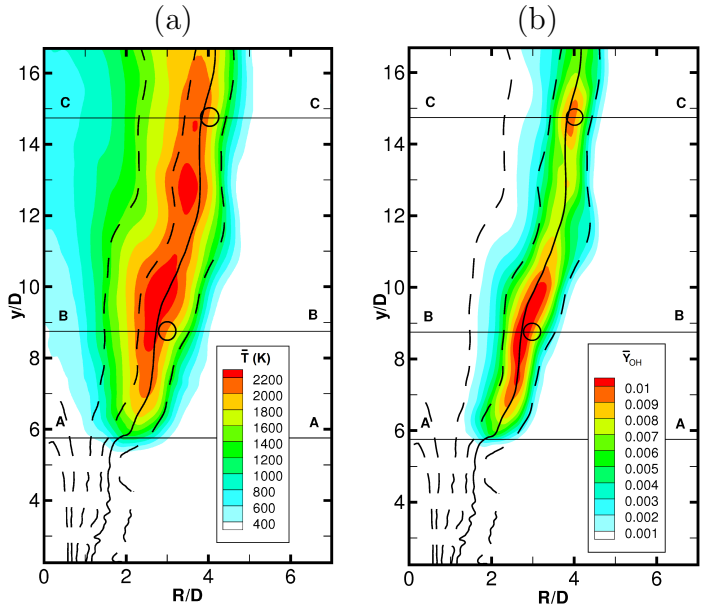

Figure 3.4: Reynolds averaged quantities. (a) temperature. (b) Y_{OH}. Stoichiometric mixture fraction contour $\overline{Z} = 0.03$ (Solid black). $\overline{Z} = 0.01$, 0.05, 0.10, 0.20 and 0.30 (Dash black). Positions **B1** and **C1** are also highlighted.

Three streamwise positions are selected for detailed investigation as illustrated in Fig.3.1 and 3.4. The location A-A is at $5.75D$ from the nozzle exit, i.e. close to the stabilization height observed in the DNS; the location B-B is at $8.75D$. A-A and B-B, are selected to enable comparison with the experimental data [46]. C-C is at $14.75D$ which is the most downstream location where grid spacing is uniform and occasional diffusion flame islands are observed in the instantaneous fields [126, 163].

Figure 3.5 illustrates the time averaged mean hydrogen consumption rate in

g/cm^3/s and the stoichiometric mixture fraction contour as solid line for the chosen three positions. In general, the reaction rate is an order of magnitude larger at position A-A while downstream the flow expands and moderate reaction rates occur in a distributed manner. At the position A-A, the reaction zone is wrinkled by turbulence and exhibits a thin flame. At the position C-C, the most intense reaction occurs along the stoichiometric mixture fraction as isolated pockets, in agreement with the observation of "diffusion flame islands" in [126].

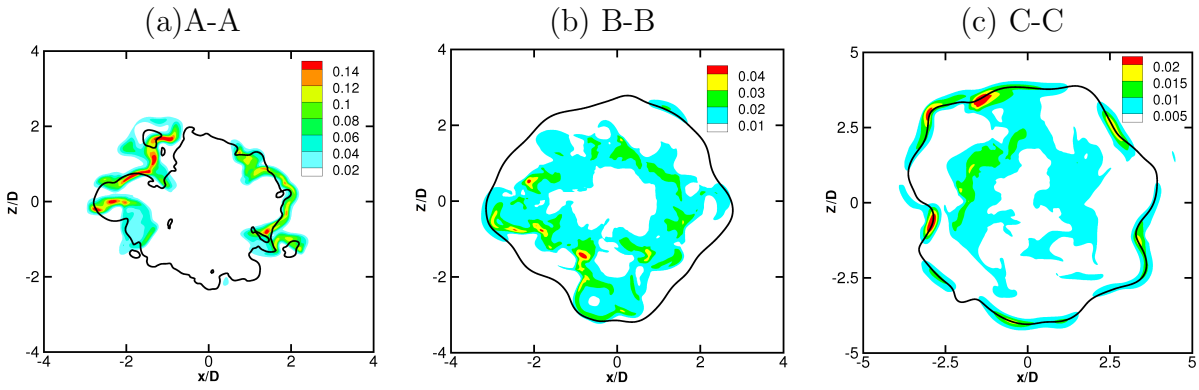

Figure 3.5: Time averaged hydrogen reaction rate in $g/cm^3/s$ for 3 axial positions. Stoichiometric mixture contour in solid black line.

Radial variations of mean temperature and species mole fractions are shown in Fig. 3.6 for six different streamwise locations in the DNS. The experimental results [46] are shown for two locations ($7D$ and $9.5D$). The DNS results show that the mean temperature increases downstream of position A-A up to a roughly constant peak value of about 2300 K for axial distances of $8.5D$ and beyond. The maximum mean temperature occurs at R/D ranging from 2 to 3, corresponding roughly to the instantaneous stoichiometric region as shown in Fig. 3.1. The mean temperature at position A-A agrees reasonably well with the experimental results at $7D$, where both positions are close to the respective stabilisation heights. It must be noted that the position A-A is at $y \approx 5.7D$. Mizobuchi et al. [125] explained that the difference in stabilisation height is because the DNS resolves the small eddies of turbulence in the flame stabilisation region but not in the flow close to nozzle exit. This causes differences in air entrainment by the turbulent jet and thus in turbulent mixing, resulting in a shift of the stabilisation height. The comparison of mean H_2 mole fractions between the DNS and the experiment is

considered to be very good. The DNS shows a slight decrease of centreline values for the positions A-A, $6.5D$ and $7D$ as one would expect. The radial gradient of mean mole fraction is decreasing, indicating that the flame brush is increasing in thickness. The mean H_2O mole fractions from the DNS and the experimental results agree reasonably well, while the mean OH mole fraction in the DNS is about twice as large as that in the experiment (compare the DNS result for the position A-A to the experimental measurement at $7D$ and the DNS for the position B-B to the experimental data at $9.5D$). The difference in stabilisation heights complicates the comparison. Nevertheless, the flames are well-resolved in the DNS, and Fig. 3.6 shows that the agreement is generally reasonable. If one offsets the difference in the flame stabilisation height, which is about $1.5D$, then the comparisons can be regarded as acceptable and this observation concurs with the observation made by Mizobuchi et al. [125].

The radial variation of $\widetilde{Z}$ and $\widetilde{c}$ at the selected three axial positions is shown in Fig. 3.7. Since the fuel is consumed, the centreline value of $\widetilde{Z}$ decreases as one moves in the downstream direction. The radial spread of the mixture fraction field can also be observed in this figure. The Favre mean progress variable increases from the centreline and then decreases gradually after reaching a peak value. The increase is due to the formation of H_2O in the flame brush and its diffusion towards the jet centre. Thus, the centreline value of $\widetilde{c}$ increases as one moves in the downstream direction. The decrease of $\widetilde{c}$ after reaching a peak value in the radial direction is due to the mixing of combustion products with the quiescent air. One can also observe that the peak value of $\widetilde{c}$ shifts radially outward from position A-A to C-C. The variation of $\widetilde{c}$ in Fig. 3.7 also suggests that the flame brush thickness increases in the downstream direction. All of these behaviours are as expected for the flow and flame configuration considered in the DNS.

Figure 3.8 shows radial variation of the mean hydrogen consumption rate and heat release rate. The ring-averaged mean reaction zone, indicated by the peak value in this figure, moves gradually inwards as axial distance increases. At the downstream position C-C, there are two reaction zones, indicated by the two peaks. The inner one corresponds to a rich premixed flame while the outer one results from the diffusion flame (see Fig.3.5). This is consistent with the contours shown in Fig.3.5 and earlier observations [125, 126]. There is little sign of heat

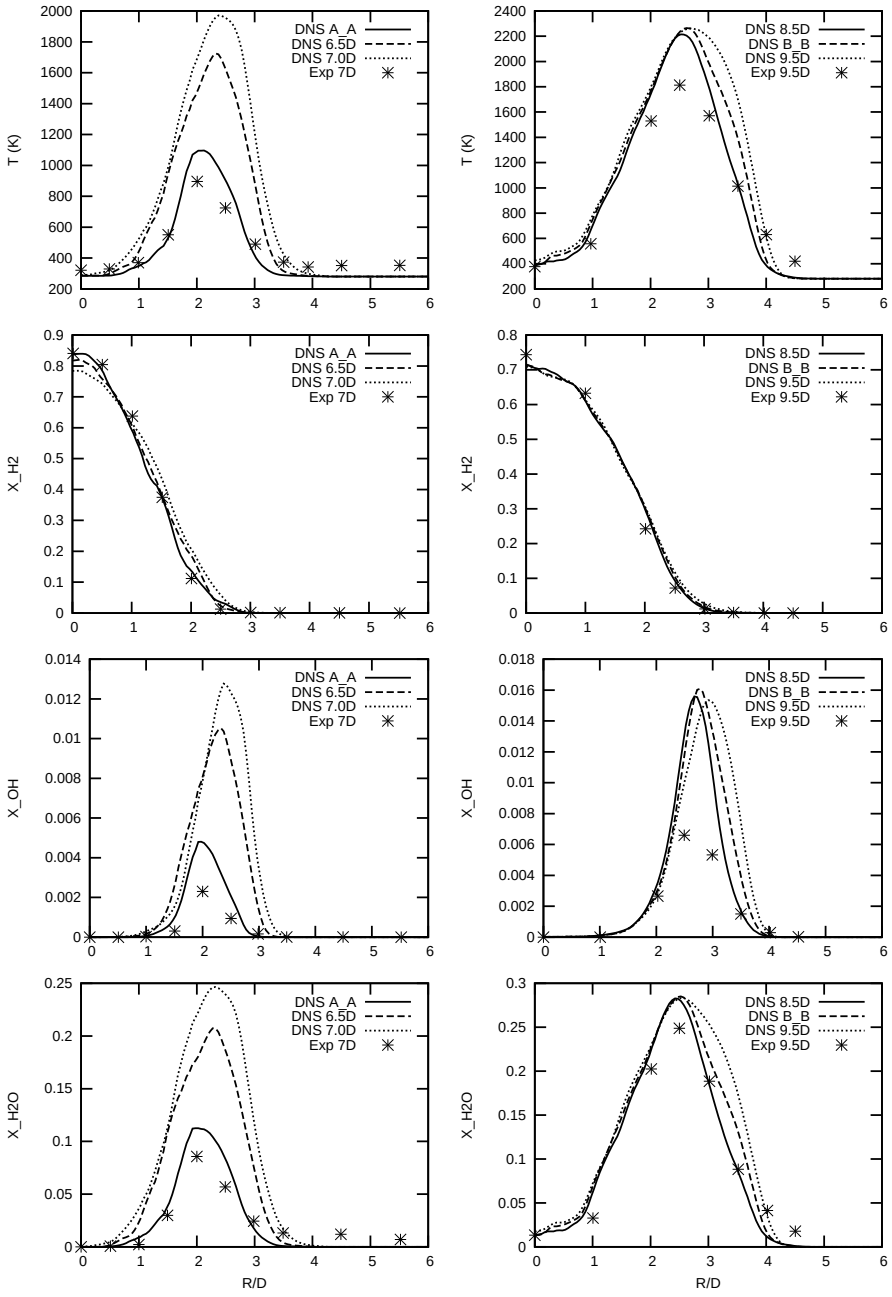

Figure 3.6: Comparison of Experiment[46] and DNS results [125, 126].

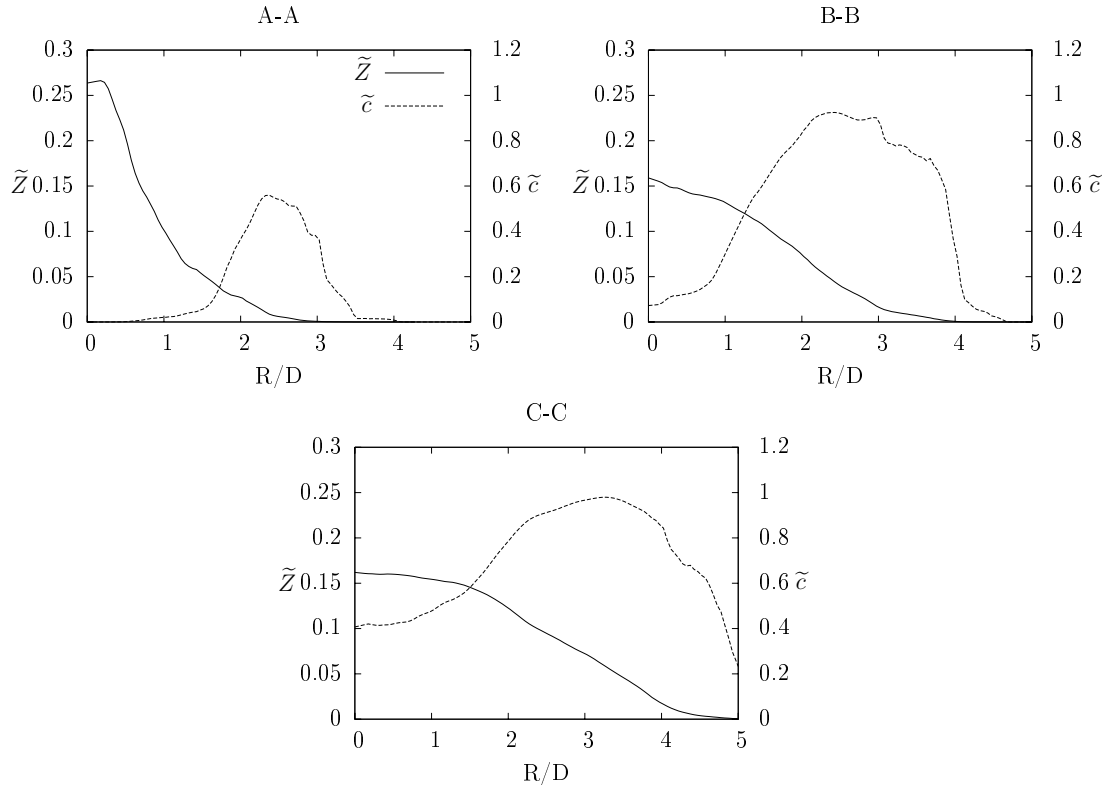

Figure 3.7: Radial variation of $\widetilde{Z}$ (solid) and $\widetilde{c}$ (dash) at 3 axial positions.

release due to the outer lean premixed flame at any of these locations.

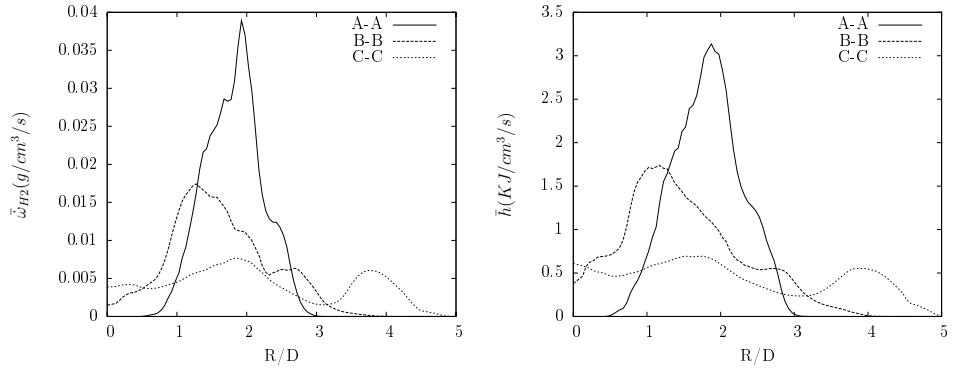

Figure 3.8: Radial variation of mean (a) H_2 consumption rate, $\bar{\omega}_{H_2}$ and (b) heat release rate $\bar{h}$ at three axial positions.

3.4 The Partially Premixed Nature

In turbulent jet lifted flames, as the surrounding air is entrained by turbulence and mixed with the turbulent jet before the flame is encountered, some partially premixed combustion characteristics can be expected, especially in the flame leading edge close to the flame stabilisation point. For lifted flames, triple flame behaviour has been observed in experiments [191] and DNS [113] at the flame leading edge with a trailing diffusion flame established further downstream. In this section, the instantaneous and averaged reaction rates are examined along with the flame index introduced in Chapter 2 to investigate whether the flame in this DNS is partially premixed or not.

The presence of premixed and non-premixed combustion modes can be easily identified by plotting the fuel consumption rate along with the flame index [193], defined in Eq.(2.62) as noted in chapter 2. The flame index is negative for non-premixed mode since the hydrogen and oxygen are diffusing in opposite directions. This index is positive for premixed mode because the fuel and oxidiser gradients are aligned with one another. Hence, the non-premixed and premixed regions can be demarcated using the FI = 0 contour. This can be applied in an instantaneous as well as an averaged sense.

The instantaneous fuel consumption rate is shown in Fig. 3.9 for two arbitrary time steps in the X-Y cross section and in Fig. 3.10 for the X-Z cross section at B-B. The stoichiometric mixture fraction and FI = 0 contours are shown respectively by solid and dashed lines. The FI contour is shown only for the region $2D \leq |x| \leq 7D$ in Fig. 3.9 for clarity. If one plots this contour for the entire range of x then these contours become very crowded near the central region, as shown in Fig. 3.10. Close to the jet centre, flame index is positive indicating a rich premixed burning mode. Along the stoichiometric mixture fraction line, flame index is negative indicating diffusion flames. Multiple reaction zones are thus clearly in evidence. One can observe that the diffusion mode of fuel consumption occurs in isolated islands on the outer side of the jet and it extends down to $y = 5.5D$ in instantaneous pictures. The rich partially premixed branch can persist throughout the computational domain of the DNS. This is because hydrogen has a very broad reaction zone and broad flammability limit compared to a hydrocarbon

flame.

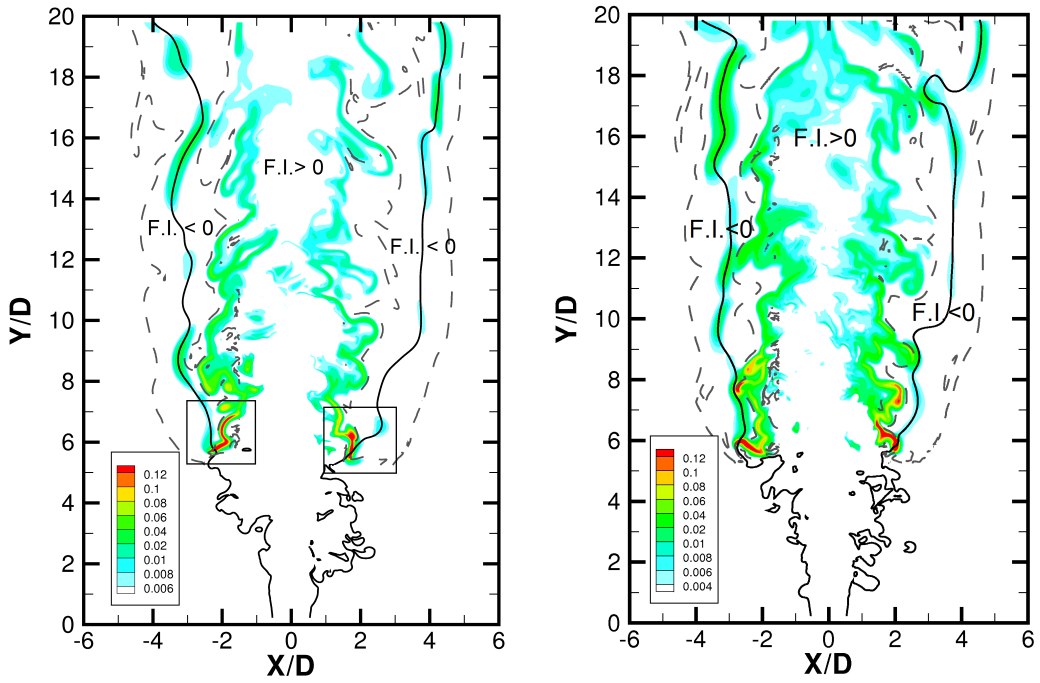

Figure 3.9: Instantaneous hydrogen reaction rate in $(g/cm^3/s)$ with flame index (dash) and stoichiometric mixture fraction (solid) for two different time steps.

The flame leading edges for one time instance in the boxes in Fig. 3.9 are enlarged in Fig.3.11. The lean premixed branch can only be seen on the right of the flame leading edge in Fig.3.11(b). The diffusion flame branch is not continuous even in the leading edge here. It detaches to form diffusion island downstream. The triple flame like features can be clearly seen in Fig.3.11(b) while only two branches can be seen in Fig.3.11(a), consistent with observation in DNS by Mizobuchi et al. [125, 126] and Luo [113].

A close comparison of the two time steps in Fig. 3.9 suggests that the diffusion burning mode is highly intermittent in the region $5.5D \leq y \leq 9.5D$ resulting in premixed combustion in an averaged sense even for the outer region of the jet. This is signified by the $\overline{\mathrm{FI}} = 0$ contour shown in Fig. 3.12, where a short lean "wing" of premixed combustion in the flame leading edge can be seen and the diffusion burning mode only appears downstream of 9.5D in the mean sense as it gradually separates from the central rich premixed core.

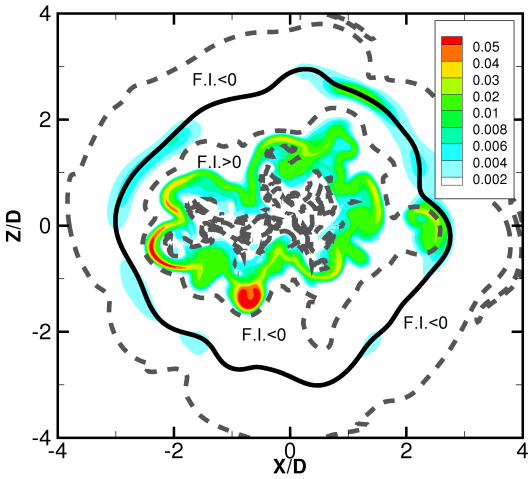

Figure 3.10: Instantaneous hydrogen reaction rate in $(g/cm^3/s)$ with flame index (dash) and stoichiometric mixture fraction (solid) for an arbitrary time step at cross section B-B.

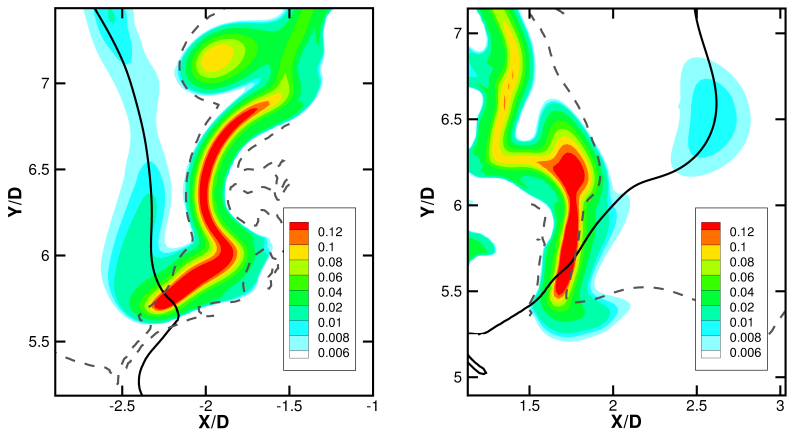

Figure 3.11: Enlarged views in flame leading edge. (a) Left and (b) right. Instantaneous hydrogen reaction rate in $(g/cm^3/s)$ with flame index (dash) and stoichiometric mixture fraction (solid).

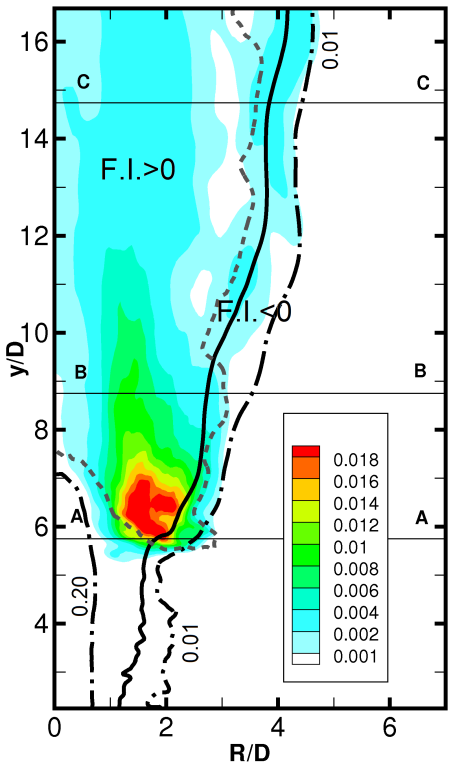

Figure 3.12: Time averaged hydrogen reaction rate in $(g/cm^3/s)$ with flame index (dash) and stoichiometric mixture fraction (solid line) and mixture fraction contour of 0.01 and 0.2 (dash-dot line).

The stoichiometric mixture fraction value is $Z_{st} = 0.03$ and, the lean and rich flammability limits [104] are respectively $Z_l = 0.005$ and $Z_r = 0.17$ for the hydrogen-air mixture used in the DNS. If the combustion occurs predominantly in non-premixed mode then the peak $\widetilde{c}$ would be roughly around $\widetilde{Z} = Z_{st}$, which is not the case as shown in Fig. 3.7. The peak location is on the lean side at position A-A suggesting a lean premixed combustion mode. For the downstream locations the peak is broad and covers a significant portion of the flammability range suggesting partially premixed mode: rich, stoichiometric and lean premixed with non-premixed combustion. These observations are consistent with the insights obtained from Figs. 3.9 to 3.12 and lend support to call this flame a partially premixed flame.

From these results one can conclude that the premixed and non-premixed modes coexist in this jet flame and the predominant fuel consumption is through premixed combustion with variable equivalence ratio. On this basis it may be more appropriate to call this flame as a partially premixed flame rather than a lifted jet diffusion flame.

3.5 Summary

In this chapter, the JAXA DNS data of a turbulent hydrogen jet lifted flame established in ambient air without coflow has been introduced. The data processing techniques used to calculate spatial and temporal averaged quantities were presented. The general feature of this flame was then explored and the flame brush structure was compared to the experimental measurements. The instantaneous and averaged fuel consumption rate have been studied along with the flame index to ascertain the partially premixed nature of this flame. It is found that triple flame-like structure exists in the flame leading edge in the flame stabilisation regions. The Flame index indicates both premixed and non-premixed burning modes coexist. There is a rich premixed flame in the jet centre and an intermittent and broken diffusion flames branch that extends to downstream positions in the computational domain due to the broad flammability limits of hydrogen. Because multiple burning modes coexist and substantial fuel is consumed in the rich premixed branch with varying equivalence ratio, it is more appropriate to

consider this flame as a partially premixed flame rather than the traditional lifted jet diffusion flame.

Chapter 4

Turbulent Flame Stretch

Turbulent partially premixed combustion occur in many practical devices, such as stratified charge direct injection engines and lean premixed pre-vaporized (LPP) gas turbine combustor. Models are required to close the mean reaction rate in Reynolds-Averaged-Navier-Stokes (RANS) and filtered chemical reaction rate in Large Eddy Simulation (LES). One popular approach for modelling turbulent premixed and stratified combustion is the flame surface density based modelling [26, 153, 182, 187].

The instantaneous flame stretch can be positive or negative; the positive value implies that the flame surface area increases due to the combined effects of turbulence and flame propagation and the negative stretch suggests that the flame surface is compressed resulting in the loss of flame area per unit volume. Earlier numerical [17, 39, 165] experimental [136, 157] and theoretical [100] studies have demonstrated that there is 20-50% probability for the flame stretch to be negative. In the view of RANS methodology the average value of the flame stretch, $\langle \Phi \rangle_s$, is expected to be positive predominantly and many modelling methods have been proposed in the past with this view. A summary of these studies is provided by Veynante and Vervisch [189] and Cant [27].

It is well recognised that the scales involved in LES modelling are different from those involved in RANS. Thus, the contributions of the negative stretch can become important and must be considered appropriately. From Eq. (2.51) one can observe that there will be three contributions to the filtered stretch rate; the first contribution comes from the filtered tangential strain rate part, the

second contribution comes from the filtered curvature related term and the third contribution comes from the sub-grid scales. Some models have been proposed in the past and can be found in Veynante and Vervisch [189] and Cant [27]. The aim of this chapter is not to develop new or improved models but to provide possible physical reasoning for the negative flame stretch. The focus is on the partially premixed flames because of its practical relevance and importance, specifically for gas turbine combustion. This is achieved by analysing direct numerical simulation (DNS) data of a laboratory scale lifted turbulent jet flame [125, 126].

Many studies using DNS data [31, 35, 36, 89, 133, 134, 159, 178] and laser diagnostics [74, 131, 171] of premixed flames, and DNS data of mildly stratified flames [118] have demonstrated that the reactive scalar gradient vector aligns with the most extensive principal component of the turbulent strain rate when the local heat release is strong. This is in contrast to the passive scalar physics where the scalar gradient is known to align with the most compressive component. This change in the alignment of scalar gradient with the principal strain rate results in a decrease of the scalar gradient in turbulent premixed flames. The rotation of principal strain planes due to dilatation effects might also be a possible cause for the decrease of the scalar gradient when the heat release is moderate [69]. It is well known [178] that this alignment is directly related to the tangential strain rate part of the flame stretch in Eq. (2.51) and thus the negative stretch rate can result from a change in the scalar gradient alignment. The questions of interest to this chapter are: is this alignment change solely responsible for the negative stretch rate or the curvature term in Eq. (2.51) play a role as well? What are their relative roles?

As it is clear from Eq. (2.51), the displacement speed, S_d, magnitude must be taken into consideration while analysing the flame stretch and its components. The behaviour of S_d in perfectly premixed flame has been studied extensively [30, 39, 40, 58, 75]. However, it has received limited attention in partially premixed or stratified flames [22, 78, 117]. The dependence of progress variable on mixture fraction yields additional contributions, as noted by Bray et al. [22] in Eq.(2.72) in chapter 2. It contains contributions from the chemical reaction rate and molecular diffusion as for the perfectly premixed flames. The additional contributions for partially premixed flames come from three scalar dissipation rates,

defined in Eq.(2.71) in chapter 2. Malkeson and Chakraborty [117] observed that these additional contributions were small while analysing their DNS data of turbulent planar stratified flames with initial mixture inhomogenity introduced in a direction normal to the mean flame propagation direction. The combustion kinetics of hydrocarbon flame was simulated using a single step reaction with activation energy and heat release depending on local equivalence ratio. The effect of mixture stratification in transverse direction has also been studied in turbulent [5] and laminar [52] flames, but its influence on the additional contributions in Eq. (2.72) has not been addressed yet, as already noted in chapter 2.

It has been observed in the past studies that the mixture stratification in the transverse direction yields triple flame [90, 147, 164]. Also, the behaviour and contributions of these additional terms in the presence of significant flame curvature, complex chemical kinetics, differential diffusion effects and a wide range of local flow and mixture conditions are not yet clear. Furthermore, their contributions to the flame stretch are yet to be studied. The DNS dataset of a laboratory scale lifted turbulent hydrogen flame simulated with detailed chemistry and transport offers a good opportunity to address these effects. Thus, the specific objectives of the current chapter are

- To investigate the behaviour of scalar-turbulence interaction and its effect on the flame stretch in partially premixed flames,
- To investigate the effects of partial premixing on the turbulent flame displacement speed and its correlation with curvature, and
- To clarify whether negative mean flame stretch can occur and how in partially premixed flames.

4.1 Turbulence-scalar interaction

The tangential strain rate a_T has been shown [178] to relate closely to the turbulence-scalar interaction process, which is signified by the inner scalar product of scalar gradient vector and the turbulent strain tensor. This can be written

as

$$T_3 = \underbrace{-2\overline{\rho D}\frac{\partial \widetilde{c}}{\partial x_i}\left(\widetilde{\frac{\partial c''}{\partial x_j}\frac{\partial u_i''}{\partial x_j}}\right)}_{T_{31}} \underbrace{-2\overline{\rho D\frac{\partial c''}{\partial x_j}\frac{\partial u_i''}{\partial x_j}\frac{\partial c''}{\partial x_i}}}_{T_{32}} \underbrace{-2\overline{\rho D\frac{\partial c''}{\partial x_i}\frac{\partial c''}{\partial x_j}\frac{\partial \tilde{u}_i}{\partial x_j}}}_{T_{33}}. \quad (4.1)$$

The radial variation of these three terms, normalised using the stoichiometric unburnt mixture density, $\rho_{u,st}$, and its flame time $t_f = \delta^0_{L,st}/S^0_{L,st}$, is shown in Fig. 4.1 for the three axial locations. It is clear that the mean scalar and velocity gradients terms, T_{31} and T_{33}, are small and the dominant contribution comes from the triple correlation T_{32}. This quantity shown in Fig. 4.1 is little noisy because of the sample size available for averaging. However, increasing the sample size by increasing the ring width does not unduly change the results, specifically the positive and negative contributions. Thus, these contributions are physical and not due to insufficient sample size. The T_{32} term is observed to be positive in general implying the generation of the iso-scalar surface area by turbulence. The negative values imply that T_{32} dissipates the surface area as have been observed in previous DNS studies of turbulent premixed [31, 32, 178] and stratified flames [118]. However, the negative values are seen for narrow regions in Fig. 4.1. This dissipation is because of stronger heat release effects in comparison to turbulence processes (cf. Fig. 3.4).

The RMS (root-mean-square) value of turbulent velocity fluctuations may be used as an indicator for the local turbulence level at a given radial location and the laminar flame speed may be compared to this RMS value to understand relative roles of the heat release and turbulence processes. One must also bear in mind that the local flame speed can vary significantly in partially premixed flames since the local mixture fraction can change. Figure 4.2 shows the radial variation of the RMS velocity normalised by the laminar flame speed for the local Favre averaged mixture fraction value. The RMS velocity is obtained using $U_{rms} = \sqrt{2\widetilde{k}/3}$, where $\widetilde{k}$ is the Favre averaged turbulent kinetic energy at a given radial location. By comparing Figs. 4.1 and 4.2 it is clear that the RMS velocity and laminar flame speed are of the same order, more precisely the normalised RMS velocity is smaller than five, in the regions of negative T_{32}, specifically for

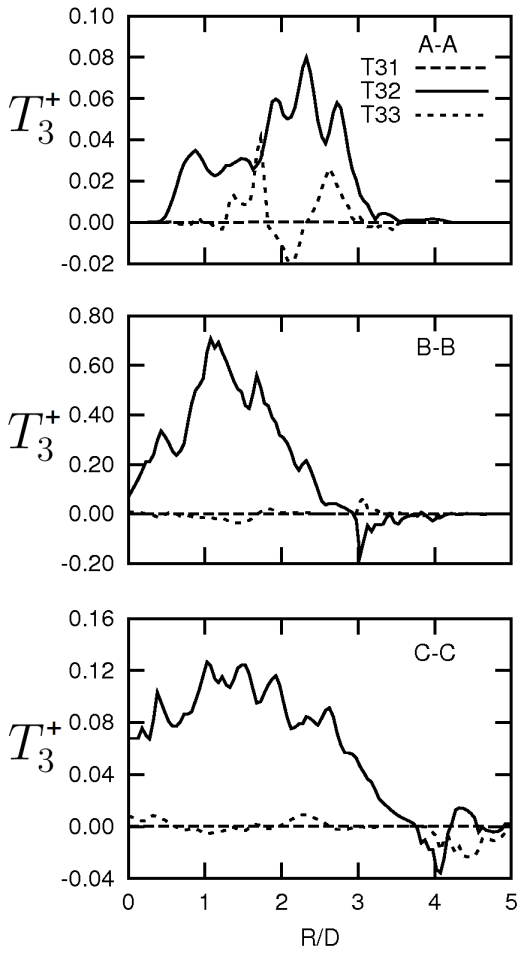

Figure 4.1: Typical radial variation of $T_3^+ = T_3\, t_f^2/\rho_{u,st}$, with $t_f = \delta_{L,st}^0/S_{L,st}^0$. Results are shown for three axial positions.

$R/D \approx 3$ at location B-B and $R/D \approx 4$ at location C-C. Although U_{rms}^+ is about three at $R/D \approx 2$ for location A-A, there is no strong flame at this location as one can clearly observe in Figs. 3.1 and 3.4. Since it is the base of the lifted flame, the turbulence effects dominate leading to the generation of iso-scalar surface area.

Through eigenvalue decomposition of $\partial u_i''/\partial x_j$, where a square matrix A can be decomposed into the form $A = Q\Lambda Q^{-1}$, here Q is the square matrix whose ith column is the eigenvector i and Λ is the diagonal whose diagonal elements are the corresponding eigenvalues, Q^{-1} is the transpose of matrix Q, T_{32} in Eq. (4.1)

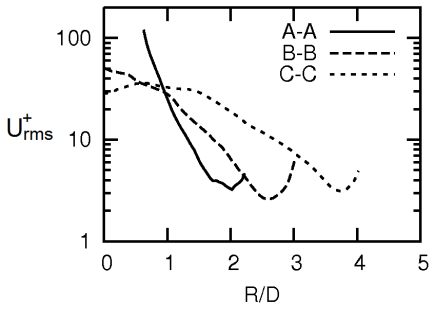

Figure 4.2: Typical radial variation of $U^+_{rms} = U_{rms}/S^0_L(\tilde{Z})$ for three axial locations.

can be written as [31, 32, 118, 178]

$$T_{32} = -2\rho D \overline{\left(\frac{\partial c''}{\partial x_i}\frac{\partial c''}{\partial x_i}\right)(\alpha\cos^2\theta_\alpha + \beta\cos^2\theta_\beta + \gamma\cos^2\theta_\gamma)}, \qquad (4.2)$$

where $\alpha > \beta > \gamma$ are the eigenvalue of the symmetric turbulent strain tensor $e''_{ij} = 0.5(\partial u''_i/\partial x_j + \partial u''_j/\partial x_i)$, with α as the most extensive and γ as the most compressive principal strains. The angles between the scalar gradient vector and the eigenvector i is denoted by θ_i. The sign of T_{32} is determined by the predominant alignment of the scalar gradient with the principal direction, which determines the characteristics of the scalar-turbulence interaction. The T_{32} will be positive or negative if the predominant alignment is with the γ or α strain respectively.

The PDFs of direction cosines are shown in Fig. 4.3 for α and γ strains at various radial and axial positions in the lifted flame investigated here. In general, alignment with the most compressive strain is observed for almost all the locations shown except for $R/D = 3$ at B-B and $R/D = 4$ at C-C. An alignment with the most extensive strain is observed for $R/D = 3$ at the location B-B where $T_{32} < 0$ as noted earlier. However, there is no clear preferential alignment at $R/D = 4$ for the location C-C although negative T_{32} is observed for this location. A careful and thorough analysis of the DNS data at this location indicates that the flame fronts are intermittent and thus this kinematic statistics may be biased. However, one must note that the sign of T_{32} is also influenced by the relative magnitude of α and γ in Eq. (4.2) and it is apparent from the behaviour of T_{32} in Fig. 4.1 that the

magnitude of α is larger than γ at $R/D = 4$ for the location C-C. This position is marked as **C1** in Fig. 3.4 and we shall investigate, the temporal variation of flame stretch, flame surface density, tangential strain rate and curvature related term at this position for a closer understanding.

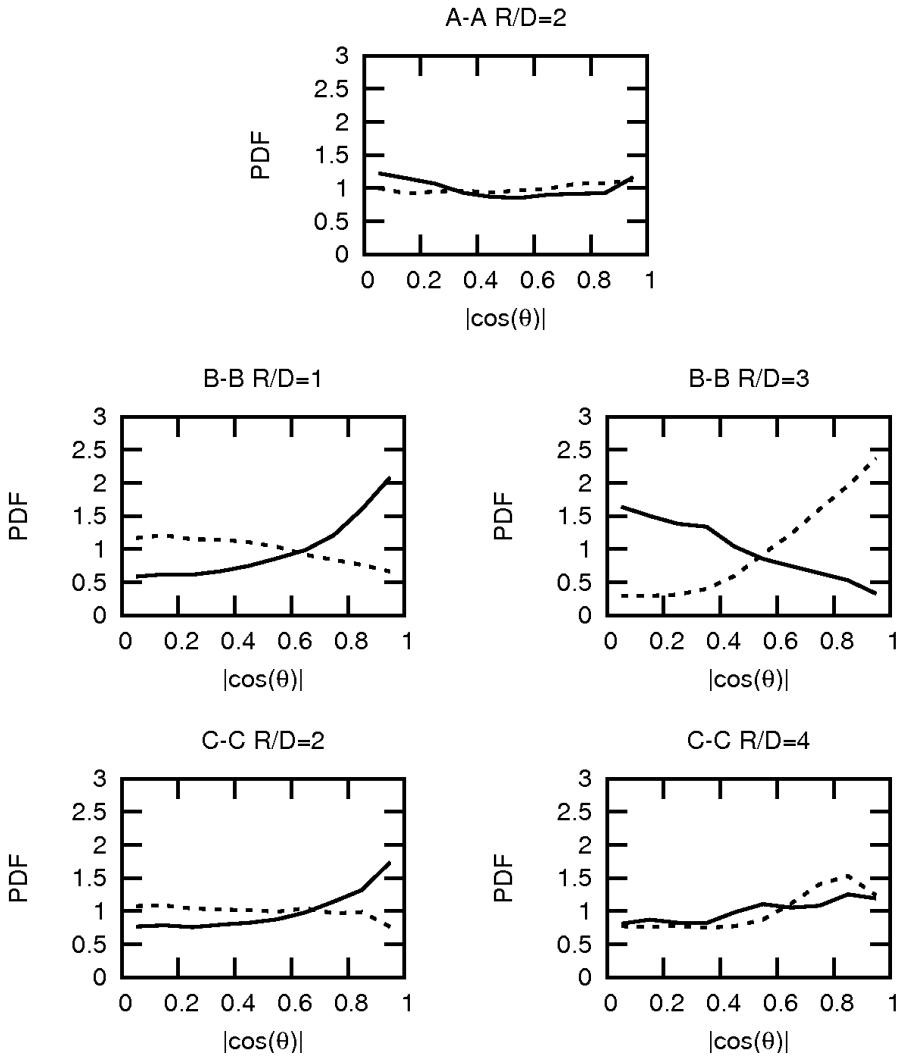

Figure 4.3: PDF of scalar gradient alignment with the principal compressive, γ (solid) and extensive, α (dotted) strains at various axial and radial locations.

In order to address the objective on the negative flame stretch, one must also study the curvature related term in Eq. (2.51), which involves the iso-surface displacement speed. As noted earlier, the role of additional contributions to the

displacement speed need to be investigated first before studying the curvature-displacement speed correlation in partially premixed flames.

4.2 The effect of partial premixing on displacement speed

As noted in Chapter 2, Bray et al. [22] discussed the additional contributions due to partial premixing and wrote the displacement speed in Eq. (2.72) as $S_d^* = S_d^0 + A^* + B^*$, where S_d^0 is given by Eq. (2.73). Using the definition of c in Eq. (3.3) one gets

$$A^* = \frac{2N_{cz}}{|\nabla c| Y_{H2O}^{Eq}(Z)} \frac{\mathrm{d}Y_{H2O}^{Eq}(Z)}{\mathrm{d}Z}, \tag{4.3}$$

$$B^* = \frac{c\, N_{ZZ}}{|\nabla c| Y_{H2O}^{Eq}(Z)} \frac{\mathrm{d}^2 Y_{H2O}^{Eq}(Z)}{\mathrm{d}Z^2}, \tag{4.4}$$

for $Y_i = Y_{\mathrm{H_2O}}$ iso-surface. The additional contributions include chemical kinetic effect and the turbulent mixing at small scales. The chemical kinetic effects come through the first and second derivatives in the mixture fraction space and the small-scale turbulent mixing is felt through the scalar dissipation rates, N_{ZZ} and N_{cZ}.

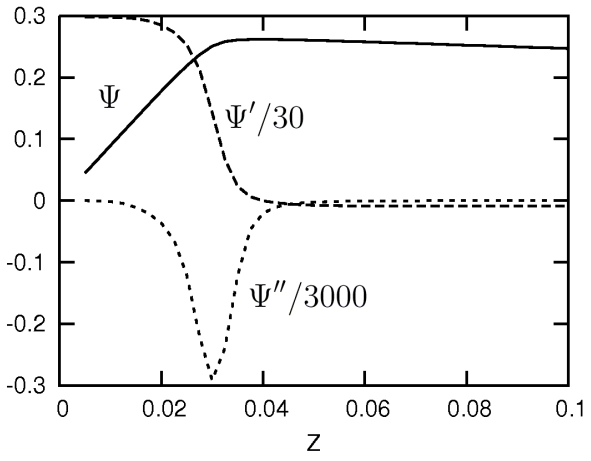

Figure 4.4: Variation of $\Psi = Y_{H2O}^{Eq}$, $d\Psi/dZ$ and $d^2\Psi/dZ^2$ with the mixture fraction Z.

The chemical kinetic terms are shown in Fig. 4.4, by plotting the variation of $\Psi = Y^{Eq}_{H_2O}$, $\Psi' = d\Psi/dZ$ and Ψ'' with Z. Note that the values are scaled appropriately to fit within the range shown in this figure. These values are obtained by performing equilibrium calculations by allowing the species involved in the chemical kinetic mechanism used in the DNS to be present in the equilibrium mixture. The burnt side values of these species in freely propagating adiabatic planar laminar flames are also used to verify the equilibrium values. As one would expect, large changes in Ψ' and Ψ'' are close to the stoichiometric value, $Z_{st} = 0.03$. The first derivative is positive for $Z < 0.04$, zero for $Z = 0.042$ and approaches a value of about -0.275 for $Z > 0.07$. The second derivative is negative reaching a peak at Z_{st} and approaching zero for $Z < 0.015$ and $Z > 0.05$ and thus the additional contribution of B^* will be significant only in this narrow range around stoichiometric mixture. Also, the second derivative is nearly 100 times larger than the first derivative and thus the contribution of B^* is expected to be larger than A^*. The contribution of A^* is expected only for $Z < 0.042$ and this will be compounded by the behaviour and magnitude of the cross dissipation rate. Ruan *et al.* [163] have shown that the cross dissipation rate is an order of magnitude smaller than the mixture fraction dissipation rate and thus the combined contributions of chemical kinetics and mixing through A^* are expected to be negligible. These observations have been confirmed by calculating the gradient weighted averages of the displacement speed, S^*_d, and its components, and the results are shown in Fig. 4.5 as the radial variation of these quantities for the three axial locations, A-A, B-B and C-C. In general $\langle S^0_d \rangle_s$ is positive and contributes predominantly to the total displacement speed, S^*_d, which is also positive. The contributions of A^* can be both positive and negative and it is an order of magnitude smaller than S^0_d for the reasons noted above. Thus, it can be neglected from further consideration. The contribution of B^* is negative and mainly around the stoichiometry. Its relative importance increases at downstream locations; a contribution of about 40% can be observed for the location C-C, which is consistent with previous DNS studies [78]. The increased contribution at downstream location is because of the presence of diffusion flame islands and the form of B^* in Eq. (4.4), the second derivative in the mixture fraction space multiplied by the mixture fraction dissipation rate, clearly notes that this contribution is from non-

premixed combustion mode. These results demonstrate the relative importance of partial premixing effects on the displacement speed of iso-scalar surfaces.

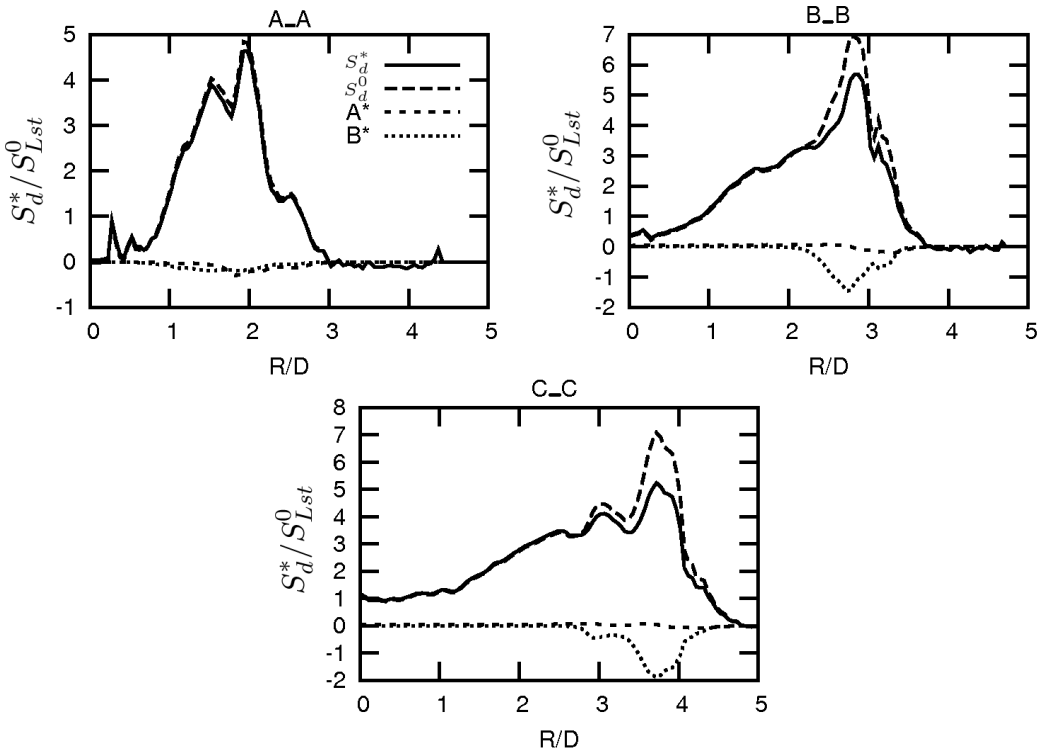

Figure 4.5: Radial variation of normalised displacement speed, $\langle S_d^* \rangle_s / S_{L,st}^0$, and its components at three axial positions.

As expected, while analysing Fig. 4.4, the effect of partial premixing is seen only near the mean stoichiometric iso-surface in Fig.4.5 (cf. Fig. 3.7). The relative importance of these effects can also be influenced by the extent of partial premixing, typically quantified by the ratio of the RMS of mixture fraction fluctuation to its mean value, $Z_{rms}/\widetilde{Z}$, the level of heat release and turbulence intensity. The value of the heat release parameter is about 7 and level of stratification is typically larger in the current DNS than in many previous studies. At $R/D = 2.75$ for the position B-B, $Z_{rms}/\widetilde{Z} \approx 0.6$ and $U_{rms}^+ \approx 3.0$. For $R/D = 3.75$ at position C-C, $Z_{rms}/\widetilde{Z} \approx 0.4$ and $U_{rms}^+ \approx 3.5$.

4.3 Curvature and its correlation with displacement speed

The effect of partial premixing have been shown to decrease the total displacement speed in general for this flame. Now, we like to examine its effect on S_d^*-curvature correlation. The PDF of curvature, normalised using the thermal thickness of a planar unstrained laminar flame with a mixture fraction value equal to $\widetilde{Z}$ at a given position of interest, ie., $K_m^+ = K_m \delta_L^0(\widetilde{Z})$, is shown in Fig. 4.6 for several radial and axial positions. Since the position A-A is close to the base, the curvature PDF at this location is shown only for comparison. The PDFs show some long positive or negative tails. The positive tail is seen near the flame lift-off height, whereas the negative tail is observed for a downstream location. This behaviour is purely due to the flame geometry, nevertheless the mean curvature is close to zero in general as observed in many earlier studies.

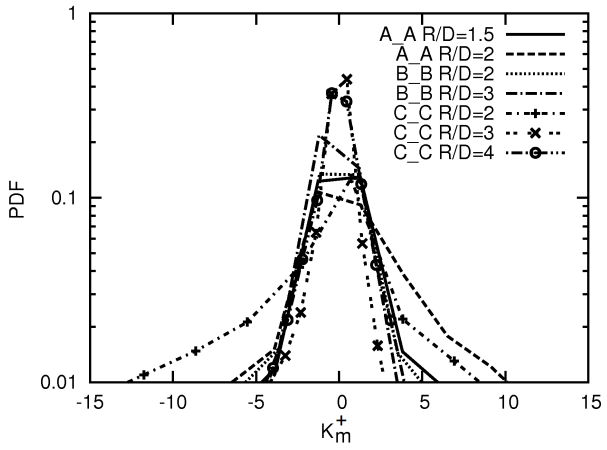

Figure 4.6: PDF of normalised curvature, $K_m^+ = K_m \delta_L^0(\widetilde{Z})$, at various axial and radial locations.

The joint PDF of the curvature and the total displacement speed, $P(K_m^+, S_d^*/S_L^0(\widetilde{Z}))$, is shown for few radial and axial locations in Fig. 4.7. The displacement speed is normalised using the laminar flame speed S_L^0 corresponding to local $\widetilde{Z}$ for a given position. Since the prime interest is on the negative flame stretch, the locations for this joint PDF are chosen to be inside the flame brush so that the laminar flame speed is non-zero, and the Favre averaged mixture fraction value is well

within the flammability limits for the hydrogen-air mixture (cf. Fig. 3.7). Also, the mean values of K_m^+ and S_d^*/S_L^0 are marked using a solid circle to help us to understand change in the correlation easily. The numerical values for these means are also given in this figure. The correlation coefficients calculated using the joint PDFs shown in Fig. 4.7 are -0.22, -0.04, -0.32 and -0.37 respectively for $R/D = 2$ and 3 at B-B, and $R/D = 2$ and 3.75 at C-C locations. It is apparent from these values that this correlation is negative even for this partially premixed flame. This negative correlation is consistent with previous studies on turbulent premixed [30, 39, 40, 71, 75] and stratified [117] flames. The instantaneous flame surface with positive curvature can have negative displacement speed as noted by Gran *et al.* [71], which is also seen in this flame. It is worth noting that Gran *et al.* considered premixed stoichiometric methane-air flame while the flame considered in this study is a hydrogen-air partially premixed flame. The negative displacement speed occurs due to the non-unity Lewis number effects on the diffusive flux (see Eq. 2.73).

As one moves radially outwards for a given axial position, except for A-A, the correlation becomes more negative which is signified by the shift of the mean S_d^* value away from the PDF peak. This is because of the change in the intensity of chemical reactions resulting in increased reaction rate as indicated by the mean temperature and OH mass fraction fields in Fig. 3.4. To elucidate the effect of partial premixing on this correlation, the joint PDF, $P(K_m^+, S_d^0/S_L^0(\widetilde{Z}))$, after excluding the additional contributions from partial premixing is shown in Fig. 4.8 for $R/D = 3.75$ at the position C-C. This particular position is chosen for this because of the significant contribution of B^* to the total displacement speed as shown in Fig. 4.5. The overall pattern of the joint PDF in Fig. 4.8 is very similar to that of $P(K_m^+, S_d^*/S_L^0(\widetilde{Z}))$ in Fig. 4.7 and since the partial premixing acts to decrease S_d^*, the negative correlation is strengthened by excluding the partial premixing contributions. The value of correlation coefficient decreases to -0.43 from -0.37 when the partial premixing terms are excluded. At other positions with small contributions from partial premixing, the joint PDFs, $P(K_m^+, S_d^*/S_L^0(\widetilde{Z}))$ and $P(K_m^+, S_d^0/S_L^0(\widetilde{Z}))$, remain similar with almost no change to the correlation coefficient noted earlier. This was also noted by Malkeson and Chakraborty for stratified flames [117].

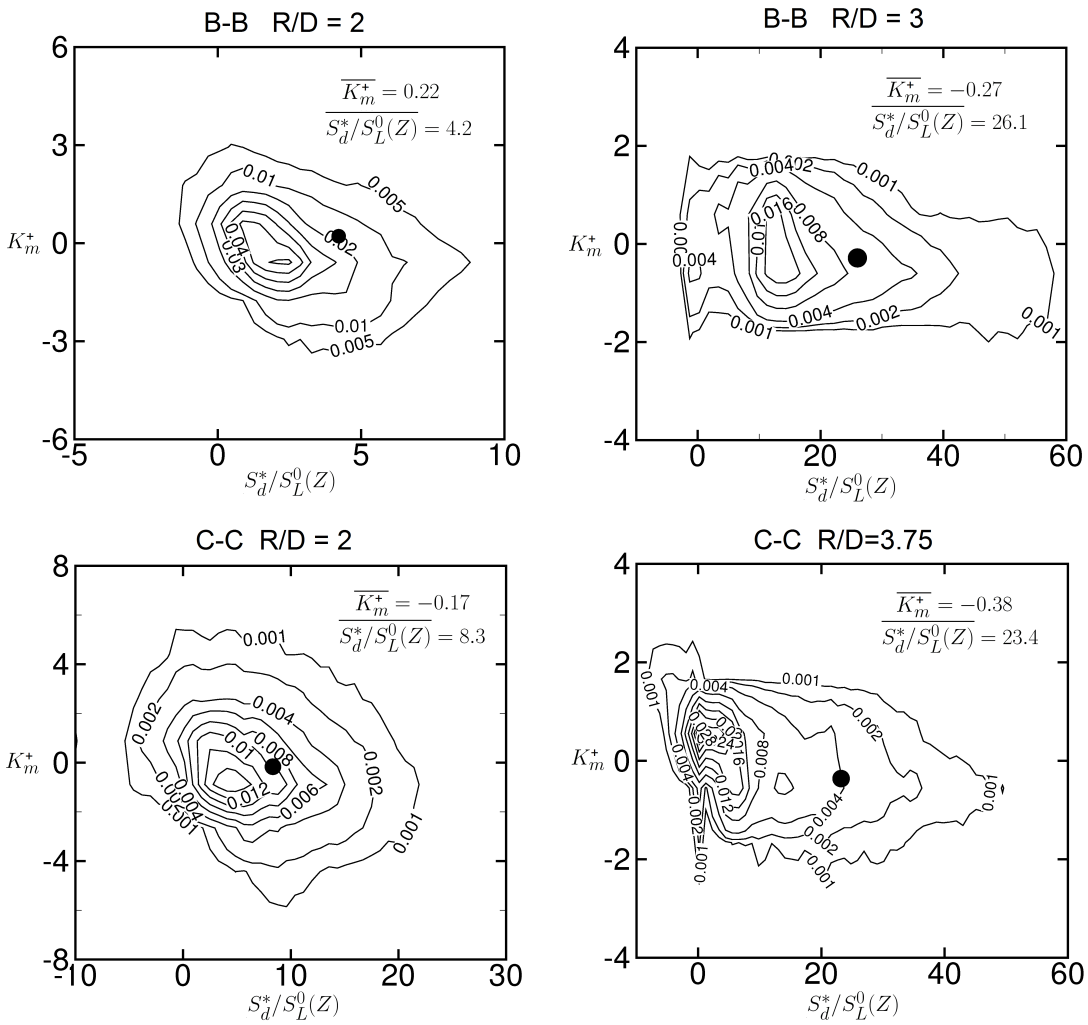

Figure 4.7: Joint PDFs of normalised curvature, K_m^+, and total displacement speed, $S_d^*/S_L^0(\widetilde{Z})$, for various axial and radial positions. Mean values noted are marked using solid circles.

To summarise, the effects of partially premixing on the displacement speed are non-negligible at downstream positions and they act to slightly reduce the negative correlation between the displacement speed and curvature. Also, these effects do not influence the alignment characteristics of the progress variable gradient with the principal strain directions observed in turbulent premixed flames. Next, we like to consider the question on negative flame stretch, ie., can $\langle\Phi\rangle_s$ in Eq. (2.49) be negative in partially premixed flames or not? If so, what are the

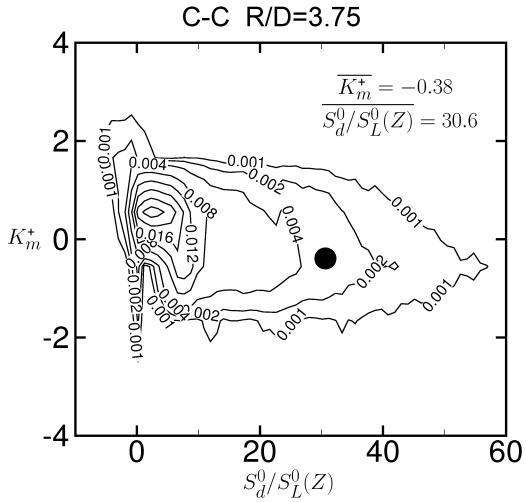

Figure 4.8: Joint PDFs of normalised curvature, K_m^+, and normalised total displacement speed, $S_d^0/S_L^0(\widetilde{Z})$, for $R/D = 3.75$ at position C-C. Mean values noted are marked using a solid circle.

causes?

4.4 Flame Surface Density and Flame stretch

The PDF of flame stretch computed using Eq. (2.51) is shown in Fig. 4.9 for few radial and axial locations. The flame stretch is normalised using the flame time of stoichiometric premixed unstrained planar flame, ie. $\Phi^+ = \Phi\delta^0_{L,st}/S^0_{L,st}$. The locations chosen are within the flame brush and they are for $T_{32} > 0$, $R/D = 2$ and $R/D = 2.5$ at axial locations B-B and C-C respectively, and $T_{32} < 0$ $R/D = 3$ and 4 respectively at B-B and C-C (see Fig. 4.1). The PDF peak is near zero which does not imply that the mean is zero. The PDF shows a long positive tail for locations with $T_{32} > 0$, whereas for locations with $T_{32} < 0$ the PDF has a long negative tail. In general, the instantaneous flame stretch takes both positive and negative values as noted in previous studies [17, 39, 100, 136, 157, 165]. However, these earlier studies have suggested that there is 50% or less probability for the flame stretch to be negative and this probability can be calculated by integrating this PDF from $-\infty$ to 0. These integrated values for the locations shown in Fig. 4.9 are 0.44 and 0.57 respectively for $R/D = 2$ and 3 at the axial position

B-B. This integral takes a value of 0.41 and 0.6 respectively for $R/D = 2.5$ and 4 at the axial position C-C. These integral values for locations with $T_{32} > 0$ are in agreement with observations in earlier studies. However, this probability larger than 50% is observed for locations with $T_{32} < 0$, where the progress variable gradient predominantly aligns with the most extensive strain.

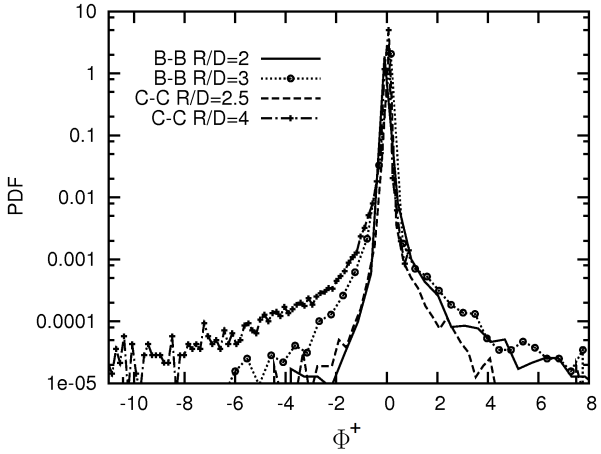

Figure 4.9: PDFs of normalised flame stretch, $\Phi^+ = \Phi\delta^0_{L,st}/S^0_{L,st}$ for various axial and radial positions.

These large probabilities for negative flame stretch are bound to yield negative mean values and it is indeed observed in Fig. 4.10 showing the radial variation of normalised surface averaged flame stretch, $\langle\Phi\rangle^+_s$. The positive and negative values for $\langle\Phi\rangle^+$ and the general trend are found to be retained when the sample size is reduced by half. A comparison of this figure to Fig. 4.1 suggests the following point. The normalised surface averaged flame stretch, $\langle\Phi\rangle^+_s$, is negative in regions where $T_{32} < 0$ for the flame considered in this study.

Equation (2.51) shows that there are two components in the flame stretch expression and so to understand the origin of the negative flame stretch, let us rewrite Eq. (2.49) as

$$\frac{1}{\Sigma}\frac{\mathrm{d}\Sigma}{\mathrm{d}t} = \langle\Phi\rangle_s - \frac{\partial\langle u_j + S_d n_j\rangle_s}{\partial x_j} \tag{4.5}$$

after some simple rearrangement. It is worth noting that the second term in the

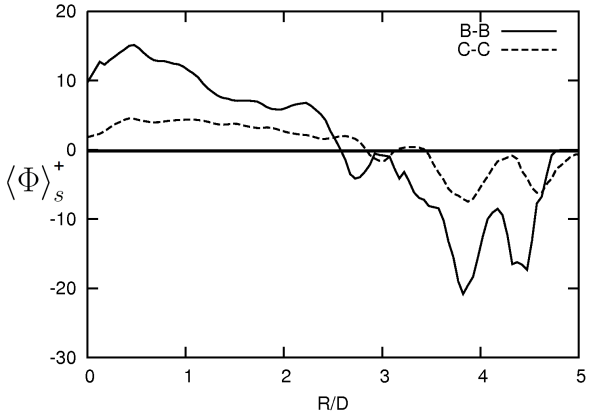

Figure 4.10: Radial variation of surface averaged flame stretch $\langle\Phi\rangle_s^+ = \langle\Phi\rangle_s \delta^0_{L,st}/S^0_{L,st}$ for position B-B and C-C.

right hand side of Eq. (4.5) is nothing but $(\mathrm{d}(\delta V)/\mathrm{d}t)/\delta V$ as shown by Candel and Poinsot [26], where δV is the elemental fluid volume following the flame element and thus, this term is positive. To elucidate the role of the alignment characteristics one writes the above equation, after using Eq. (2.51), as

$$\begin{aligned} \frac{1}{\Sigma}\frac{\mathrm{d}\Sigma}{\mathrm{d}t} &= -\left\langle n_i n_j \frac{\partial u_i}{\partial x_j}\right\rangle_s - \left\langle n_i \frac{\partial S_d}{\partial x_i}\right\rangle_s \\ &= \underbrace{-\left\langle \alpha\cos^2\theta_\alpha + \beta\cos^2\theta_\beta + \gamma\cos^2\theta_\gamma\right\rangle_s}_{\widehat{T_1}} \underbrace{-\left\langle n_i\frac{\partial S_d}{\partial x_i}\right\rangle_s}_{\widehat{T_2}}. \end{aligned} \tag{4.6}$$

The following observations are made using the second line of Eq. (4.6):

1. For a material surface $S_d = 0$ and the alignment is known to be with γ strain and thus $\mathrm{d}\Sigma/\mathrm{d}t = \langle|\gamma|\rangle_s\Sigma$ resulting in an exponential growth of the surface density. This is well known from many studies in the past.

2. For a propagating passive surface with a constant S_d one observes the exponential growth of Σ with t as for the material surface. It is known that the constant S_d leads to possibilities for cusp formation resulting from possible self intersection of the surface [98, 99, 153]. The surface density transport equation is known to be singular when the surface interactions occur [99, 153] and the above analysis does not hold. When the molecular diffusion

is present, which is so in real situations, S_d is less likely to be constant (see Eq. 2.73) and the possibilities for the cusp formation are greatly reduced.

3. For high Damkohler number premixed flames with unity Lewis number one get $\mathrm{d}\Sigma/\mathrm{d}t = -\langle\alpha\rangle_s\Sigma$ since the alignment is expected to be with the most extensive strain in regions of intense heat release. This leads to the loss of flame surface density. However, for regions with small heat release effects one observes the growth of Σ. These effects can be compounded by the response of the displacement speed to the curvature in non-unity Lewis number flames, depending on the Markstein number of the reactant mixture [13].

4. The balance of contributions from $\widehat{T}_1$ and $\widehat{T}_2$ determines the temporal, in the Lagrangian sense, variation of Σ as per Eq. (4.6) in partially premixed flames. If one presumes a flamelet type combustion in these flames then $\widehat{T}_2$ can be shown to be $\widehat{T}_2 = -\left\langle\left(\mathrm{d}S_L/\mathrm{d}Z\right)\left(\nabla c\cdot\nabla Z\right)/|\nabla c|\right\rangle_s$. Now, one realises the role of the cross dissipation, which is non-zero in the partially premixed flames, here.

The contributions of $\widehat{T}_1$ and $\widehat{T}_2$ can be obtained from the DNS data, however one must recognise that it is not straightforward to calculate $\mathrm{d}\Sigma/\mathrm{d}t$ following a flame element. Before discussing the results on these two terms, let us first study temporal variation of Σ at locations **B1** and **C1** , which are inside the flame brush as in Fig. 3.4.

This and other statistics presented in this section for these two locations are constructed following the second method of data processing described in Chapter 3.

These two locations are not at the same axial, y, distance from the nozzle exit; **B1** is on the plane B-B marked in Fig. 3.1a and **C1** is on the plane C-C. These two locations are also marked in Fig. 3.4 as black circles to indicate their relevance with respect to the averaged temperature and OH mass fraction. The filter widths, radial positions and other relevant scales at these two locations are given in Table 4.1. The laminar flame thermal thickness is calculated using a hydrogen-air mixture with a value of mixture fraction, Z, equal to the Favre

Position	R/D	Δ	δ_L^0	Λ	η	τ_f
B1	3	0.53	0.47	1.02	0.16	0.23
C1	4	0.68	0.44	0.71	0.14	0.17

Table 4.1: Turbulence integral, Λ, and Kolmogorov, η, length scales, integral time scale, τ_f, and planar laminar premixed flame thermal thickness, δ_L^0, at positions **B1** and **C1**. Length scales are in mm and time scale in ms.

averaged values at these locations. The turbulence scales are estimated using the Favre averaged turbulent kinetic energy and its dissipation rate at these locations. There is no significant change in the turbulence scales at these two locations due to the contributions from shear generated turbulence. Ideally one would like to have $\Delta \leq \Lambda$, which is satisfied at **C1**. The conditions at **B1** give $\Delta/\delta_L^0 \approx 1.1$, $\delta_L^0/\eta \approx 2.8$ and $\Lambda/\delta_L^0 \approx 2.2$.

The flame surface density in Eq. (2.49) can be calculated directly from the DNS using [153, 154, 187].

$$\Sigma\left(c^*\right) = \langle |\nabla c| | c = c^* \rangle \, \overline{P}\left(c^*\right), \tag{4.7}$$

where $\overline{P}$ is the marginal PDF of c. In this study a generalised flame surface density $\Sigma_g = \int_0^1 \Sigma\left(c^*\right) \, dc^*$ is used [189]. The temporal evolution of $\Sigma_g^+ = \Sigma_g \delta_L^0(\widetilde{Z})$ is shown in Fig. 4.11a for the two locations, **B1** and **C1**, of interest inside the flame brush. The time in Fig. 4.11 is normalised using the eddy turnover time at **B1**, calculated as $\widetilde{k}^{3/2}/\widetilde{\varepsilon}$ with the Favre averaged turbulent kinetic energy, $\widetilde{k}$, and its dissipation rate, $\widetilde{\varepsilon}$, obtained over the period marked with a small rectangle in Fig. 4.11a. The horizontal axis on the top side of this figure indicates the time normalised using the eddy turnover time at the location **C1**. The initial sharp drop of Σ_g^+ for the location **B1** and its sharp rise at about $\widehat{t} = 1$ for the location **C1** might be due to initial numerical transient in the simulation since the 200 million grid simulation used in this study was started using results of a simulation with 23 million grid points used by Mizobuchi *et al.* [125, 126] In order to minimise the effects of initial transients, the period marked with the small rectangle is chosen for the analysis of negative flame stretch.

A close-up view of the temporal variation of Σ_g^+ for the chosen period of analysis is shown in Figs. 4.11b for the location **B1** and 4.11c for the location

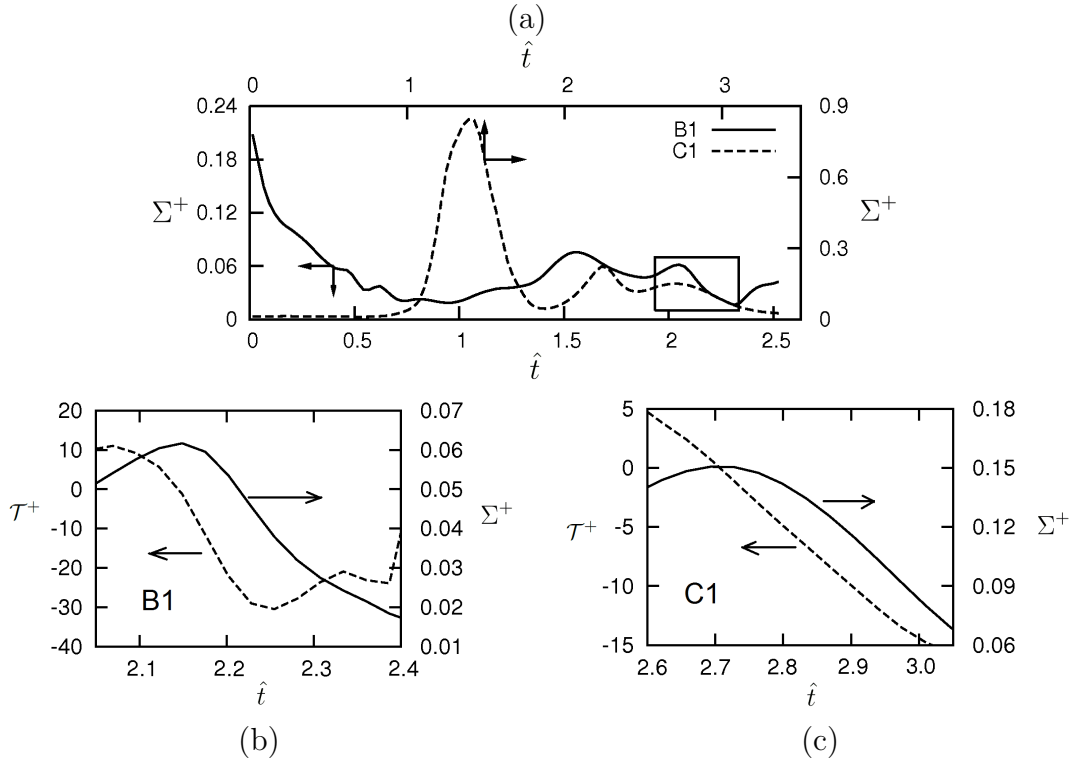

Figure 4.11: Temporal variation of normalised FSD, $\Sigma_g^+ = \Sigma_g \delta_L^0(\widetilde{Z})$, and its time derivative, $\mathcal{T}^+ = \left(\partial\Sigma_g^+/\partial t\right)/\Sigma_g^+$ at position **B1** in (b) and **C1** in (c). The variation of Σ_g^+ over the entire simulation period is shown in (a) for the two locations.

C1. The temporal change, $\mathcal{T}^+ = (\partial\Sigma_g^+/\partial t^+)/\Sigma_g^+$, is also shown. This quantity takes both positive and negative values and its negative value is of interest here. As noted earlier, computing the Lagrangian derivative is not easy and thus the Eulerian frame is chosen for further analysis. By simply rearranging Eq. (2.49) one writes $\langle\Phi\rangle_s = \mathcal{T} + [\nabla\cdot\langle(\mathbf{u}+S_d\mathbf{n})\rangle_s\Sigma_g]/\Sigma_g$. In this expression, the convective term is simply a transport term since it appears as a divergence and thus the behaviour of $\mathcal{T}^+$ has direct bearing on the behaviour of flame stretch $\langle\Phi\rangle_s^+$. As noted in Eq. (2.51) the flame stretch consists of two components and the variations of these two components are shown in Figs. 4.12a and 4.12b respectively for the locations **B1** and **C1**. These quantities are normalised as indicated in the figure caption. The tangential strain rate is expected to be positive in general but negative values are observed for location **C1**. To ascertain the physics behind

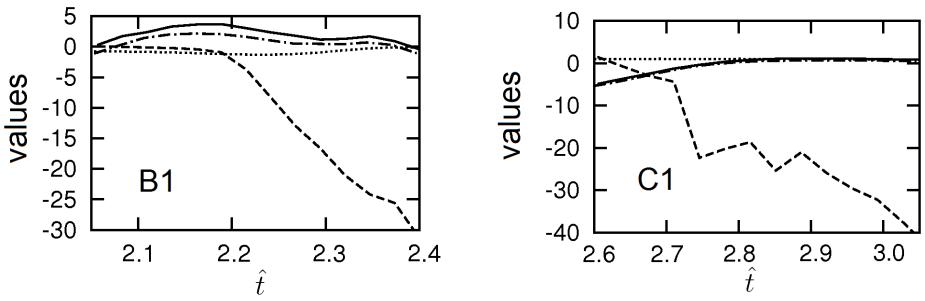

(a) (b)

Figure 4.12: Temporal variation of normalised tangential strain rate, $\langle a_T \rangle_s^+ = \langle a_T \rangle_s t_c$ (solid line) curvature term, $\langle 2S_d^* K_m \rangle_s^+ = \langle 2S_d^* K_m \rangle_s t_c$ (dashed), $\widehat{T_1^+} = \langle -n_i n_j \left(\partial u_i / \partial x_j\right) \rangle_s t_c$ (dash-dotted) and $\widehat{T_2^+} = \langle (dS_L^0/dZ) \left(\nabla c \cdot \nabla Z / |\nabla c|\right) \rangle_s$ (dotted) at positions (a) **B1** and (b) **C1**. The local chemical time scale is $t_c = \delta_L^0(\widetilde{Z})/S_L^0(\widetilde{Z})$.

this negative $\langle a_T \rangle_s^+$, the surface averaged value of the normal strain rate, $\widehat{T_1}$ in Eq. (4.6), is also shown in Fig.4.12. It is clear that the magnitude of $\nabla \cdot \mathbf{u}$ contribution to the tangential strain is small and the behaviour of $\langle a_T \rangle_s$ is dominated by the normal strain rate behaviour. One must note that the scalar gradient alignment characteristics dictate the behaviour of the normal strain rate. A gradual change of the scalar gradient alignment with the most extensive strain to the compressive strain is observed in the analysis (not shown), which causes $\langle a_T \rangle_s$ to gradually change from negative to positive value as shown in Fig. 4.12b for the location **C1**. There is no such interesting change at the location **B1** since $\langle a_T \rangle_s > 0$ over the period of analysis.

The contribution of the curvature related term shown in Fig. 4.12 is predominantly negative as one would expect from the joint PDF results discussed earlier. Also, the negative values are much larger than the positive values of $\langle a_T \rangle_s$ resulting in the negative flame stretch. One may also like to recall that the Lewis number is significantly different from unity and its significant spatial variation in the hydrogen-air partially premixed flame analysed here can lead to such pronounced effects of curvature related term. The variation of the cross dissipation related term, $\widehat{T_2}$ in Eq. (4.6), shown in Fig. 4.12 suggests that its contribution is small for the conditions of the flame analysed here. The variation of equivalence

ratio at the location **B1** is very small but for the location **C1** it varies in the range $0.83 \leq \phi \leq 1.52$. Despite this large variation, the small contribution of $\widehat{T}_2$ for this location is because of small cross dissipation rate (non-alignment of ∇c and ∇Z).

It is expected that the balance of various source and sink terms similar to that shown here to hold appropriately if one moves the observation window to another instant (see Fig. 4.11a). From the results shown in Fig. 4.12, it is apparent that the negative surface averaged flame stretch results from curvature related term and the negative stretch can persist for substantially long duration in turbulent partially premixed flames with complex thermo-chemistry compounded by the sensitivity of curvature effects to the Lewis number.

4.5 Summary

DNS data of a turbulent jet lifted hydrogen flame, simulated by Mizobuchi *et al.* [125, 126], have been analysed to shed physical insights on the behaviour of turbulent flame stretch dynamic and its relation to other physical processes, in particular, the scalar-turbulence interaction, the effects of partial premixing on the displacement speed of iso-scalar surface and its correlation with the surface curvature. This lifted flame is a good example for partially premixed combustion since the hydrogen is mixed with quiescent air by jet entrainment and turbulence processes in the near field of the fuel jet. This mixing process is unsteady creating spatially and temporally inhomogeneous reactant mixture and thus governs the combustion in downstream positions. The analysis of this DNS dataset by Ruan *et al.* [163] showed that the flame lift-off height and the flame brush structure compare reasonably well with the experimental measurements.

In this study, mean negative flame stretch has been observed within the flame brush. A detailed analysis is conducted to identify the cause of the negative flame stretch and to explore if there is a link to the alignment of scalar gradient with principal components of turbulent strain. The following conclusions can be drawn from this study.

- The alignment of scalar gradient with the most compressive strain changes

to the most extensive strain in regions where heat release effects tend to dominate the turbulence. This is consistent with many previous studies on perfectly premixed flames. This alignment change creates negative normal strain rate which can result in negative values for surface averaged tangential strain rate.

- The partial premixing affects the flame stretch through its effects on the flame surface displacement speed. Two contributions, as shown in Eqs. (2.72), (4.3) and (4.4), arise due to partially premixing. The first contribution involves the cross dissipation rate and a first derivative in the mixture fraction space as in Eq. (4.3). Its contribution to the displacement speed can be positive or negative depending on the sign of the cross dissipation rate and the local stoichiometry. For the conditions of the flame analysed in this study, this contribution is small and can be neglected. The second contribution involves the mixture fraction dissipation rate and a second derivative in the mixture fraction space as in Eq. (4.4). Hence its contribution is significant only near the stoichiometric mixture. The source or sink contribution from this term depends on the sign of the second derivative and there is a sink contribution for the definition of c used in this paper.

- The correlation of curvature and displacement speed is found to be negative in general and the effects of partial premixing act to reduce this correlation, but overall shape of their joint PDFs remains similar to those for perfectly premixed flames.

- Temporal variation of generalised flame surface density, surface averaged tangential strain rate and curvature related term are obtained using an appropriate LES-type filter for the DNS data to study the cause of the negative flame stretch. Time series of the flame surface density, its Eulerian time derivative, surface averaged tangential strain rate and its components, and surface averaged curvature term are investigated to elucidate their role on the negative mean flame stretch. Negative surface averaged tangential strain rates are generally observed in regions with scalar gradient aligning with the most extensive strain. This, with negative value for the curvature

related term yields negative flame stretch. The contribution of curvature related term is observed to be predominantly negative in general. These observations are supported through a simple analysis of the flame surface density evolution equation.

The negative flame stretch may not be ignored in LES as well as RANS simulations of partially premixed flames which are thermo-diffusively unstable. This becomes relevant especially from the modelling of turbulent combustion of future multicomponent fuels, resulting from either bio-fuels or by blending hydrocarbons with hydrogen, containing substantial amount of hydrogen. The multicomponent fuels are projected to be more environmentally friendlier.

Chapter 5

Scalars and their Disspation Rates

As noted in Eq.(2.70) of Chapter 2, there are three scalar dissipation rates (SDR) that can contribute to the overall mean reaction rate. These dissipation rates are for the mixture fraction N_{ZZ}, the progress variable N_{cc} and their cross dissipation rate (CDR) N_{cZ}, which arises due to the dependence of the reaction progress variable on the mixture fraction. Scalar gradients and dissipation rates are therefore important quantities to study in order to develop fundamental understanding of these small-scale turbulent mixing processes which are closely tied to the chemical reactions. Furthermore, scalar dissipations appear as central quantities in various modelling approaches for turbulent combustion [189] as noted in Chapter 2, for example, in the transported PDF method [152] and CMC [92] formulations, involve the conditional SDR.

Direct measurement of the scalar dissipation rates is difficult as it requires all three components of scalar gradients, which are driven by either the small scales (Kolmogorov scale) of turbulence or the scales of chemical reactions. These scales are generally not fully resolved by laser diagnostic techniques in relatively high Reynolds number flows. Some previous studies have attempted to measure N_{ZZ} [135, 172, 173] and N_{cc} [43, 44, 139], providing very useful information. Direct information for the cross dissipation rate N_{cZ} is only available recently [55, 119, 163]. Accurate and reliable measurements of these quantities would

be very valuable for the development of combustion models and would help to improve our understanding of turbulent combustion phenomena. The JAXA DNS having a wealth of information, is best suited to study the three dissipation rates. Furthermore, the JAXA DNS is for a laboratory-scaled turbulent jet lifted flame, which can help us to shed lights on the effects of the three dissipation rates in terms of the flame stabilisation mechanism. Previous studies [24, 135, 143] focus primarily on the dissipation rate of mixture fraction, while the dissipation of progress variable and the cross dissipation in the flame stabilisation region have not been studied. It would be of interest to study the three dissipation rates in a unified framework.

The specific objectives of this chapter are,

- To examine the behaviour of the three dissipation rates in the flame stabilisation region.
- To report their axial and radial variations for later model development and validation.
- To test whether the currently available simple algebraic models, involving a constant ratio of scalar to fluid mechanical time scales, together with scalar variances and covariance, are satisfactory for these dissipation rates.

It is noted here that the results presented in this Chapter used a c definition with fuel mass fraction as in Eq.(3.4). The influence of the choice of progress variable on the scalar dissipation rate modelling would be clear later when DNS results are compared with algebraic models.

5.1 Dissipation Rates and Flame Stabilisation

5.1.1 Stabilisation Mechanism for Turbulent Lifted Flame

Although turbulent lifted jet flame has been the subject of many studies, the mechanisms of flame stabilisation still remain elusive and an open question [114, 146]. Several different theories have been developed but so far none of them can explain all the phenomena observed [114]. One controversy is centred on the

degree of "premixedness" of the reactants upstream of the lifted flame base. Vanquickenborne and van Tiggenlen [185] suggest that flame stabilisation occurs due to the balance between the local jet flow velocity and the local burning velocity of the "premixed" fluid upstream of the flame base along the stoichiometric mixture contour. Peters and Williams [143] suggest that quenching of laminar diffusion flamelet at the flame base due to excessive stretching or scalar dissipation is the major stabilisation mechanism. However, as Pitts [146] points out, this theory ignores the partial premixing of fuel and oxidizer upstream of the flame. There are controversies on different interpretation of "mean values of scalar dissipation and shorter lived regions of high scalar dissipation" [114]. Nevertheless, quenching through stretching of large vortices is considered to be a relevant mechanism for lifted flame stabilisation. Recently, autoignition was identified as one of the major stabilisation mechanism for lifted flame in the presence of heated coflow. DNS studies of hydrogen [112, 195] and ethylene [194] turbulent jet lifted flames have been explored to reveal the role of autoignition in flame stabilisation.

As these theories are assessed and new experimental data emerge, the notion of partially premixed combustion [142] and the edge flame concept [25, 61, 183] are in increasing favour. Laminar triple flame has been observed experimentally [90, 144]. Its role in the stabilisation of laminar propane lifted flame has been supported by experiments [42]. The triple flame is considered to be partially premixed, and it can propagate upstream and modifies the flow field upstream by heat release [61, 164]. Experimental evidences [129, 167, 191] and DNS studies [113, 125, 126] seem to support the concept of triple flame in the turbulent lifted flame base, depending on the flow and mixing conditions. As noted earlier there are three dissipation rates generally present in partially premixed flames, while SDR of the mixture fraction has been extensively studied to assess the flamelet quenching theory in the lifted flame stabilisation mechanism suggested by Peters and Williams [143], SDR of the progress variable and the CDR in the stabilisation region have not received any attention. In particular, the role of CDR is not clearly understood. There quantities become central if the concepts based on the premixed flames propagation [185] and the partially premixed combustion [142] apply at the lifted flame base.

Figure 5.1 shows the stoichiometric mixture fraction contour and a representa-

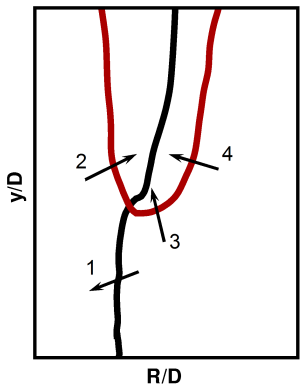

Figure 5.1: A general turbulent lifted flame configuration. Flame position (red solid). Stoichiometric mixture (black solid). Arrow 1 indicates the direction of mixture fraction gradient vectors. Arrow 2-4 indicates direction for progress variable gradient vectors.

tive progress variable contour indicating the flame position, illustrating a general configuration for lifted flames. Simple argument for gradient vectors reveals an interesting characteristic of CDR, as shown in Fig.5.1. Arrow 1 here indicates that the gradient of mixture fraction is generally pointing toward the jet centre where the mixture is rich. Arrows 2-4 show gradients of the progress variable, firstly pointing away from the jet centre (Arrow 2), then pointing downstream at flame leading edge (Arrow 3), and then toward the jet centre (Arrow 4). These directions are indicative only. In general, the gradients of the mixture fraction and progress variable are likely to be perpendicular at the flame leading edge and parallel at downstream positions. This may lead to a change of sign in N_{cZ} at flame leading edge or a value close to zero in the flame stabilisation region. This implies that CDR may be used as a marker for the flame stabilisation position.

In this section, we will conduct a detailed study for the SDR of the mixture fraction Z, a reaction progress variable c and their CDR in the flame stabilisation region. Also the role of the cross dissipation rate in flame stabilisation is explored. Furthermore, to what extend the gradient alignments suggested in Fig.5.1 are applicable and whether this can be used effectively as a marker to identify stabilisation region are investigated.

5.1.2 Comparison of Flame Stabilisation Position

The lift-off height in a lifted flame is typically measured from the nozzle exit to the flame leading edge. Various definitions for this height exist in the literature and it is likely to depend on the experimental techniques used. A reference value of CH [191] and OH [195] radicals have been used to denote the flame front. The start of high temperature marked by a temperature threshold is another popular choice in experiments using PIV techniques and it is tracked by the disappearance of the PIV seeding particles [129, 167]. It can also be done by visual observation of a particular temperature level [46] from the images obtained from the experiments. In numerical simulation, a maximum reaction rate or heat release rate [63] is commonly used to define a stabilisation point to which a lift-off height is measured. In order to obtain consistent comparison, we first examine the difference in the lift-off height L using various definitions for the flame leading edge.

Figure 5.2 shows contours of averaged OH mass fraction, heat release rate, progress variable c and temperature near the stabilisation region. The stoichiometric mixture fraction contour is included as black solid line. These averaged quantities are obtained from DNS using techniques described in Chapter 3. The most leading edge defined by $\tilde{Y}_{\mathrm{OH}} = 0.001$, 10% of maximum heat release, $\bar{c} = 0.1$ and $\tilde{T} = 900$ K respectively are also hightlighed. The lift-off heights obtained using these measures are 5.6D, 5.4D, 5D and 5.7D respectively. Difference is small except when $\bar{c}$ contour is used. This is expected because c is defined using hydrogen which has a Lewis number significantly less than one and thus can diffuse farther upstream. The spread for the $\bar{c}$ contour is the broadest, followed by the temperature contour and the OH mass fraction contours have the narrowest spread. While the maximum Y_{OH} and temperature coincide closely with the stoichiometric mixture fraction line, the combustion product region denoted by large value of $\bar{c}$ can occur in a relatively low temperature region. It is also observed that the flame stabilises in the lean mixture but within the lean flammability limit.

Figure 5.3 shows the velocity vectors in the flame stabilisation region. Significant flow divergence can be seen in the upstream region with intensive heat

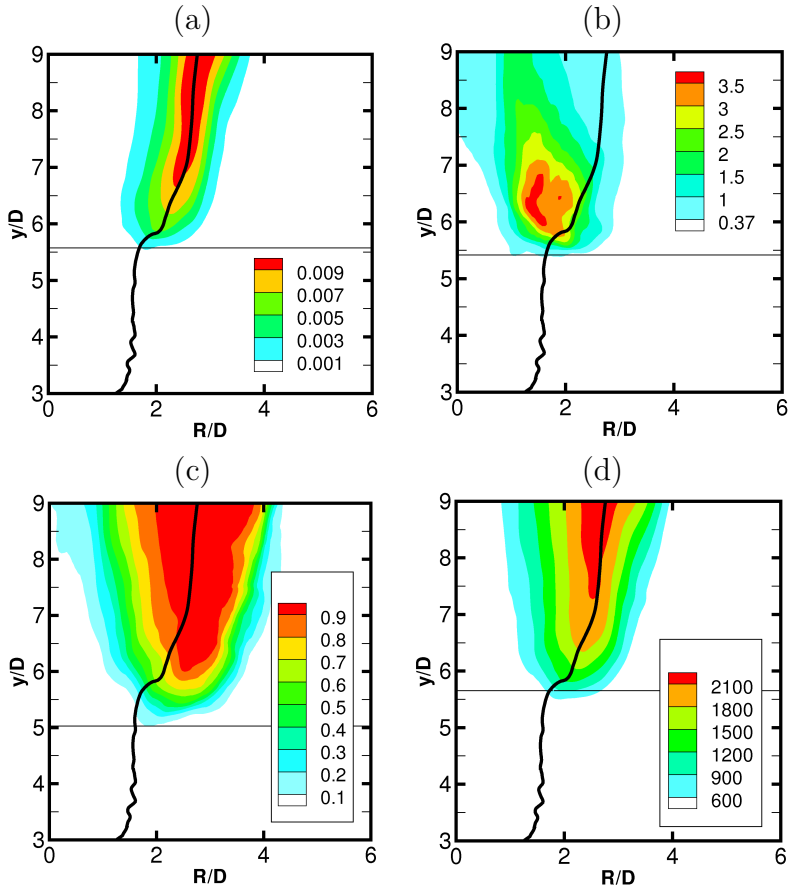

Figure 5.2: Contours for Reynolds averaged (a) Y_{OH}, (b) heat release rate ($kJ/cm^3/s$), (c) progress variable c ,(d) temperature (K) at stabilisation region. Stoichiometric mixture fraction (Black solid).

release, which occurs in rich mixture and in the form of a propagating flame kernel. The deflection of the stoichiometric mixture fraction contour away from the flame kernel is also evident.

Since the difference in the lift-off height is small, we use the most upstream position of the $\bar{T} = 900$ K as the flame stabilisation point hereafter. This definition is consistent with the experimental study in [46] and a CMC simulation for this flame [88]. At this point, it is found that $\bar{Z} \approx 0.02$ and the axial flow velocity is about 2.2 times of the stoichiometric laminar flame speed S_L^0. This observation is consistent with the finding in [129]. Within $\pm 0.1D$ in the radial direction from this point, the variation in the mean mixture fraction is $0.015 < \bar{Z} < 0.03$,

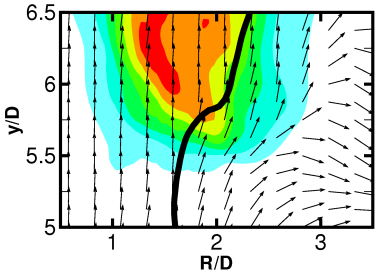

Figure 5.3: Enlarged view of flame stabilisation region. Colour map is for heat release rate. Black solid line is stoichiometric Z contour. Arrows are velocity vectors (not in scaled).

for which the laminar flame speed variation is about $0.3 - 1.0$ times of the one correspond to stoichiometric mixture. This is consistent with observation in experiment [129].

5.1.3 Mean SDR and CDR

Figure 5.4 presents the time averaged contours for the scalar dissipation rates, $\bar{N}_{ZZ}$ and $\bar{N}_{cc}$. Also included in the figure are the contours of $\bar{Z} = Z_{st}$, $\bar{T} = 900K$ and 80%-90% maximum heat release rate. $\bar{N}_{ZZ}$ has been normalised by a reference quenching value $N^q_{ZZ} = 73$ s^{-1} for stoichiometric mixture, which was used in [88]. Figure 5.4(a) clearly shows that at the flame leading edge, $\bar{N}_{ZZ}$ is about $0.03N^q_{ZZ}$, and in the high heat release region with rich mixture, $\bar{N}_{ZZ}$ can be as higher as about $0.65N^q_{ZZ}$. This is consistent with experimental observation [24] and numerical simulation [88]. Lean mixtures generally experience low $\bar{N}_{ZZ}$, which allows the flame to propagate more easily upstream and the flame stabilises in the lean part. This can be seen clearly in Fig.5.4(a).

The $\bar{N}_{cc}$ contours in Fig. 5.4(b) has been normalised using a reference value $N^r_{cc} = 4735s^{-1}$ which is the scalar dissipation rate at $T = 900K$ in the stoichiometric unstrained laminar premixed flame. This reference value for $Z = 0.015$ is $0.21N^r_{cc}$. It is clear that $\bar{N}_{cc}$ is an order of magnitude larger than $\bar{N}_{ZZ}$. High $\bar{N}_{cc}$ occur in rich mixture and they coincide well with the maximum heat release region, which implies that $\bar{N}_{cc}$ is due to intense chemical reaction. In the lean side, $\bar{N}_{cc}$ is generally smaller and in temperature region $\bar{T} < 900$ K, indicating

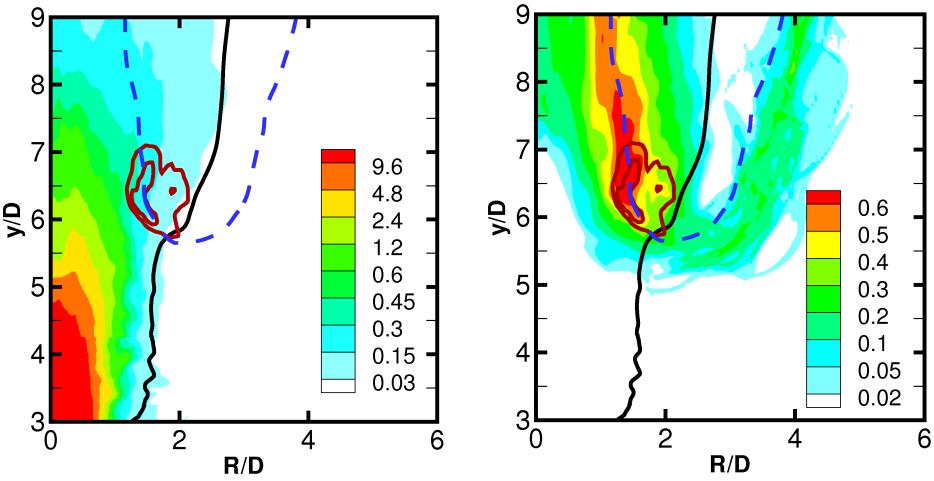

(a) (b)

Figure 5.4: Contours for normalised (a) $\bar{N}_{ZZ}$ and (b) $\bar{N}_{cc}$ near stabilisation region. The contours of $\bar{Z} = Z_{st}$ (black solid), $\bar{T} = 900K$ contour (blue dashed), and $80\% - 90\%$ of maximum heat release rate (red solid) are also shown.

the reactions are less intense. However, a value of unity is not see in Fig.5.4(b) and the typical value is only about 20-30% of N^r_{cc} when $\bar{Z} = Z_{st}$ and $\bar{T} = 900$K. Mizobuchi et al. [125] tracked an arbitrary flame leading edge position and found that the turbulent intensity level was very low and the flow was almost laminar. They found that the flow velocity at that position was in the same order of the laminar flame speed. These observations suggest that the leading edge flame is almost laminar.

Figure 5.5 presents the variation of $\bar{N}_{cZ}$ and shows that $\bar{N}_{cZ}$ is negative in the rich side. In the lean side, $\bar{N}_{cZ}$ can be both weakly positive and negative. A close inspection at the flame leading edge shows that there is a change of sign for $\bar{N}_{cZ}$. The maximum positive $\bar{N}_{cZ}$ also occurs at the lift-off height for slightly lean mixture. The $\bar{T} = 900K$ contour at the leading edge and on the lean side closely follows $\overline{N}_{cZ} \approx 0$. Further to the right of this contour, there is a region where $\bar{N}_{cZ}$ is weakly positive due to the mixing of burnt gas with entrained air. This clearly supports our postulation earlier that in the rich side, the two gradients, ∇Z and ∇c, oppose each other and lead to negative $\bar{N}_{cZ}$; while at the flame leading edge, these gradients are aligned in a perpendicular fashion yielding $\bar{N}_{cZ}$ close to zero; while on the lean side, gradients point to the same direction leading to positive

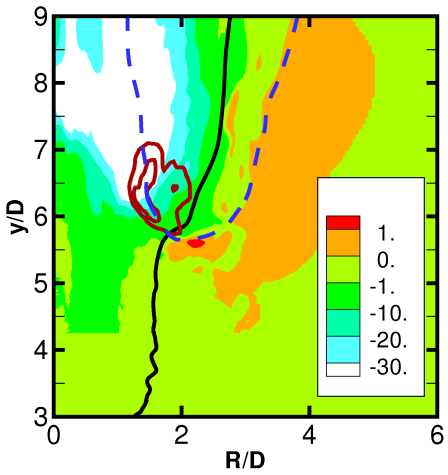

Figure 5.5: Contours for $\bar{N}_{cZ}$ near stabilisation region. The contours of $\bar{Z} = Z_{st}$ (black solid), $\bar{T} = 900K$ contour (blue dashed), and $80\% - 90\%$ of maximum heat release rate (red solid) are also shown.

$\bar{N}_{cZ}$. It is noted that there is another $\bar{N}_{cZ} \approx 0$ line on the further right in the very lean mixture. This is considered not relevant because both the mixture fraction and progress variable would almost be zero in this quiescent surrounding region.

The cross dissipation rate contains information about the mixture fraction and the progress variable gradients, which are influenced by the interaction among turbulence, scalar mixing and chemical reactions. The coincidence of the flame leading edge and the $\bar{N}_{cZ} = 0$ contour observed here is not incidental. It is postulated that the flame stabilises in region having favourable condition in terms of not only the mixture fraction and its dissipation rate, but also on the small scale mixing rate of hot products and cold reactant, which is dictated by the scalar-turbulence interaction and its influence on the progress variable gradient. The cross dissipation rate reflects these compounded effects well. Therefore, the cross dissipation rate is a good marker for flame lift-off height and it is an important parameter in the stabilisation mechanism that deserves more attention. Further statistics on the gradient alignment characteristics at the flame leading edge from laser diagnostics are desirable and would help to further our understanding.

5.2 Scalar Variances and Covariance

Since scalar dissipation rates are measures of the rate of decay of the respective variances, it is beneficial to examine these quantities. The variances and covariance are presented in Fig.5.6, which are obtained by following the post processing method in Section 3.2. The statistical convergence of these second moments is verified by changing the sample size and duration and the line with symbols in Fig.5.6 shows the worst comparison obtained when the sample size and duration are increased by 2.6 times. Small differences demonstrate the level of statistical convergence for these results. A similar level of agreement is observed for gradient related quantities discussed in the next section.

The mixture fraction variance, $\widetilde{Z''^2}$, for $R \leq D$ is large near the flame base because of the large inhomogeneity. For downstream locations the peak value shifts towards the mixing layers as one would expect. The progress variable variance, $\widetilde{c''^2}$, has two peaks, the inner one is due to reactions and the outer one is due to mixing phenomena near the mixing layer at the edge of the shear layer. The covariance, $\widetilde{Z''c''}$, is negative in the inner jet and becomes positive near the outer edge of the mixing layer. It is also to be noted that the negative troughs are generally bigger in magnitude than the positive peaks. A negative $\widetilde{Z''c''}$ indicates a negative correlation between these two fluctuations, which is consistent with an earlier study on stratified flames [116]. For example at the position A-A, $R/D < 2$, the overall mixture is rich as indicated by Fig.5.6(a) and it is substantially unburnt as indicated by Fig.5.6(b). When this local mixture is mixed with richer pockets from the centre, which bring in mixture with an even lower value of the progress variable, this causes a local negative c fluctuation, resulting in negative $\widetilde{Z''c''}$. At $R/D = 2.75$ and beyond, the overall mixture is very lean and $\tilde{c}$ reaches a maximum and starts to decrease as in Fig.5.6(b), where locally richer pockets of mixture not only bring in more burnt products but also tend to promote reaction and thus $\widetilde{Z''c''}$ becomes positive.

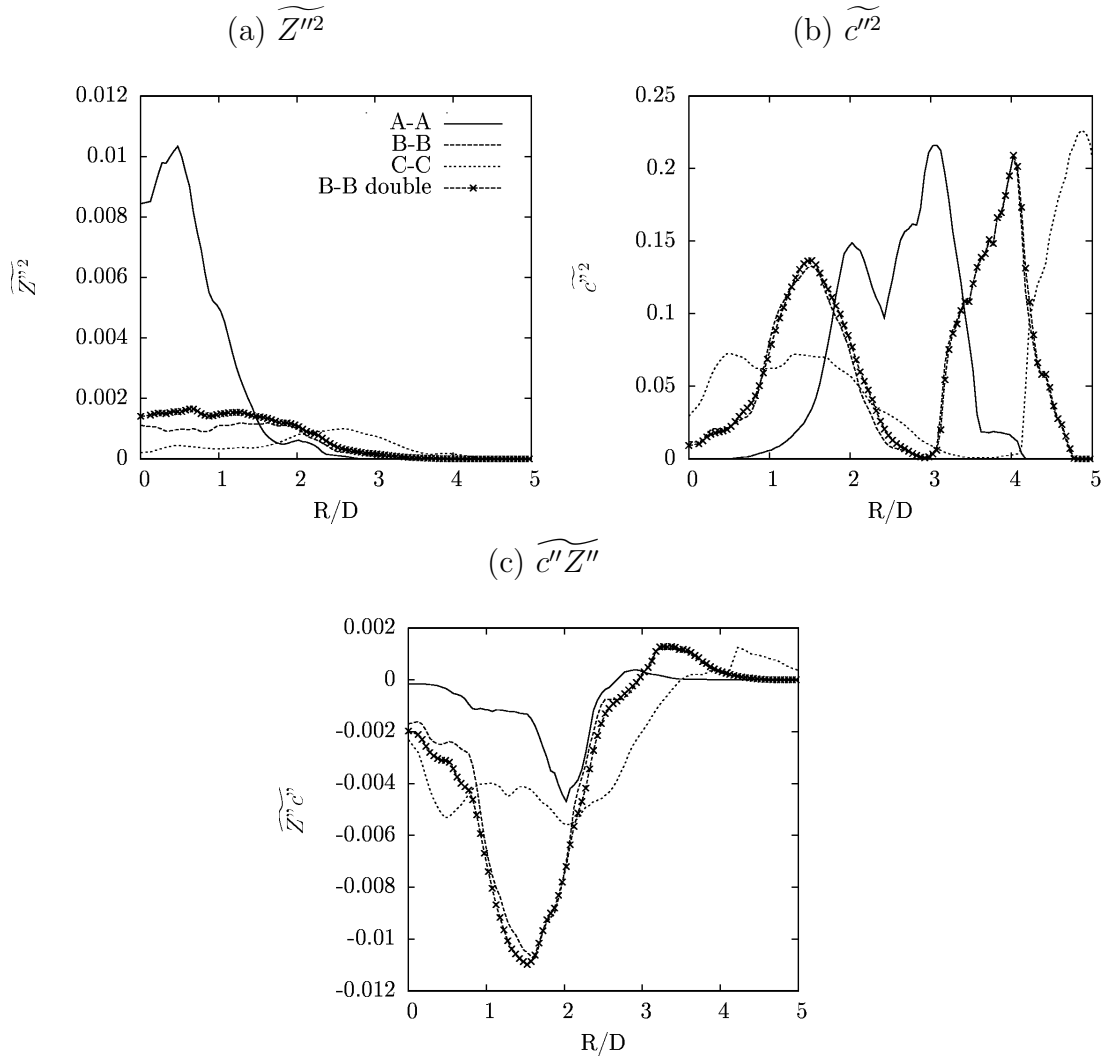

Figure 5.6: Radial variation of Favre variances and covariance of Z and c at positions A-A, B-B and C-C (lines). Symbols are worst case comparison for statistics with more than doubling the sample size and duration.

5.3 SDR Statistics and Modelling

5.3.1 Axial and Radial Variation

The centre line variations of ensemble averaged quantities are shown in Fig. 5.7. These mean values are obtained by appropriately averaging the volume data sampled 969 times in the DNS over 0.2ms as noted in Section 3. The mean mixture fraction $\bar{Z}$ decreases to about 0.2 at around $y/D = 7$ where reactions start to occur and the mean progress variable $\bar{c}$ starts to increase. It is to be noted that the centreline value of $\bar{Z}$ does not reach the stoichiometric value of 0.03 implying that the mean stoichiometric contour does not intersect the centre line in the computational volume considered for the DNS. Hence the mean progress variable does not reach its maximum value of unity. This occurs because of the limited size of the computational domain chosen to make the simulation feasible. It is clear that the potential core extends to about $2D$ since the coherent structures at the mixing layers start to interact with the inner region after $2D$. This is evident in Fig. 3.1. Although Figs. 3.1 and 3.5 show that significant reactions occur at about $5D$ in the outer mixing layers, the consumption of H_2 along the centre line does not occur until about $7.5D$.

Figure 5.7b shows the centre line variations of $\bar{N}_{ZZ}$ and $\bar{N}_{cc}$ in a log-log scale. It can be seen that $\bar{N}_{ZZ}$ reach a maximum of $1000s^{-1}$ at about $y/D = 4$ and starts to decrease with axial distance. Initially the slope is found to be about -7.2, until about $y/D = 7.5$ where the reaction at the centre line starts to occur. This decrease then becomes more gentle with a slope of about -4 as noted in Fig. 5.7b. The latter scaling agrees with Peters and Williams [143], who suggest $\bar{N}_{ZZ} \sim (y/D)^{-4}$ based on the similarity of turbulent kinetic energy dissipation for round jet. This scaling applies in the self-similar region of the flow ($y/D > 10$), where the jet flow half-width increase in proportion to y and the averaged velocity decreases inversely with y. For planar jet, similar argument suggests a scaling with a power of -3. However, Su et al. [172] reported a scaling with downstream distance of the power of -1.4 in a turbulent plane jet, which is weaker than the expected -3 from the scaling argument noted earlier. Bilger [10] discussed this result and emphasised the importance of spatial resolution to obtain meaningful

scalar dissipation rate statistics. In the present case, as the DNS is well-resolved slightly upstream of the flame stabilisation region, the power of -4 scaling is free from resolution issues. This is also consistent with RANS calculations with a $k-\epsilon$ type of turbulence model [28]. One can still argue that under resolved fields near the nozzle exit region can duly impart their contributions to this behaviour. More DNS and experimental measurements can surely help to resolve this point.

The variation of cross dissipation along the centre line is shown in Fig. 5.7c. One can clearly observe that this quantity is an order of magnitude smaller than the other two dissipation rates. This does not imply that this quantity can be neglected or ignored as noted by Bray et al. [22]. It starts to increase at about the same location where $\overline{N}_{cc}$ begins to rise and is only marginally affected by $\overline{N}_{ZZ}$. This seems to suggest that the variation and negative sign of the cross dissipation rate are strongly influenced by the chemical reactions. Furthermore, the contributions of the gradients of fluctuations are dominant compared to the gradients of mean quantities [163], thus $\tilde{\epsilon}_{ZZ} \approx \widetilde{N}_{ZZ}$, $\widetilde{\epsilon}_{cc} \approx \widetilde{N}_{cc}$ and $\widetilde{\epsilon}_{cZ} \approx \widetilde{N}_{cZ}$.

The radial variations of the Favre mean scalar dissipation rates are shown in Fig. 5.8 for three axial locations. In general, the mixture fraction dissipation rate, $\tilde{\epsilon}_{ZZ}$, is larger upstream and peaks at an area with maximum shear generated turbulence. The progress variable dissipation rate, $\widetilde{\epsilon}_{cc}$, shows two distinct peaks which move apart with increasing downstream location. These peaks are formed because of two completely different mechanisms: the inner one is caused by the positive gradients generated as a result of the chemical reactions whereas - in the absence of significant heat release due to lean premixed flames - the outer peak comes from negative gradients due to turbulent mixing between hot products and cold surrounding air, where excessive hydrogen may also react in diffusion flame islands [126], see Figure 3.5 in Section 3.4. This can be seen in Fig. 3.7 in Chapter 3, where $\widetilde{c}$ increases from the jet centre to a maximum and then decreases radially outwards. As more products accumulate in this region where gradients are small, the two peaks in $\widetilde{\epsilon}_{cc}$ move further apart at further downstream positions. This is also consistent with the double peaks in Fig. 5.6(b) showing the radial variation of $\widetilde{c''^2}$.

It is easy to see that $\widetilde{\epsilon}_{cc}$ is much larger than $\tilde{\epsilon}_{ZZ}$ and $\widetilde{\epsilon}_{cZ}$ at the positions investigated, while $\tilde{\epsilon}_{ZZ}$ is larger than $\widetilde{\epsilon}_{cZ}$ at the position A-A, but smaller than

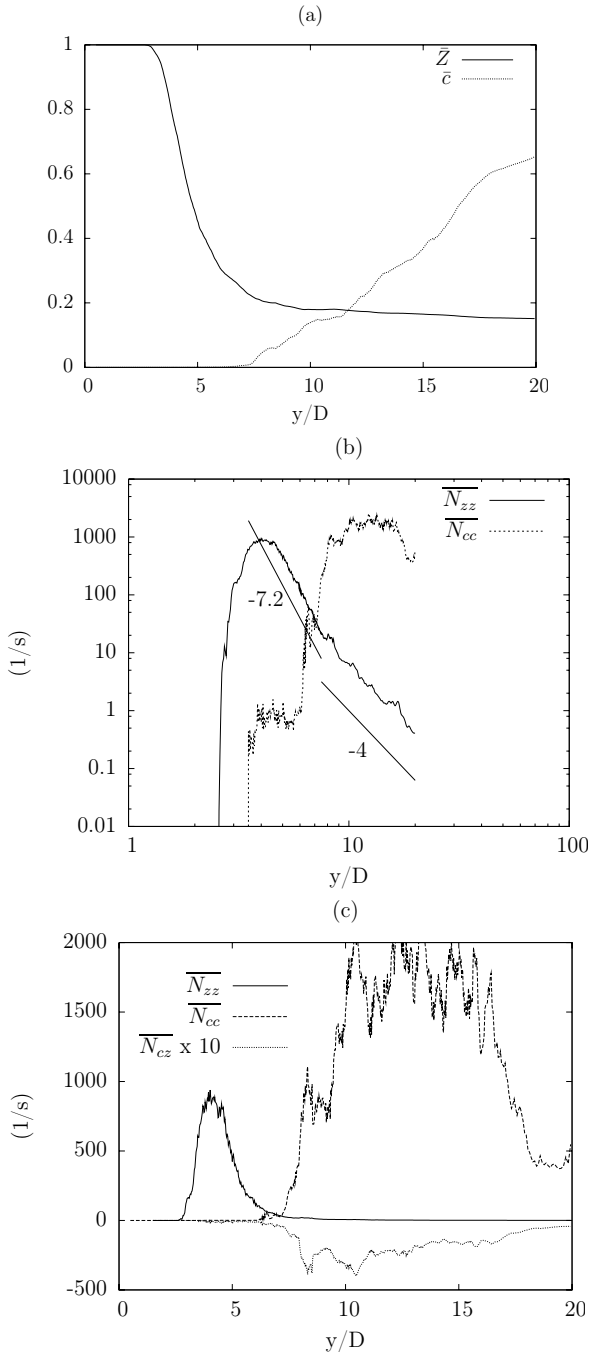

Figure 5.7: Variation of centreline mean quantities: (a) $\bar{Z}$ and $\bar{c}$, (b)$\overline{N}_{ZZ}$ and $\overline{N}_{ZZ}$, (c)$\overline{N}_{ZZ}$, $\overline{N}_{cc}$ and $10\,\overline{N}_{cZ}$.

$\widetilde{\epsilon}_{cZ}$ at the positions B-B and C-C. The cross dissipation rate, $\widetilde{\epsilon}_{cZ}$, is mostly negative as the mixture fraction gradient is towards the jet centre while flame grows away from the centre. It is only weakly positive in a very small region far away from the jet centre. It is striking that, comparing $\widetilde{\epsilon}_{cc}$ and $\widetilde{\epsilon}_{cZ}$, similar patterns are found at the positions B-B and C-C, although with different orders of magnitude and signs. The mixture fraction dissipation $\tilde{\epsilon}_{ZZ}$ has little effect on the cross dissipation at these downstream locations.

5.3.2 Algebraic Models

Simple model for $\widetilde{\epsilon}_{ZZ}$ has been given in Eq.(2.34) in chapter 2. This model value is compared with the DNS results in Fig. 5.9 with $C_d = 1$. It is clear that this model gives a reasonable approximation for $\widetilde{\epsilon}_{ZZ}$ at all axial positions, although it over-estimates the scalar dissipation rate at locations away from the jet centre.

As noted in section 2.4.3.4, simple algebraic model exists for $\widetilde{\epsilon}_{cc}$ which again assumes a constant ratio between the scalar and the turbulence time scale, as in Eq.(2.55). However this was shown [121, 176] to be insufficient. Kolla et al. [97] proposed a new model which included the detailed physics of reactive scalar mixing and a chemical time scale as in Eq(2.56) and Darbyshire et al. [50] modified it to account for the mixture fraction variation, given by

$$\overline{\rho}\,\widetilde{\epsilon}_{cc} = \overline{\rho\mathcal{D}_c(\nabla c'' \cdot \nabla c'')} \simeq \frac{\bar{\rho}}{\beta'}\left([2K_c^* - \tau(Z)C_4]\,\frac{S_L^0(Z)}{\delta_L^0(Z)} + C_3\frac{\tilde{\epsilon}}{\tilde{k}}\right)\widetilde{c''^2}, \tag{5.1}$$

with

$$C_3 = \frac{1.5\sqrt{\mathrm{Ka}}}{1+\sqrt{\mathrm{Ka}}} \quad \text{and} \quad C_4 = 1.1(1+\mathrm{Ka})^{-0.4}, \tag{5.2}$$

where $\beta' \simeq 6.7$ is derived from DNS of fully premixed flames. The planar laminar hydrogen-air flame calculations suggest that $K_c^*/\tau \approx 0.65$ is a good approximation for the stoichiometric and rich hydrogen-air flames [162]. The parameter $\tau(Z) = (T_b(Z) - T_u)/T_u$ is the normalised temperature rise, with the subscripts b and u indicating burnt and unburnt states. The unstrained laminar flame speed and its thermal thickness for a mixture with the mixture fraction value Z are denoted

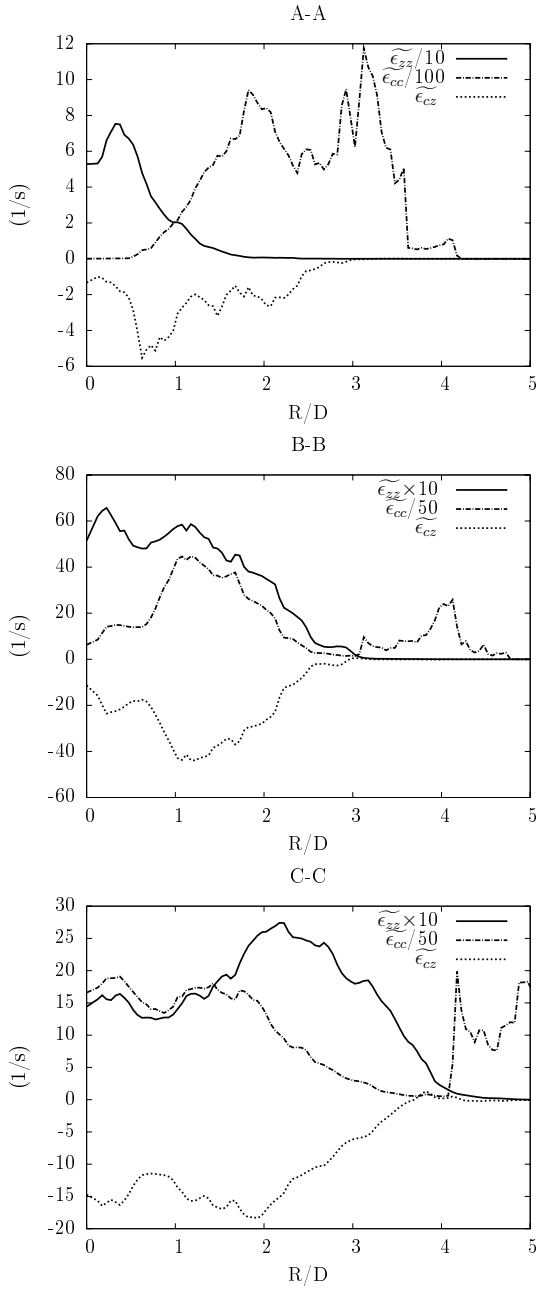

Figure 5.8: Radial variation of the three dissipation rates at three streamwise positions A-A, B-B and C-C. Note the scaling, applied for some quantities, in the legend.

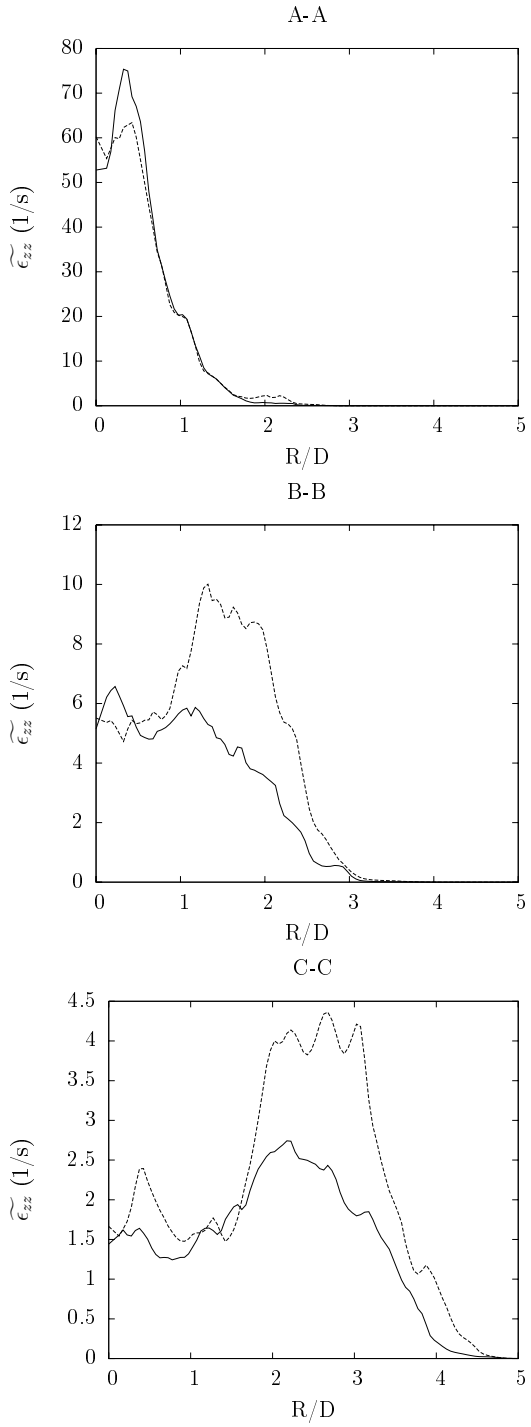

Figure 5.9: Model comparison for the mixture fraction dissipation rate, $\widetilde{\epsilon}_{ZZ}$, at three streamwise positions. Solid line is the DNS data and dashed line is Eq.(2.34) with C_d=1.0.

respectively as $S_L^0(Z)$ and δ_L^0. The Karlovitz number, Ka, is defined as

$$\mathrm{Ka} \equiv \frac{t_c}{t_k} \simeq \frac{\delta(Z)/S_L^0(Z)}{\sqrt{\nu/\tilde{\epsilon}}}, \tag{5.3}$$

where t_c is the chemical time scale defined as δ/S_L^0 with δ as the Zeldovich thickness which is related to the thermal thickness by $\delta_L^0(Z)/\delta(Z) \approx 2(1+\tau(Z))^{0.7}$, t_k is the Kolmogorov time scale and ν is the kinematic viscosity.

Figure 5.10 compares values from these two models with DNS results. The model in Eq.(2.55) with $C_c = 1$ captures the trend for $\widetilde{\epsilon}_{cc}$ correctly, but generally gives an underestimation. This is to be expected as a chemical time scale is missing in this model for reactive scalar dissipation, as noted by Mantel and Bilger (Figure 2 in [120]). The model in Eq. (5.1) gives poor results. It is because c is defined here using the mass fraction of hydrogen, which has a higher diffusivity and the Lewis number significantly lower than unity. The model in Eq.(2.55) is derived based on unity Lewis number assumption. New model with Lewis number dependence for premixed flames is only studied recently [33]. As noted in Chapter 3, one can defined c based on mass fraction of water as in Eq.(3.3), which has a Lewis number close to unity. Scatter plots of these two definitions in Fig. 3.3 show good agreement in most part of the flame brush other than that in the burnt part. Figure 5.11 presents the comparison of $\widetilde{\epsilon}_{cc}$, where c is defined with Y_{H2O}, for the models and the DNS. It can be seen that the classic model Eq.(2.55) tends to give over-prediction while the model in Eq.(2.55) gives under-prediction. The model parameter β' of 6.7 is obtained based on DNS studies of hydrocarbon flame, a smaller number, β' of 2.2, seems more appropriate for hydrogen flames here. The task of evaluating this constant and the other parameters in Eq. (5.1) is not of prime interest and will be the subject for future study.

A model similar to Eq. (2.34) can be written for the cross dissipation rate as

$$\bar{\rho}\,\widetilde{\epsilon}_{cZ} = \overline{\rho \mathcal{D}_Z (\nabla c'' \cdot \nabla Z'')} \simeq C_{cZ}\bar{\rho}\,\frac{\tilde{\epsilon}}{\tilde{k}}\widetilde{c''Z''}. \tag{5.4}$$

The model parameter is $C_{cZ} = 1$ in this study. Also noting that $N_{cZ} = \mathcal{D}_Z\sqrt{\frac{N_{ZZ}}{\mathcal{D}_Z}\frac{N_{cc}}{\mathcal{D}_c}}$,

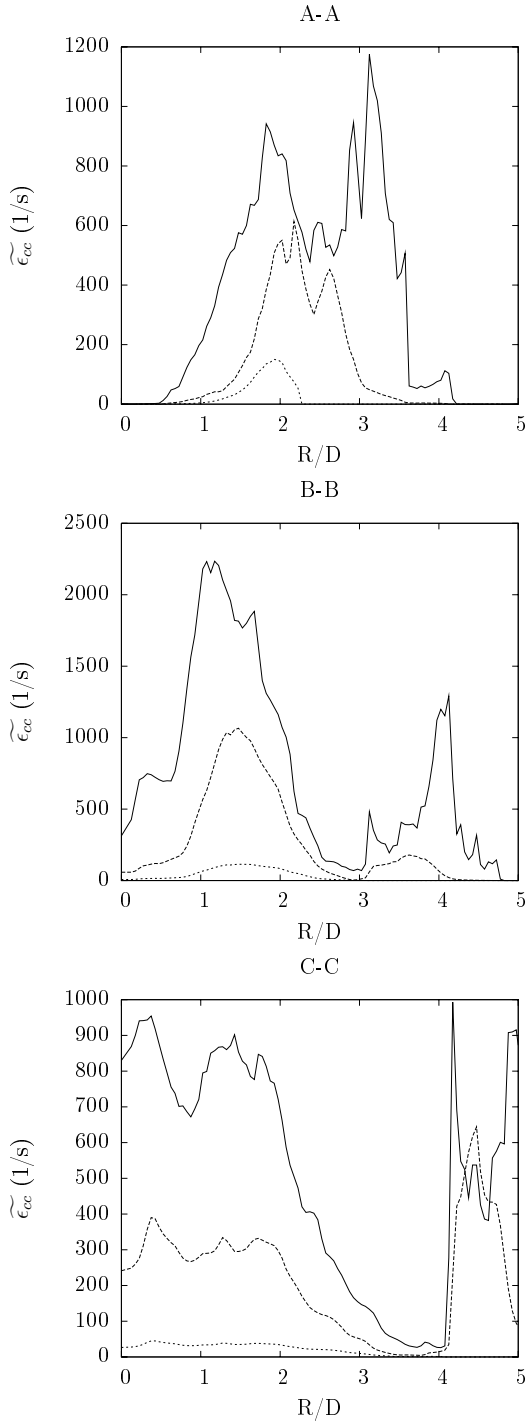

Figure 5.10: Model comparison for the progress variable dissipation rate, $\widetilde{\epsilon}_{cc}$, at three axial positions. Solid line is the DNS data, dashed line is Eq.(2.55) and dotted line is Eq. (5.1).

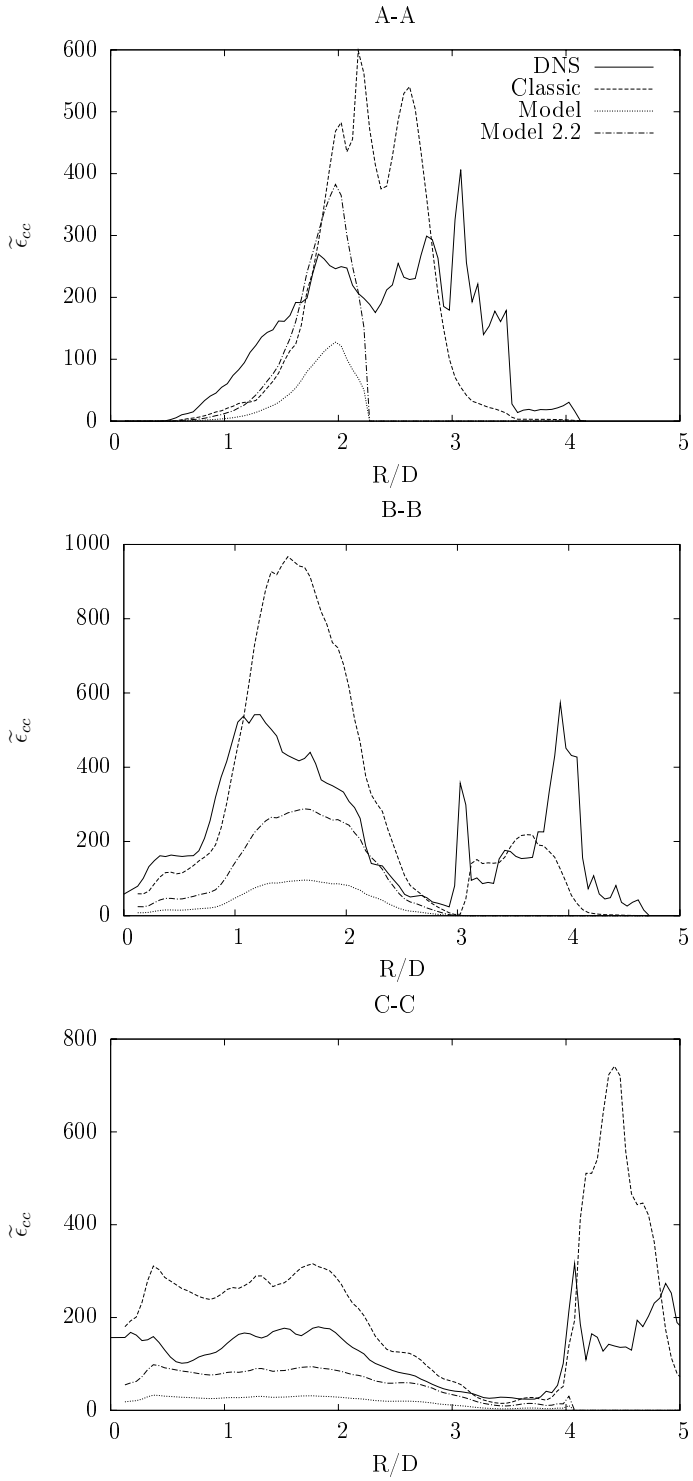

Figure 5.11: Model comparison for the progress variable dissipation rate, $\widetilde{\epsilon}_{cc}$, at three axial positions. c is defined with Y_{H2O} as in Eq.(3.3) here. Solid line is the DNS data, dashed line is Classic model in Eq.(2.55) and dotted line is Eq. (5.1). Dash-dot line is Eq. (5.1) with $\beta' = 2.2$.

it is worth to test whether $\widetilde{\epsilon}_{ZZ}$ and $\widetilde{\epsilon}_{cc}$ can be used to estimate $\widetilde{\epsilon}_{cZ}$ using

$$\bar{\rho}\widetilde{\epsilon}_{cZ} = \overline{\rho\mathcal{D}_Z \left|\nabla Z\right| \left|\nabla c\right| \cos\theta} \simeq \pm\bar{\rho}\tilde{\mathcal{D}}_Z \sqrt{\frac{\widetilde{\epsilon}_{ZZ}}{\tilde{\mathcal{D}}_Z}\frac{\widetilde{\epsilon}_{cc}}{\tilde{\mathcal{D}}_c}}, \tag{5.5}$$

where θ is the angle between the two gradients. For simplicity, $\cos\theta$ is taken to be ± 1 to get the maximum and minimum of the cross dissipation rate. The values of the other two dissipation rates, $\widetilde{\epsilon}_{ZZ}$ and $\widetilde{\epsilon}_{cc}$, are obtained from the DNS. This is similar to the model in reference [57] in the context of Large Eddy Simulation where an effective diffusivity is used.

The above two models for $\widetilde{\epsilon}_{cZ}$ are compared to the DNS results in Fig. 5.12. Equation (5.4) gives reasonable agreement at the position C-C, but its accuracy decays at upstream locations since it cannot capture the trend correctly at the position A-A. The negative part of model in Eq.(5.5) also gives good results at downstream location C-C while it over predicts the negative values at upstream location A-A. In the next section, the statistics of the scalar gradients are examined to shed light on further modelling of these quantities.

5.3.3 Scalar Gradients Statistics

Another approach to model the dissipation rates is to use the PDF of scalar and its gradients. For N_{ZZ} and N_{cc}, simple scalar gradient statistics are enough, while for N_{cZ}, the joint statistics of the gradients are necessary. Ideally, the statistics from both premixed and non-premixed burning modes based on the Takeno Flame Index [193] should be presented, as the gradients have different characteristic scales in premixed and diffusion flame structures. However, at the locations investigated here, fuel rich premixed burning is the dominant mode. The samples required to calculate meaningful statistics for the non-premixed mode which tends to occur in the form of "diffusion flame islands" downstream and at large radii [126] are found to be insufficient for a given axial location in the JAXA DNS data. As a result, the statistics presented here are not distinguished by the mode of burning.

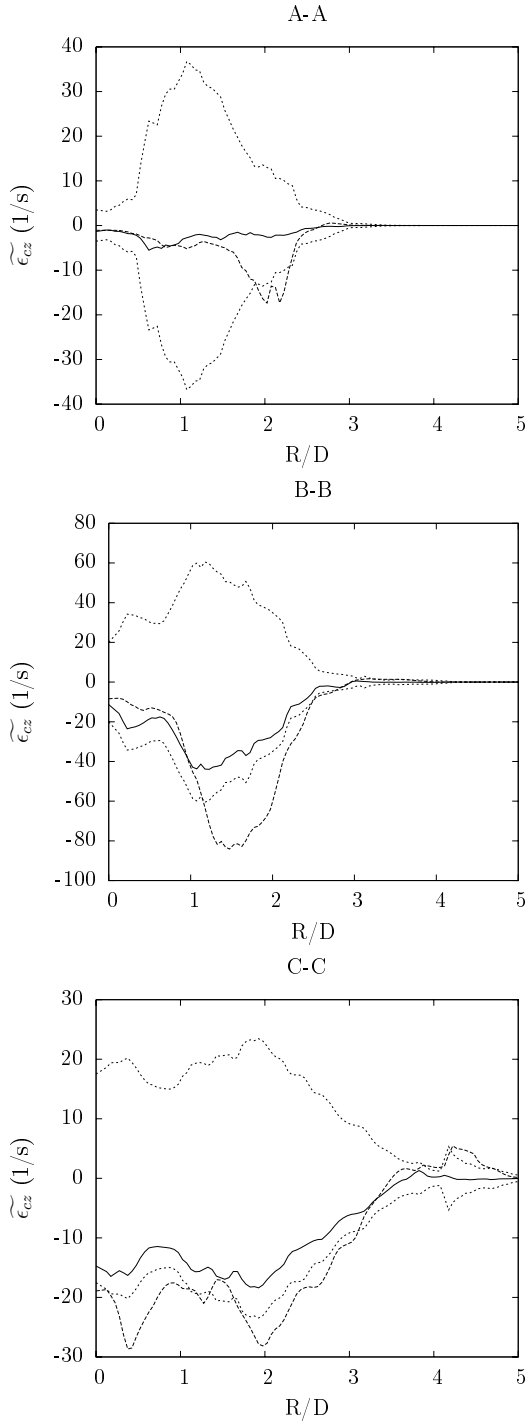

Figure 5.12: Model comparison for the cross dissipation rate, $\widetilde{\epsilon}_{cZ}$, at three axial positions. Solid line is the DNS data, dashed line is Eq. (5.4) and dotted line is Eq. (5.5).

5.3.3.1 Marginal PDFs of scalar gradients

Figure 5.13 shows the PDFs of mixture fraction gradient magnitude in logarithmic scales at different axial and radial locations. A reference lognormal curve is also plotted for comparison. Let ψ denote a random variable of the scalar gradient magnitude, with a mean of $\bar{\psi}$ and a variance of g^2. The lognormal shape is given by [140],

$$P(\psi) = \frac{1}{\psi\sigma\sqrt{2\pi}} \exp\left(\frac{-[\ln\,\psi - \mu]^2}{2\sigma^2}\right), \tag{5.6}$$

where the mean and variance of the natural logarithm of the scalar gradient magnitude are respectively denoted as μ and σ^2. These two quantities are related to $\overline{\psi}$ and g^2, which can be obtained from the DNS, by $\bar{\psi} = \exp(\mu + 0.5\sigma^2)$ and $g^2 = \bar{\psi}^2(\exp\,\sigma^2 - 1)$.

Figure 5.13a clearly shows that a lognormal distribution is an excellent approximation at the position A-A. At the locations B-B and C-C, Fig. 5.13(b) and Fig. 5.13(c) show that the lognormal approximation is an accurate representation for large gradients. The PDF is asymmetrical, skewed towards smaller gradients close to the jet centre (see Fig. 5.13(b) and (c) for $R/D = 0.5$) and skewed towards larger gradients away from the jet centre (see Fig. 5.13(b) and (c) for $R/D = 2.5$). In general, this approximation is very good which is in agreement with previous studies [59, 135].

Figure 5.14 presents PDF of the progress variable gradient magnitude at several radial locations for the three axial positions. The lognormal curve is also included for comparison. Note that the radial positions shown in Fig. 5.14 correspond to a region where c gradients are created mainly by chemical reactions, and not by the strong c gradients in the outer mixing layer between hot products and the surrounding air (see Fig. 3.5 where the outer c contours are almost merging together). At the position A-A, Fig. 5.14(a) shows that the PDF has a fat negative tail close to the jet centre where there is only minor reaction and thus a small gradient (e.g. $R/D = 0.5$); and a fat positive tail away from the jet centre where reaction is more intense and thus a large gradient (e.g. $R/D = 2.0$). As a result, a lognormal distribution cannot capture this feature.

Figure 5.14(b) and (c) show clearly that the large gradients created by chemical reactions can be captured accurately by the lognormal distribution. While

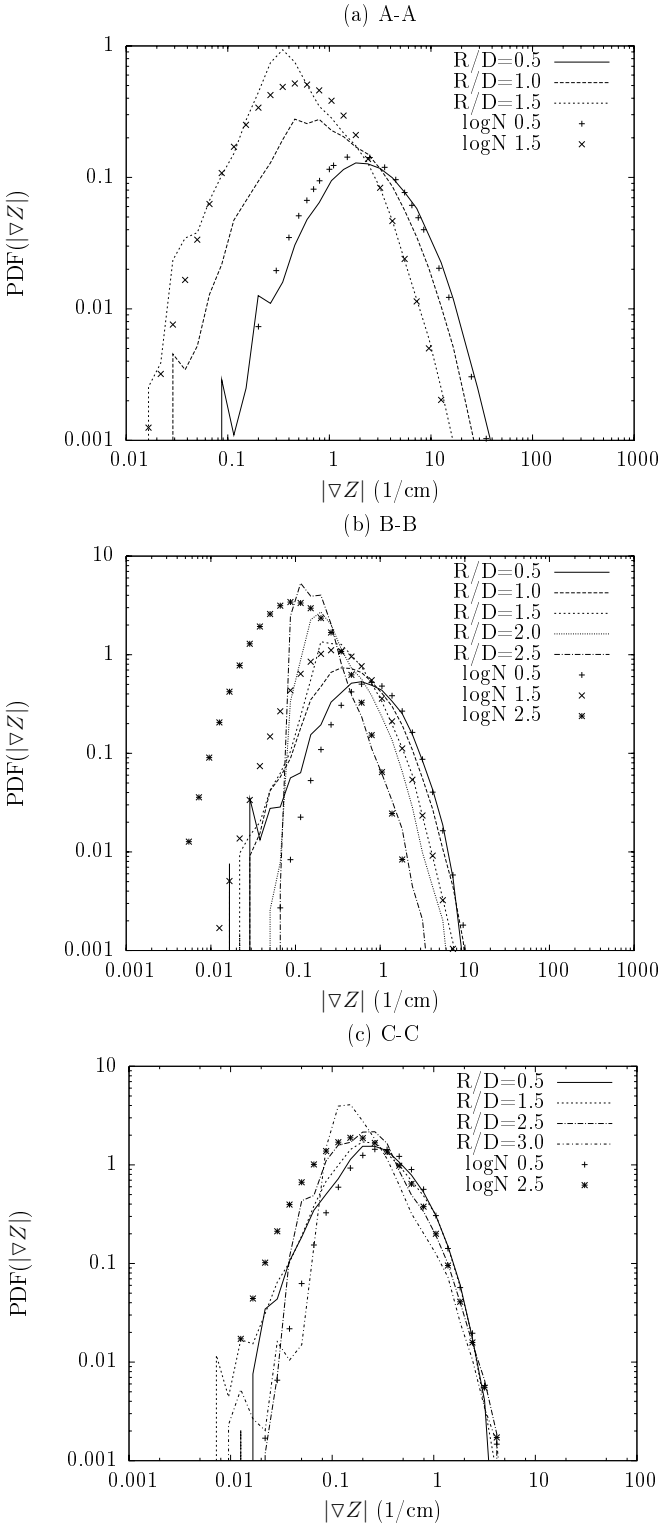

Figure 5.13: The marginal PDF of mixture fraction gradient magnitude, $|\nabla Z|$ at three axial and several radial locations. Lines are DNS results, symbols are the corresponding lognormal PDF. Gradient magnitudes are in cm^{-1}.

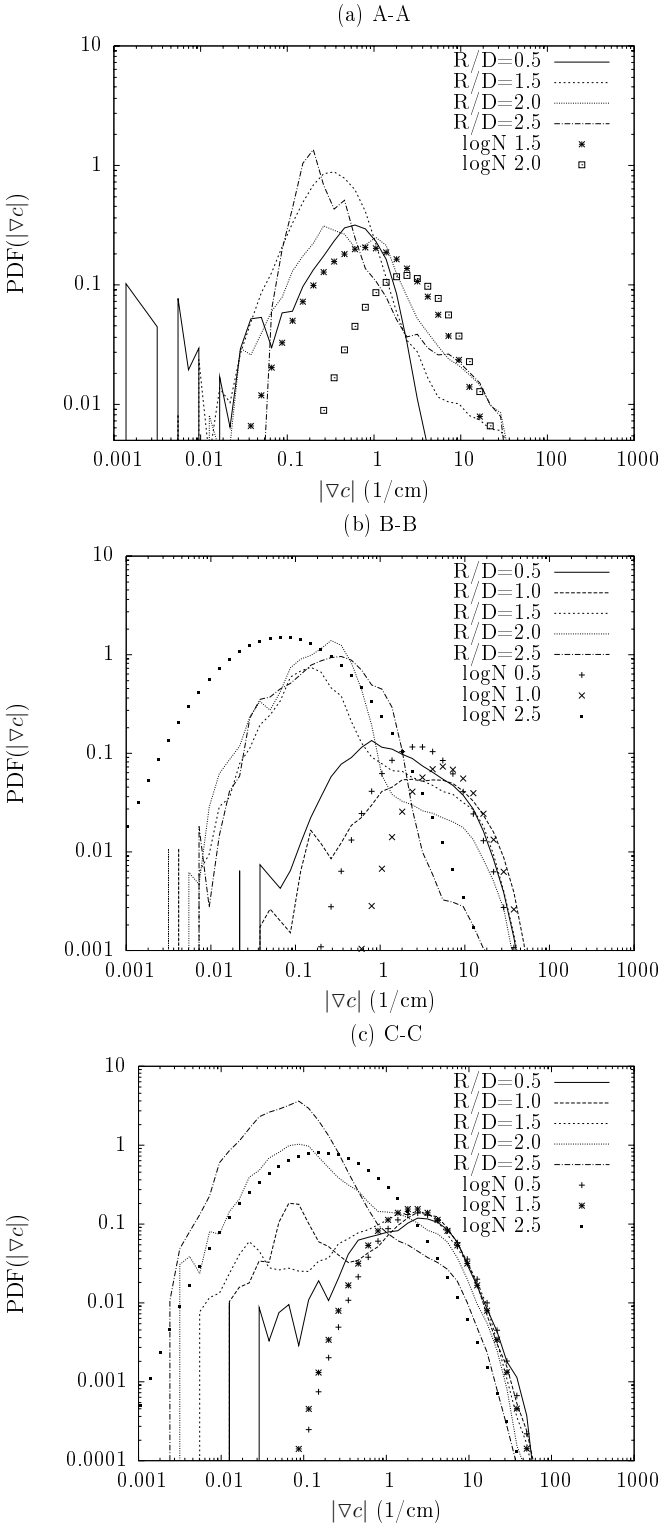

Figure 5.14: The marginal PDF of progress variable gradient magnitude, $|\nabla c|$, at three axial and several radial positions. Gradient magnitudes are in cm^{-1}.

mild reactions occur in a more distributed manner at the positions B-B and C-C and create relatively larger gradients of c, turbulent mixing of products results in a high probability of small gradients. Moving radially outwards, the increase in the proportion of small gradients can be seen clearly in Fig. 5.14(c). For $R/D = 1.0$, there are two distinct peaks of comparable height (≈ 0.2), one at $|\nabla c| \approx 0.1\text{cm}^{-1}$ and another one at $|\nabla c| \approx 3.0\text{cm}^{-1}$. Further out at $R/D = 2.5$, the peak at $|\nabla c| \approx 0.1\text{cm}^{-1}$ is significantly larger in magnitude as a larger proportion of products can be found in this radial region. The fat negative tail contributes less significantly to the overall mean and there is a good agreement for the large gradients. Thus, the lognormal distribution is acceptable for progress variable gradient modelling. This is consistent with observations in premixed flame experiments [45] and DNS studies [162, 174].

5.3.3.2 Joint PDFs of scalar gradients

Scatter plots for scalar gradients $|\nabla Z|$ and $|\nabla c|$ at several axial and radial locations are shown in Fig. 5.15. At the position A-A, there seems to be no correlation between these two gradient magnitudes (although the two scalars are not necessarily independent). A correlation becomes more obvious at off-centre locations at the downstream position C-C. This is because partially premixed flame propagation is dominant in the region of flame stabilisation and diffusion between iso-surfaces of mixture fraction is less significant. In the far field of this computational domain, fuel consumption occurs over a wide range of mixture fraction values as has been shown in Fig. 3.7 and Fig. 3.8. Thus, the mixing, resulting from ∇Z and chemical reaction , creating ∇c occur together in downstream position. Furthermore, the progress variable is a measure of progress towards chemical equilibrium, and the dissipation rate of this reactive scalar is strongly influenced by the extent of both molecular diffusion and chemical reaction. As a result the coupling between the mixture fraction and progress variable gradients become more significant at downstream positions.

Figure 5.16 presents the joint PDF of the magnitude of the two gradients at several axial and radial locations. The behaviour is consistent with the previous scatter plot. The JPDF for the location A-A at radial position $R/D = 1.5$

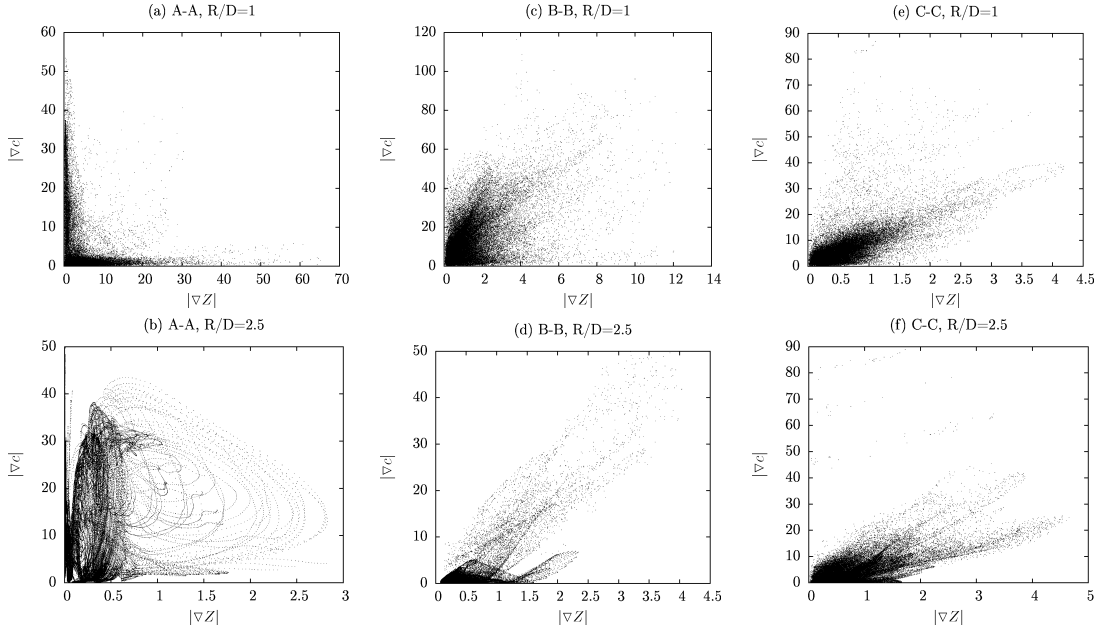

Figure 5.15: Scatter plots for $|\nabla Z|$ and $|\nabla c|$ at several axial and radial locations. Unit is cm^{-1}

suggests that these two gradient magnitudes may be statistically independent and it is not so at other locations shown in Fig. 5.16. To assess this more clearly and to explore a plausible model for this joint behaviour, a bivariate lognormal distribution is used. This bivariate distribution is given by

$$P(\psi_1, \psi_2) = \frac{1}{2\pi\,\psi_1\,\psi_2\,\sigma_1\,\sigma_2\,\sqrt{1-p^2}}\,\exp\left(-\frac{q}{2}\right), \tag{5.7}$$

where ψ_1 and ψ_2 are the random variables for the two scalar gradient magnitudes with means $\overline{\psi}_1$ and $\overline{\psi}_2$. The variances of these two random variables are denoted by g_1^2 and g_2^2 respectively. The correlation coefficient p is defined as $p \equiv E\left[(\ln\,\psi_1 - \mu_1)\,(\ln\,\psi_2 - \mu_2)\right]/\sigma_1\sigma_2$, where $E[\mathcal{G}]$ denotes the expected value of the variable $\mathcal{G}$. The variable q in Eq. (5.7) is given by

$$\begin{aligned} q \;&=\; \frac{1}{1-p^2}\left(\frac{\ln\,\psi_1 - \mu_1}{\sigma_1}\right)^2 + \frac{1}{1-p^2}\left(\frac{\ln\,\psi_2 - \mu_2}{\sigma_2}\right)^2 \\ &-\; \frac{2p}{1-p^2}\left(\frac{\ln\,\psi_1 - \mu_1}{\sigma_1}\right)\left(\frac{\ln\,\psi_2 - \mu_2}{\sigma_2}\right). \end{aligned} \tag{5.8}$$

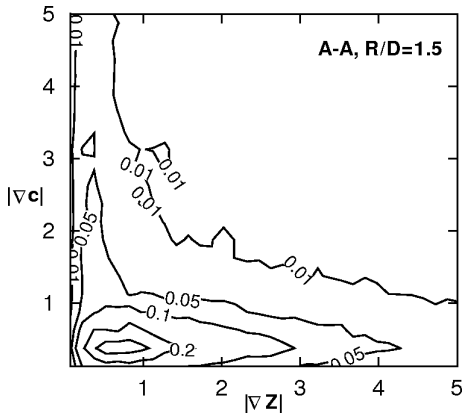

(a)

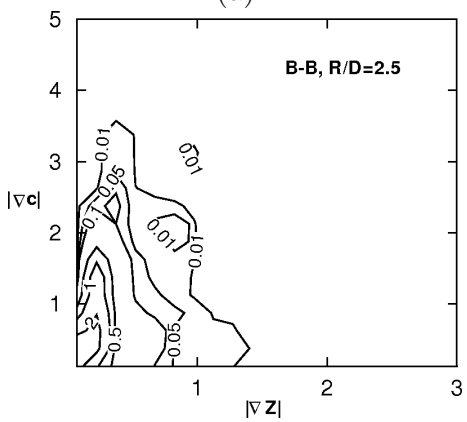

(b)

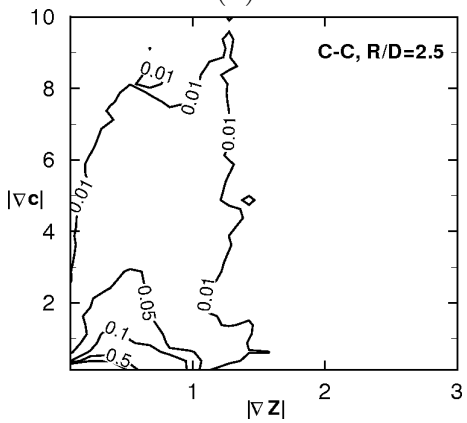

(c)

Figure 5.16: The JPDF, $P(|\nabla Z|, |\nabla c|)$, at three axial and arbitrarily chosen radial locations. Gradient magnitudes are in cm^{-1}.

The means and variances of natural logarithm of ψ_1 and ψ_2 are denoted as μ_1, σ_1, μ_2 and σ_2 respectively. μ_i and σ_i are related to its marginal mean $\overline{\psi}_i$ and variance g_i^2 by the same relation as for the univariate case.

It is clear that the correlation coefficient p is zero when the two scalar gradient magnitudes are statistically independent. This would give the JPDF to be a product of two lognormal distributions as

$$P(\psi_1, \psi_2) = \frac{1}{2\pi\,\psi_1\,\psi_2\,\sigma_1\,\sigma_2}\,\exp\left(-\frac{(\ln\psi_1-\mu_1)^2}{2\sigma_1^2}-\frac{(\ln\psi_2-\mu_2)^2}{2\sigma_2^2}\right). \tag{5.9}$$

Figure 5.17 shows the JPDF calculated using the above two lognormal variations. The figures in the left column are for the statistically independent scenario in Eq. (5.9) and the right column is for the joint lognormal variations in Eq. (5.7), for the values of the correlation coefficient, p, given in the figure. It is obvious that the two statistically independent lognormal variations are a good representation for the position $y/D = 6$, $R/D = 1.5$ by comparing Fig. 5.16a with the results in top left part of Fig. 5.17. The joint lognormal form is considered reasonable for other locations also shown in Figs. 5.17. As noted while discussing Fig. 5.14, the lognormal model captures the PDF well when the gradients are large. The difference in the small gradient parts noted earlier can cause a substantial difference in the joint PDF, $P(|\nabla Z|, |\nabla c|)$. However, a χ^2 null hypothesis test has been carried out to verify the statistical agreement between the PDFs obtained from the DNS and using the model Eq.(5.7). Test results suggest that joint lognormal PDF is a reasonable approximation. The correlation coefficient, p, seems to increase with downstream distance for a given radial position and its scaling with y/D is unclear at this time. This scaling, required for RANS calculation, will be investigated further in a future study.

5.4 Summary

In this chapter, we first examined the three dissipation rates in the flame stabilisation region. It is found that $\bar{N}_{ZZ}$ at the flame leading edge is well below the quenching value for the stoichiometric mixture. $\bar{N}_{cc}$ is of the same order with stoichiometric unstrained laminar flame. The cross dissipation rate $\bar{N}_{cZ}$ changes

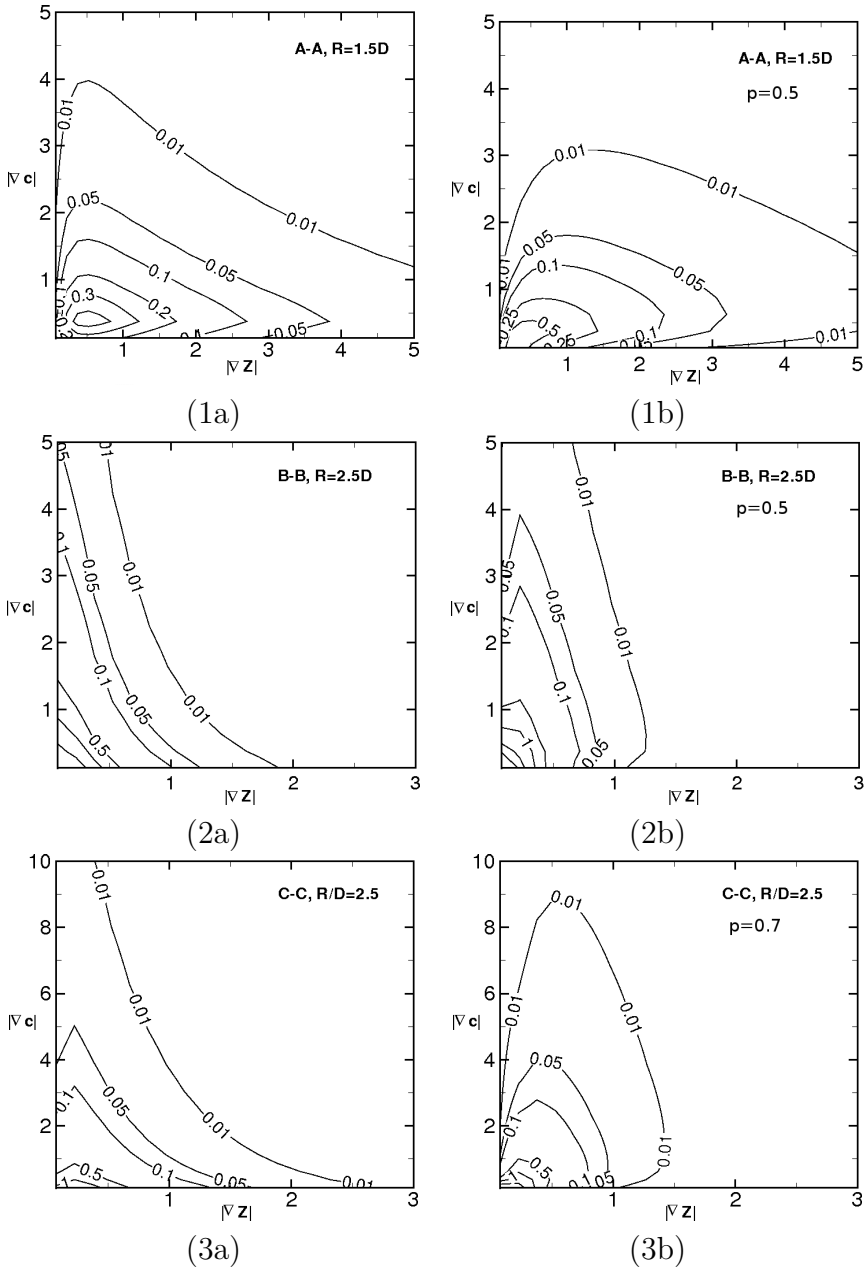

Figure 5.17: Modelled JPDF, $P(|\nabla Z|, |\nabla c|)$. The left column is the statistically independent scenario, see Eq. (5.9), and the right column is the correlated JPDF in Eq. (5.7) with the correlation coefficient, p, given in the figure. The gradient magnitudes are in cm^{-1}.

from negative to weakly positive in the leading edge. This is due to the change in the alignment characteristics of the gradients of mixture fraction and progress variable. It is clear that the CDR, which contains information for both gradients that are favourable for flame stabilisation and represent the interaction between turbulent mixing and the chemical reaction in partially premixed combustion, is a good marker for stabilisation region and an important quantity in the flame stabilisation mechanism.

The statistics and modelling of various scalar dissipation rates are investigated. It is found that the classical model for the passive scalar dissipation rate $\widetilde{\epsilon}_{ZZ}$ gives good agreement with the DNS, while models developed based on premixed flames for the reactive scalar dissipation rate $\widetilde{\epsilon}_{cc}$ can provide reasonable agreement when a suitable definition of c is used. It gives good results for c defined by water mass fraction as in Eq.(3.3). Improvement of model agreement may be possible if model constants are revisited in detail or recent development in Lewis number dependence is included, which are not attempted here. The cross dissipation rate $\widetilde{\epsilon}_{cZ}$ is mostly negative and can be reasonably approximated at downstream positions once $\widetilde{\epsilon}_{ZZ}$ and $\widetilde{\epsilon}_{cc}$ are known, although the sign cannot be determined. This approach gives better results than one employing a constant ratio of turbulent timescale and the scalar covariance $\widetilde{c''Z''}$. The statistics of scalar gradients are further examined and lognormal distributions are shown to be very good approximations for the passive scalar and acceptable for the reactive scalar. The correlation between the two gradients increases downstream. A bivariate lognormal distribution is tested and found to be a reasonable approximation for the joint PDF of the two scalar gradients.

Based on these results discussed in this chapter, the following points are noted for the subsequent chapters in this thesis.

1. Linear relaxation models for $\widetilde{\epsilon}_{ZZ}$ in Eq.(2.34) and $\widetilde{\epsilon}_{cZ}$ in Eq.(5.4) are reasonable and will be used.

2. The model in Eq.(5.1) is sufficient for $\widetilde{\epsilon}_{cc}$ although there may be possibilities to improve this model further.

From the perspective of the mean reaction rate closure for partially premixed combustion, possible closure for $\overline{\dot{\omega}_c}$ still needs to be explored. This is carried out

in the next chapter.

Chapter 6

A priori assessment of mean reaction rate closure

This chapter aims to examine various mean reaction rate closures and to assess the modelling assumptions involved. Specifically, a closure of the form in Eq.(2.65), rewritten here for convenience,

$$\overline{\dot{\omega}} = \int_0^1 \int_0^1 \dot{\omega}(\zeta,\xi) P(\zeta,\xi)\, d\zeta\, d\xi \tag{6.1}$$

is of interest because of its simplicity. The specific issues investigated in this chapter are

- To what extent the turbulent flame front in partially premixed combustion can be approximated by unstrained and strained laminar premixed and non-premixed flamelets. This helps us to find an appropriate canonical form for $\dot{\omega}(\zeta,\xi)$ in Eq.(6.1).
- Choosing a model for the joint PDF $P(\zeta,\xi)$. This PDF is commonly modelled using two marginal PDFs by assuming statistical independence between mixture fraction ξ and progress variable ζ. But results in Fig.5.6 for $\widetilde{c''Z''}$ clearly demonstrate that this assumption does not hold in partially premixed combustion. An alternative proposition to model this joint PDF using a "copula" [48, 49] will be studied in the modelling framework proposed above.

The various forms of presumed PDF/flamelets models are presented in Section 6.1. The structure of the flame front in partially premixed combustion is investigated in Section 6.2 using the JAXA DNS data. The modelling of the joint PDF is presented in Section 6.3. The comparison of various closures is presented in Section 6.4 and helps to identify a reasonably accurate closure which can be used in RANS simulation discussed in the next chapter.

6.1 Presumed PDF/Flamelet Models

Presumed PDFs together with flamelet models, either from counter-flow diffusion flamelets or freely propagating premixed flamelets as noted in Chapter 2, are popular for turbulent combustion due to their simplicity and accuracy. Here the application of this modelling approach to the mean reaction rate will be examined in detail.

Presumed beta PDFs are commonly used for both ξ and ζ. If statistical independence is assumed then Eq.(6.1) becomes

$$\bar{\dot{\omega}}_c = \int\int \dot{\omega}_c(\zeta,\xi) P_\beta(\zeta) P_\beta(\xi) d\zeta d\xi, \tag{6.2}$$

Or with a JPDF including the correlation, we have

$$\bar{\dot{\omega}}_c = \int\int \dot{\omega}_c(\zeta,\xi) P_{c\beta}(\zeta,\xi) d\zeta d\xi. \tag{6.3}$$

The non-premixed flamelet model [140] is also of interest as the jet flame is traditionally considered to be a diffusion flame. With a presumed beta PDF for mixture fraction and a lognormal PDF for its scalar dissipation rate, Eq.(2.26) is rewritten as

$$\bar{\dot{\omega}}_c = \int\int \dot{\omega}_c(\xi,\chi_{st}) P_\beta(\xi) P_{ln}(\chi) d\zeta d\chi. \tag{6.4}$$

As noted in chapter 2, a strained flamelet formulation has been developed by Kolla and Swaminathan [95, 96] for turbulent premixed flames. Here we attempt to extend this approach, see Eq(2.57), to partially premixed flame by including another integral over the mixture fraction space. The mean reaction rate can be

calculated as

$$\bar{\dot{\omega}}_c = \int\int\int \dot{\omega}_c(\zeta,\xi,\psi)P(\zeta,\xi,\psi)d\zeta d\xi d\psi, \tag{6.5}$$

where ψ is the sample space variable for the scalar dissipation N_{cc} of the progress variable c. As noted in chapter 2, the joint PDF is calculated as $P(\zeta,\xi,\psi) = P(\psi|\zeta)P(\zeta)P(\xi)$. The conditional PDF $P(\psi|\zeta)$ is presumed to be a lognormal distribution, as in Eqs.(2.58)-(2.59) and the PDFs $P(\zeta)$ and $P(\xi)$ are presumed to be beta PDFs, as in Eqs.(2.27)-(2.28). Here statistical independence between mixture fraction and progress variable is also assumed. Now, for the extended strained flamelet formulation, with the presumed PDFs noted above, the model in Eq.(6.5) is rewritten as

$$\bar{\dot{\omega}}_c = \int\int\int \dot{\omega}_c(\zeta,\xi,\psi)P_\beta(\zeta)P_\beta(\xi)P_{ln}(\psi|\xi)d\zeta d\xi d\psi. \tag{6.6}$$

Table 6.1 summarises the various laminar flamelets and presumed PDFs for scalars used in these four models.

Model Equation	Laminar Flamelet	Presumed PDFs	$Z-c$ correlation?
M1 Eq.(6.2)	Unstrained freely propagating premixed	β PDFs for Z and c	No
M2 Eq.(6.3)	Unstrained freely propagating premixed	β PDFs for Z and c	Yes
M3 Eq.(6.4)	Strained Counterflow diffusion	β PDF for Z and log-normal PDf for ξ_{st}	No
M4 Eq.(6.6)	Strained Counterflow Reactant-to-Product premixed	β PDF for Z and log-normal PDf for ψ_{st}	No

Table 6.1: Summary of laminar flamelet and presumed PDFs used in the models

6.2 Turbulent Flame Front Structure

6.2.1 Comparison with unstrained laminar premixed flamelet

One may wish to model the turbulent lifted jet flame using the flamelet approach in composition space [142] in either RANS or LES framework, where the chemical reaction rates are tabulated using canonical non-premixed or premixed flames [54, 184]. It has been shown [190] that these two types of flamelets are equally good for hydrocarbon flames (Sandia flames D and F). This approach is evaluated qualitatively for the hydrogen flame considered in the DNS. Figure 6.1 presents the DNS data at position A-A from 146 time steps, in which the instantaneous values of hydrogen consumption rate $\dot{\omega}_{H2}$, and OH and H_2O mole fractions are compared with one dimensional, unstrained, planar laminar premixed flame solution calculated using CHEMKIN [86]. The first column shows DNS samples with local equivalence ratio ϕ ranging from 0.95 to 1.05 and for the laminar premixed flame having $\phi = 1.0$. The second column is for $1.55 < \phi < 1.65$ in the DNS and $\phi = 1.6$ in the laminar premixed flame. The agreement for these two cases is very good, especially for the stoichiometric case. The rich laminar premixed flame overestimates the hydrogen consumption rate and the OH mole fraction. At this axial position, detailed comparisons (not shown here) indicate that the agreement between the DNS results and laminar flame solutions is reasonably good for $0.01 < Z < 0.07$ ($0.33 < \phi < 2.5$). The mixture in this range corresponds roughly to the region $1.5 < R/D < 2.5$ which has a high mean hydrogen consumption rate and heat release rate as shown in Fig. 3.8. This suggests that laminar premixed flamelet is a good approximation of the flame in regions with intense reaction close to the stabilisation height.

At the other positions B-B and C-C (not shown here), one dimensional laminar premixed flame solutions give similar agreement with the DNS results in the region where substantial reactions occur, for example, $R/D = 1.0$ for B-B and $R/D = 2.0$ for C-C. One may also wish to compare the data with laminar flames in physical space since the flamelet approximation is likely to be less robust here than in composition space. Figure 6.2 shows the variation of the conditional mean gradient of c, with respect to c for one radial location at three axial positions.

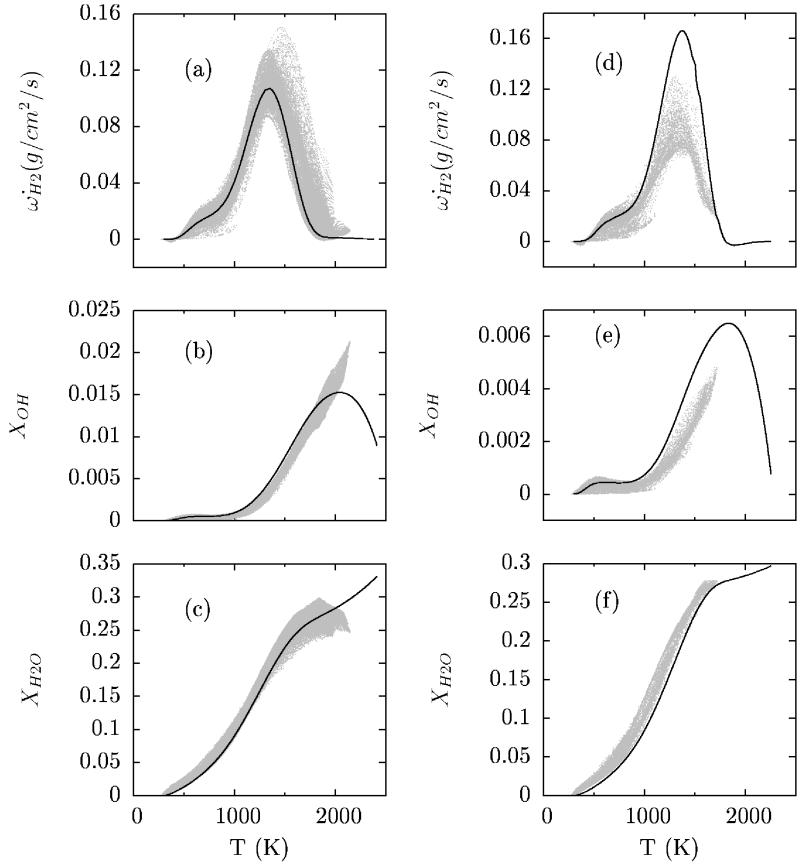

Figure 6.1: Comparison of DNS (dot) and laminar premixed flame results (solid line) for position A-A. For (a)(b)(c), DNS data has $0.95 < \phi < 1.05$ and laminar flame has $\phi = 1.0$. For (d)(e)(f), DNS data has $1.55 < \phi < 1.65$ and laminar flame has $\phi = 1.6$.

The DNS results are normalised using the laminar flame thickness δ_L^0 for the corresponding mean mixture fraction. The gradient of c in these laminar flames are also presented for comparison. As expected, the DNS values are generally smaller than laminar flamelet values as preheat zones are known to be thickened by intense turbulence. It is noted that for the lean flames close to the stabilisation height (A-A), the flamelets seem to survive better on the high temperature side, as indicated by Fig. 6.2(a), where the DNS and laminar data for $0.65 < c < 0.85$ are nearly identical. For $c > 0.85$ the turbulent strains seem to increase the progress variable gradient. In the rich regions of the DNS, it is clear that the thickness of the turbulent reaction zone is generally larger than that of the corresponding premixed laminar flames.

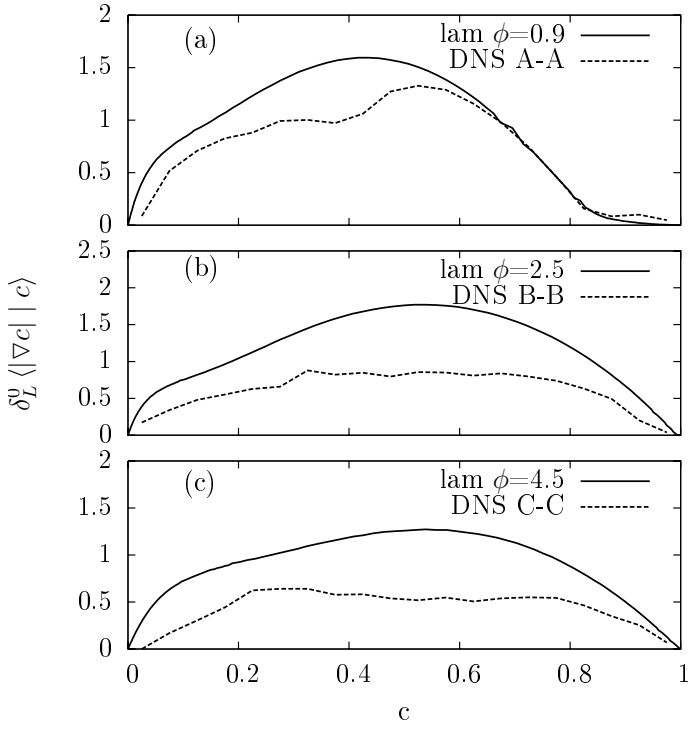

Figure 6.2: Comparison of DNS (dash) and laminar premixed flamelet (solid) conditional mean c-gradient, conditioned on c for $R/D = 2.0$ at positions A-A, B-B and C-C. The equivalence ratios of laminar calculations are based on the DNS mean value at those positions. Results are normalised by the laminar flame thickness.

6.2.2 Comparison with laminar diffusion flamelet

In the outer reaction zone at position C-C identified in Figs. 3.5 and Fig. 3.8 as "diffusion flame islands", it seems that a laminar premixed flame is not a satisfactory model, but a range of diffusion flame solutions from low to intermediate strain rates give better agreement. This can be seen clearly in Fig. 6.3, where the instantaneous hydrogen consumption rate normalised by the peak value from the stoichiometric premixed flame is compared with unstrained premixed flamelet and diffusion flamelet with three strain rates. The typical extinction strain rate for hydrogen-air diffusion flame is of the order 12,000 s^{-1} [181]. Cheng et al.[47] compared experimental results to both a typical counterflow laminar diffusion flame and partially premixed flame established in a counterflow premixed-reactants-to-air configuration in order to study the strain rates experienced by the flames. Laminar premixed flamelets have been used to model diffusion flames by Bradley

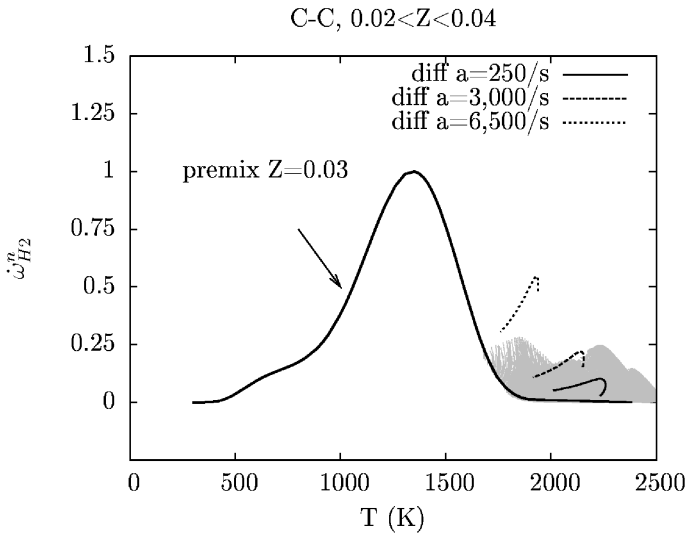

Figure 6.3: Comparison of DNS (symbol), unstrained laminar premixed and diffusion flame results at position C-C. The reaction rate has been normalised by the peak value from the stoichiometric H_2/air unstrained premixed laminar flame. Three different strain rates are considered for the diffusion flame.

et al.[14] with good results. Vreman et al.[190] compared LES simulations for piloted partially premixed flames (Sandia D and F) with the manifold generated by laminar premixed and diffusion flamelets and found equally satisfactory re-

sults. Here since the diffusion flame islands are typically occurred in downstream locations whereas in upstream locations, the rich premixed burning mode dominates, we can expect premixed flamelet model to give reasonable results in most regions.

6.2.3 Comparison with Strained Premixed flamelet

Figure 6.4 presents the DNS results for the position B-B, R/D=2.5, compared to laminar strained premixed flamelet obtained from a counterflow reactant-to-product (RtP) configuration . The DNS data at this position are conditioned on local mixture fraction. The variations of the instantaneous reaction rate $\dot{\omega}_c$ with respect to the dissipation rate N_{cc} of progress variable c are plotted. At this position, $\widetilde{Z} \approx 0.05$ and $\tilde{c} \approx 0.9$. Also shown for comparison are the laminar strained flamelet calculations for different mixtures, each for a range of strain rates. For the stoichiometric case ($Z = 0.03$), only the unstrained case and one strained case are shown. Fig.6.4(a) shows that increasing strain rate does not dramatically change the reaction rate unless extremely high strain rates are encountered. This is due to the flame configuration, where there is a pre-existing temperature gradient between the unburnt reactants and burnt products that supports combustion. Stoichiometric mixture is easily flammable and thus is very difficult to quench even with extremely high strain rates. For the rich mixtures in Fig.6.4(b)-(f), six strained cases including the strained case and the unstrained case are shown. The highest strain value shown corresponds to the extinction strain rate for this mixture. The arrows in the figures indicate the direction of increasing strain rate. From the figure, it is clear that for rich laminar flames in Fig.6.4(b)-(f), the reaction rate decreases as the strain rate increases.

Figure 6.4(a) and (b) show that for stoichiometric and slightly rich mixture, reaction rates and dissipation rates are low. In Fig.6.4(c)-(e), DNS results are comparable with the strained flamelet values. In terms of the scatter, the DNS has a similar shape to the loop-like feature of the laminar flames, although they are shifted toward lower dissipation rates for the same reaction rates. The dissipation rates experienced in the turbulent flames are generally smaller than the strained flamelets. This is consistent with observation from Fig.6.2. For very

rich mixture, Fig.6.4(f) shows that turbulent flame tends to have much higher reaction rates than the laminar flame. Overall, the strained premixed flamelet of RtP configuration tends to underpredict the reaction rates observed in this DNS.

6.3 Validation of presumed PDFs

6.3.1 Scalar PDFs

Figures 6.5 and 6.6 present the marginal PDF for the mixture fraction and progress variable respectively, extracted from the DNS. A comparison to the presumed β PDF, with means and variances extracted directly from the DNS is also shown in the figures. Good agreement with the mixture fraction ditribution is evident in Fig. 6.5. For the progress variable, the distribution tends to be bimodal in the upstream position (A-A, R/D=2.5) with non-negligible burning part. Further downstream, close to the jet centre and far away from the centre where local mixture tends to be unburnt gas and burnt products respectively, the distribution is monomodal. The comparisons shown in Fig.6.6 are also reasonable except in outer regions where reaction rates are generally small and products are mixed with surrounding air.

6.3.2 Conditional PDFs

Previously in Chapter 5 the unconditional statistics of the magnitude of c gradient were studied, but the conditional statistics $P(N_{cc}|c)$ is required in the strained flamelet formulation and is often assumed to be a lognormal shape *a priori* [95, 96]. Here we like to test this presumed shape. Figure 6.7 presents the conditional PDFs extracted from the DNS in comparison to the lognormal distribution. The means and variances required to calculate this distribution are extracted from the DNS and the results are shown for four axial and radial positions. Note the log-log scale in the figure. For all c values, reasonable agreement is seen, despite considerable noise in the DNS. This is due to a combination of spatial intermittency of the flame and insufficient samples due to conditioning on various c values at these positions.

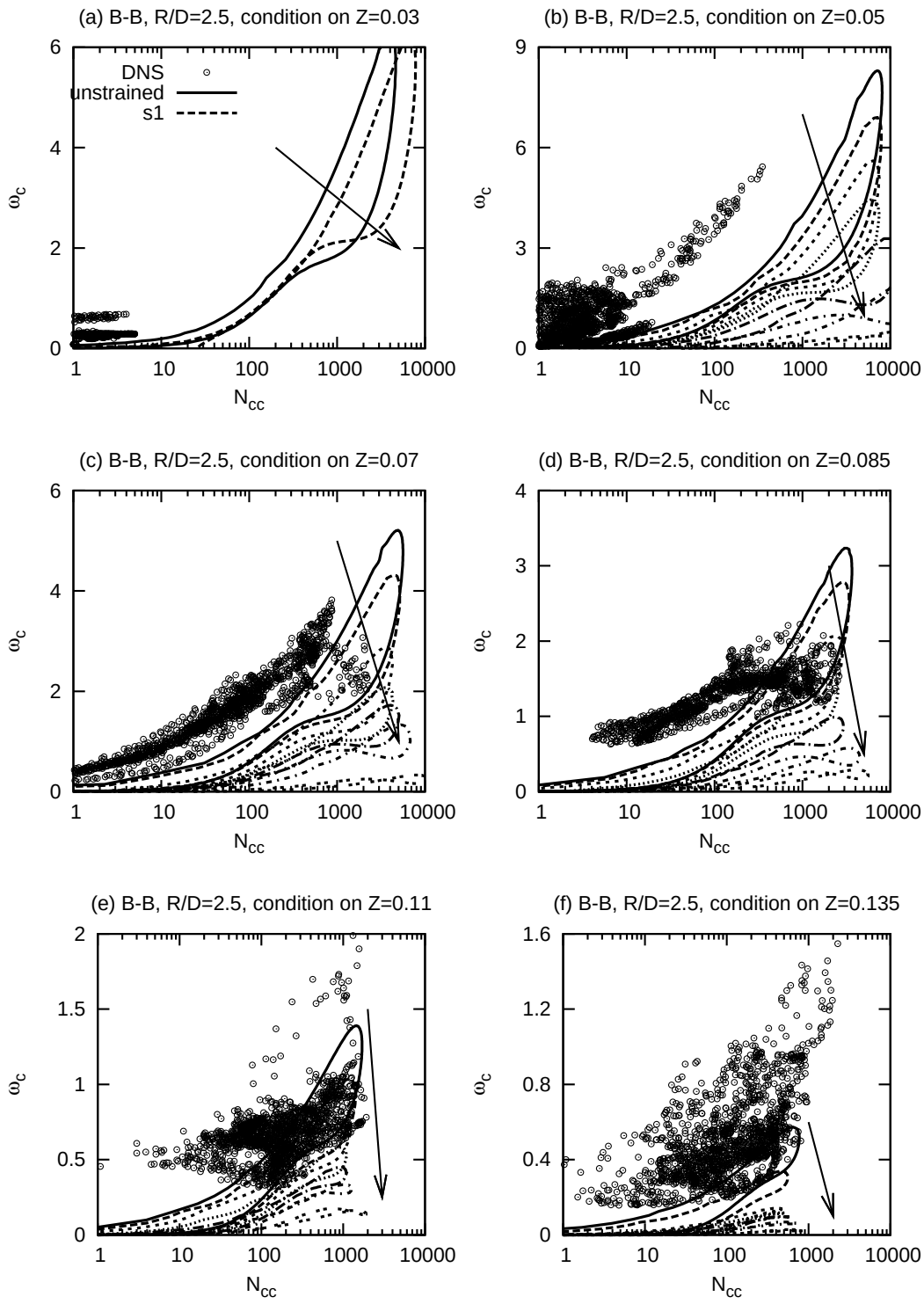

Figure 6.4: Comparison between DNS reaction rates, conditioned on six different mixture fractions, and laminar RtP strained premixed flamelets with different strain rates. The arrow indicates the direction of increasing strain rate.

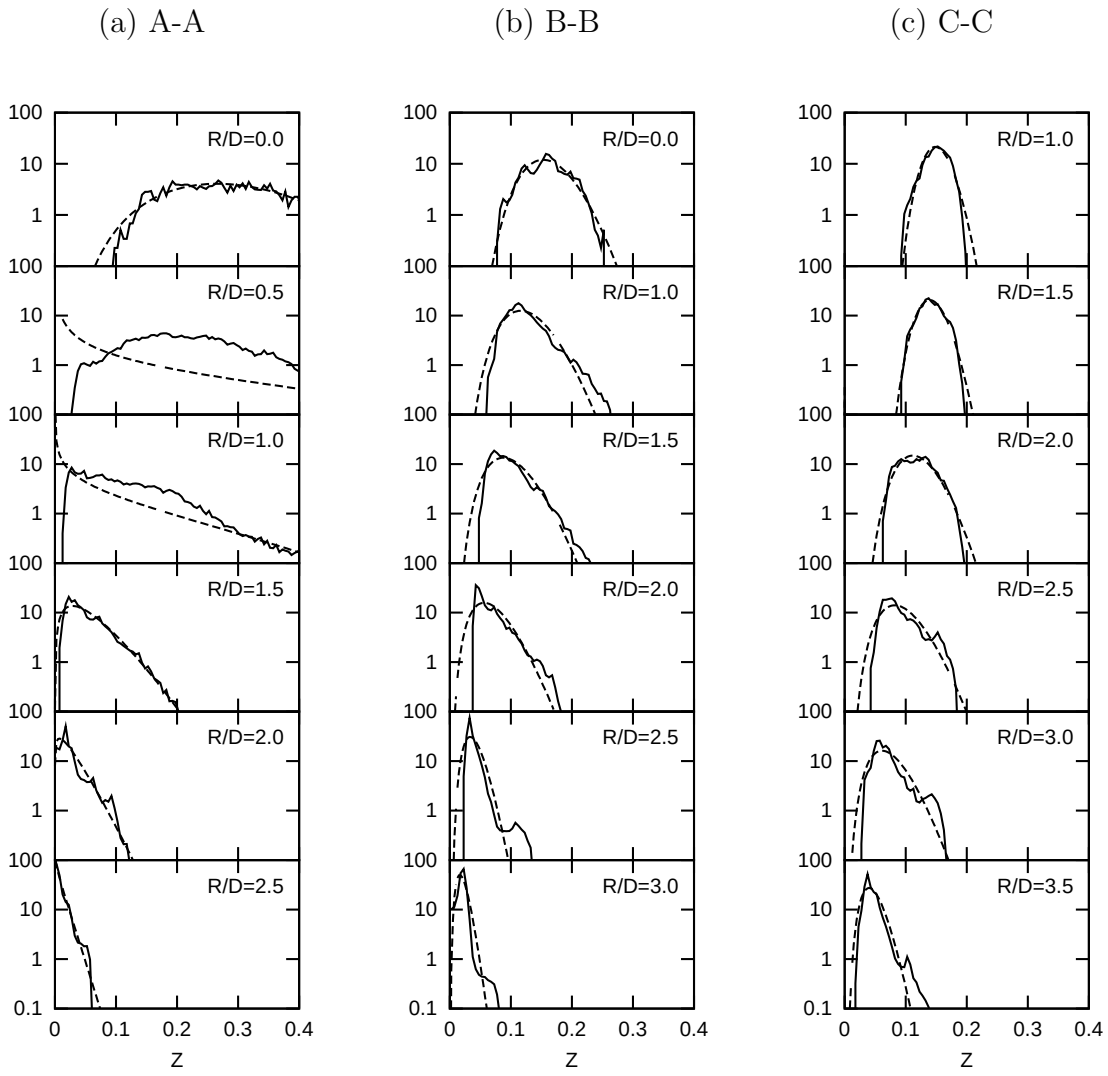

Figure 6.5: Comparison of mixture fraction PDF from the DNS (solid) and a presumed β shape (dashed) at different axial and radial positions.

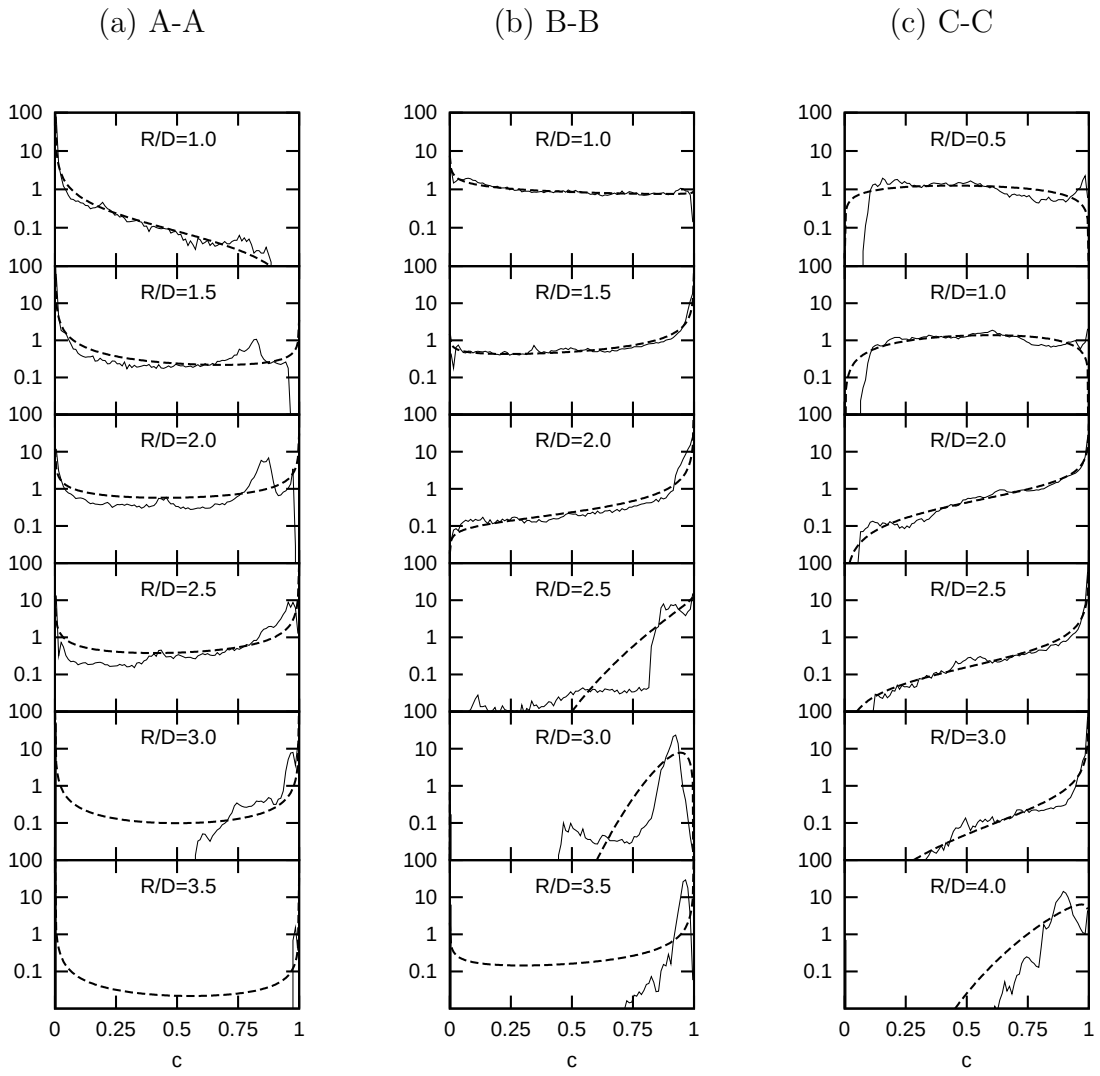

Figure 6.6: Comparison of progress variable PDF from the DNS (solid) and a presumed β shape (dashed) at different axial and radial positions.

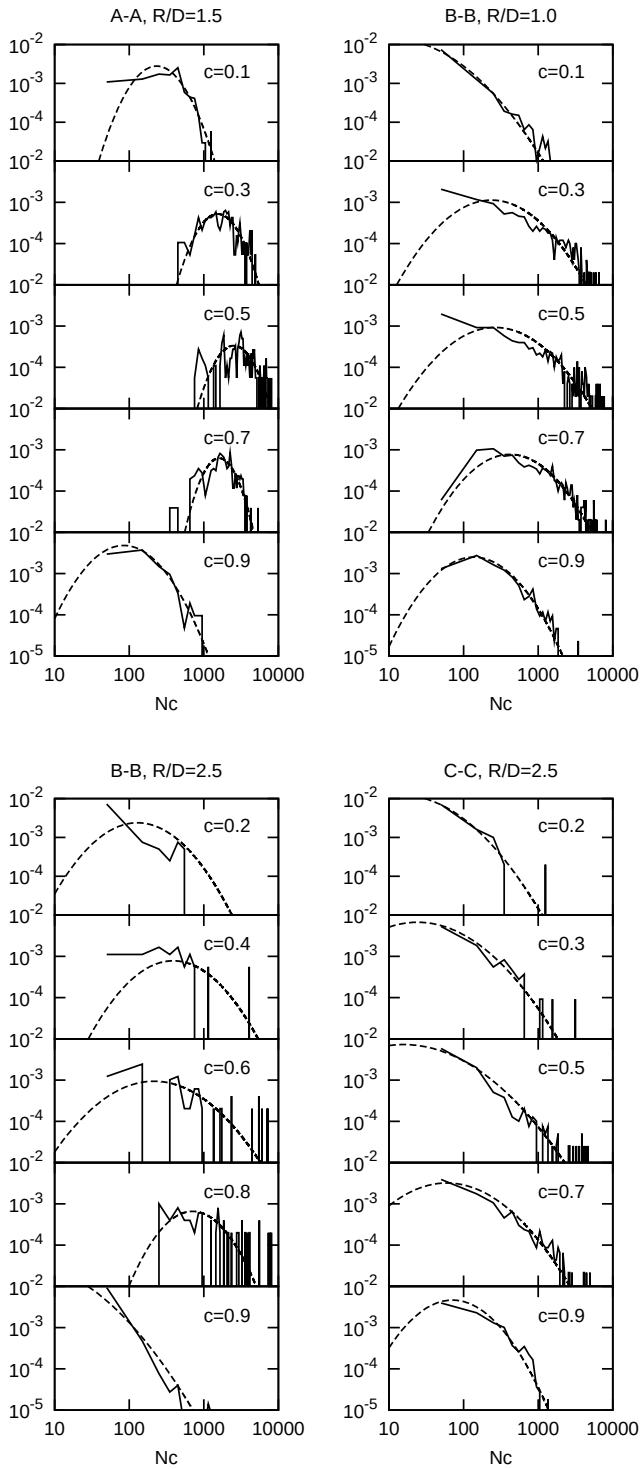

Figure 6.7: Comparison of the conditional PDF $P(N_{cc}|c)$ from DNS (solid) and a presumed lognormal shape (dashed) at different axial and radial positions.

6.3.3 Joint PDFs for scalars

It is noted by Ruan et al.[163] that the assumption of statistical independence between the mixture fraction and progress variable is only reasonable in upstream locations where the flame is stabilised but not valid at downstream positions. This can also be seen in Chapter 5, Fig.5.6 for the radial variation of $\widetilde{c''Z''}$ at several axial positions. Nevertheless, statistical independence has been assumed in many previous studies [66, 188].

Recently Darbyshire [48, 49] developed a method to include the correlation between the mixture fraction and progress variable. The joint PDF with the desired correlation can be calculated using the individual marginal PDF and a copula. A copula can be understood as a function that couples multivariate distributions to their marginal distributions. The general procedure involved in this approach is briefly summarised as follows [48, 49].

1. The correlation coefficient is calculated from a prescribed covariance of ξ and ζ and their respective standard deviations σ_ξ and σ_ζ using

$$r_{\xi\zeta} = \mathrm{Covar}(\xi, \zeta)/\sigma_\xi\sigma_\zeta. \tag{6.7}$$

2. Two large, say 5000, sets of random numbers, X_i and Y_i are generated from a standard normal distribution.

3. The correlation coefficient r_{XY} of the random variables X_i and Y_i is related to the desired correlation $r_{\xi\zeta}$ by

$$r_{XY} = 2\sin\left(\frac{\pi r_{\xi\zeta}}{6}\right). \tag{6.8}$$

4. A new set of random variables are calculated with the required correlation r_{XY}

$$Y_i^{new} = X_i r_{XY} + Y_i\sqrt{1 - r_{XY}^2}. \tag{6.9}$$

5. X_i and Y_i^{new} are transformed back to a uniform distribution by using the cumulative density function (CDF) Φ for the standard normal distribution

$$\xi_i = \Phi(X_i) = \frac{1}{2}\left[1 + erf\left(\frac{X_i}{\sqrt{2}}\right)\right] \quad \text{and} \quad \zeta = \Phi(Y_i^{new}), \tag{6.10}$$

where erf the error function appears in CDF Φ.

6. The odds ratio θ required in the construction of a copula is calculated by plotting the uniform distribution of ξ and ζ in the contingency table, illustrated in Fig.6.8. One can count the number of samples N_i falling in each of the four quadrants shown in the figure. The regions are divided by $\zeta = 0.5$ and $\xi = 0.5$. The odds ratio θ is then obtained as

$$\theta = \frac{N_1 N_4}{N_2 N_3}. \tag{6.11}$$

7. Finally the joint PDF with the desired correlation is calculated as

$$p(\xi, \zeta) = \begin{cases} \frac{\theta f g\{1+(\theta-1)[F+G-2FG]\}}{[S^2-4\theta(\theta-1)FG]^{3/2}} & \text{if } (\theta \neq 1) \\ fg & \text{if } (\theta = 1) \end{cases} \tag{6.12}$$

where $S = 1 + (\theta - 1)(F + G)$, and f and g are the marginal beta PDFs of ξ and ζ respectively. F and G are their marginal CDFs respectively.

The details of this approach can be found in [48, 49].

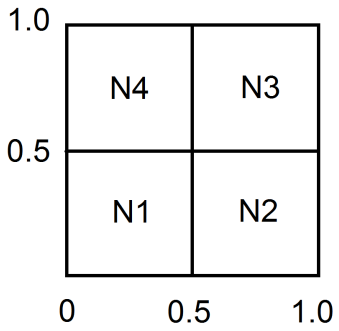

Figure 6.8: Contingency table. N_i is the number of samples falling within each square.

The modelled joint PDF including the correlation has been previously validated using experimental data of a stratified V flame and one arbitrary axial

location of the JAXA DNS data [48, 49]. Here, its performance at various axial and radial positions are examined closely with the DNS data.

Figure 6.9 compares the DNS results and the modelled joint PDFs with and without correlation. The Reynolds statistics required for the modelling are extracted from the DNS. Both models give reasonable results at position A-A, as the correlation here is quite small. At downstream locations, one radial position at B-B in the burning part of the flame and two radial positions at C-C, one in burning part and another closer to the burnt gas are selected. It is clear that significant negative correlations are present and have to be included. The correlated joint PDFs give excellent results. The peak value of the PDF, its location and more importantly the correlation are accurately captured in this joint PDF model. The assumption of statistical independence at these positions leads to incorrect peak values and the peak locations, especially in the burning part of the flame. Close to the burnt side where $\widetilde{c} \approx 1$, the local mixture with various mixture fraction values all approach to their equilibrium products, as shown in bottom row of Fig.6.9. This phenomenon and the mixing of equilibrium products lead to a reduction in the correlation and thus modelling the joint PDF with two independent PDFs can become acceptable, although the correlated JPDF model gives better agreement with the DNS results as shown in Fig.6.9.

6.4 Mean Reaction Rates Closure

As noted in Eq.(2.70), the source term $\dot{\omega}_c^*$ of the progress variable in partially premixed combustion, rewritten here for the sake of convenience,

$$\overline{\dot{\omega}_c^*} = \overline{\dot{\omega}_c} + \overline{\frac{1}{\partial Y_i/\partial c}\left(2\rho N_{cZ}\frac{\partial^2 Y_i}{\partial c \partial Z} + \rho N_{zz}\frac{\partial^2 Y_i}{\partial Z^2} + \rho N_{cc}\frac{\partial^2 Y_i}{\partial c^2}\right)}, \tag{6.13}$$

has four components. Here, the focus is on the first term $\overline{\dot{\omega}_c}$ and its possible closure. The other terms will be dealt with as needed in Chapter 7.

Four possible closure strategies for $\overline{\dot{\omega}_c}$ have been discussed in Section 6.1 all of which are based on flamelet and presumed PDF approach. The first strategy uses unstrained premixed flamelets of various mixture fractions and assumes Z and c

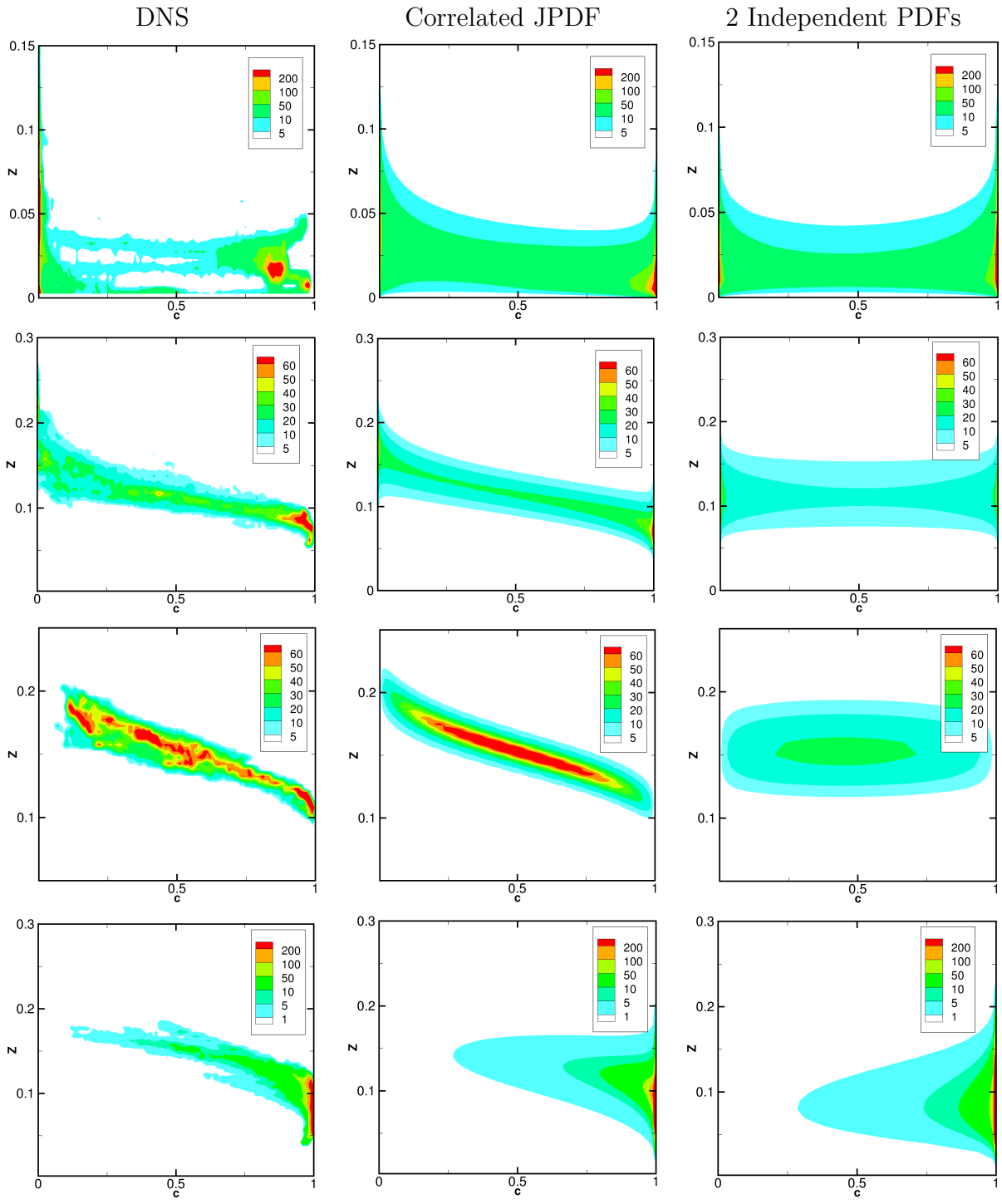

Figure 6.9: Comparison of joint PDF extracted from the DNS (left) and model with correlation (middle) and without correlation (right). (a)A-A, R/D=2.0 (1st row), (b)B-B, R/D=1.0 (2nd row),(c) C-C, R/D=1.0 (3rd row), (d) C-C, R/D=2.5 (bottom row).

to be statistically independent, as noted in Eq.(6.2). The second model relaxes the assumption of statistical independence and uses the correlated joint PDF with unstrained premixed flamelets, as in Eq.(6.3). The third closure is based on diffusion flamelets as in Eq.(6.4) and the fourth is based on the extended strained premixed flamelet as in Eq.(6.6).

Figure 6.10 compares the mean reaction rate for the progress variable based on water mass fraction as in Eq.(3.3), calculated from the DNS data and using the above four closures. A number of observations can be made from the figure.

- For the upstream position A-A, the premixed flamelet models of Eq.(6.2) and Eq.(6.3) give equally good results. This is because the covariance $\widetilde{c''Z''}$ at this position is smaller than that in the downstream positions, as has been illustrated in Fig.5.6 in Chapter 5. Thus, the statistical independence of mixture fraction and progress variable is a good approximation at this position, which is also supported by results in Fig. 6.9. At the downstream positions, the correlation increases and thus Eq.(6.3) gives improved results compared to Eq.(6.2).

- The diffusion flamelet model of Eq.(6.4) tends to give a broader reaction region for the upstream position A-A with considerable underprediction for the mean reaction rate. For the downstream positions, this model is reasonable only in outer radial regions where the local burning is diffusion dominated, whereas it yields zero reaction rate for inner regions close to the jet centre where the DNS data show substantial amount of reaction due to rich partially premixed combustion. This illustrates the limitation of the diffusion flamelet model for this partially premixed flame, even though it is commonly considered as a lifted jet diffusion flame.

- The extended strained flamelet model of Eq.(6.6) tends to underpredict the mean reaction rates for almost all axial positions while it gives reasonable results in outer radial regions where the local combustion is diffusion-controlled. This underprediction is consistent with observation made in Fig. 6.4.

In general, the unstrained premixed flamelets with a presumed joint PDF as in

Eq.(6.3) is the most appropriate closure model for this partially premixed flame.

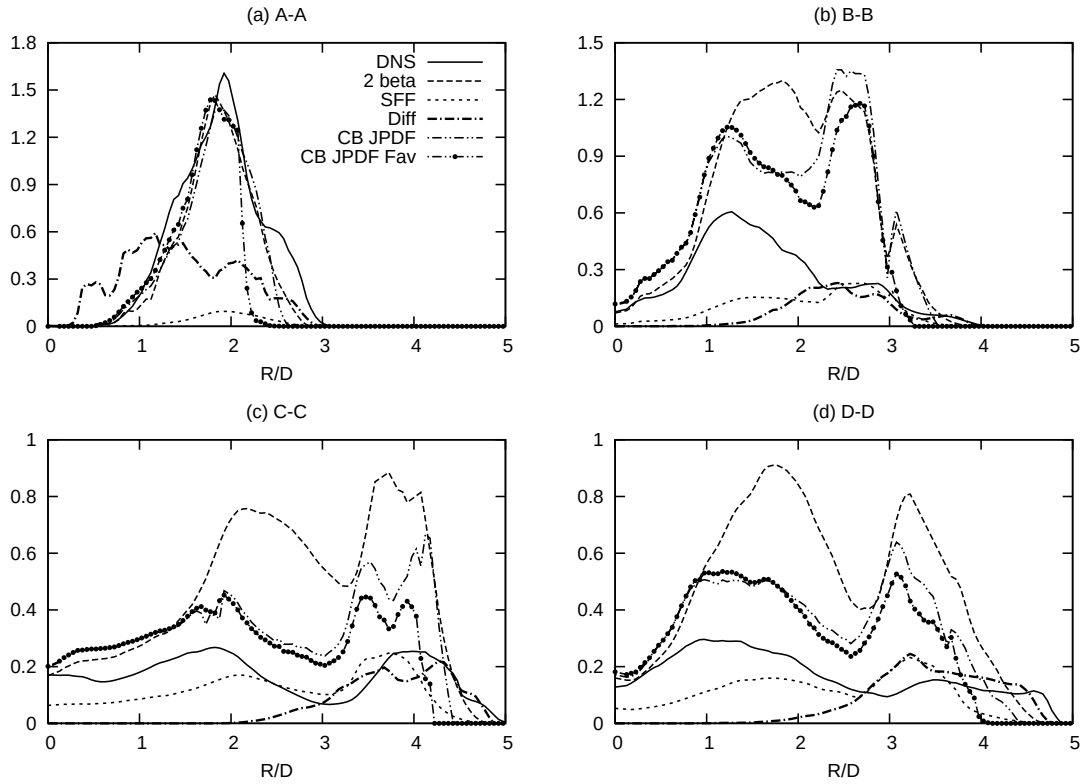

Figure 6.10: Comparison of DNS and models mean reaction rates $\overline{\dot{\omega}_c}(g/cm^3/s)$ at positions (a) A-A, (b) B-B, (c) C-C and (d) D-D which is at 11.75D. "2 beta" denotes model using 2 independent beta PDF in Eq.(6.2), "SFF" is the extended strained flamelet formulation in Eq.(6.6), "Diff" is the diffusion flamelet model in Eq.(6.4). "CB JPDF" is the correlated joint PDF model in Eq.(6.3). "CB JPDF Fav" is the correlated joint PDF model approximated using marginal Favre PDFs in Eq.(6.14).

A close study of Eq.(6.3) shows that the Reynolds PDF, and therefore the Reynolds statistics, $\overline{Z}$, $\overline{c}$, $\overline{Z''^2}$, $\overline{c''^2}$ and $\overline{c''Z''}$, are required to get the mean reaction rate. However, numerical simulation of turbulent reacting flows involves Favre averages, allowing us to obtain Favre marginal PDFs through the presumed beta PDF. It is not always easy to construct Reynolds statistics from Favre statistics. This introduces some difficulties in obtaining the joint PDF required in Eq.(6.3), although the Reynolds and Favre PDFs are related through $\bar{\rho}\widetilde{P}(\xi,\zeta) = \rho P(\xi,\zeta)$. For example one cannot strictly write $\widetilde{P}(\xi,\zeta) = \widetilde{P}(\xi)\widetilde{P}(\zeta)$, involving two Favre

marginal PDFs, even when statistical independence of ξ and ζ is satisfied. To overcome this difficulty, an approximation $\widetilde{P}(\xi,\zeta) \approx \widetilde{P}(\xi)\widetilde{P}(\zeta)$ is made here following Darbyshire and Swaminathan [49] when the statistical independence is observed, otherwise the two marginal Favre PDFs are combined, as per Eq.(6.12), to get $\widetilde{P}(\xi,\zeta)$. Now the mean reaction rate is calculated using

$$\bar{\dot{\omega}}_c = \bar{\rho}^* \int\int \left[\frac{\dot{\omega}_c(\zeta,\xi)}{\rho(\zeta,\xi)}\right] \widetilde{P}(\zeta,\xi)\, d\zeta\, d\xi, \tag{6.14}$$

where $\bar{\rho}^*$ here is the mean density obtained from DNS. In a numerical simulation, this is the mean density from the CFD code. The quantities within the square bracket come from the unstrained premixed laminar flamelets. The mean reaction rate calculated with Eq.(6.14) is also shown in Fig.6.10 as "CB JPDF Fav". The error introduced by the above approximation of using Favre PDFs is generally small as one can see in Fig.6.10.

6.5 Summary

In this chapter, the performance of four different presumed PDF/flamelet models for the mean reaction rate has been assessed using DNS results. The turbulent flame front structure from the DNS has been compared with unstrained premixed flamelets, strained diffusion flamelets and strained premixed flamelets. It is found that unstrained premixed flamelets give reasonable agreement with the DNS results in most parts of this flame, while diffusion flamelets are reasonable only in downstream and radially outer regions where local combustion is predominantly diffusion-controlled. The strained premixed flamelets tend to underpredict the instantaneous reaction rates for the same dissipation rates experienced by the flame front in the DNS.

Various presumed PDF models have been compared with DNS results. The beta PDF is a good approximation for mixture fraction and progress variable marginal PDFs. For their JPDF, the assumption of statistical independence leads to poor prediction in the burning parts of partially premixed flames as the correlation is strong. Statistical independence is a reasonable approximation only at the upstream position where the flame is stabilised. Therefore, the correlation

must be included in the PDF modelling in general. The correlated JPDF model gives very good agreement with the DNS results in all locations.

The diffusion flamelet model fails to predict mean reaction rate in the inner regions where significant fuel is consumed in a rich partially premixed flame. However, a reasonable agreement is observed for radially outer regions where local burning is diffusion-controlled. The extended strained premixed flamelet model generally underpredicts the mean reaction rate as the straining effects are overestimated by the flamelet model. The unstrained premixed flamelet with the joint PDF assuming statistical independence of Z and c overpredicts the mean reaction rate at downstream positions. The same model with the correlated JPDF model gives an improved agreement with DNS results. This model performance is observed to be weakly sensitive to the type of, Reynolds or Favre, statistics used when constructing the joint PDF. Thus this model is recommended for the simulation of partially premixed combustion. The *a posteriori* testing of this reaction rate closure and various dissipation rate models discussed in previous chapters is conducted in the next chapter.

Chapter 7

RANS Simulation

In this Chapter, RANS simulations of turbulent lifted jet flames are performed with the combustion models identified in Chapter 6 and scalar dissipation rate models discussed in Chapter 5.

7.1 Modelling Methodology

The equations solved are the conservation of mass, momentum and enthalpy given in Eq.(2.9), Eq.(2.10) and Eq.(2.12). For turbulence modelling, the standard $k-\epsilon$ model as given in Eqs.(2.16)-(2.18) is used. Standard model constants, as noted in Chapter 2, are used unless otherwise stated.

This flame has been simulated using the Conditional Moment Closure (CMC) method in earlier studies [51, 88]. The main challenge in simulating such flames is to obtain the lift-off height correctly. Here, the presumed joint PDF with unstrained premixed flamelets given in Eq.(6.14), discussed in chapter 6, is used to close the mean reaction rate. Thus, extra transport equations for the mixture fraction $\widetilde{Z}$, its variance $\widetilde{Z''^2}$, the progress variable $\widetilde{c}$, its variance $\widetilde{c''^2}$ and the covariance $\widetilde{c''Z''}$ need to be solved. These equations are given in Chapter 2 as Eq.(2.29), Eq.(2.30), Eq.(2.41), Eq.(2.42) and Eq.(2.66) respectively. Furthermore, the source terms $\bar{\dot{\omega}}_c$ in Eq.(2.41) must be replaced by $\overline{\dot{\omega}_c^*}$ in Eq.(6.13) for partially premixed combustion.

In the variance and covariance equations, the scalar dissipation rate and the

cross dissipation rate appear. The linear relaxation models for $\widetilde{\epsilon}_{ZZ}$ in Eq.(2.34) and $\widetilde{\epsilon}_{cZ}$ in Eq.(5.4), as discussed in Chapter 5, are used here. For $\widetilde{\epsilon}_{cc}$, the model in Eqs.(5.1)-(5.3) is used without any changes to the model parameters as a first step.

In the equations for $\widetilde{c''^2}$ of Eq.(2.42) and covariance $\widetilde{c''Z''}$ of Eq.(2.66), there are source terms $\overline{c''\dot{\omega}_c''}$ and $\overline{Z''\dot{\omega}_c''}$ that require modelling. These are calculated as follows.

$$\overline{c''\dot{\omega}_c''} \approx \overline{c''\dot{\omega}_c} = \bar{\rho}\int_0^1\int_0^1 (\zeta - \widetilde{\zeta})\frac{\dot{\omega}_c(\xi,\zeta)}{\rho(\xi,\zeta)}\widetilde{P}(\xi,\zeta)\,d\xi\,d\zeta, \tag{7.1}$$

$$\overline{Z''\dot{\omega}_c''} \approx \overline{Z''\dot{\omega}_c} = \bar{\rho}\int_0^1\int_0^1 (\xi - \widetilde{\xi})\frac{\dot{\omega}_c(\xi,\zeta)}{\rho(\xi,\zeta)}\widetilde{P}(\xi,\zeta)\,d\xi\,d\zeta, \tag{7.2}$$

The temperature is calculated using the total enthalpy $\widetilde{h}$ computed in the simulation. This includes the sensible and chemical contributions,

$$\widetilde{h} = c_{p,\text{mix}}(\widetilde{T} - T_0) + \Delta h^0_{f,\text{mix}}, \tag{7.3}$$

where $T_0 = 298\text{K}$ is a reference temperature. The mixture averaged specific heat capacity $c_{p,\text{mix}}$, enthalpy of formation $\Delta h^0_{f,\text{mix}}$ and the mixture molecular weight W_{mix} required in the state equation Eq.(2.13), are calculated as follows.

$$c_{p,\text{mix}} = \sum \widetilde{Y}_i\, c_{p,i} = \sum \int_0^1\int_0^1 Y_i\, c_{p,i}\, \widetilde{P}(\xi,\zeta)\,d\zeta\,d\xi, \tag{7.4}$$

$$\Delta h^0_{f,\text{mix}} = \sum \int_0^1\int_0^1 Y_i\, \Delta h^0_{f,i}\, \widetilde{P}(\xi,\zeta)\,d\zeta\,d\xi, \tag{7.5}$$

$$W_{\text{mix}} = \int_0^1\int_0^1 (\sum (Y_i/W_i))^{-1}\, \widetilde{P}(\xi,\zeta)\,d\zeta\,d\xi. \tag{7.6}$$

Figure 7.1 illustrates the calculation procedure for Eqs.(7.4)-(7.6). Laminar unstrained planar flame quantities are used within the flammability limits. Outside this range, air and fuel properties are interpolated with the laminar flame quantities appropriately before the integrations are performed.

These quantities, together with the mean species $\widetilde{Y}_i$, the mean reaction rate $\overline{\dot{\omega}_c}$, the source terms $\overline{c''\dot{\omega}_c''}$ and $\overline{Z''\dot{\omega}_c''}$ are tabulated with $\widetilde{Z}$, $\widetilde{c}$, $\widetilde{Z''^2}$, $\widetilde{c''^2}$ and $\widetilde{c''Z''}$

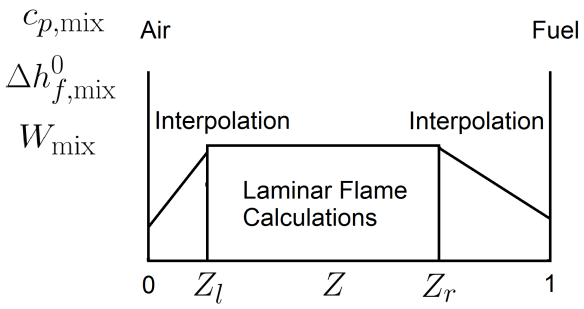

Figure 7.1: Calculation illustration for mixture properties such as $c_{p,\mathrm{mix}}$, $\Delta h^0_{f,\mathrm{mix}}$ and W_{mix}.

as controlling variables. This table is used in RANS calculation to give the required quantities. Temperature becomes a function of $\widetilde{Z}$, $\widetilde{c}$, $\widetilde{Z''^2}$, $\widetilde{c''^2}$, $\widetilde{c''Z''}$ and Eq.(7.3). Density relates to temperature through the equation of state in Eq.(2.13). Temperature and density are calculated "on the fly" when RANS simulations are performed.

For the progress variable defined using water mass fraction in Eq.(3.3), the derivatives involved in Eq.(6.13) can be obtained as

$$\frac{\partial Y_{H2O}}{\partial Z} = c\frac{\mathrm{d}Y^{Eq}_{H2O}}{\mathrm{d}Z} \quad \text{and} \quad \frac{\partial^2 Y_{H2O}}{\partial Z^2} = c\frac{\mathrm{d}^2 Y^{Eq}_{H2O}}{\mathrm{d}Z^2},$$

$$\frac{\partial Y_{H2O}}{\partial c} = Y^{Eq}_{H2O}(Z), \qquad \frac{\partial^2 Y_{H2O}}{\partial c^2} = 0 \quad \text{and} \quad \frac{\partial^2 Y_{H2O}}{\partial Z \partial c} = \frac{\mathrm{d}Y^{Eq}_{H2O}}{\mathrm{d}Z}. \tag{7.7}$$

Substituting Eq.(7.7) into the source term $\overline{\dot{\omega}^*_c}$ in Eq.(6.13), one gets

$$\overline{\dot{\omega}}^*_c = \underbrace{\overline{\dot{\omega}}_c}_{\text{(I)}} + \underbrace{\overline{\rho \frac{c}{Y^{Eq}_{H2O}(Z)} \frac{\mathrm{d}^2 Y^{Eq}_{H2O}}{\mathrm{d}Z^2} N_{ZZ}}}_{\text{(II)}} + \underbrace{\overline{2\rho \frac{1}{Y^{Eq}_{H2O}(Z)} \frac{\mathrm{d}Y^{Eq}_{H2O}}{\mathrm{d}Z} N_{cZ}}}_{\text{(III)}}. \tag{7.8}$$

There are two extra source terms, (II) and (III), contributing to the overall mean reaction rate. The term (II) is due to the dissipation rate of mixture fraction and is considered as the contribution from the non-premixed burning mode and the effects of partial premixing on the overall reaction rate. The term (III) is due to the cross dissipation rate. As shown in Chapter 5, N_{ZZ} is typically an order of

magnitude larger than N_{cZ}. The second derivative $\mathrm{d}^2Y^{Eq}_{H2O}/\mathrm{d}Z^2$ is much larger than the first derivative $\mathrm{d}Y^{Eq}_{H2O}/\mathrm{d}Z$ as shown in chapter 4, Fig. 4.4. Thus, the overall contribution from term (III) is expected to be small and it is neglected here for simplicity. Similar treatment of this term was also adopted in previous studies [54, 63] and has been justified by other DNS studies [55]. The effect of the mixture fraction dissipation rate on the overall mean reaction rate is also noted by Müller et al. [128] in a different context. By using the G-equation for the scalar fields and mixture fraction to account for the partial premixing, Müller et al. [128] derived an expression for the turbulent flame speed which involved the scalar dissipation rate of the mixture fraction, as shown in Eq.(2.63). They assumed a *priori* a functional dependence whereby the turbulent flame speed decreases as scalar dissipation rate N_{ZZ} increases. In the current modelling approach, no such assumption has been made, rather, the contributions from the three dissipation rates naturally occur in the transport equation.

The term (II) requires modelling and it is modelled as follows:

$$\overline{\rho\frac{c}{Y^{Eq}_{H2O}(Z)}\frac{\mathrm{d}^2Y^{Eq}_{H2O}}{\mathrm{d}Z^2}N_{ZZ}} \simeq \bar{\rho}\widetilde{c}\,\widetilde{\epsilon}_{ZZ}\int_{\xi_{st}-\triangle\xi}^{\xi_{st}+\triangle\xi}\frac{1}{Y^{Eq}_{H2O}(\xi)}\frac{\mathrm{d}^2Y^{Eq}_{H2O}(\xi)}{\mathrm{d}Z^2}\widetilde{P}_\beta(\xi)d\xi, \quad (7.9)$$

where ξ is the sample space variable for mixture fraction Z. Since the derivatives are significant only around the stoichiometric region, as shown in Fig. 4.4 in Chapter 4, $\triangle\xi$ is set to be a constant of 0.02. This is essentially consistent with Müller et al. [128] where they considered the effect of scalar dissipation rate on the turbulent burning velocity to be important only in the range of mixture fractions where laminar flame speed is a significant fraction of that of the stoichiometric mixture.

7.2 Model Implementation

Figure 7.2 presents a schematic diagram of the computational domain for a 2D axisymmetric model of the turbulent lifted jet flame. The computational grid contains 13800 nodes and 13532 rectangular cells, and extends to 50D in the radial direction r and 200D in the axial direction, y, where D = 2 mm . A few

trials with coarser and finer grids for the non-reacting and reacting flows have been attempted to confirm the grid-independent of the results presented in this chapter.

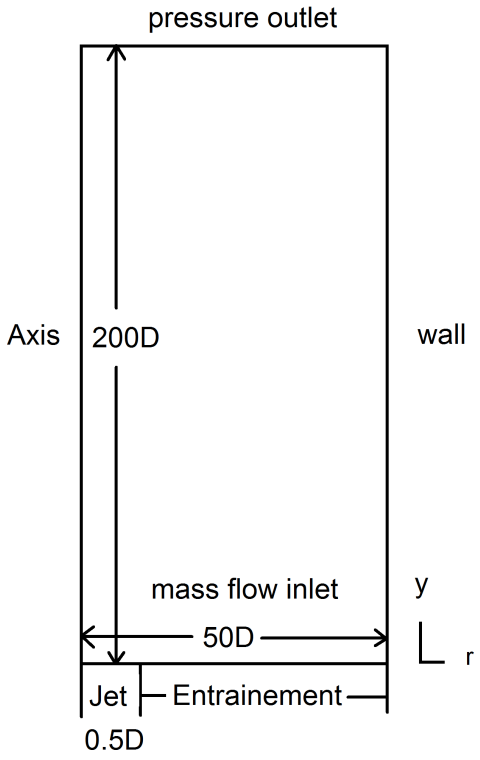

Figure 7.2: Schematic diagram of RANS simulation domain.

7.2.1 Boundary Conditions

Boundary conditions are also noted in Fig.7.2. The jet and entrainment have mass-flow-inlet boundary conditions. The inlet velocity profile in the jet is prescribed using a 1/7 power law with a bulk mean velocity of 680 m/s as suggested in the DNS calculation [125]. Turbulent intensity is set to be 5% with a turbulence integral length scale of 2 mm [51]. In the jet boundary, the mixture fraction is specified to be 1.0 and the enthalpy of -258460 J/kg for hydrogen at 280K is used. All other scalars have zero values at the jet boundary.

The mass flow rate at the entrainment boundary is specified according to Spalding [169] using

$$\frac{\mathrm{d}\dot{m}}{\mathrm{d}r} \approx 0.28\rho_{air}^{\frac{1}{2}}F^{\frac{1}{2}} \quad \text{with} \quad F = \rho_j U_j^2 \pi r_j^2, \tag{7.10}$$

where $\dot{m}$ is the entrained mass flow rate and the subscript j denotes jet values. A small constant entrainment velocity of 0.1 m/s has also been tested and results were found to have no significant difference. Turbulent intensity is set to a low value of 0.001% at the boundary. All scalars have zero values here and the corresponding enthalpy of air is used.

An axis boundary is applied at the symmetry axis and a wall boundary condition is used for the boundary parallel to the axis as it is far away from the jet. This wall boundary helps to stabilise the calculation. At the wall boundary, the enthalpy of ambient air is used and zero values are set for all other scalars. At the flow exit, a pressure outlet boundary condition and zero gradient flux for scalars are used.

7.2.2 Fluent UDF and UDS

The pressure based solver in Fluent is used for this calculation. The default momentum equations and the $k-\epsilon$ turbulence modelled equations are solved. Extra transport equations for a total of six User-defined-scalars (UDS) are implemented in Fluent with various sources and sinks specified using the User-defined-functions (UDF). The UDS are $\widetilde{Z}$, $\widetilde{c}$, $\widetilde{Z''^2}$, $\widetilde{c''^2}$, $\widetilde{c''Z''}$ and $\widetilde{h}$. Figure 7.3 presents a flow chart for the calculation procedure. The calculation steps bounded by dashed lines have been developed in this work. Temperature and density are calculated in UDFs for each iteration. User-defined-memory (UDM) is used to store the results and is passed to other UDFs to calculate the various sink and source terms of the transport equations. It is worth noting that Fluent solves the flow and turbulence equations as in an isothermal non-reacting case. No default energy equation or Fluent combustion models are used. Rather, combustion is coupled to the flow field calculation through density variation which is computed through UDS and UDFs, i.e. the Fluent program is "unaware" that it is solving for a

reacting case.

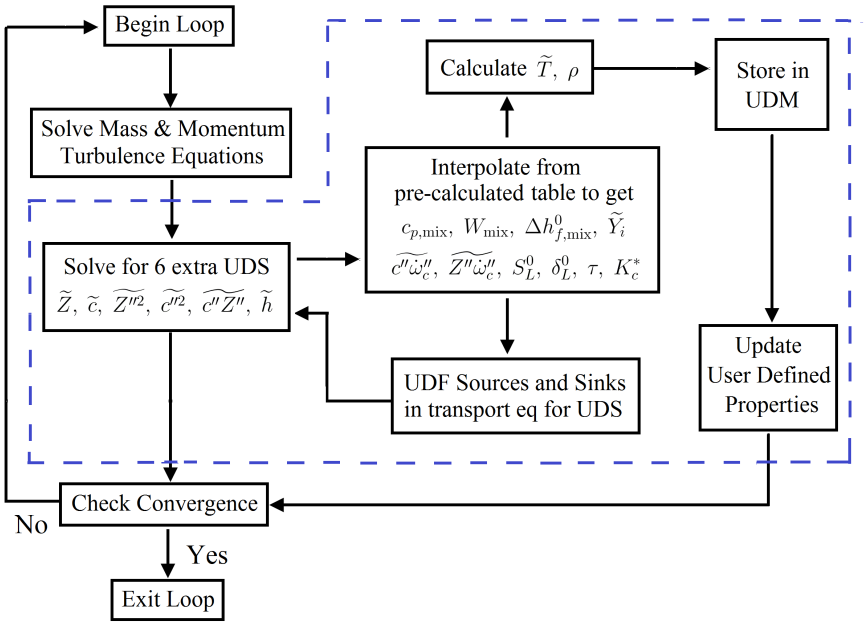

Figure 7.3: Program flow chart for the RANS calculation.

7.2.3 Initialisation of Flame Kernel

A converged non-reacting solution is first calculated. A small flame kernel is then initialised by setting one or two cells with $\widetilde{c} = 1.0$ and $\widetilde{h} = -36871 J/kg$ corresponding to burnt products of stoichiometric mixture at a certain axial position. Two axial positions, 9D and 12D chosen arbitrarily, have been tested for flame kernel initialisation. The flame is allowed to develop, propagate and reach the final lift-off height. The sizes of the kernels are 0.3×1.0 and 0.7×0.75 squared mm, while the energy supplied to the kernels is about 0.010 J/m and 0.018 J/m respectively.

7.3 Results and Discussions

7.3.1 Flows Field

Since the experiment [46, 47] does not provide information for the velocity field, a comparison to the mixture fraction field as suggested in previous studies [51, 88] is shown in Fig.7.4. This figure presents the RANS calculation for mean mixture fraction and its fluctuation normalised by centreline values at 7D and 9.5D. Also shown are the experimental measurements [46]. A reasonable agreement is observed. In the $k-\epsilon$ turbulence model, the model parameter $c_{\epsilon 2}$ is increased slightly ($c_{\epsilon 2} = 1.96$) to provide better overall agreement, consistent with previous studies [51, 88]. This has the effect of increasing the turbulent viscosity and diffusion, however, previous CMC studies [51, 88] suggest that this change is small enough not to significantly alter the spatial diffusion.

7.3.2 Flame Brush comparison

The lift-off height based on the leading edge of $T = 900K$ isoline, as used in the experiment [24] and CMC calculation [88], is 7.5D in this study when both the correlated joint PDF model in Chapter 6 and Eq.(7.9) for term (II) are included. This agrees reasonably well with the experimental observation [46] of 7D. Thus it is possible to make a direct and unambiguous comparison of the scalar variation in the flame brush between the experiment and the RANS simulation.

The computed radial variations of temperature, mole fractions of H_2, O_2, OH, H_2O and N_2 are compared with experimental measurements for axial positions of 7, 9.5, 30, 50 and 100D in Figs. 7.5-7.9 respectively. Note that in Fig. 7.7, the experimental measurement for temperature at 30D is not available and only RANS results are shown. Previous results of the CMC calculation by Devaud and Bray [51] for axial position of 7D, and by Kim and Mastorakos [88] for 9.5D are included for comparison in Figs. 7.5 and 7.6 respectively. Note that temperature for the CMC calculation [88] is not available at 9.5D.

In Fig. 7.5, the current model gives a lower peak temperature of about 650K compared to the 900K observed in experiment [46], while the CMC calculation [51] gives slightly higher values at axial position of 7D. This is due to the small

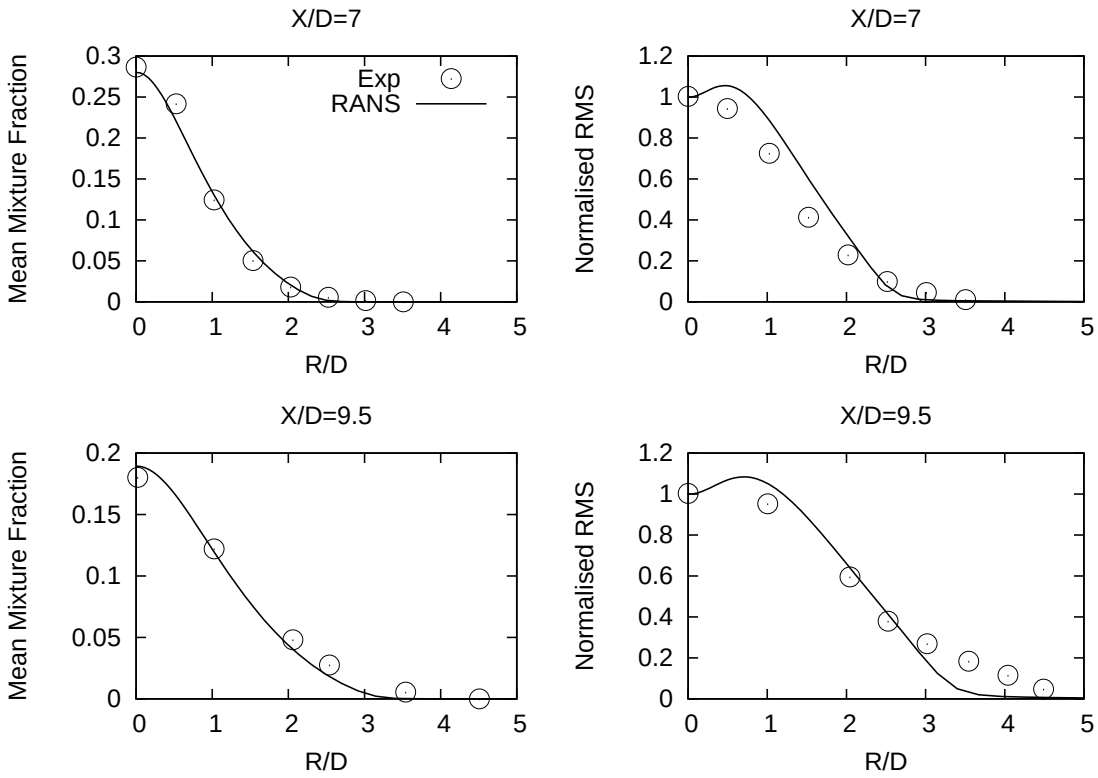

Figure 7.4: Comparison of RANS results with experimental measurements [46] for the mean mixture fraction and RMS normalised by centreline values at 7D and 9.5D.

difference in lift-off height, 7.5D in current model and 7D in experiment [46] based on the most leading edge of the T=900K contour. This causes the flame to have a lower temperature, slightly higher H_2 and slightly lower OH and H_2O mole fractions, as the flame at 7D is not as fully developed as that in the experiment. In general, this agreement is acceptable and comparable to what was achieved in previous CMC calculations.

In Fig. 7.6, the current model under-predicts both the tempeature and the scalar mole fraction in the region close to the jet centre while the agreement is good away from the jet centre. Close to jet centre, local mixture is rich and can be beyond the flammability limit of 0.17. It seems that the current premixed flamelet model underpredicts the burning rate in very rich mixtures. Temperature profile is not available from previous CMC calculation [88] for comparison. The

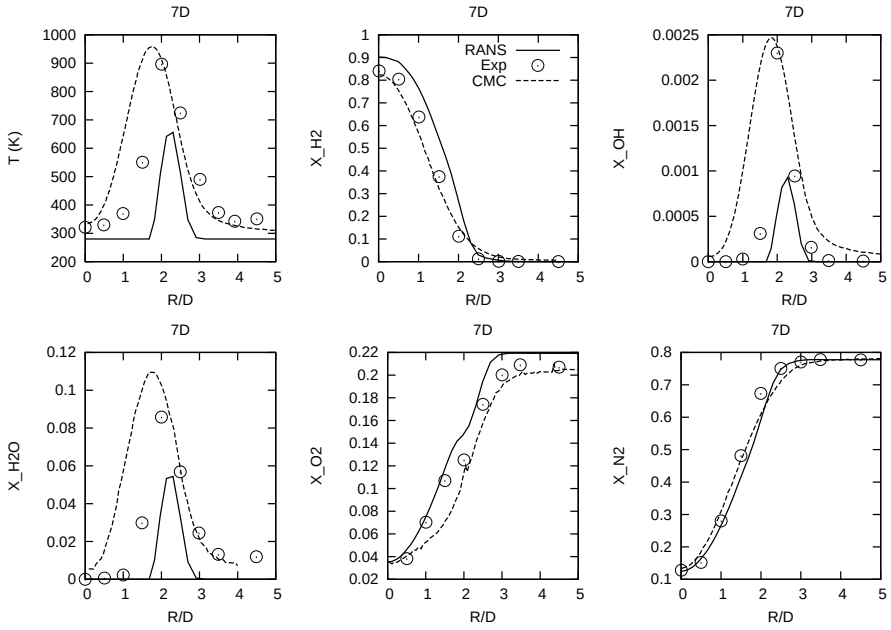

Figure 7.5: Comparison of simulation results, experimental measurements [46] and CMC calculation [51] for scalar radial variation at an axial position of 7D.

scalar profiles from the current model and CMC are in good agreement with experiment. It is worth noting that the decrease of O_2 mass fraction observed in the experiment at R/D=2 is captured by the current model whereas the previous CMC calculation [88] does not seem to capture this feature.

For downstream positions, Figs. 7.7-7.9 show that current model gives reasonable agreement with experimental measurements although reaction rate is underpredicted in regions close to jet centre, especially at 30D, leading to lower temperature and higher H_2 mole fraction. For other downstream positions, the agreement improves as the flame approaches equilibrium. In general, the overall agreement is reasonable for the current modelling approach.

7.3.3 Modelling Effects on lift-off height

The combination of different choices of model options results in four different scenarios. The details are listed in Table 7.1. This helps us to evaluate the influence of different models on the flame lift-off heights.

Figure 7.10 presents the temperature field and mixture fraction contour for

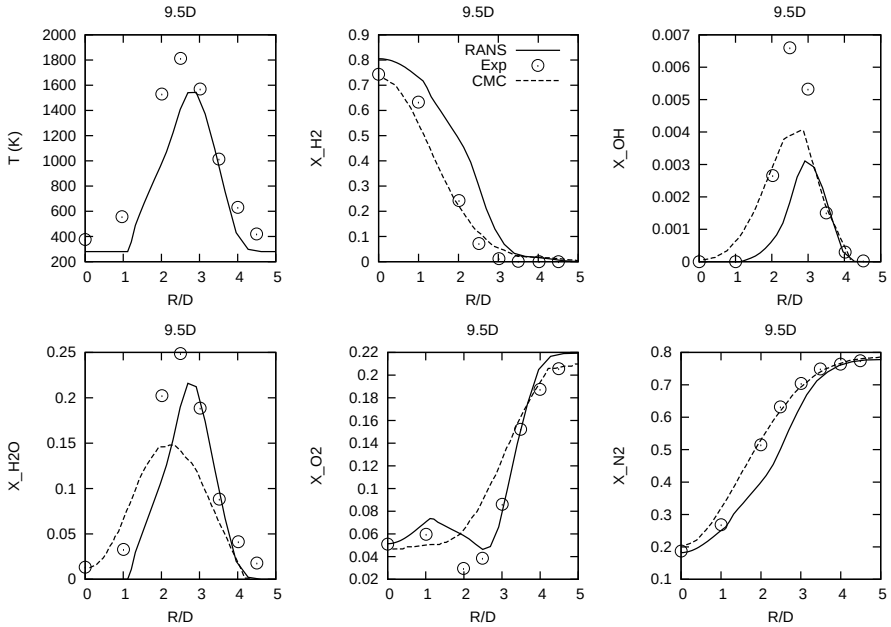

Figure 7.6: Comparison of simulation results, experimental measurements [46] and CMC calculation [88] for scalar radial variation at axial position of 9.5D. Temperature calculation is unavailable for CMC.

Case	A	B	C	D
$\widetilde{c''Z''}$ Equation	No	No	Yes	Yes
Term (II) Model	No	Yes	No	Yes
Lift-off Height (H/D)	4.5	5.2	6	7.5

Table 7.1: Lift-off heights for different modelling cases.

the four cases listed in Table 7.1. Case-A in Figure 7.10(a) is the standard unstrained flamelets model with the joint PDF calculated from the statistically independent marginal PDFs of the mixture fraction and progress variable. No model is included for the effect of partial premixing represented by term (II). The lift-off height based on the most leading edge of $T = 900K$, is 4.5D, i.e. less than the 7D observed in the experiment. Case-B in Fig. 7.10(b) includes the model for term (II). It seems that the effect of partial premixing act to push the flame to stabilise at an increased lift-off height of 5.2D, which is also not close to the experimental value. Case-C in Fig. 7.10(c) includes the correlated joint PDF model but excludes term (II). This causes the flame to stabilise at a height of 6D.

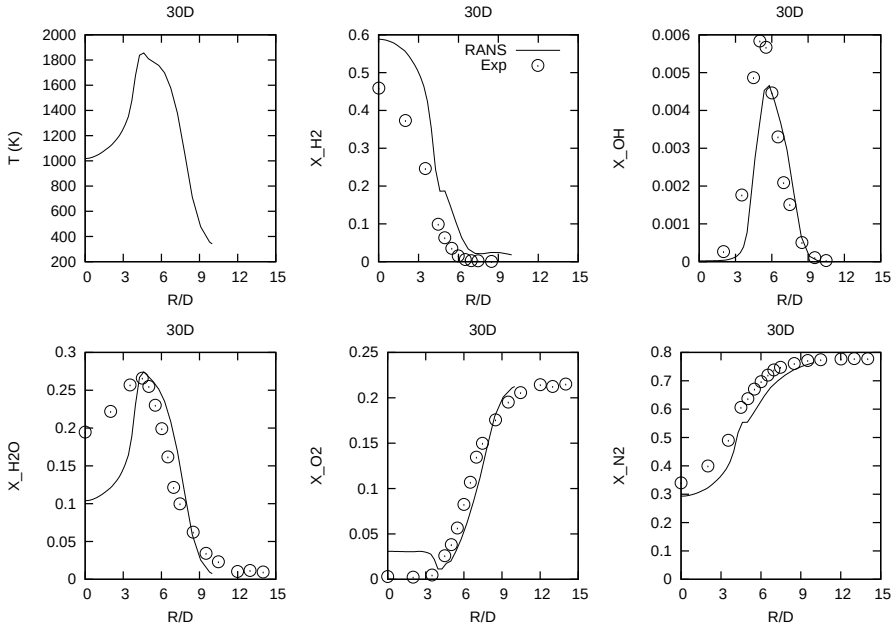

Figure 7.7: Comparison of simulation results and experimental measurements [46] for scalar radial variation at axial position of 30D. Temperature measurement is unavailable in the experiment.

Case-D in Fig. 7.10(d) is the full model including both the correlated joint PDF and the partial premixing effects in term (II). The lift-off height is 7.5D, which is in reasonable agreement with experimental observation.

The effects of partial premixing on the overall mean reaction rates are best illustrated by decomposing the total reaction rate $\overline{\dot{\omega}}_c^*$, shown in Fig.7.11(a), into its individual components: (i) due to premixed combustion mode $\overline{\dot{\omega}}_c$, shown in Fig.7.11(b) and (ii) the partial premixing effects denoted by term (II), shown in Fig.7.11(c). Here the components for Case-D and the stoichiometric mixture fraction contour lines are also shown. From Fig.7.11(b), the two branches of the premixed combustion modes, one for rich and one for mixture close to stoichiometric, can be clearly seen. Flow divergence ahead of the flame, suggested by the deflection in the mixture fraction contour, is also observed. Figure 7.11(c) shows that the diffusive burning contribution is negative and the partial premixing acts as a sink term which reduces the overall reaction rate along stoichiometric mixture contour. The maximum negative contribution is about 30% of the premixed reaction rate. This makes the double branched feature more prominent, as shown

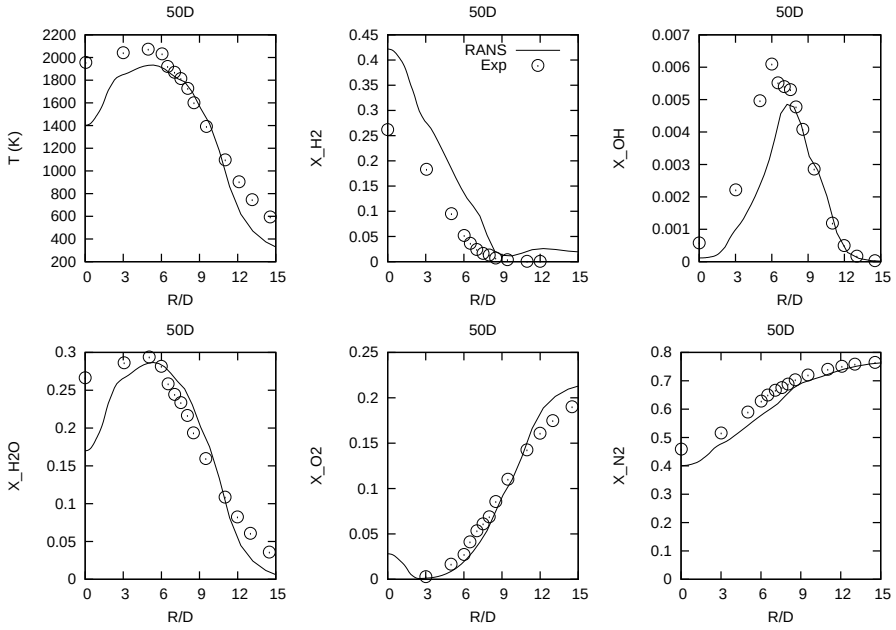

Figure 7.8: Comparison of simulation results and experimental measurements [46] for scalar radial variation at axial position of 50D.

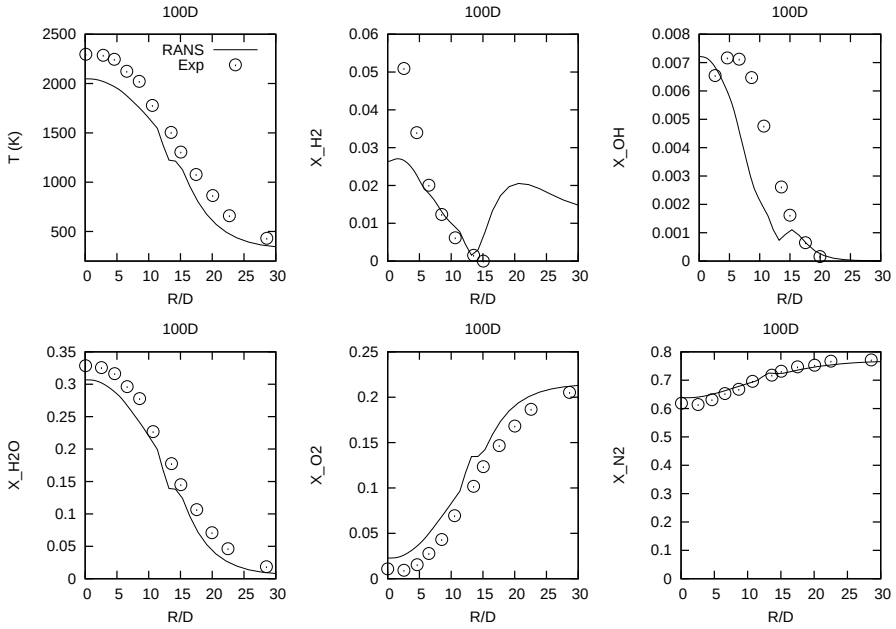

Figure 7.9: Comparison of simulation results and experimental measurements [46] for scalar radial variation at axial position of 100D.

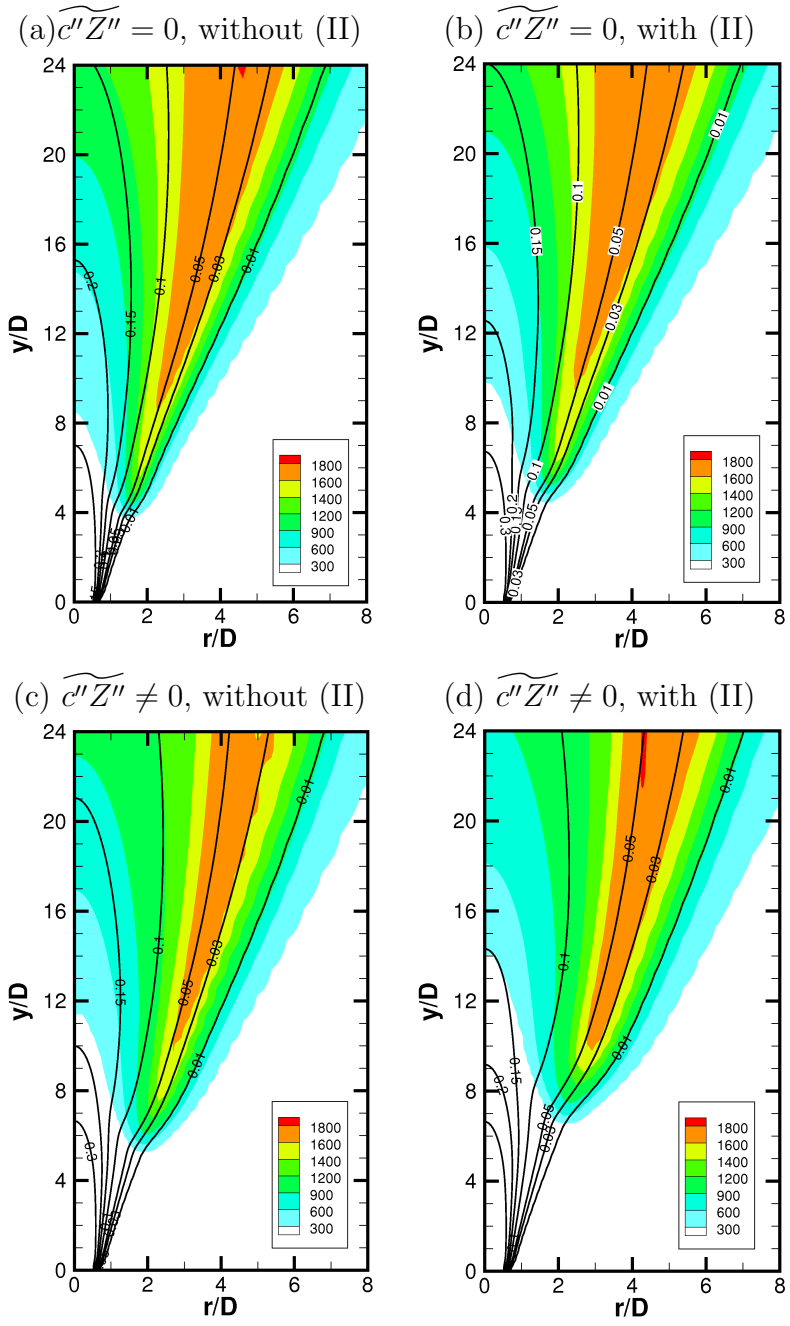

Figure 7.10: Comparison of lift-off heights for four different cases. (a) Case-A, (b) Case-B, (c) Case-C, (d) Case-D.

in Fig.7.11(a). The leading edge of the propagating flame kernel is stabilised in the lean mixture.

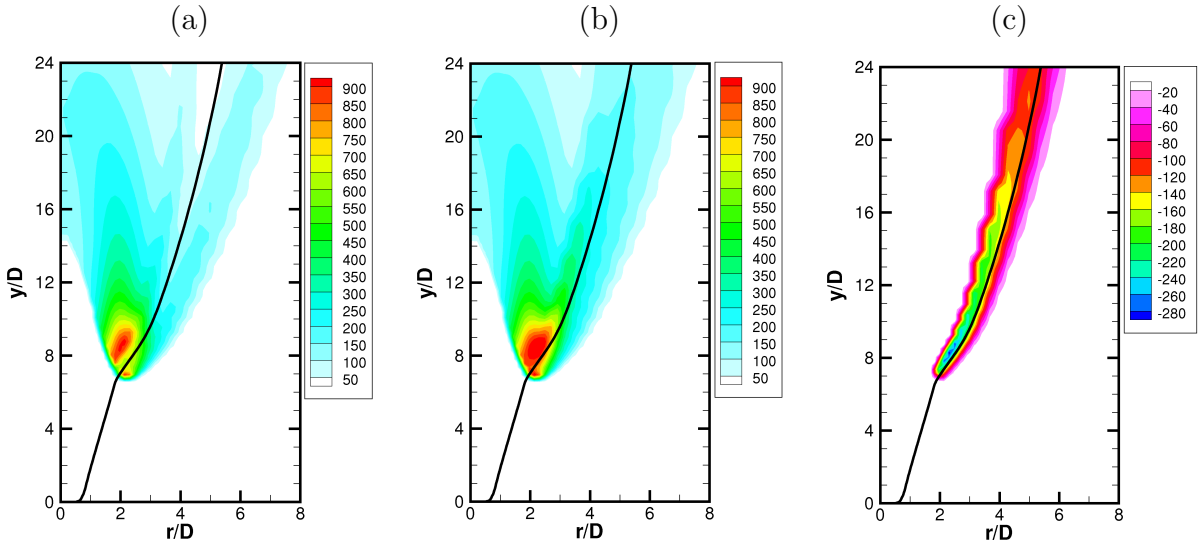

Figure 7.11: Reaction rate for Case-D. (a) Total reaction rate $\overline{\dot{\omega}}_c^*$ in Eq.(7.8). (b) Term (I) $\overline{\dot{\omega}}_c$ in Eq.(7.8). (c) Term (II) as in Eq.(7.9). Reaction rate unit in kg/m^3/s.

The effects of including the correlation between Z and c in $\overline{\dot{\omega}_c}$ can be easily seen in Fig. 7.12 , where the mean reaction rate for Case-A and Case-C are presented. Since no model for term (II) is included in these two cases, the difference is due entirely to the effects of the correlated joint PDF on the mean reaction rate. From Fig. 7.12, it is clear that including the correlation reduces the mean reaction and this leads to an increase in the lift-off height. Including the correlation also makes the flame tip more rounded and the reaction zone slightly broader compared to the case without the correlation. The two branches seen in the uncorrelated case, Fig.7.12(a), become closer and partly merge with each other when the correlation is included as in Fig.7.12(b).

7.3.4 Flame stabilisation

Figure 7.13 presents the temperature fields and the SDR of mixture fraction $\widetilde{\epsilon}_{ZZ}$, normalised by a reference quenching value of 73 s^{-1} [88], near the flame

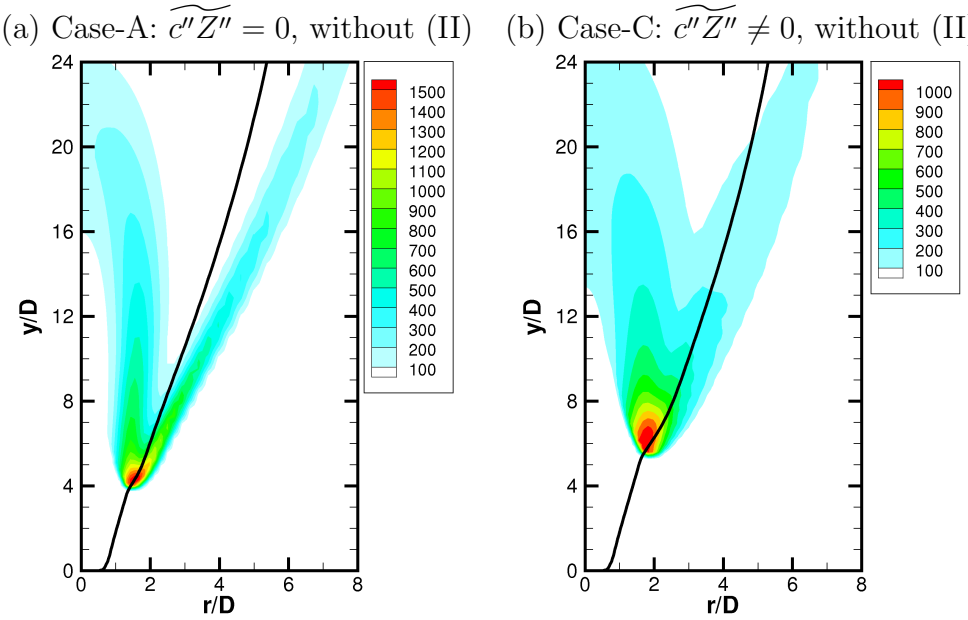

Figure 7.12: Effects of including the correlation between mixture fraction and progress variable in the mean reaction rate. (a) Case-A: $\widetilde{c''Z''} = 0$, without (II), (b) Case-C: $\widetilde{c''Z''} \neq 0$, without (II).

stabilisation region for Case-D. It is clear that the local $\widetilde{\epsilon}_{ZZ}$ is well below the quenching value. The flame leading edge generally experiences a low SDR, about 5% of the quenching value. This is consistent with experimental observation in [24] and the DNS results discussed in chapter 5. Although SDR may not be the single determining factor for flame stabilisation, it is nevertheless an important factor as it affects the mean reaction rate through term (II) in Eq.(6.13).

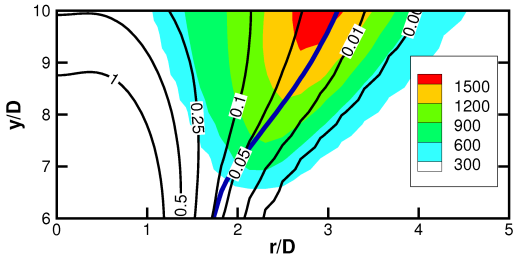

Figure 7.13: Temperature contours with normalised SDR $\widetilde{\epsilon}_{ZZ}$ near the flame stabilisation region for Case-D. Values are normalised by 73/s from laminar flame calculation.

Figure 7.14 presents the temperature isoline for 900K, the covariance $\widetilde{c''Z''}$ and the CDR $\widetilde{\epsilon}_{cZ}$ contour at the flame stabilisation region for Case-D. The flame is stabilised in a slightly lean mixture where the local covariance and the cross dissipation rate are slightly positive and very close to zero. This result is consistent with DNS observation discussed in Chpater 5 and the physical insights shown in Fig.5.1.

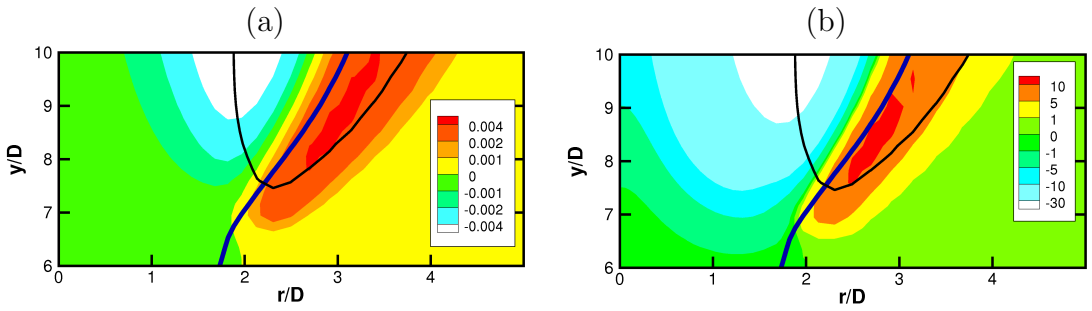

Figure 7.14: Temperature contour at 900K (black line), stoichiometric mixture fraction (blue thick line) with (a) covariance $\widetilde{c''Z''}$, (b) the cross dissipation rate $\widetilde{\epsilon}_{cZ}$, near flame stabilisation region for Case-D.

Figure 7.15 presents the temperature field together with the velocity contours for Case-D near the flame stabilisation region. At the flame leading edge, the local velocity is about 5 m/s, which is the same order of magnitude as the laminar flame speed of stoichiometric hydrogen-air mixture having a reactant temperature equal to the local fluid temperature. It is consistent with experimental observation [129].

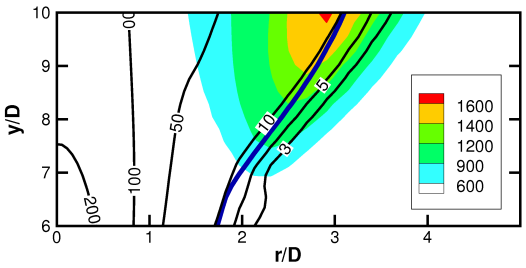

Figure 7.15: Temperature field with velocity in m/s (black thin line) and stoichiometric mixture fraction (blue thick line) for Case-D.

7.3.5 Lift-off height vs jet velocity

Figure 7.16 presents the variation of lift-off heights with jet inlet velocities from the experiments and RANS simulations. The experiment with inlet velocity of 680 m/s has been studied independently by Cheng et al. [46, 47] reporting detailed scalar measurements, and by Brochhinke et al. [24] reporting the lift-off height for various jet inlet velocities. The lift-off heights reported by these two studies for the case of 680 m/s seem to be considerably different (about 1.5D), as shown in the figure.

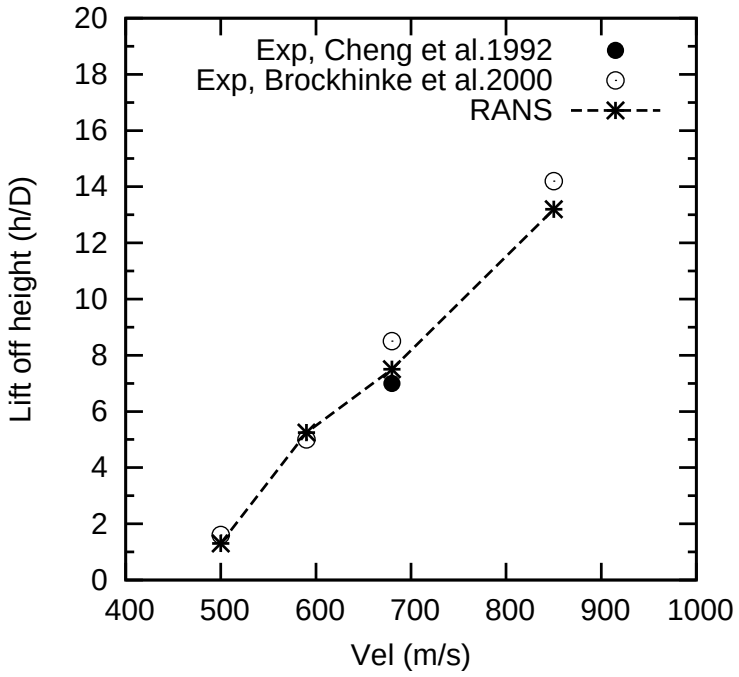

Figure 7.16: Lift-off height versus inlet velocity.

The simulations predict a lift-off height of 1.3D for an inlet velocity of 500 m/s, 5.2D for inlet velocity of 590 m/s and 13D for inlet velocity of 850 m/s with turbulent intensity level at the jet exit specified to be 25%, 15% and 0.1% respectively. Also, the model constant $C_{\epsilon 2} = 1.84$ is used for the case of 850 m/s. Changing the turbulent intensity in this manner has the effect of increasing the turbulent diffusion in the cases of 500 m/s and 590 m/s while decreasing turbulent diffusion in 850 m/s case. Without using these values, the model gives

lift-off heights of 5.2D, 6.5D and 9D respectively. The standard $k-\epsilon$ model parameters are known to produce incorrect flows in the very near field (<2-3D) where self-similarity may not apply in general; as well as in the far field of the self-similar region in a round jet [150]. The turbulence model constant needs to be chosen carefully, either by decreasing $C_{\epsilon 2}$ or increasing $C_{\epsilon 1}$ [150] in order to get the correct turbulent diffusion. Ideally these model constants should be calibrated against experiments of a non-reacting case and then used for the reacting case. Unfortuantely, the flow field information and turbulent boundary conditions are unavailable from the experiments. For lifted flames stabilised close to the jet nozzle, the flow field calculations must be as accurate as possible and therefore LES may be a better candidate than RANS to capture the large scale structures interacting with the flame leading edge and affecting the lift-off height [23, 195]. Nevertheless, the simple but carefully constructed modelling approach used in this chapter gives a reasonable level of agreement with experimental results.

7.4 Summary

In this Chapter, RANS simulations have been performed with various levels of modelling complexity in order to capture the lift-off height and the flame brush structure. It is found that the standard unstrained premixed flamelet model with the assumption of statistical independence between mixture fraction and progress variable tends to overpredict reaction rate and yields a smaller lift-off height. Including the correlation in the joint PDF modelling dramatically changes the mean reaction zones, from distinctly separated lean-rich double branches to more closely merged ones. This results in a decrease in reaction rate and thus an increase of the lift-off height. The effect of partial premixing is included through the term related to N_{zz} and the second derivative $\partial^2 Y^{Eq}/\partial Z^2$. A model is proposed for this term and it is found that it has the effect of decreasing the reaction in the mixture close to stoichiometric value. This results in an increase in the lift-off height. The combined effects of including the correlation in the joint PDF and the effects of partial premixing lead to reasonable agreement with experimental measurement of the lift-off height. The flame brush structure is also reasonably well reproduced. The following points are noted for the flame

stabilisation

- Although the scalar dissipation rate of mixture fraction in the flame leading edge is an order of magnitude smaller than the reference quenching value, it is still an important mechanism as it affects the term related to partial premixing and the diffusion burning contribution, which acts to decrease the mean reaction rate.

- The covariance $\widetilde{c''Z''}$ and cross dissipation rate $\widetilde{\epsilon}_{cZ}$ are close to zero in the flame leading edge due to the change in alignment between the mixture fraction gradient and progress variable gradient at these locations as suggested in Chapter 5.

- The velocity at the flame leading edge is about 3 to 5 m/s, which is the same order of magnitude as the laminar flame speed. This is consistent with experimental observations [129] and support the theory that the balance between partially premixed flame propagation and local flow velocity contribute to the flame stabilisation [105, 114].

Calculations for different inlet velocities are also performed and lift-off heights are found to be affected significantly by inlet turbulence level and turbulent diffusion. Because the flow field information is not available from the experiments, it is difficult to avoid some imprecision in the calculation. However, a reasonable agreement in lift-off heights between simulation and experiments is achieved when the inlet turbulence level is carefully selected. This illustrates the importance of an accurate flow field calculation to get the correct lift-off height and a more advanced approach such as LES which is capable of capturing the large scale structures in the flow field may be required, if the inflow conditions are not fully characterised by experiments.

Chapter 8

Conclusions

The aim of this thesis is to develop an understanding of various physical processes in turbulent partially premixed combustion; to develop and validate models by analysing DNS data and apply these in RANS calculations for partially premixed flames of interest. The main findings of this thesis are summarised here first and avenues for further research are also identified.

8.1 Summary of Main Findings

Chapter 3 first introduced the DNS data of a turbulent hydrogen jet lifted flame that was used in subsequent analyses. By analysing the fuel consumption rates and the flame index, it was shown that there are rich premixed flames with a broad range of equivalence ratio in the jet centre, while increasing numbers of diffusion flame islands exist at the downstream locations along the stoichiometric mixture contour. This confirms the partially premixed nature of this flame.

Chapter 4 investigates the turbulent flame stretch in partially premixed flames, in particular, the tangential strain rate, the displacement speed and the curvature are analysed and their combined effects are explored. The main findings are

- The scalar gradient changes from aligning with the most compressive strain rate to aligning with the most extensive strain in regions where heat release effects dominate the turbulence. This change creates negative normal strain rates which can result in negative surface averaged tangential strain rate.

- The effects of partial premixing result in two additional contributions to the flame surface displacement speed. The first contribution involves the cross dissipation rate and a first derivative in the mixture fraction space, and can be positive or negative depending on the sign of the cross dissipation rate and the local stoichiometry. This contribution is small and can be neglected for the case studied here. The second contribution involves the mixture fraction dissipation rate and a second derivative in the mixture fraction space. Hence its contribution is significant only near the stoichiometric mixture. The source or sink contribution from this term depends on the sign of the second derivative and there is a sink contribution for the definition of c used in this paper.

- The correlation of curvature and displacement speed is found to be negative in general and the effects of partial premixing act to reduce this correlation, but the overall shape of their joint pdf remains similar to those for perfectly premixed flames.

- Temporal variation of the flame surface density, surface averaged tangential strain rate and curvature related term are obtained using an appropriate LES-type filter for the DNS data to study the cause of negative flame stretch. Negative surface averaged tangential strain rates are generally observed in regions where scalar gradient aligns with the most extensive strain. This along with a negative value for the curvature related term, yields negative flame stretch. The contribution of tje curvature related term is observed to be predominantly negative. These observations are supported through a simple analysis of the flame surface density evolution equation.

In Chapter 5, the scalar dissipation rates of the mixture fraction, the progress variable and their cross dissipation were investigated. Their roles in the flame stabilisation process were first studied in a unified framework and their statistical behaviour were studied to shed light on their modelling. It is found that

- $\bar{N}_{ZZ}$ at the flame leading edge is well below the quenching value for the stoichiometric mixture. $\bar{N}_{cc}$ is the same order as that in a stoichiometric unstrained laminar flame.

- The cross dissipation rate $\bar{N}_{cZ}$ changes from negative to weakly positive in the leading edge due to the change in alignment characteristics of the gradients of mixture fraction and progress variable.

- The classical linear relaxation model for the passive scalar dissipation rate $\tilde{\epsilon}_{ZZ}$ gives good agreement with the DNS.

- Models developed based on premixed flames for the reactive scalar dissipation rate $\tilde{\epsilon}_{cc}$ give reasonable results when c is defined with the mass fraction of H_2O.

- The cross dissipation rate $\tilde{\epsilon}_{cZ}$ is mostly negative and can be reasonably approximated at downstream positions once $\tilde{\epsilon}_{ZZ}$ and $\tilde{\epsilon}_{cc}$ are known, although the sign cannot be determined. This approach gives better results than one employing a constant ratio of turbulent timescale to the scalar covariance $\widetilde{c''Z''}$ if the sign is known.

- The statistics of scalar gradients are further examined and lognormal distributions are shown to be very good approximations of the passive scalar and also acceptable for the reactive scalar.

- The correlation between the two gradients increases downstream. A bivariate lognormal distribution is tested and found to be a reasonable approximation of the joint PDF of the two scalar gradients.

Chapter 6 compared four different flamelet/presumed PDFs modelling approaches with the DNS. The turbulent flame front structure from the DNS was compared with laminar unstrained premixed flamelets, strained diffusion flamelets and strained premixed flamelets in the RtP configuration. Various forms of presumed PDFs involved in the modelling approaches were compared with DNS results. The respective performance of the four models for mean reaction rate closure was assessed. It was found that

- Unstrained premixed flamelets compare reasonably with DNS in most parts of this flame.

- Diffusion flamelets only yield good agreement in downstream and radially outward regions where local combustion is predominantly diffusion-controlled
- Strained premixed flamelets tend to have lower reaction rates for the same dissipation rates experienced in the DNS.
- The beta PDF gives a good approximation of both mixture fraction and progress variable.
- For their JPDF, the correlated JPDF model with a "copula" method gives very good results in downstream regions and in the burning part of the flames where correlations are strong and can not be ignored.
- Statistical independence between Z and c is a reasonable approximation only in upstream positions where the flame is stabilised.
- Among the four models, the unstrained premixed flamelet with the correlated JPDF model gives the best prediction of the mean reaction in comparison with the DNS.

In Chapter 7, RANS simulations of turbulent lifted flames were performed with varying degrees of modelling complexity. The liftoff height and the flame structures can be captured reasonably well compared to experiments. It is found that

- The standard unstrained premixed flamelet model with the assumption of statistical independence between mixture fraction and progress variable tends to overpredict reaction and thus a smaller liftoff height.
- Including the correlation of Z and c in the joint PDF modelling changes the characteristics of the double reaction zones and results in a decrease in reaction rate and thus an increase of the liftoff height.
- A new model is proposed for the term related to the effects of partial premixing and diffusion burning contribution on the mean reaction rate. It has the effect of decreasing the reaction in the mixture close to the stoichiometric value. This results in an increase in the liftoff height.

- The combined effects of including the correlation in the joint PDF and the effects of partial premixing yield reasonable agreement with the liftoff height measured in experiments.

The flame stabilisation mechanism has also been explored.

- Although the scalar dissipation rate of mixture fraction in the flame leading edge is an order of magnitude smaller than the reference quenching value, it is still an important quantity as it affects the term related to partial premixing and the diffusion burning contribution, which acts to decrease the mean reaction rate.
- The covariance $\widetilde{c''Z''}$ and cross dissipation rate $\widetilde{\epsilon}_{cZ}$ are close to zero in the flame leading edge due to the change in alignment between the mixture fraction gradient and progress variable gradient.
- The velocity in the flame leading edge is the same order of magnitude as the laminar flame speed which supports the theory that the balance between partially premixed flame propagation and local flow velocity contributes to the flame stabilisation.

Calculations of a range of inlet velocities are also performed and reasonable agreement with liftoff heights from the experiments can be obtained when turbulent intensity level is appropriately changed. For the case studied here ther is no flow field information available from the experiments.

8.2 Future Work

There are several avenues to explore which can further our understanding on the physics of partially premixed combustion and lead to improvements of the models.

- The Scalar Dissipation Rate model of Eq.(5.1) may be improved by studying the effects of changing the model constants, as noted in Chapter 5. Also, this model does not have a Lewis number dependence. Recent advances

[33] in this area can be utilised and tested with this DNS and incorporated into the model.

- Since accurate flow field information is important for lifted flame calculation, and there is an explicit dependence on $\widetilde{k}$ and $\widetilde{\epsilon}$ in the scalar dissipation rate model, it is of interest to test other turbulence models such as $k-\omega$ and the Reynolds stress modelling approach.

- In this thesis, only a hydrogen lifted flame has been calculated using RANS. It is of interest to assess the model's performance for other lifted flames with different fuels.

- The modelling framework needs to be tested for more complex geometry and industrial burners.

- The model can be extended to a LES formulation.

Appendix A

List of Publications

A.1 Journal paper

1. S. Ruan, N. Swaminathan, K.N.C. Bray, Y. Mizobuchi and T. Takeno. "Scalar and its dissipation in the near field of turbulent lifted jet flame", Combustion and Flame, 159 (2012) 591-608.

2. S. Ruan, N. Swaminathan and Y. Mizobuchi. "Investigation of turbulent flame stretch in partially premixed flames with DNS", under review, Physics of Fluids (2012).

3. S. P. Malkeson, S. Ruan, N. Swaminathan and N. Chakraborty. "Statistics of the gradients of reaction progress variable and mixture fraction for turbulent partially premixed flames: A Direct Numerical Simulation study ", under review, Combustion Science and Technology (2013).

A.2 Conference paper

1. S. Ruan and N. Swaminathan. "On the Stabilisation of Turbulent Lifted Flames", Proceedings of 5th European Combustion Meeting (ECM), Cardiff, UK, 2011.

2. H. Kolla, S. Ruan, T. D. Dunstan and N. Swaminathan. "Scalar Gradients and Dissipation Rates in Strained Laminar Premixed flames", Proceedings of 8th Asia-Pacific Conference on Combustion (ASPACC), Hyderabad, India, 2010.

3. S. Ruan and N. Swaminathan. "Modelling of Partially Premixed Turbulent Combustion". Proceedings of 3rd International Forum on Multidisciplinary Education and Research Center for Energy Science, (Energy-GCoE), Ishigaki, Japan, 2010.

4. S. Ruan and N. Swaminathan. "Strained Flamelet Formulation for Partially Premixed Turbulent Flames". Proceedings of 1st International Forum on Multidisciplinary Education and Research Center for Energy Science, (Energy-GCoE), Nikko, Japan, 2008.

A.3 Book Chapter

1. V. K. Veera, M. Masood, S. Ruan, N. Swaminathan and H. Kolla. "Modelling of Turbulent Premixed and Partially Premixed Combustion", in Chapter 7, Advanced Fluid Dynamics, Edited by Hyoung Woo Oh, InTech, 2012.

A.4 In preparation

1. S. Ruan, O. Darbyshire, N. Swaminathan, K.N.C. Bray, Y. Mizobuchi and T. Takeno. "A Priori Assessment of Presumed PDF/Flamelets Mean Reaction Rate Closure for Turbulent Lifted Jet Flames using DNS data".

2. S. Ruan and N. Swaminathan. "RANS simulation of Lifted Jet Flames using Scalar Dissipation Rate Modelling".

References

[1] P. G. Aleiferis, A. M. K. P. Taylor, K. Ishii, and Y. Urata. The nature of early flame development in a lean-burn stratified-charge spark-ignition engine. *Combust. Flame*, 136: 283–302, 2004.

[2] S. Amzin. *Computations of Turbulent Premixed Flames Using Conditional Moment Closure*. PhD thesis, University of Cambridge, 2012.

[3] S. Amzin, N. Swaminathan, J. Rogerson, and J. H. Kent. Conditional moment closure for turbulent premixed flames. *Combust. Sci. Technol.*, 184:1743–1767, 2012.

[4] M. S. Anand and S. B. Pope. Calculations of premixed turbulent flames by pdf methods. *Combust. Flame*, 67:127–142, 1987.

[5] P. Anselmo-Filho, S. Hochgreb, R. S. Barlow, and R. S. Cant. Experimental measurements of geometric properties of turbulent stratified flames. *Proc. Combust. Inst.*, 32: 1763–1770, 2009.

[6] R. A. Antonia and L. W. B. Browne. The destruction of temperature fluctuations in a turbulent plane jet. *J. Fluid Mech.*, 134:67–83, 1983.

[7] R. W. Bilger. The structure of diffusion flames. *Combust. Sci. Technol.*, 13:155–170, 1976.

[8] R. W. Bilger. The structure of turbulent nonpremixed flames. *Proc. Combust. Inst.*, 22: 475–488, 1988.

[9] R. W. Bilger. Conditional Moment Closure for turblent reacting flow. *Phys. Fluids A*, 5: 436–444, 1993.

[10] R. W. Bilger. Some aspects of scalar dissipation. *Flow Turbulence Combust.*, 72:93–114, 2004.

[11] R.W. Bilger, S.B. Pope, K.N.C. Bray, and J.F. Driscoll. Paradigms in turbulent combustion research. *Proc. Combust. Inst.*, 30:21–42, 2005.

[12] R. Borghi. Turbulent premixed combustion: Further discussions on the scales of fluctuations. *Combust. Flame*, 80:304–312, 1990.

[13] D. Bradley. Problems of predicting turbulent burning rates. *Combust. Theory Model.*, 6 (2):361–382, 2002.

[14] D. Bradley, P. H. Gaskell, and A. K. C. Lau. A mixedness-reactedness flamelet model for turbulent diffusion flames. *Proc. Combust. Inst.*, 23:685–692, 1990.

[15] K. N. C. Bray. The interaction between turbulence and combustion. *Proc. Combust. Inst.*, 17:223–233, 1979.

[16] K. N. C. Bray. Turbulent flows with premixed reactants. In P. A. Libby and F. A. Williams, editors, *Turbulent Reacting Flows*, page 115. Springer-Verlag, 1980.

[17] K. N. C. Bray and R. S. Cant. Some applications of Kolmogorov's turbulence research in the field of combustion. *Proc. R. Soc. Lond. A*, 434:217–240, 1991.

[18] K. N. C. Bray and P. A. Libby. Recent developments in the BML model of premixed turbulent combustion. In P. A. Libby and F. A. Williams, editors, *Turbulent Reacting Flows*, pages 115–151. Academic Press, New York, 1994.

[19] K. N. C. Bray and J. B. Moss. A unified statistical model of the premixed turbulent flame. *Acta Astronautica*, 4:291–319, 1977.

[20] K. N. C. Bray and N. Peters. Laminar flamelets in turbulent flames. In P. A. Libby and F. A. Williams, editors, *Turbulent Reacting Flows*, pages 63–113. Academic Press, New York, 1994.

[21] K. N. C. Bray, P. A. Libby, and J. B. Moss. Flamelet crossing frequencies and mean reaction rates in premixed turbulent combustion. *Combust. Sci. Technol.*, 41:143–172, 1984.

[22] K. N. C. Bray, P. Domingo, and L. Vervisch. Role of the progress variable in models for partially premixed turbulent combustion. *Combust. Flame*, 141:431–437, 2005.

[23] J. E. Broadwell, W. J. A. Dahm, and M. G. Mungal. Blowout of turbulent diffusion flames. *Proc. Combust. Inst.*, 20:303–310, 1984.

[24] A. Brockhinke, S. Haufe, and K. Kohse-Höinghaus. Structural properties of lifted hydrogen jet flames measured by laser spectroscopic techniques. *Combust. Flame*, 121:367–377, 2000.

[25] J. Buckmaster. Edge flames. *Prog. Energy Combust. Sci.*, 28:435–475, 2002.

[26] S. M. Candel and T. J. Poinsot. Flame stretch and the balance equation for flame surface area. *Combust. Sci.Technol.*, 70(1-3):1–15, 1990.

[27] R. S. Cant. RANS and LES modelling of premixed turbulent combustion. In T. Echekki and E. Mastorakos, editors, *Turbulent Combustion Modeling*. Springer-Verlag, 2011.

[28] R. S. Cant and E. Mastorakos. *An Introduction to Turbulent Reacting Flows*. Imperial College Press, 2008.

[29] R.S. Cant, S.B. Pope, and K.N.C. Bray. Modelling of flamelet surface-to-volume ratio in turbulent premixed combustion. *Proc. Combust. Inst.*, 23:809–815, 1991.

[30] N. Chakraborty and R. S. Cant. Effects of strain rate and curvature on surface density function transport in turbulent premixed flames in the thin reaction zones regime. *Phys. Fluids*, 17:065108, 2005.

[31] N. Chakraborty and N. Swaminathan. Influence of the Damköhler number on turbulence-scalar interaction in premixed flames. I. physical insight. *Phys. Fluids*, 19:045103, 2007.

[32] N. Chakraborty and N. Swaminathan. Influence of the Damköhler number on turbulence-scalar interaction in premixed flames. II. model development. *Phys. Fluids*, 19:045104, 2007.

[33] N. Chakraborty and N. Swaminathan. Effects of Lewis number on scalar dissipation transport and its modeling in turbulent premixed combustion. *Combust. Sci. Technol.*, 182:1201–1240, 2010.

[34] N. Chakraborty, J. W. Rogerson, and N. Swaminathan. A priori assessment of closures for scalar dissipation rate transport in turbulent premixed flames using Direct Numerical Simulation. *Phys. Fluids*, 20:045106, 2008.

[35] N. Chakraborty, M. Klein, and N. Swaminathan. Effects of lewis number on the reactive scalar gradient alignment with local strain rate in turbulent premixed flames. *Proc. Combust. Inst.*, 32:1409–1417, 2009.

[36] N. Chakraborty, J. W. Rogerson, and N. Swaminathan. The scalar gradient alignment statistics of flame kernels and its modelling implications for turbulent premixed combustion. *Flow Turbulence Combust.*, 85:25–55, 2010.

[37] N. Chakraborty, M. Champion, A. Mura, and N. Swaminathan. Scalar-dissipation-rate approach. In N. Swaminathan and K. N. C. Bray, editors, *Turbulent Premixed Flames*, chapter 2.3, pages 74–102. Cambridge University Press, 2011.

[38] J. H. Chen. Petascale Direct Numerical Simulation of turbulent combustion-fundamental insights towards predictive models. *Proc. Combust. Inst.*, 33:99–123, 2011.

[39] J. H. Chen and H. G. Im. Correlation of flame speed with stretch in turbulent premixed methane/air flames. *Proc. Combust. Inst.*, 27:819–826, 1998.

[40] J. H. Chen and H. G. Im. Stretch effects on the burning velocity of turbulent premixed hydrogen/air flames. *Proc. Combust. Inst.*, 28:211–218, 2000.

[41] M. Chen, M. Herrmann, and N. Peters. Flamelet modeling of lifted turbulent methane/air and propane/air jet diffusion flames. *Proc. Combust. Inst.*, 28:167–174, 2000.

[42] Y-C. Chen and R. W. Bilger. Stabilization mechanisms of lifted laminar flames in axisymmetric jet flows. *Combust. Flame*, 123:23–45, 2000.

[43] Y-C. Chen and R. W. Bilger. Simultaneous 2D imaging measurements of reaction progress variable and OH radical concentration in turbulent premixed flames: Experimental methods and flame brush structure. *Combust. Sci. Technol.*, 167:131–167, 2001.

[44] Y-C. Chen and R. W. Bilger. Simultaneous 2D imaging measurements of reaction progress variable and OH radical concentration in turbulent premixed flames: Instantaneous flame-front structure. *Combust. Sci. Technol.*, 167:187–222, 2001.

[45] Y-C. Chen and R. W. Bilger. Experimental investigation of three-dimensional flame-front structure in premixed turbulent combustion -I: Hydrocarbon/air bunsen flames. *Combust. Flame*, 131:400–435, 2002.

[46] T.S. Cheng, J. A. Wehrmeyer, and R. W. Pitz. Simultaneous temperature and multi-species measurement in a lifted hydrogen diffusion flame. *Combust. Flame*, 91:323–345, 1992.

[47] T.S. Cheng, J.A. Wehrmeyer, and R.W. Pitz. Conditional analysis of lifted hydrogen jet diffusion flame experimental data and comparison to laminar flame solutions. *Combust. Flame*, 150:340–354, 2007.

[48] O. Darbyshire. *Modelling of Turbulent Stratified Flames.* PhD thesis, University of Cambridge, 2011.

[49] O. Darbyshire and N. Swaminathan. A presumed joint pdf model for turbulent combustion with varying equivalence ratio. *Combust. Sci. Technol.*, 184:2036–2067, 2012.

[50] O. R. Darbyshire, N. Swaminathan, and S. Hochgreb. The effects of small-scale mixing models on the prediction of turbulent premixed and stratified combustion. *Combust. Sci. Technol.*, 182:1141–1170, 2010.

[51] C.B. Devaud and K. N. C . Bray. Assessment of the applicability of Conditional Moment Closure to a lifted turbulent flame: first order model. *Combust. Flame*, 132:102–114, 2003.

[52] J. W. Dold. Flame propagation in a nonuniform mixture: Analysis of a slowly varying triple flame. *Combust. Flame*, 76:71–88, 1989.

[53] P. Domingo and L. Vervisch. Triple flames and partially premixed combustion in autoignition of non-premixed turbulent mixtures. *Proc. Combust. Inst.*, 26:233–240, 1996.

[54] P. Domingo, L. Vervisch, and K. N. C. Bray. Partially premixed flamelets in LES of non-premixed turbulent combustion. *Combust. Theory Model.*, 6:529–551, 2002.

[55] P. Domingo, L. Vervisch, and J. Réveillon. DNS analysis of partially premixed combustion in spray and gaseous turbulent flame-bases stabilized in hot air. *Combust. Flame*, 140: 172–195, 2005.

[56] C. Dopazo. Recent development in pdf methods. In P. A. Libby and F. A. Williams, editors, *Turbulent Reacting Flows*, chapter 7, pages 375–474. Academic Press, 1994.

[57] C. Duwig and C. Fureby. Large Eddy Simulation of unsteady lean stratified premixed combustion. *Combust. Flame*, 151:85–103, 2007.

[58] T. Echekki and J. H. Chen. Unsteady strain rate and curvature effects in turbulent premixed methane-air flames. *Combust. Flame*, 106:184–202, 1996.

[59] E. Effelsberg and N. Peters. Scalar dissipation rates in turbulent jets and jet diffusion flames. *Proc. Combust. Inst.*, 22:693–700, 1988.

[60] V. Eswaran and S. B. Pope. Direct Numerical Simulation of the turbulent mixing of a passive scalar. *Phys. Fluids*, 31:506–520, 1988.

[61] V. Favier and L. Vervisch. Investigating the effects of edge flames in liftoff in non-premixed turbulent combustion. *Proc. Combust. Inst.*, 27:1239–1245, 1998.

[62] V. Favier and L. Vervisch. Edge flames and partially premixed combustion in diffusion flame quenching. *Combust. Flame*, 125:788–803, 2001.

[63] S. A. Ferraris and J. X. Wen. Large Eddy Simulation of a lifted turbulent jet flame. *Combust. Flame*, 150:320–339, 2007.

[64] B. Fiorina, O. Gicquel, L. Vervisch, S. Carpentier, and N. Darabiha. Premixed turbulent combustion modelling using tabulated detailed chemistry and pdf. *Proc. Combust. Inst.*, 30:867–874, 2005.

[65] B. Fiorina, O. Gicquel, L. Vervischc, S. Carpentier, and N. Darabiha. Approximating the chemical structure of partially premixed and diffusion counterflow flames using FPI flamelet tabulation. *Combust. Flame*, 140:147–160, 2005.

[66] B. Fiorina, O. Gicquel, and D. Veynante. Turbulent flame simulation taking advantage of tabulated chemistry self-similar properties. *Proc. Combust. Inst.*, 32:1687–1694, 2009.

[67] R.O. Fox. *Computational Models for Turbulent Reacting Flows*. Cambridge University Press, 2003.

[68] F. Gao and E. O' Brien. Joint probability density function of a scalar and its gradient in isotropic turbulence. *Phys. Fluids A*, 3:1625–1632, 1991.

[69] M. Gonzalez and P. Paranthoën. Effect of variable mass density on the kinematics of scalar gradient. *Phys. Fluids*, 23:075107, 2011.

[70] F. C. Gouldin, K. N. C. Bray, and J. Y. Chen. Chemical closure model for fractal flamelets. *Combust. Flame*, 77:241–259, 1989.

[71] I. R. Gran, T. Echekki, and J. H. Chen. Negative flame speed in an unsteady 2-D premixed flame: A computational study. *Proc. Combust. Inst.*, 26:323–329, 1996.

[72] R. W. Grout. *DNS supported modelling for lean and stratified premixed flames*. PhD thesis, University of Cambridge, 2007.

[73] K. Hanjalić and S. Jakirlić. Second-moment turbulence closure modelling. In B. E. Launder and N. D. Sandham, editors, *Closure Strategies for Turbulent and Transitional Flows*, pages 47–101. Cambridge University Press, 2002.

[74] G. Hartung, J. Hult, .C. F. Kaminski, J. W. Rogerson, and N. Swaminathan. Effect of heat release on turbulence and scalar-turbulence interaction in premixed combustion. *Phys. Fluids*, 20:035110, 2008.

[75] E. R. Hawkes and J. H. Chen. Evaluation of models for flame stretch due to curvature in the thin reaction zones regime. *Proc. Combust. Inst.*, 30:647–655, 2005.

[76] D. C. Haworth, R. J. Blint, B. Cuenot, and T. J. Poinsot. Numerical simulation of turbulent propane-air combustion with nonhomogeneous reactants. *Combust. Flame*, 121:395–417, 2000.

[77] D.C Haworth. Progress in probability density function methods for turbulent reacting flows. *Prog. Energy Combust. Sci.*, 36:168–259, 2010.

[78] J. Helié and A. Trouvé. Turbulent flame propagation in partially premixed combustion. *Proc. Combust. Inst.*, 27:891–898, 1998.

[79] M. Herrmann. Numerical simulation of turbulent bunsen flames with a level set flamelet model. *Combust. Flame*, 145:357–375, 2006.

[80] J. B. Heywood. Pollutant formation and control in spark ignition engines. *Prog. Energy Combust. Sci.*, 1:135–164, 1976.

[81] H. G. Im and J. H. Chen. Effects of flow strain on triple flame propagation. *Combust. Flame*, 126:1384–1392, 2001.

[82] C. Jiménez, B. Cuenot, T. J. Poinsot, and D. C. Haworth. Numerical simulation and modeling for lean stratified propane-air flames. *Combust. Flame*, 128:1–21, 2002.

[83] W. P. Jones. Turbulence modelling and numerical solution methods for variable density and combusting flows. In P. A. Libby and F. A. Williams, editors, *Turbulent Reacting Flows*, number 309-347. Academic Press, New York, 1994.

[84] W. P. Jones and B. E. Launder. The prediction of laminarization with a two equation model of turbulence. *Int. J. Heat Mass Transfer.*, 15:301–314, 1972.

[85] W. P. Jones and P. Musonge. Closure of the Reynolds stress and scalar flux equations. *Phys. Fluids*, 31:35893604, 1988.

[86] R. J. Kee, J. F. Grcar, M. D. Smooke, and J. A. Miller. A Fortran program for modeling steady laminar one-dimensional premixed flames. Technical Report SANDS5-8240, Sandia National Laboratories, 1985.

[87] C. A. Kennedy, M. H. Carpenter, and R. M. Lewis. Low-storage, explicit Runge-Kutta schemes for the compressible Navier-Stokes equations. *Appl. Numer. Math.*, 35:117–219, 2000.

[88] I.S. Kim and E. Mastorakos. Simulations of turbulent lifted jet flames with two-dimensional conditional moment closure. *Proc. Combust. Inst.*, 30:911–918, 2005.

[89] S. H. Kim and H. Pitsch. Scalar gradient and small-scale structure in turbulent premixed combustion. *Phys. Fluids*, 19:115104, 1–14, 2007.

[90] P. N. Kioni, B. Rogg, K. N. C. Bray, and A. Linán. Flame spread in laminar mixing layers: The triple flame. *Combust. Flame*, 95:277–290, 1993.

[91] P. N. Kioni, K. N. C. Bray, D. A. Greenhalgh, and B. Rogg. Experimental and numerical studies of a triple flame. *Combust. Flame*, 116:192–206, 1999.

[92] A. Y. Klimenko and R. W. Bilger. Conditional Moment Closure for turbulent combustion. *Prog. Energy Combust. Sci.*, 25:595–687, 1999.

[93] A.Y Klimenko. Multicomponent diffusion of various admixtures in turbulent flow. *Fluid Dyn.*, 25:327331, 1990.

[94] E. Knudsen and H. Pitsch. A general flamelet transformation useful for distinguishing between premixed and non-premixed modes of combustion. *Combust. Flame*, 156:678–696, 2009.

[95] H. Kolla and N. Swaminathan. Strained flamelets for turbulent premixed flames, I: Formulation and planar flame results. *Combust. Flame*, 157:943–954, 2010.

[96] H. Kolla and N. Swaminathan. Strained flamelets for turbulent premixed flames II: Laboratory flame results. *Combust. Flame*, 157:1274–1289, 2010.

[97] H. Kolla, J. W. Rogerson, N. Chakraborty, and N. Swaminathan. Scalar dissipation rate modeling and its validation. *Combust. Sci. Technol.*, 181:518–535, 2009.

[98] W. Kollmann and J. H. Chen. Dynamics of the flame surface area in turbulent non-premixed combustion. *Proc. Combust. Inst.*, 25:1091–1098, 1994.

[99] W. Kollmann and J. H. Chen. Pocket formation and the flame surface density equation. *Proc. Combust. Inst.*, 27:927–934, 1998.

[100] L. W. Kostiuk and K. N. C. Bray. Mean effects of stretch on laminar flamelets in a premixed turbulent flame. *Combust. Sci. Technol.*, 95:193–212, 1993.

[101] A. Kronenburg and M. J. Cleary. Multiple mapping conditioning for flames with partial premixing. *Combust. Flame*, 155:215–231, 2008.

[102] A. Kronenburg and E. Mastorakos. The conditional moment closure model. In T. Echekki and E. Mastorakos, editors, *Turbulent Combustion Modelling*, chapter 5, pages 91–118. Springer, 2011.

[103] B. E. Launder, G. J. Reece, and W. Rodi. Progress in the development of a Reynolds stress turbulence closure. *J. Fluid Mech.*, 68:269–289, 1975.

[104] C. K. Law. *Combustion Physics*. Cambridge University Press, 2006.

[105] C.J. Lawn. Lifted flames on fuel jets in co-flowing air. *Prog. Energy Combust. Sci.*, 35: 1–30, 2009.

[106] S. K. Lele. Compact finite difference schemes with spectral-like resolution. *J. Comput. Phys.*, 103:16–42, 1992.

[107] P. A. Libby and K. N. C. Bray. Countergradient diffusion in premixed turbulent flames. *AIAA J.*, 15:1186–1193, 1981.

[108] P. A. Libby and F. A. Williams. Fundamental aspects and a review. In P. A. Libby and F. A. Williams, editors, *Turbulent Reacting Flows*, chapter 1, pages 1–57. Academic Press, 1994.

[109] P. A. Libby and F. A. Williams. A presumed pdf analysis of partially premixed turbulent combustion. *Combust. Sci. Technol.*, 161:351–390, 2000.

[110] R. P. Lindstedt. Transported probability density function methods for premixed turbulent flames. In N. Swaminathan and K. N. C. Bray, editors, *Turbulent Premixed Flames*, chapter 2.4, pages 102–132. Cambridge University Press, 2011.

[111] A. J. Lock, A. M. Briones, X. Qin, S. K. Aggarwal, I. K. Puri, and U. Hegde. Liftoff characteristics of partially premixed flames under normal and microgravity conditions. *Combust. Flame*, 143:159–173, 2005.

[112] T. F. Lu, J. H. Chen C. S. Yoo and, and C. K. Law. Three-dimensional Direct Numerical Simulation of a turbulent lifted hydrogen jet flame in heated coflow: a chemical explosive mode analysis. *J. Fluid Mech.*, 652:45–64., 2010.

[113] K. H. Luo. A study of partial premixing in flames by Direct Numerical Simulation. *Proc. Euro. Combust. Meeting*, 2003.

[114] K. M. Lyons. Toward an understanding of the stabilization mechanisms of lifted turbulent jet flames: Experiments. *Prog. Energy Combust. Sci.*, 33:211–231, 2007.

[115] B. Magnussen and B. Hjertager. On mathematical modelling of turbulent combustion with special emphasis on soot formation and combustion. *Proc. Combust. Inst.*, 16:719–727, 1977.

[116] S. P. Malkeson and N. Chakraborty. A priori Direct Numerical Simulation of algebraic models of variances and dissipation rates in the context of Reynolds-Averaged Navier Stokes simulation for low Damköhler number patially premixed combustion. *Combust. Sci. Technol.*, 182:960–999, 2010.

[117] S. P. Malkeson and N. Chakraborty. Statistical analysis of displacement speed in turbulent stratified flames: A Direct Numerical Simulation study. *Combust. Sci. Technol.*, 182(11-12):1841–1883, 2010.

[118] S. P. Malkeson and N. Chakraborty. Alignment statistics of active and passive scalar gradients in turbulent stratified flames. *Phys. Rev. E*, 83:046308, 2011.

[119] S. P. Malkeson and N. Chakraborty. Statistical analysis of cross scalar dissipation rate transport in turbulent partially premixed flames: A Direct Numerical Simulation study. *Flow Turbulence Combust.*, 87(2-3):313–349, 2011.

[120] T. Mantel and R. W. Bilger. Some conditional statistics in a turbulent premixed flame derived from Direct Numerical Simulation. *Combust. Sci. Technol.*, 110-111:393–417, 1995.

[121] T. Mantel and R. Borghi. A new model of premixed wrinkled flame propagation based on a scalar dissipation equation. *Combust. Flame*, 96:43–457, 1994.

[122] F. E. Marble and J. E. Broadwell. The coherent flame model of non-premixed turbulent combustion. project Squid TRW-9-PU. Technical report, Purdue University, 1977.

[123] S. M. Martin, J. C. Kramlich, G. Kosály, and J. J Riley. The premixed Conditional Moment Closure method applied to idealized lean premixed gas turbine combustors. *J. Eng. Gas Turb. Power*, 125:895–900, 2003.

[124] N. Miyamoto, H. Ogawa, T. Shudo, and F. Takeyama. Combustion and emissions in a new concept DI stratified charge engine with two-stage fuel injection. *SAE Technical Paper 940675*, 1994. doi: doi:10.4271/940675.

[125] Y. Mizobuchi, S. Tachibana, J. Shinio, S. Ogawa, and T. Takeno. A numerical analysis of the structure of a turbulent hydrogen jet lifted flame. *Proc. Combust. Inst.*, 29:2009–2015, 2002.

[126] Y. Mizobuchi, J. Shinjo, S. Ogawa, and T. Takeno. A numerical study on the formation of diffusion flame islands in a turbulent hydrogen jet lifted flame. *Proc. Combust. Inst.*, 30:611–619, 2005.

[127] H. C. Mongia. Aero-thermal design and analysis of gas turbine combustion systems - current status and future direction. In *AIAA Paper 98-3982*, Cleveland, OH, July 13-15 1998. AIAA/ASME/SAE/ASEE Joint Propulsion Conference and Exhibit, 34th.

[128] C. M. Müller, H. Breitbach, and N. Peters. Partially premixed turbulent flame propagation in jet flames. *Proc. Combust. Inst.*, 25:1099–1106, 1994.

[129] L. Muniz and M. G. Mungal. Instantaneous flame-stabilization velocities in lifted-jet diffusion flames. *Combust. Flame*, 111:16–31, 1997.

[130] A. Mura and R. Borghi. Towards an extended scalar dissipation equation for turbulent premixed combustion. *Combust. Flame*, 133:193–196, 2003.

[131] A. Mura and M. Champion. Relevance of the Bray number in the small-scale modeling of turbulent premixed flames. *Combust. Flame*, 156(3):729 – 733, 2009.

[132] A. Mura, V. Robin, and M. Champion. Modeling of scalar dissipation in partially premixed turbulent flames. *Combust. Flame*, 149:217–224, 2007.

[133] A. Mura, K. Tsuboi, and T. Hasegawa. Modelling of the correlation between velocity and reactive scalar gradients in turbulent premixed flames based on DNS data. *Combust. Theory Model.*, 12:671, 2008.

[134] A. Mura, V. Robin, M. Champion, and T. Hasegawa. Small scale features of velocity and scalar fields in turbulent premixed flames. *Flow Turbulence Combust.*, 82:339–358, 2009.

[135] S. P. Nandula, T. M. Brown, and R. W. Pitz. Measurements of Scalar Dissipation in the Reaction Zones of Turbulent Nonpremixed H2-Air Flames. *Combust. Flames*, 99: 775–783, 1994.

[136] D. A. Nye, J. G. Lee, T.-W Lee, and D. A. Santavicca. Flame stretch measurements during the interaction of premixed flames and kármán vortex streets using PIV. *Combust. Flame*, 105:167–179, 1996.

[137] E. E. O' Brien and T. L. Jiang. The conditional dissipation rate of an initially binary scalar in homogeneous turbulence. *Phys. Fluids A*, 3:3121–2123, 1991.

[138] R. Ovink and A. Lamers. Modelling and calculation of a partially premixed turbulent flame. *Combust. Sci. Technol.*, 149:249–266, 1999.

[139] F. O'Young and R. W. Bilger. Scalar gradient and related quantities in turbulent premixed flames. *Combust. Flame*, 109:682–700, 1997.

[140] N. Peters. Laminar diffusion flamelet models in non-premixed turbulent combustion. *Prog. Energy Combust. Sci.*, 10:319–339, 1984.

[141] N. Peters. The turbulent burning velocity for large-scale and small-scale turbulence. *J. Fluid Mech.*, 384:107–132, 1999.

[142] N. Peters. *Turbulent Combustion*. Cambridge University Press, 2000.

[143] N. Peters and F. A. Williams. Liftoff characteristics of turbulent jet diffusion flames. *AIAA J.*, 21:423–429, 1983.

[144] H. Phillips. Flame in a buoyant methane layer. *Proc. Combust. Inst.*, 10:1277–1283, 1965.

[145] H. Pitsch. Large-Eddy Simulation of turbulent combustion. *Ann. Rev. Fluid Mech.*, 38: 453–482, 2006.

[146] W. M. Pitts. Assessment of theories for the behavior and blowout of lifted turbulent jet diffusion flames. *Proc. Combust. Inst.*, 22:809–816, 1988.

[147] T. Plessing, P. Terhoeven, N. Peters, and M. S. Mansour. An experimental and numerical study of a laminar triple flame. *Combust. Flame*, 115:335–353, 1998.

[148] T. Poinsot and D. Veynante. *Theoretical and Numerical Combustion*. R. T. Edwards, Philadelphia, USA, 2nd edition, 2005.

[149] T. Poinsot, S. Candel, and A. Trouvé. Applications of Direct Numerical Simulation to premixed turbulent combustion. *Prog. Energy Combust. Sci.*, 21:531–576, 1995.

[150] S. B. Pope. An explanationof the turbulent round-jet/plane-jet anomaly. *AIAA J.*, pages 279–281, 1978.

[151] S. B. Pope. A Monte Carlo method for the pdf equation of turbulent reacting flow. *Combust. Sci. Technol.*, 25:159–174, 1981.

[152] S. B. Pope. Pdf methods for turbulent reacting flows. *Prog. Energy Combust. Sci.*, 11: 119–192, 1985.

[153] S. B. Pope. The evolution of surfaces in turbulence. *Int. J. Engng. Sci.*, 5:445–469, 1988.

[154] S. B. Pope. Computations of turbulent combustion: Progress and challenges. *Proc. Combust. Inst.*, 23:591–612, 1990.

[155] S. B. Pope. *Turbulent Flows*. Cambridge University Press, 2000.

[156] I. K. Puri, S. K. Aggarwal, S. Ratti, and R. Azzoni. On the similitude between lifted and burner-stabilized triple flames: A numerical and experimental investigation. *Combust. Flame*, 124:311–325, 2001.

[157] B. Renou, A. Boukhalfa, D. Puechberty, and M. Trinité. Effects of stretch on the local structure of freely propagating premixed low-turbulent flames with various lewis numbers. *Proc. Combust. Inst.*, 27:841–847, 1998.

[158] G. Ribert, M. Champion, and P. Plion. Modeling turbulent reactive flows with variable equivalence ratio: Application to the calculation of a reactive shear layer. *Combust. Sci. Technol.*, 176:907–923, 2004.

[159] E. S. Richardson, R. Sankaran, R. W. Grout, and J. H. Chen. Numerical analysis of reaction-diffusion effects on species mixing rates in turbulent premixed methane-air combustion. *Combust. Flame*, 157:506–515, 2010.

[160] V. Robin, A. Mura, M. Champion, and P. Plion. A multi-dirac presumed pdf model for turbulent reactive flows with variable equivalence ratio. *Combust. Sci. Technol.*, 178: 1843–1870, 2006.

[161] V. Robin, A. Mura, M. Champion, O. Degardin, B. Renou, and M. Boukhalfa. Experimental and numerical analysis of stratified turbulent V-shaped flames. *Combust. Flame*, 153:288–315, 2008.

[162] J. W. Rogerson and N. Swaminathan. Correlation between dilatation and scalar dissipation in turbulent premixed flames. *Proc. European Combustion Meeting 2007*, 2007.

[163] S. Ruan, N. Swaminathan, K. N. C. Bray, Y. Mizobuchi, and T. Takeno. Scalar and its dissipation in the near field of turbulent lifted jet flame. *Combust. Flame*, 159:591–608, 2012.

[164] G. R. Ruetsch, L. Vervisch, and A. Linán. Effects of heat release on triple flames. *Phys. Fluids*, 7 (6):1447–1454, 1995.

[165] C. J. Rutland and A. Trouvé. Direct simulations of premixed turbulent flames with nonunity Lewis numbers. *Combust. Flame*, 94:41–57, 1993.

[166] J. P. H. Sanders and I. Gökalp. Scalar dissipation rate modelling in variable density turbulent axisymmetric jets and diffusion flames. *Phys. Fluids*, 10 (4):938–948, 1998.

[167] R. W. Schefer, M. Namazian, and J. Kelly. Stabilization of lifted turbulent-jet flames. *Combust. Flame*, 99:75–86, 1994.

[168] D. B. Spalding. Concentration fluctuations in a round turbulent free jet. *Chem. Eng. Sci.*, 26:95–107, 1971.

[169] D. B. Spalding. *Combustion and Mass Transfer*. Oxford University Press, 1979.

[170] S. Sreedhara, K.Y. Huh, and D.H. Ahn. Comparison of submodels for conditional velocity and scalar dissipation in CMC simulation of piloted jet and bluff body flames. *Combust. Flame*, 152:282–286, 2008.

[171] A. M. Steinberg, J. F. Driscoll, and N. Swaminathan. Statistics and dynamics of turbulence-flame alignment in premixed combustion. *Combust. Flame*, 159:2576–2588, 2012. doi: 10.1016/j.combustflame.2011.12.001.

[172] L. K. Su and N. T. Clemens. Planar measurements of the full three-dimensional scalar dissipation rate in gas-phase turbulent flows. *Exp. Fluids*, 27:507–521, 1999.

[173] L. K. Su and N. T. Clemens. The structure of fine-scale scalar mixing in gas-phase planar turbulent jets. *J. Fluid Mech.*, 488:1–29, 2003.

[174] N. Swaminathan and R. W. Bilger. Scalar dissipation, diffusion and dilatation in turbulent H2-air premixed flames with complex chemistry. *Combust. Theory Model.*, 5:429–446, 2001.

[175] N. Swaminathan and R. W. Bilger. Analyses of Conditional Moment Closure for turbulent premixed flames. *Combust. Theory Model.*, 5:241–260, 2001.

[176] N. Swaminathan and K. N. C. Bray. Effect of dilatation on scalar dissipation in turbulent premixed flames. *Combust. Flame*, 143:549–565, 2005.

[177] N. Swaminathan and K. N. C Bray, editors. *Turbulent Premixed Flames*. Cambridge University Press, 2011.

[178] N. Swaminathan and R. W. Grout. Interaction of turbulence and scalar fields in premixed flames. *Phys. Fluids*, 18(4):045102, 2006.

[179] N. Swaminathan, R. W. Bilger, and B. Cuenot. Relationship between turbulent scalar flux and conditional dilatation in premixed flames with complex chemistry. *Combust. Flame*, 126:1764–1779, 2001.

[180] H. Tennekes and J. L. Lumley. *A First Course in Turbulence*. MIT Presss, 1972.

[181] C. Trevino and F. Mauss. Reduced kinetic mechanisms for premixed hydrogen flames. In Norbert Peters and Bernd Rogg, editors, *Reduced kinetic mechanisms for applications in combustion systems*, pages 159–176. Springer-Verlag, 1993.

[182] A. Trouvé and T.J. Poinsot. The evolution equation for the flame surface density in turbulent premixed combustion. *J. Fluid Mech.*, 278:1–31, 1994.

[183] A. Upatnieks, J.F. Driscoll, C.C. Rasmussen, and S.L. Ceccio. Liftoff of turbulent jet flames-assessment of edge flame and other concepts using cinema-PIV. *Combust. Flame*, 138:252–272, 2004.

[184] J. A. van Oijen and L. P. H. de Goey. Modelling of premixed laminar flames using flamelet-generated manifolds. *Combust. Sci. Technol.*, 161:113–137, 2000.

[185] L. Vanquickenborne and A. van Tiggenlen. The stabilisation mechanism of lifted diffusion flames. *Combust. Sci. Technol.*, 10:59–69, 1966.

[186] L. Vervisch and T. Poinsot. Direct Numerical Simulation of non-premixed turbulent flames. *Ann. Rev. Fluid Mech.*, 30:655–691, 1998.

[187] L. Vervisch, E. Bidaux, K. N. C. Bray, and W. Kollmann. Surface density function in premixed turbulent combustion modeling, similarities between probability density function and flame surface approaches. *Phys. Fluids*, 7(10):2496–2503, 1995.

[188] L. Vervisch, R. Hauguel, P. Domingo, and M. Rullaud. Three facets of turbulent combustion modelling: DNS of premixed V-flame, LES of lifted nonpremixed flame and RANS of jet-flame. *J. Turbulence*, 5:004, 2004.

[189] D. Veynante and L. Vervisch. Turbulent combustion modelling. *Prog. Energy Combust. Sci.*, 28:193–266, 2002.

[190] A. W. Vreman, B. A. Albrecht, J. A. van Oijen, L. P. H. de Goey, and R. J. M. Bastiaans. Premixed and nonpremixed generated manifolds in Large Eddy Simulation of Sandia flame D and F. *Combust. Flame*, 153:394–416, 2008.

[191] K. A. Watson, K. M. Lyons, J. M. Donbar, and C. D. Carter. Observations on the leading edge in lifted flame stabilization. *Combust. Flame*, 119:199–202, 1999.

[192] C. K. Westbrook. Hydrogen oxidation kinetics in gaseous detonations. *Combust. Sci. Technol.*, 29:67–82, 1982.

[193] H. Yamashita, M. Shimada, and T. Takeno. A numerical study on flame stability at the transition point of jet diffusion flames. *Proc. Combust. Inst.*, 26:27–34, 1996.

[194] Chun Sang Yoo, Edward S. Richardson, Ramanan Sankaran, and Jacqueline H. Chen. A DNS study on the stabilization mechanism of a turbulent lifted ethylene jet flame in highly-heated coflow. *Proc. Combust. Inst.*, 33:1619–1627, 2011.

[195] C.S. Yoo, R. Sankaran, and J.H. Chen. Three-dimensional Direct Numerical Simulation of a turbulent lifted hydrogen jet flame in heated coflow: flame stabilization and structure. *J. Fluid Mech.*, 640:453–481, 2009.